PNNL-17305

Pacific Northwest
National Laboratory
Operated by Battelle for the
U.S. Department of Energy

Advanced Large-Area Plastic Scintillator Project (ALPS): Final Report

DV Jordan
PL Reeder
LC Todd
GA Warren
KR McCormick
DL Stephens, Jr.
BD Geelhood
JM Alzheimer
SL Crowell
WA Sliger

July 2007

Prepared for the U.S. Department of Energy
under Contract DE-AC05-76RL01830

DISCLAIMER

This report was prepared as an account of work sponsored by an agency of the United States Government. Neither the United States Government nor any agency thereof, nor Battelle Memorial Institute, nor any of their employees, makes **any warranty, express or implied, or assumes any legal liability or responsibility for the accuracy, completeness, or usefulness of any information, apparatus, product, or process disclosed, or represents that its use would not infringe privately owned rights**. Reference herein to any specific commercial product, process, or service by trade name, trademark, manufacturer, or otherwise does not necessarily constitute or imply its endorsement, recommendation, or favoring by the United States Government or any agency thereof, or Battelle Memorial Institute. The views and opinions of authors expressed herein do not necessarily state or reflect those of the United States Government or any agency thereof.

PACIFIC NORTHWEST NATIONAL LABORATORY
operated by
BATTELLE
for the
UNITED STATES DEPARTMENT OF ENERGY
under Contract DE-ACO5-76RL01830

PNNL-17305

Advanced Large-Area Plastic Scintillator Project (ALPS): Final Report

Project P.I.: D.V. Jordan

Report contributors: P.L. Reeder, D.V. Jordan, L.C. Todd, G.A. Warren

Project team: P.L. Reeder, K.R. McCormick, D.L. Stephens, G.A. Warren, B.D. Geelhood, L.C. Todd, J.M. Alzheimer, S.L. Crowell, W.A. Sliger

July 2007

Prepared for the U.S. Department of Energy
under Contract DE-AC05-76RL01830

Pacific Northwest National Laboratory
Richland, Washington 99352

Executive Summary

The Advanced Large-area Plastic Scintillator (ALPS) project at Pacific Northwest National Laboratory investigated possible technological avenues for substantially advancing the state-of-the-art in gamma-ray detection via large-area plastic scintillators. The three predominant themes of these investigations comprised the following:

- Maximizing light collection efficiency from a single large-area sheet of plastic scintillator, and optimizing hardware event trigger definition to retain detection efficiency while exploiting the power of coincidence to suppress single-PMT "dark current" background;
- Utilizing anti-Compton vetoing and supplementary spectral information from a co-located secondary, or "Back" detector, to both (1) minimize Compton background in the low-energy portion of the "Front" scintillator's pulse-height spectrum, and (2) sharpen the statistical accuracy of the front detector's low-energy response prediction as implemented in suitable energy-windowing algorithms; and
- Investigating alternative materials to enhance the intrinsic gamma-ray detection efficiency of plastic-based sensors.

Activities in early phases of the ALPS project [Jordan et al. 2003, Reeder et al. 2003] included (a) Monte Carlo modeling of light collection properties of various configurations of plastic scintillator and photomultiplier tubes (PMTs), and (b) design, fabrication, and testing of a large-area, unwrapped plastic scintillator sensor housed in a light-tight box intended for laboratory experimentation (the so-called "ALPS I"). The main goals of the ALPS I experimental campaign were to quantify the energy deposition resolution improvement afforded by the increase in PMT coverage of a scintillator sheet's edge area, and to understand the variation in pulse height response as a function of the primary ionizing radiation's interaction position within the plastic scintillator sheet. These laboratory experiments indicated roughly a 60% improvement in the Compton-edge energy resolution (for the 835 keV gamma from ^{54}Mn) as the PMT coverage increased from a single PMT to six PMTs, with only a small improvement resulting from the increase from 4 to 6 PMTs (see Figure S1).

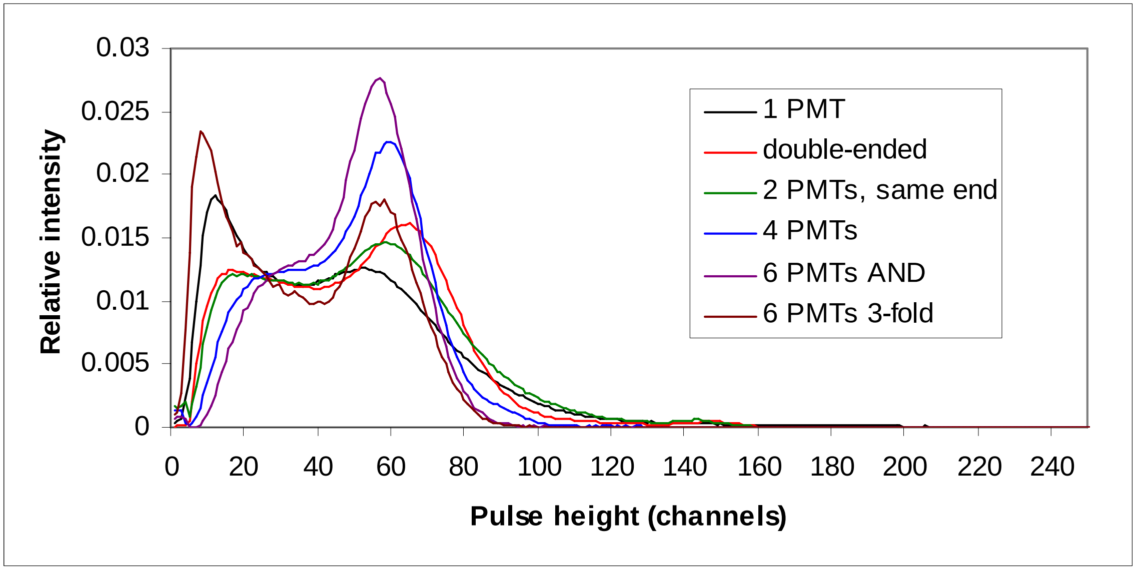

Figure S1. ^{54}Mn gamma pulse-height spectra recorded with the ALPS I sensor. Six PMT configurations are compared: Single PMT; 2 PMTs at opposite ends ("double-ended"); 2 PMTs at same scintillator end; 4 PMTs (two at each end); 6 PMTs with trigger configured to require coincident firing of all 6 ("AND"); and 6 PMTs with readout electronics configured to take the hardware sum of 3 PMTs at each end ("3-fold").

The present report details the design, fabrication and testing of a field-deployable version of the ALPS, referred to herein as the "ALPS II". The ALPS II consists of dual slabs of Bicron/Saint Gobain BC-408 scintillators of dimensions 127 × 57.15 × 5.08 cm^3 separated by a gap of 13 cm. The two slabs are referred to as the "Front" (F) and "Back" (B) detectors, respectively. In contrast to the ALPS I sensor, which was housed in a light-tight box, the PVT slabs of the ALPS II are mounted vertically in a light-tight, Pb-lined, steel-walled enclosure representative of a field-deployable radiation portal monitor (RPM) form factor. The sensor system and accompanying rack-mounted readout electronics are mounted on a pallet for convenient transport and outdoor deployment. As in the laboratory version of the sensor, each scintillator slab is outfitted with 3 Hamamatsu R1250 127-mm (5-in.) diameter PMTs mounted on each end, for a total of 12 PMTs. The scintillators are mounted vertically and shielded on the bottom, sides, and back by 5.08-cm of lead. A light-tight plastic panel on the front of the steel enclosure door permits entry of gammas to the scintillator detectors through material of low-Z.

A variety of gamma-ray point-source measurements were performed in order to quantify the detection sensitivity of the ALPS II sensor. Two types of instrument response were investigated: (1) the "single-sheet" response, in which the detection sensitivity of the Front detector alone was mapped as a function of PMT coverage; and (2) the "dual-sheet" response, which measured the impact of the co-located Back detector, employed as an anti-coincidence Compton veto and/or a supplementary source of spectral information on the high-energy portion of the incident gamma-ray flux. Table S1 summarizes the variation in single-sheet detection sensitivity as a function of PMT coverage. The minimum detectable activity (MDA) is computed using several algorithms:

- A spectral (two energy-window) algorithm that uses the high-energy response in the Front detector to predict its low-energy response, based upon the previously-measured ratio of these responses for terrestrial background;
- A gross-count algorithm that uses the count sum of the entire measured spectrum, and assumes that the terrestrial background flux is unaltered during the source measurement (e.g., a vehicle traversal in an RPM application);
- A "narrow-window" algorithm, intermediate between the spectral and gross-count algorithms, that defines the same low-energy window containing the source counts of interest, but does not use the high-energy response to predict the background in the low-energy window (assuming instead, as in the gross-count algorithm, that this background is unaltered during the sensor traversal).

Table S1. ALPS II Single-sheet ^{57}Co and ^{133}Ba MDAs for various MDA algorithms, 99% detection probability (DP), 0.1% false alarm probability (FAP).

	^{57}Co MDA (microCi)			^{133}Ba MDA (microCi)		
# PMTs	Spectral (2-window) Algorithm	Narrow-window Algorithm	Gross-count	Spectral (2-window) Algorithm	Narrow-window Algorithm	Gross-count
6	1.35	0.82	1.05	1.49	0.57	0.65
4	1.34	0.86	1.13	1.45	0.58	0.68
2 (opposite)	1.39	0.92	1.21	1.52	0.60	0.66
2 (same)	1.35	0.90	1.19	1.54	0.67	0.74
1	2.48	1.17	1.36	2.66	0.72	0.77

Although the results indicate that single-sheet readout schemes consisting of two or more PMTs have markedly greater sensitivity than a single-PMT readout scheme, relatively little further improvement in detection sensitivity results from increasing the number of PMTs beyond two. This evaluation depends to some extent upon the MDA algorithm used and, in turn, upon the portal monitor application of interest. For example, the spectral (two energy-window) algorithm is expected to be most relevant to RPM scenarios in which attenuation of the terrestrial gamma-ray flux during a vehicle traversal ("baseline suppression") can seriously compromise the sensitivity of gross-counting alarms. The measured ALPS results indicate that this type of spectral source-detection algorithm is relatively insensitive to improvements in PMT coverage beyond the two-PMT configuration. One important reason for this insensitivity is that, as the light collection efficiency increases, both the source gamma-ray detection efficiency *and* the terrestrial background detection efficiency increase. These competing effects partially cancel each other, so that the single-sheet MDA does not improve linearly with the PMT coverage.

The primary physical motivation for a dual-sheet sensor is to exploit anti-Compton vetoing as a means of minimizing low-energy continuum background in the Front scintillator arising from Compton-scattering of relatively high-energy terrestrial background gamma rays. To implement the anti-Compton veto, events in which a high-energy scattering event is observed in the Back detector *in coincidence* with a low-energy event in the Front detector are rejected. Care must be taken to minimize unintentional "over-vetoing" of source-generated gamma-rays of interest that deposit only a small amount of energy in the Front scintillator, then fire the Back detector. One means of avoiding this is the insertion of a gamma-absorbing material between the two detectors. The main experimental results for the dual-sheet ALPS II sensor response, in which the co-located Back detector provides anti-Compton vetoing of background events in the Front detector, can be summarized briefly as follows:

1. The anti-coincidence gating system resulted in 10% to 15% fewer background counts in the low-energy pulse height region.
2. The detection efficiency for low-energy gamma sources is not significantly compromised by the imposition of the anti-coincidence requirement, provided an intermediate shield is used between the Front and Back detectors.
3. There is a significant reduction of the count rates in the low-energy region due to sources emitting high-energy gammas. The size of the reduction depends on whether or not an intermediate shield is used between the Front and Back detectors.
4. The present data indicate that the background reduction factor increases rapidly as the energy of the gamma increases. Thus the reduction factor for ^{40}K (1461 keV), which is a common interference when looking for low-energy sources, might be much greater than the reduction factor of about 25-40% observed here for ^{54}Mn (835 keV). Depending on whether or not an intermediate shield is used, an additional reduction of about 12-15% of the environmental background can be obtained.

Tables S2 and S3 summarize the impact of anti-Compton vetoing on the ALPS II low-energy detection sensitivity for ^{57}Co and ^{133}Ba sources, respectively. The tables compare several sensor configurations and MDA algorithms: The “ALPS” configuration refers to the standard ALPS II sensor, consisting of dual sheets of PVT scintillator, with or without a thin (1/8”) Pb absorber placed between the detector sheets. The acronym “CASP” (Cherenkov And Scintillator Portal) refers to an alternative configuration in which the Back detector consists of a plastic sheet (Bicron/Saint Gobain BC-499-76 blue wavelength shifting plastic) designed to respond only to the Cherenkov radiation emitted by high-energy electrons following a gamma-ray interaction in the plastic. The motivation for this technique is to avoid the “over-vetoing” effect not by using a passive absorber, but by relying on the fact that low-energy gammas that Compton scatter in the Front detector will not produce a scattered gamma with sufficient energy to produce Cherenkov light from a second scattering in the Back detector. Conversely, higher-energy gammas that scatter in the Front detector and deposit a relatively small amount of energy in the low-energy window will retain sufficient energy to produce Cherenkov light following a second Compton scatter in the Back detector.

Table S2. ALPS II and CASP dual-sheet ^{57}Co MDAs for various sensor configurations, trigger conditions, and MDA algorithms, 99% DP, 0.1% FAP.

Configuration	Hardware Trigger Logic	Intrinsic Efficiency (%)	Background Rate (cps)	^{57}Co MDA (microCi)		
				Spectral (2-window) Algorithm	Dual-sheet Spectral Algorithm	Gross-count
ALPS, Pb in	F OR B	54.5	4840	1.41	1.26	1.12
ALPS, Pb in	F AND (~B)	54.2	4800	1.39	--	1.10
ALPS, Pb out	F OR B	48.6	4390	1.59	1.37	1.22
ALPS, Pb out	F AND (~B)	48.4	4440	1.54	--	1.18
CASP	F OR B	56.8	5330	1.45	--	1.13
CASP	F AND (~B)	55.0	5430	1.49	--	1.17

Table S3. ALPS II and CASP dual-sheet ^{133}Ba MDAs for various sensor configurations, trigger conditions, and MDA algorithms, 99% DP, 0.1% FAP.

Configuration	Hardware Trigger Logic	Intrinsic Efficiency (%)	Background Rate (cps)	^{133}Ba MDA (microCi)		
				Spectral (2-window) Algorithm	Dual-sheet Spectral Algorithm	Gross-count
ALPS, Pb in	F OR B	32.7	4740	1.57	1.29	0.68
ALPS, Pb in	F AND (~B)	32.3	4800	1.57	--	0.68
ALPS, Pb out	F OR B	27.9	4380	1.78	1.41	0.78
ALPS, Pb out	F AND (~B)	28.5	4430	1.69	--	0.73
CASP	F OR B	35.3	5340	1.56	--	0.67
CASP	F AND (~B)	33.9	5420	1.64	--	0.70

The detection sensitivity analysis indicates that the benefits of anti-Compton vetoing as a means of enhancing low-energy source detection sensitivity in the presence of typical terrestrial gamma-ray backgrounds are modest, whether implemented using standard PVT or a Cherenkov plastic slab as the co-located "Back" detector. However, as noted above, the ALPS II measurement results indicate that the background suppression capability of the dual-sheet sensor increases as the gamma energy increases. Thus for relatively high-energy radioisotopes (such as ^{40}K) contained in naturally occurring radioactive materials (NORM), anti-Compton vetoing may provide a substantially more effective background mitigation technique than the terrestrial-background MDA analysis presented here would suggest.

Exploiting spectral information from the Back detector, in contrast to using it as an anti-Compton veto, yields an appreciable enhancement in low-energy detection sensitivity (in the presence of typical terrestrial background), on the order of 10% to 20% for ^{57}Co and ^{133}Ba sources, respectively. This is evident from the column labeled "Dual-sheet Spectral Algorithm" in Tables S2 and S3, representing the MDA computed when high-energy spectral information from the Back scintillator (in the standard ALPS II configuration) is exploited to sharpen the statistical precision of the Front detector's predicted low-energy response in the spectral (two energy-window) source detection algorithm. (This Back-sheet spectral information is available when the hardware trigger is configured to record data if either Front or Back sheets fire, as denoted by "F OR B" in the table. The hardware veto trigger "F AND (~B)", in contrast, does not result in collection of the Back-sheet spectrum required for this approach.) The experimental work performed in this project alone, however, cannot rule out the possibility that similar (or better) sensitivity enhancements could be achieved simply by using a single scintillator slab with substantially greater thickness than the 2" (5.08 cm) slabs used in the ALPS sensor.

A final theme of the ALPS research, conducted in parallel with the ALPS II experimental campaign, was a laboratory investigation of the feasibility of applying Pb-loaded plastic scintillator to large-area sensors. The motivation for this investigation is that the addition of a high-Z element to plastic scintillator in modest (e.g. 2% to 10%) proportions offers substantial increases in gamma interaction probability at energies below about 200 keV. Experiments were performed using a cylindrical, 50-cm long, Pb-loaded (5% loading by weight) PVT scintillator rod acquired from Bicron/Saint Gobain (BC-452). Light attenuation and gamma sensitivity were studied in this cylindrical geometry. The primary goal of these measurements was to rapidly acquire experience with Pb-loaded plastic in a low-risk geometry that would indicate the potential utility (or lack thereof) of the material as an alternative to PVT in large-area, monolithic slab geometry. These rod-geometry studies were conducted in a “double-ended” readout configuration, i.e. PMTs were mounted at both ends of the Pb-loaded scintillator rod. Similar studies were conducted with an unloaded plastic scintillator rod (BC-408) of identical dimensions to serve as a basis for comparison in order to extract as directly as possible the effects of the Pb loading. The measurement results indicate that the optical attenuation length of the Pb-loaded plastic is roughly an order of magnitude smaller than in standard BC-408 scintillator. The anticipated increase in photopeak efficiency for low-energy gammas (relative to standard PVT) was insufficient to compensate for the reduced light transmission in even these relatively short (50-cm) samples. Thus it appears unlikely that currently-available Pb-loaded PVT offers a promising candidate for monolithic slabs of dimensions useful for RPM applications.

Overall, the ALPS project demonstrated only modest improvements in PVT MDA at low energy as functions of (1) the number of PMTs participating in an (optimal) hardware trigger, and (2) the availability of anti-Compton veto and/or supplementary spectral information from a co-located monolithic detector. In particular, although single-sheet readout schemes consisting of two or more PMTs were shown to have markedly greater sensitivity than a single-PMT readout scheme, relatively little further improvement in detection sensitivity resulted from increasing the number of PMTs beyond two. These results suggest that, in general, it is unlikely that the low-energy detection sensitivity *per se* of PVT can be substantially improved for typical RPM applications. This evaluation depends to some extent upon the MDA algorithm used and, in turn, upon the portal monitor application of interest. For large-vehicle traversals of RPMs in which the vehicle itself significantly attenuates the terrestrial background incident on the sensor, the use of an energy-windowing algorithm is intended to mitigate the effect of “baseline suppression” that can severely limit the sensitivity of simple gross-count algorithms. The improvement in light collection efficiency and energy-deposition resolution afforded by the ALPS sensor’s increased PMT coverage was not found to yield corresponding sensitivity benefits to this type of two-window algorithm. However, an alternative spectral algorithm that assumes an *unattenuated* terrestrial background distribution during the RPM traversal can benefit significantly from the reduction in ROI width afforded by improved resolution. The effects of baseline suppression can be safely ignored in this limit, which is expected to describe most passenger-automobile and human foot-traffic scenarios to a reasonable approximation. Enhanced-resolution PVT readout schemes, such as those developed in this project, may well offer an attractive means of improving source detection sensitivity in sensors intended for these applications.

In contrast to the limited prospects for low-energy detection sensitivity enhancement, the project results indicate that substantial improvements in the source characterization capability of PVT are possible. Note that PVT suffers from two significant disadvantages as a spectroscopic detector material: low average Z (and thus, correspondingly poor photopeak fraction for reasonable sensor thickness), and poor energy resolution. As summarized above, investigations of Pb-loaded PVT offer little promise for this particular material as a practical means of remedying the photopeak efficiency shortfall in large-area, monolithic-geometry sensors. However, as Figure S1 indicates, there is no question that a sufficient increase in light collection efficiency can yield a dramatic improvement in energy-deposition resolution (on the order of 60% improvement, for a six-PMT readout in comparison to a single PMT) for a large-area plastic scintillator sensor. That this resolution enhancement is achievable without sacrificing intrinsic detection efficiency, via application of an appropriate “multiplicity” trigger in which any two PMTs firing in coincidence suffices to register a valid event, is a significant project outcome. We do not suggest that this improvement in energy resolution remedies entirely the lack of significant photopeak detection efficiency in PVT (in any but the thickest monolithic slabs), but it does encourage investigation of alternative spectroscopic techniques that seek to extract maximal source identification information from the shape of the Compton continuum. Sensor applications that require identification of, or discrimination among, a limited set of gamma-ray emissions from a few candidate sources of interest, as measured under relatively well-understood background conditions, might well benefit from a spectroscopic characterization technique that exploits a relatively high-resolution measurement of the shape of the Compton edge. Although a thorough investigation of Compton-continuum spectroscopy techniques fell somewhat outside the ALPS project's scope, the project has helped to quantify the extent to which reasonably practical enhancements in the light-collection efficiency of large-area PVT sensors can be expected to improve their measurement of the Compton continuum.

Acronyms

ADC	Analog-to-digital converter
ALPS	Advanced Large-area Plastic Scintillator
CASP	Cherenkov and Scintillator Portal
FAP	false alarm probability
MDA	minimum detectable activity
NORM	naturally occurring radioactive material
PD	probability of detection
PMT	photomultiplier tube
PNNL	Pacific Northwest National Laboratory
PVT	polyvinyl toluene
ROI	region of interest
RPM	radiation portal monitor
TDC	Time-to-digital converter

Contents

Executive Summary iii

Acronyms xi

1.0 Introduction 1.1

2.0 ALPS II Mechanical Design 2.1

- 2.1 ALPS II Detector Design 2.1
  - 2.1.1 Detector Design 2.1
  - 2.1.2 Instrument Components 2.2
  - 2.1.3 Detector Construction 2.3
  - 2.1.4 PMT Installation 2.4
  - 2.1.5 Instrument Enclosure 2.5
  - 2.1.6 Electronics Enclosure 2.6

3.0 ALPS II Single-Sheet Experiments 3.1

- 3.1 Introduction 3.1
- 3.2 Experiment 3.1
  - 3.2.1 Apparatus 3.1
  - 3.2.2 Data Acquisition System 3.2
  - 3.2.3 Data Collection 3.3
- 3.3 Results
  - 3.3.1 Resolution as a Function of the Number of PMTs 3.4
  - 3.3.2 Relative Efficiency as a Function of the Number of PMTs 3.5
  - 3.3.3 Efficiency of ^{57}Co as a Function of the Number of PMTs Using “OR” trigger 3.5
  - 3.3.4 Effect of high channel resolution at low energies 3.6
  - 3.3.5 Comparison of calculated and experimental spectra 3.7
- 3.4 Discussion 3.7

4.0 ALPS II Dual-sheet Plastic Scintillator Experiments 4.1

- 4.1 Introduction 4.1
- 4.2 Experiment 4.1
  - 4.2.1 Apparatus 4.1
  - 4.2.2 Data Acquisition System and Sensor Trigger Modes 4.2
  - 4.2.3 Data Collection 4.4
- 4.3 Results
  - 4.3.1 Background Efficiencies 4.5
  - 4.3.2 Low-Energy Source Efficiencies 4.7
  - 4.3.3 High-Energy Source Efficiencies 4.7
  - 4.3.4 Calibration of Energy Axis 4.8
  - 4.3.5 Effect of Discriminator 4.9
  - 4.3.6 Effect of Livetime Differences 4.9
  - 4.3.7 Spectra for Sum of Front and Back Detectors 4.9

4.4 Conclusions 4.10

5.0 ALPS II Cerenkov Slab (“CASP”) Experiments 5.1

5.1 Introduction 5.1

5.2 Experiment 5.1
  5.2.1 Apparatus 5.1
  5.2.2 Data Acquisition System 5.2
  5.2.3 Data Collection 5.4

5.3 Results
  5.3.1 Background Efficiencies 5.5
  5.3.2 Source Efficiencies 5.6
  5.3.3 Spectra 5.7
  5.3.4 Calibration of energy axis 5.7
  5.3.5 Effect of discriminator 5.8
  5.3.6 Effect of livetime differences 5.8
  5.3.7 Comparison of spectra triggered by Back detector only 5.9

5.4 Conclusions 5.10

6.0 Minimum Detectable Activity Analysis 6.1

6.1 Introduction 6.1

6.2 Results
  6.2.1 Single-sheet configuration 6.3
  6.2.2 Dual-sheet configurations 6.9

6.3 Discussion: Light collection efficiency and MDA 6.13

7.0 Pb-Loaded Scintillator Experiments 7.1

7.1 Abstract 7.1

7.2 Introduction 7.1

7.3 Experimental 7.1
  7.3.1 Attenuation Length 7.2
  7.3.2 Relative Efficiency 7.3

7.4 Results and Discussion 7.3
  7.4.1 Attenuation Length 7.3
  7.4.2 Relative Efficiencies – All Sources 7.6
  7.4.3 Relative Efficiencies–^{54}Mn, ^{137}Cs, and ^{109}Cd–Collimated at Center 7.8
  7.4.4 Efficiency as a Function of Discriminator 7.8
  7.4.5 Efficiency as a Function of Location in Scintillator 7.9

7.5 Conclusions 7.10

8.0 ALPS TDC Analysis 8.1

8.1 Introduction 8.1

8.2 Position Reconstruction 8.1

8.3 Event Selection 8.9

8.4 Reconstruction of Signal Amplitude 8.13
8.5 Amplitude Correction 8.16
9.0 Conclusions 9.1
10.0 References 10.1

Figures

Figure 1.1. Monte Carlo model of light collection efficiency in a monolithic PVT slab, as a function of the number of PMTs mounted on the slab.. 1.2

Figure 1.2. ^{54}Mn gamma pulse-height spectra recorded with the ALPS I sensor. 1.3

Figure 1.3. Same data as in Figure 1.2, but with the 1-PMT and 6-PMT responses isolated. 1.3

Figure 1.4. Effective ALPS I energy resolution at 639 keV deposited energy (as measured by Compton peak-to-valley ratio) as a function of PMT coverage for the ^{54}Mn spectra of Figure 1.2. 1.4

Figure 1.5. Collimated beta-source pulse-height response of the ALPS I sensor for various PMT configurations. 1.5

Figure 1.6. Uniformity of light-collection response for beta-source position scan data recorded with the ALPS I sensor. 1.5

Figure 1.7. Comparison of gamma attenuation coefficients in 5% Pb-loaded and unloaded plastic scintillator. 1.7

Figure 2.1. Basic ALPS II Mechanical Configuration 2.1

Figure 2.2. Primary ALPS II Detector Components 2.2

Figure 2.3. ALPS II Assembly Section 2.3

Figure 2.4. Enclosure Assembly 2.4

Figure 2.5. Internal Support Frame 2.4

Figure 2.6. ALPS II PMT Installation 2.5

Figure 2.7. ALPS II Enclosure 2.6

Figure 2.8. ALPS II Electronics Enclosure 2.7

Figure 2.9. Custom-built HV Module for ALPS II PMTs 2.7

Figure 3.1. Schematic of ALPS II data acquisition system for single-sheet experiments 3.12

Figure 3.2. Comparison of PMT 2 and PMT 5 background pulse height spectra 3.13

Figure 3.3. Pulse height spectra for ^{57}Co source with 1, 2, 4, and 6 PMTs 3.13

Figure 3.4. Low-Energy portion of pulse height spectra for ^{133}Ba source with 1, 2, 4, and 6 PMTs 3.14

Figure 3.5. Low-Energy portion with expanded vertical scale of pulse height spectra for ^{133}Ba source with 1, 2, 4, and 6 PMTs 3.14

Figure 3.6. Low-Energy portion of pulse height spectra for ^{137}Cs source with 1, 2, 4, and 6 PMTs 3.15

Figure 3.7. Expanded vertical scale of pulse height spectra for ^{137}Cs source with 1, 2, 4, and 6 PMTs……3.15

Figure 3.8. Pulse height spectra for ^{54}Mn source with 1, 2, 4, and 6 PMTs……3.16

Figure 3.9. Pulse height spectra for ^{57}Co source with discriminators set at 30 mV and 50 mV for 6 PMT configuration……3.16

Figure 3.10. Comparison of ^{57}Co pulse height spectra for "OR" trigger and 2-or-more trigger for 4 PMT and 50 mV discriminator configuration……3.17

Figure 3.11. Comparison of ^{57}Co pulse height spectra for "OR" trigger and 2-or-more trigger for 2 PMTs at opposite ends and 50 mV discriminator configuration……3.17

Figure 3.12. Comparison of ^{57}Co pulse height spectra for "OR" trigger and 2-or-more trigger for 2 PMTs at same end and 50 mV discriminator configuration……3.18

Figure 3.13. Comparison of ^{54}Mn pulse height spectra for "OR" trigger and 2-or-more trigger for 6 PMTs and 30 mV discriminator configuration……3.18

Figure 3.14. Comparison of ^{137}Cs pulse height spectra for "OR" trigger and 2-or-more trigger for 6 PMTs and 30 mV discriminator configuration……3.19

Figure 3.15. Comparison of low-energy pulse height region for ^{137}Cs source for low and high channel resolution, 6 PMTs with discriminator at 30 mV……3.19

Figure 3.16. Comparison of low energy pulse height region for ^{137}Cs and ^{54}Mn sources with higher channel resolution, 6 PMTs with discriminator at 30 mV.……3.20

Figure 3.17. Comparison of ^{57}Co spectra at low and high channel resolution, 6 PMTs with discriminator at 30 mV……3.20

Figure 3.18. Comparison of calculated and smoothed ^{54}Mn pulse height spectra……3.21

Figure 3.19. Comparison of calculated and smoothed ^{54}Mn pulse height spectra with experimental data……3.21

Figure 3.20. Comparison of calculated and smoothed ^{137}Cs pulse height spectra……3.22

Figure 3.21. Comparison of calculated and smoothed ^{137}Cs pulse height spectra with experimental data……3.22

Figure 3.22. Comparison of calculated and smoothed ^{133}Ba pulse height spectra……3.23

Figure 3.23. Comparison of calculated and smoothed ^{133}Ba pulse height spectra with experimental data……3.23

Figure 4.1. Schematic of ALPS II electronic modules for dual-sheet data acquisition……4.15

Figure 4.2. Comparison of pulse height spectra of PMT 2 and PMT 5 for Front detector and PMT8 and PMT11 for Back detector. Background data taken with the “OR” trigger condition and with no intermediate shield. 4.15

Figure 4.3. Comparison of background pulse height spectra in Front detector with intermediate shield for low-energy region for “OR” trigger mode versus “OR with Anti” trigger mode.. .... 4.16

Figure 4.4. Comparison of background pulse height spectra in Front detector without intermediate shield for low-energy region for “OR” trigger mode versus “OR with Anti” trigger mode. 4.16

Figure 4.5. Comparison of low-energy background pulse height spectra in Back detector with and without intermediate shield. Data were obtained with “OR” trigger mode.........4.17

Figure 4.6. Comparison of ^{57}Co pulse height spectra in Front detector for low-energy region for “OR” trigger mode versus “Or with Anti” trigger mode. The intermediate shield is in place. 4.17

Figure 4.7. Comparison of ^{57}Co pulse height spectra in Front detector for low-energy region for “OR” trigger mode versus “Or with Anti” trigger mode. The intermediate shield is removed. 4.18

Figure 4.8. Comparison of ^{133}Ba pulse height spectra in Front detector for full-energy region for “OR” trigger mode versus “OR with Anti” trigger mode. Intermediate shield is in place 4.18

Figure 4.9. Comparison of ^{133}Ba pulse height spectra in Front detector for full-energy region for “OR” trigger mode versus “OR with Anti” trigger mode. Intermediate shield is removed 4.19

Figure 4.10. Comparison of ^{137}Cs pulse height spectra in Front detector for full-energy region for “OR” trigger mode versus “OR with Anti” trigger mode. Intermediate shield is in place. 4.19

Figure 4.11. Comparison of ^{137}Cs pulse height spectra in Front detector for full-energy region for “OR” trigger mode versus “OR with Anti” trigger mode. Intermediate shield is removed 4.20

Figure 4.12. Comparison of ^{54}Mn pulse height spectra in Front detector for full-energy region for “OR” trigger mode versus “OR with Anti” trigger mode. Intermediate shield is in place 4.20

Figure 4.13. Comparison of ^{54}Mn pulse height spectra in Front detector for full-energy region for “OR” trigger mode versus “OR with Anti” trigger mode. Intermediate shield is removed 4.21

Figure 4.14. Pulse height spectrum of ^{54}Mn. Blue curve is calculated energy deposition. Red, green, and magenta curves are the calculated spectrum after resolution broadening of 25%, 30%, and 35% respectively. Black points are experimental data from “OR” trigger mode normalized to 25% calculated spectrum. 4.21

Figure 4.15. Pulse height spectrum of ^{54}Mn. Blue curve is calculated energy deposition. Red, green, and magenta curves are the calculated spectrum after resolution broadening of 25%, 30%, and 35% respectively. Black points are experimental data from ‘“OR” with Anti’ trigger mode normalized to 25% calculated spectrum. 4.22

Figure 4.16. Calibration of pulse height energy versus channel number assuming peak centroids correspond to maximum Compton electron energy in scintillator. 4.22

Figure 4.17. Comparison of calculated and experimental ^{57}Co spectra. Blue curve is calculated energy deposition spectrum. Red curve is resolution-broadened calculated spectrum. Red data points are experimental spectrum normalized and with adjusted energy scale. 4.23

Figure 4.18. Comparison of ^{57}Co spectra at discriminator levels of 30 mV and 50 mV 4.23

Figure 4.19. Comparison of Front and Back detector background spectra taken with "OR" trigger mode, no intermediate shield 4.24

Figure 4.20. Comparison of ^{57}Co spectra in Front detector, Back detector, and the Sum of Front and Back detectors. Data are for "OR" trigger mode, no intermediate shield 4.24

Figure 4.21. Comparison of ^{133}Ba spectra in Front detector, Back detector, and the Sum of Front and Back detectors. Data are for "OR" trigger mode, no intermediate shield 4.25

Figure 4.22. Comparison of ^{137}Cs spectra in Front detector, Back detector, and the Sum of Front and Back detectors. Data are for "OR" trigger mode, no intermediate shield. 4.25

Figure 4.23. Comparison of ^{54}Mn spectra in Front detector, Back detector, and the Sum of Front and Back detectors. Data are for "OR" trigger mode, no intermediate shield. 4.26

Figure 5.1. Schematic of electronic modules for CASP data acquisition 5.15

Figure 5.2. Comparison of PMT 2 and PMT 5 pulse height spectra for background data taken with the "OR" trigger condition. 5.15

Figure 5.3. Comparison of background pulse height spectra in Front detector for low-energy region for "Front Only" trigger mode versus "OR" trigger mode 5.16

Figure 5.4. Comparison of background pulse height spectra in Front detector for low-energy region for ' "OR" with Anti' trigger mode versus "OR" trigger mode. 5.16

Figure 5.5. Comparison of background pulse height spectra in Front detector for low-energy region for "Front Only" trigger mode versus "Back Only" trigger mode. 5.17

Figure 5.6. Comparison of ^{57}Co pulse height spectra in Front detector for low-energy region for "Front Only" trigger mode versus "OR" trigger mode. 5.17

Figure 5.7. Comparison of ^{133}Ba pulse height spectra in Front detector for full-energy region for "Front Only" trigger mode versus "OR" trigger mode. 5.18

Figure 5.8. Comparison of ^{137}Cs pulse height spectra in Front detector for full-energy region for "Front Only" trigger mode, "OR" trigger mode, and '"OR" plus Anti' trigger mode. 5.18

Figure 5.9. Comparison of ^{54}Mn pulse height spectra in Front detector for full-energy region for "Front Only" trigger mode, "OR" trigger mode, and '"OR" plus Anti' trigger mode. 5.19

Figure 5.10. Comparison of ^{57}Co pulse height spectra in Front scintillator when triggered by Front or Back signals in "OR" mode or by anti-coincidence with Back scintillator in '"OR" plus Anti' mode…………….. 5.19

Figure 5.11. Comparison of ^{133}Ba pulse height spectra in Front scintillator when triggered by Front or Back signals in "OR" mode or by anti-coincidence with Back scintillator in '"OR" plus Anti' mode ……………… 5.20

Figure 5.12. Comparison of ^{137}Cs pulse height spectra in Front scintillator when triggered by Front or Back signals in "OR" mode or by anti-coincidence with Back scintillator in '"OR" plus Anti' mode ………………. 5.20

Figure 5.13. Comparison of ^{54}Mn pulse height spectra in Front scintillator when triggered by Front or Back signals in "OR" mode or by anti-coincidence with Back scintillator in '"OR" plus Anti' mode ……………… 5.21

Figure 5.14. Pulse height spectrum of ^{54}Mn. Blue curve is calculated energy deposition. Red, green, and magenta curves are calculated spectrum after resolution broadening of 25%, 30%, and 35% respectively. Black points are experimental data from "OR" trigger mode normalized to 25% calculated spectrum........ 5.21

Figure 5.15. Pulse height spectrum of ^{54}Mn. Blue curve is calculated energy deposition. Red, green, and magenta curves are calculated spectrum after resolution broadening of 25%, 30%, and 35% respectively. Black points are experimental data from '"OR" with Anti' trigger mode normalized to 25% calculated spectrum.. .... 5.22

Figure 5.16. Calibration of pulse height energy versus channel number assuming peak centroids correspond to maximum Compton electron energy in scintillator. 5.22

Figure 5.17. Comparison of calculated and experimental ^{57}Co spectra. 5.23

Figure 5.18. Comparison of ^{57}Co spectra at discriminator levels of 10, 30 mV, and 50 mV. 5.23

Figure 5.19. Comparison of ^{133}Ba spectra taken with Hardware Veto trigger mode. 5.24

Figure 5.20. Comparison of ^{137}Cs spectra taken with Hardware Veto trigger mode. 5.24

Figure 5.21. Comparison of ^{57}Co spectra taken with Hardware Veto trigger mode. 5.25

Figure 5.22. Comparison of ^{54}Mn spectra taken with Hardware Veto trigger mode. 5.25

Figure 5.23. Comparison of Cherenkov pulse height spectra in Back detector for Background and ^{54}Mn when data acquisition was triggered only by Back detector. 5.26

Figure 5.24. Comparison of pulse height spectra in Front detector for Background and ^{54}Mn when data acquisition was triggered only by Back detector.. .... 5.26

Figure 5.25. Comparison of Cherenkov pulse height spectra in Back detector for ^{137}Cs, ^{22}Na, and ^{60}Co when data acquisition was triggered only by Back detector. 5.27

Figure 5.26. Comparison of pulse height spectra in Front detector for ^{137}Cs, ^{22}Na, and ^{60}Co when data acquisition was triggered only by Back detector. 5.27

Figure 6.1 ALPS II Single-sheet background rates vs. PMT configuration, multiplicity trigger. 6.5

Figure 6.2 ALPS II Single-sheet ^{57}Co intrinsic detection efficiency vs. PMT configuration, multiplicity trigger. 6.5

Figure 6.3 ALPS II Single-sheet ^{57}Co MDA vs. PMT configuration, multiplicity trigger. MDAs correspond to background livetimes as measured. Spectral (two energy-window), background-prediction algorithm used for the MDA calculation, 99% DP, 0.1% FAP. 6.7

Figure 6.4 ALPS II Single-sheet ^{133}Ba intrinsic detection efficiency vs. PMT configuration, multiplicity trigger. 6.7

Figure 6.5 ALPS II Single-sheet ^{133}Ba MDA vs. PMT configuration, multiplicity trigger. MDAs correspond to background livetimes as measured. Spectral (two energy-window), background-prediction algorithm used for the MDA calculation, 99% DP, 0.1% FAP. 6.8

Figure 6.6 Schematic illustration of the relationship of the ALPS dual-sheet event classes collected using the "F OR B" hardware trigger, the pulse-height spectra formed in software, and the use of these spectra in the MDA analysis. 6.10

Figure 7.1. Pulse height spectra for ^{54}Mn in Left PMT with BC-408 scintillator. 7.10

Figure 7.2. Peak channel of the Compton edge peak as a function of source location for ^{54}Mn with BC-408 scintillator. Data points have been fitted with an exponential function. 7.11

Figure 7.3. Relative efficiency as measured by Left PMT of BC-408 and BC-452 scintillators as a function of gamma energy. 7.12

Figure 7.4. Relative efficiency as measured by Right PMT of BC-408 and BC-452 scintillators as a function of gamma energy. 7.12

Figure 7.5. Relative efficiency as measured by the coincidence of the Left PMT and Right PMT of BC-408 and BC-452 scintillators as a function of gamma energy. 7.13

Figure 7.6. Relative efficiencies for ^{109}Cd and ^{57}Co as a function of the lower channel number for a window set on the pulse height spectra. 7.13

Figure 7.7. Relative efficiency as a function of the location of the interaction as it is moved farther from a particular PMT. The scintillator is BC-408. 7.14

Figure 7.8. Relative efficiency as a function of the location of the interaction as it is moved farther from a particular PMT. The scintillator is BC-452. 7.14

Figure 8.1. Diagram of single sheet of the ALPS plastic scintillator sensor with 6 PMTs attached directly to the plastic. Orientation of coordinates and some source location "traces" are defined.. 8.2

Figure 8.2. TDC difference analysis summary for the traces using a ^{90}Sr source at various positions on the scintillator. 8.3

Figure 8.3. Simple model of TDC differences for various pairs of PMTs for 4 different traces. 8.4

Figure 8.4. Demonstration of relationship of T_2-T_5 and $(T_1$-T_4+T_3-$T_6)/2$ using the six PMT setup and a distant, uncollimated gamma source. 8.5

Figure 8.5. Plot of geometric mean of ADCs versus T_2-T_5 for distant, uncollimated ^{207}Bi data............... 8.6

Figure 8.6. Plots of T_1-T_3 versus T_2-T_5 and T_4-T_6 versus T_2-T_5. .... 8.7

Figure 8.7. Histograms of T_2-T_5 and geometric mean for various cuts for a distant ^{207}Bi source............ 8.8

Figure 8.8. Plots of the geometric mean from the ^{207}Bi run versus T_2-T_5 for various cuts. 8.8

Figure 8.9. Plot demonstrating the impact of the "No Corners" cut on the geometric mean of the ^{207}Bi run………… 8.9

Figure 8.10. Plots of the means of the distribution of individual ADCs and sums of ADCs versus source position. Data taken with a ^{90}Sr source with the 4 PMT setup. 8.11

Figure 8.11. Histograms of a distant ^{207}Bi source demonstrating the impact of various cuts................ 8.12

Figure 8.12. Plots of Compton peak positions versus various locations for the six PMT setup............ 8.14

Figure 8.13. Plots from ^{22}Na data with the 2 PMT setup... 8.15

Figure 8.14. Comparison of geometric and arithmetic means for the 6 PMT setup with a distant uncollimated ^{207}Bi source... 8.16

Figure 8.15. Comparison of techniques to determine the signal amplitude from the geometric mean of the PMTs for the 4 PMT setup. Most of the techniques are for a beta source.................................. 8.17

Figure 8.16. Comparison of amplitude dependence on TDC differences for different gamma sources and different PMT setups. 8.18

Figure 8.17. Histograms of ADC geometric mean histogram of the Compton peak from ^{137}Cs source after applying the position correction with various factors for correction amplitude. 8.19

Figure 8.18. Plots of the widths and peak/valley for various correction factors for the amplitude of the position correction. Results from two sources, ^{137}Cs and ^{207}Bi, are shown as well as results with and without applying the “No Corners” cut. 8.19

Figure 8.19. Histograms of numerical model of effect of position dependence of the signal amplitude……. 8.20

Tables

Table 3.1. Resolution of peaks as a function of the number of PMTs 3.8

Table 3.2. Count rates and count rate ratios as a function of the number of PMTs 3.9

Table 3.3. Ratio of count rates at 30 mV to 50 mV discriminator levels as a function of the number of PMTs……… 3.10

Table 3.4. Count rates (cps) for the sum of pulse height channels 1 – 20 as a function of the number of PMTs, discriminator level (50 mV and 30 mV), and type of trigger (2-or-more and “OR”). The ratios of #PMTs to 1 PMT are also given. 3.11

Table 4.1. Count rates (cps) for various sources and trigger conditions with shield 4.12

Table 4.2. Count rates (cps) for various sources and trigger conditions without shield 4.13

Table 4.3. Experiments with Plastic Scintillator Anti-Coincidence System 4.14

Table 5.1. Count rates (cps) for various sources and trigger conditions 5.11

Table 5.2. Comparison of data acquired with different livetimes 5.12

Table 5.3. Experiments with Cherenkov Anti-Coincidence System 5.13

Table 6.1 ALPS II single-sheet detection efficiencies and background rates for ^{57}Co measurements, multiplicity trigger. 6.4

Table 6.2 ALPS II single-sheet detection efficiencies and background rates for ^{133}Ba measurements, multiplicity trigger. 6.4

Table 6.3 ALPS II single-sheet ^{57}Co and ^{133}Ba MDAs, multiplicity trigger, spectral (2 energy-window) background-prediction algorithm, 99% DP, 0.1% FAP. 6.6

Table 6.4 ALPS II single-sheet ^{57}Co and ^{133}Ba MDAs, multiplicity trigger, 30 mV threshold, for various MDA algorithms, 99% DP, 0.1% FAP.. .... 6.9

Table 6.5 ALPS II and CASP dual-sheet ^{57}Co MDAs, 50 mV threshold, for various sensor configurations, trigger conditions, and MDA algorithms, 99% DP, 0.1% FAP. The MDAs are quoted assuming as-measured background livetimes. 6.11

Table 6.6 ALPS II and CASP dual-sheet ^{57}Co MDAs, 50 mV threshold, for various sensor configurations, trigger conditions, and MDA algorithms, 99% DP, 0.1% FAP. The MDAs are quoted assuming 100% background livetime. 6.11

Table 6.7 ALPS II and CASP dual-sheet ^{133}Ba MDAs, 50 mV threshold, for various sensor configurations, trigger conditions, and MDA algorithms, 99% DP, 0.1% FAP. The MDAs are quoted assuming as-measured background livetimes. 6.12

Table 6.8 ALPS II and CASP dual-sheet ^{133}Ba MDAs, 50 mV threshold, for various sensor configurations, trigger conditions, and MDA algorithms, 99% DP, 0.1% FAP. The MDAs are quoted assuming 100% background livetime. 6.12

Table 7.1. Attenuation lengths for various conditions of scintillator type, wrapping, PMT high voltages, and measurement technique 7.4

Table 7.2. Relative efficiency for a single gamma corresponding to the weighted average energy of the gamma spectrum 7.7

Table 7.3. Relative efficiencies for collimated sources at midpoint of scintillators 7.9

Table 8.1. Definition of cuts used in the TDC analysis 8.10

Table 8.2. List of the percentage of events that survive various cuts in a given region of interest in the geometric mean of the ADCs........ 8.12

1.0 Introduction

The current generation of vehicle radiation portal monitors (RPMs) deployed at international border crossings relies heavily on large-area plastic scintillators for detecting gamma rays emitted by potentially hazardous, clandestinely transported radioactive materials. A large detector area is important for portal-monitor applications to maximize gamma-detection count rate, and thus source-detection sensitivity, because spectrum acquisition times are severely limited by the need to accommodate a reasonable flow of vehicles past the portal. Plastic scintillator is relatively inexpensive per unit area and rugged in comparison to other scintillating materials, e.g., NaI(Tl), and semiconductors, e.g., high-purity germanium, and thus represents an attractive material for constructing a large-area gamma sensor. Low cost per unit area makes plastic scintillator an especially attractive option for portal monitor applications, where large detector area is essential to maximize gamma detection count rate, and thus radioactive source sensitivity, for vehicle traversals that typically last only a few seconds. Plastic scintillator is also relatively robust against mechanical shock and temperature variations.

However, the limited gamma energy spectrum information available from plastic scintillator presents challenges to reliably distinguishing radiological sources of interest from naturally occurring radioactive materials (NORM) and radioisotopes used benignly in medical applications. The Advanced Large-Area Plastic Scintillator (ALPS) project seeks to address these challenges by investigating potential radiation source detection sensitivity enhancements arising from (1) increased light collection efficiency, (2) improved uniformity of light collection versus gamma interaction position in the scintillator, (3) coincidence gamma detection in multiple scintillator sheets, and (4) potential alternatives to traditional polyvinyl toluene (PVT) as the detection material in monolithic RPMs.

The physical basis of particle detection with a scintillating material is the emission of light when ionizing radiation deposits energy in the material. Plastic scintillators typically emit about 10,000 optical photons per MeV of deposited energy, roughly a factor of 4 fewer than in NaI(Tl) crystals. The intrinsic energy resolution of plastic, which scales as the square root of the number of optical photons, is thus a factor of 2 poorer than that of NaI(Tl). On top of this, only a relatively small fraction of the scintillation light emitted in a typical large-area plastic scintillator actually reaches the photomultiplier tubes (PMTs) that convert the light into an electrical signal. In typical commercial units with one or two 2"-diameter PMTs, Monte Carlo calculations (see Figure 1.1) indicate that the light collection efficiency can be as low as 3.5% (one tube) to 7% (two tubes). Thus the effective energy resolution of a plastic scintillator sensor can be as much as a factor of 4 or 5 poorer than the plastic's intrinsic energy resolution. One important component of the ALPS project is a systematic study of the improvement of plastic scintillator energy resolution as light collection efficiency is increased.

Activities in early phases of the ALPS project [Jordan et al. 2003, Reeder et al. 2003] included (a) Monte Carlo modeling of light collection properties of various configurations of plastic scintillator and photomultiplier tubes (PMTs), (b) design and fabrication of a large-area, unwrapped plastic scintillator sensor housed in a light-tight box intended for laboratory experimentation (the so-called "ALPS I"), (c) setup of a rack-mounted, electronics module-based system for processing pulses from the PMTs, as well as a computer-controlled data acquisition system based upon the Kmax™ software tool suite, and (d) execution of a campaign of experimental measurements with various scintillator + PMT configurations of the laboratory sensor, including both broad-area exposures with a set of uncollimated gamma sources, and localized-exposure measurements with a ^{90}Sr/^{90}Y beta source. The ALPS I sensor consisted of two sheets of 127 cm × 57.2 × 5.08 cm^3 (50 × 22.5 × 2 in^3) Bicron/St. Gobain BC-408 scintillator, with three 12.7 cm (5 in) diameter Hamamatsu PMTs directly coupled to each end. Modeling results indicated that this sensor would have a light collection efficiency of approximately 40%, a factor of roughly 6 to 10 greater than efficiencies realized in commercially available portal monitors.

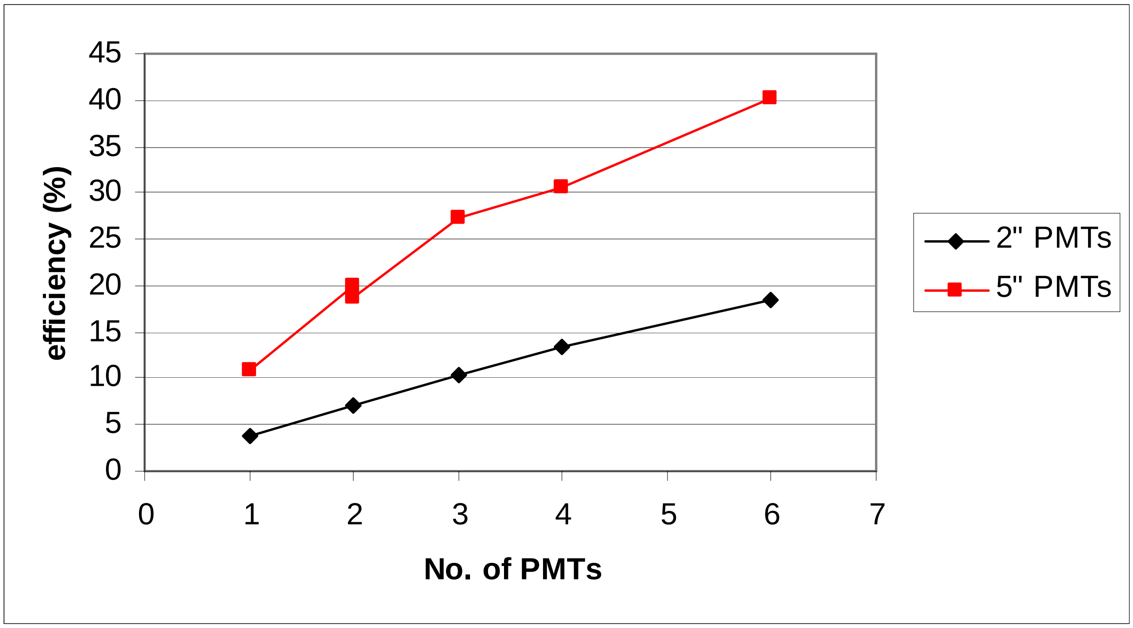

Figure 1.1. Monte Carlo model of light collection efficiency in a monolithic PVT slab, as a function of the number of PMTs mounted on the slab. The dimensions of the slab are 127 × 57 × 5.08 cm^3.

The main goals of the ALPS I experimental campaign were to quantify the energy deposition resolution improvement afforded by the increase in PMT coverage of a scintillator sheet's edge area, and to understand the variation in pulse height response as a function of the primary ionizing radiation's interaction position within the plastic scintillator sheet. Figure 1.2 displays the ^{54}Mn pulse height distribution (gamma energy 835 keV) registered in a single sheet of the ALPS I sensor as a function of PMT configuration. In all cases, the PMTs were mounted on the short edges of the sheet. The enhancement in the energy deposition resolution for the two-PMT configurations is clear from the sharpening of the Compton edge[a] visible at the high pulse-height region of the spectrum. Figure 1.3 reproduces the single-PMT and 6-PMT pulse height distributions from Figure 1.2 for convenience in comparing the spectral shapes. Figure 1.4 summarizes the variation of resolution (as measured here by a simple Compton peak-to-valley ratio for the spectra displayed in Figure 1.2) at 640 keV energy deposition as a function of PMT coverage. The data indicate roughly a 60% improvement in the resolution between the single-PMT and 6-PMT configurations, with only a small improvement resulting from the increase from 4 to 6 PMTs.

---

[a] The Compton edge corresponds to the maximum energy transferable to an electron in a single Compton scattering event, 639 keV for the 835 keV gamma.

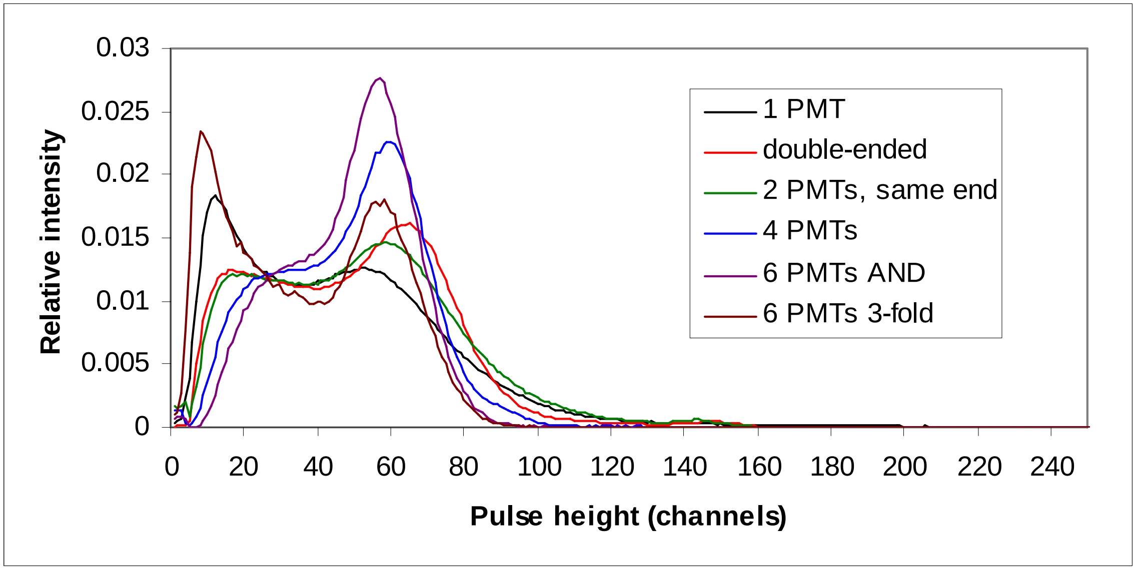

Figure 1.2. ^{54}**Mn gamma pulse-height spectra recorded with the ALPS I sensor. Six PMT configurations are compared: Single PMT; 2 PMTs at opposite ends ("double-ended"); 2 PMTs at same scintillator end; 4 PMTs (two at each end); 6 PMTs with trigger configured to require coincident firing of all 6 ("AND"); and 6 PMTs with readout electronics configured to take the hardware sum of 3 PMTs at each end ("3-fold").**

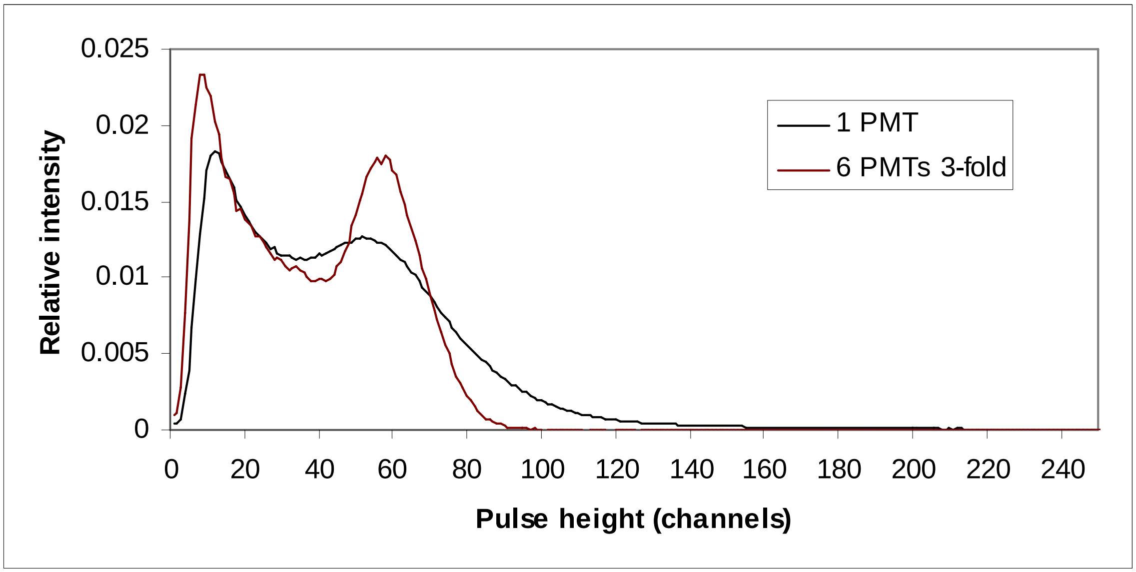

Figure 1.3. Same data as in Figure 1.2, but with the 1-PMT and 6-PMT responses isolated.

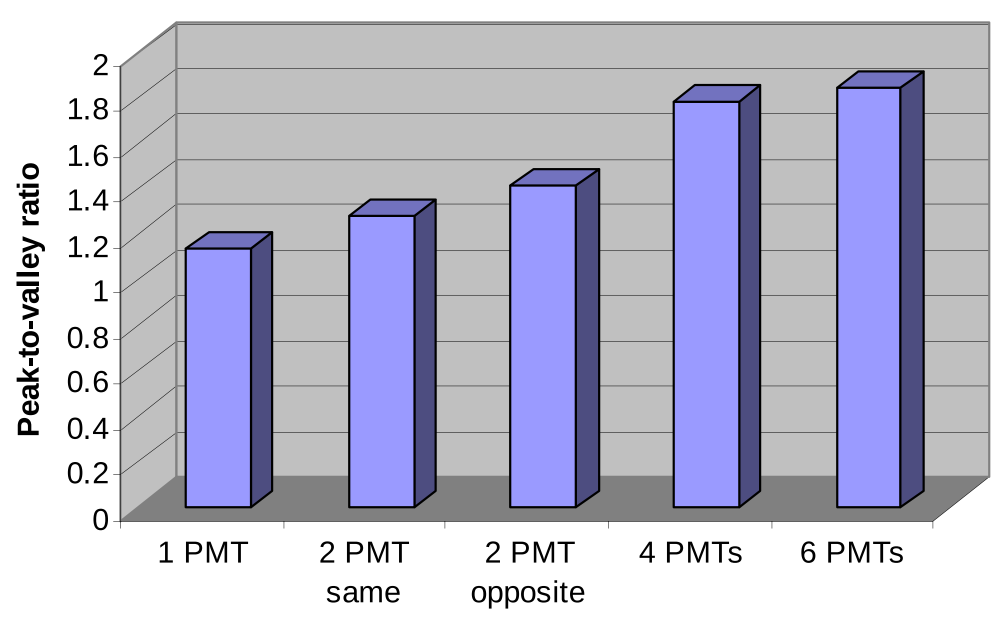

Figure 1.4. Effective ALPS I energy resolution at 639 keV deposited energy (as measured by Compton peak-to-valley ratio) as a function of PMT coverage for the ^{54}Mn spectra of Figure 1.2.

In addition to the resolution measurements under broad-area gamma source exposure, a second emphasis of the ALPS I experimental campaign focused on mapping position variations of the scintillator light collection efficiency as a function of interaction position of the incident radiation. Data were collected with a collimated ^{90}Sr beta source (for the 1, 2, and 4-PMT configurations) and the mean pulse height response determined as a function of the source's position with respect to the scintillator surface. Figure 1.5 displays the mean beta pulse height as a function of position for a set of source points (or "trace") coinciding with the long-axis of the ALPS I scintillator. Note that in the single-PMT configuration, the light collection efficiency along this trace varies by roughly a factor of 2 over the length of the scintillator. This improves to roughly a 30% variation for the 4 PMT configuration, although in this case the trace (which is centered along the short-axis of the scintillator) does not include source positions close to any PMT. A light collection uniformity index determined from beta source position scans for a variety of trace locations (on and off the scintillator short-axis) is graphed in Figure 1.6. This metric indicates roughly a factor of 2 improvement in light collection uniformity over the surface of the scintillator as the number of PMTs increases from 1 to 4.

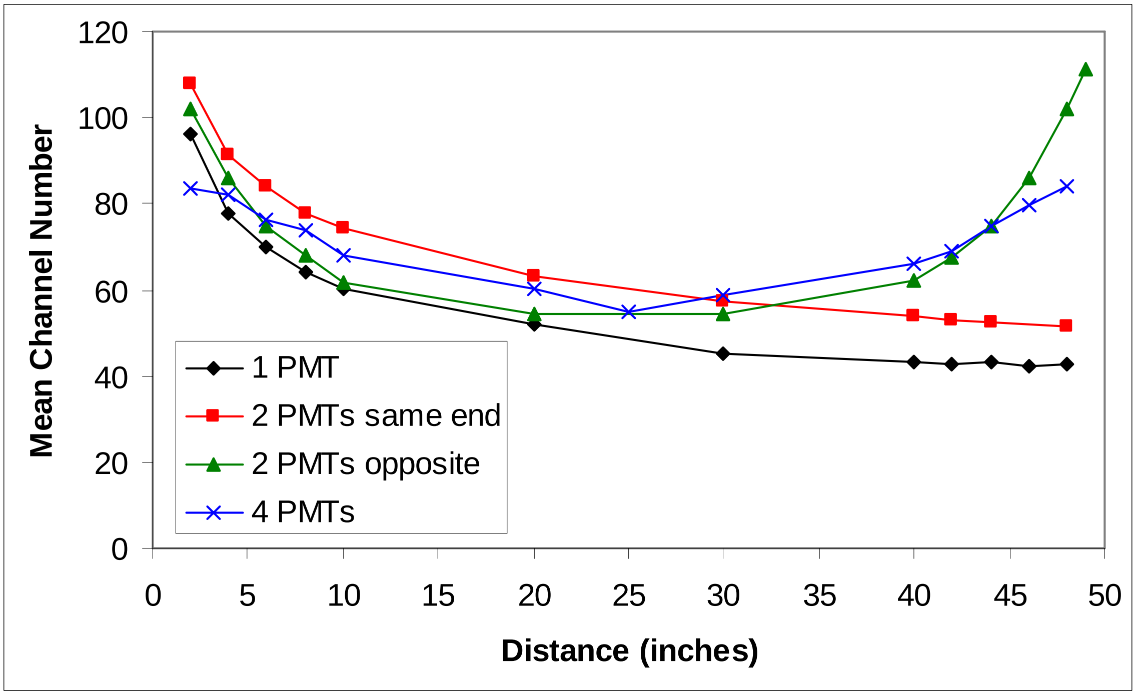

Figure 1.5. Collimated beta-source pulse-height response of the ALPS I sensor for various PMT configurations. The locus of source position points consists of a "trace" along the long axis of the scintillator. The trace is centered on the short axis.

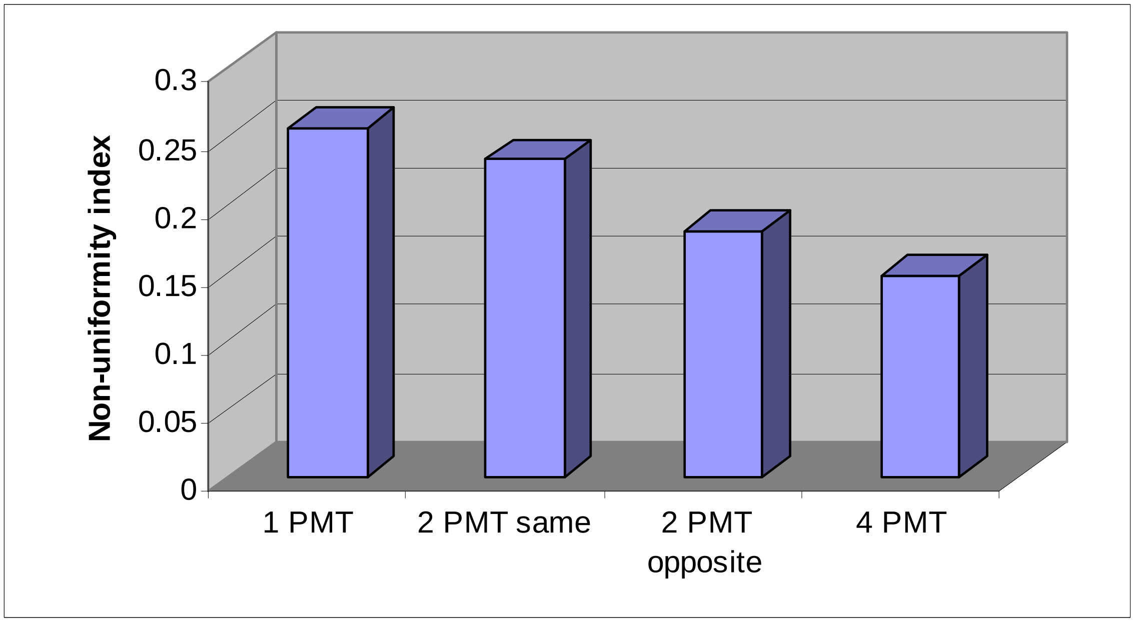

Figure 1.6. Uniformity of light-collection response for beta-source position scan data recorded with the ALPS I sensor. The non-uniformity index is defined as the standard variation of the set of pulse heights divided by the mean of the set. Smaller values of the index correspond to improved light collection uniformity.

Note that in configurations with PMTs at both ends, it is possible in principle to determine the gamma interaction position by measuring the relative timing of the PMT pulses. In the ALPS I sensor, time-to-digital converter (TDC) components were included in the pulse processing electronics. An Appendix of the present report describes efforts to extract reasonable position information from the TDC time-difference information. The goal of this aspect of the ALPS I experimental campaign was to use the PMT output pulse timing information, in conjunction with a light collection efficiency mapping, to apply a position-dependent correction to the raw pulse heights recorded from the sensor. These efforts were deemed to have only marginal utility due to complications introduced by the relative timing response for events in which the gamma interacts off the short-axis of the sensor, and thus collection of TDC information was abandoned for the field-deployable version of the ALPS sensor, the "ALPS II", which is the main subject of the present report.

Research following the ALPS I experimental campaign emphasized design, fabrication and testing of a field-deployable version of the ALPS, referred to herein as the "ALPS II". The ALPS II consists of dual slabs of Bicron/Saint Gobain BC-408 scintillators of dimensions $127 \times 57.15 \times 5.08$ cm^3 separated by a gap of 13 cm. In contrast to the ALPS I sensor, which was contained in a light-tight box, the PVT slabs of the ALPS II are mounted vertically in a light-tight, Pb-lined, steel-walled enclosure representative of a field-deployable RPM form factor. The sensor system and accompanying rack-mounted readout electronics are mounted on a pallet for convenient transport and outdoor deployment. As in the laboratory version of the sensor, each scintillator slab is outfitted with 3 Hamamatsu R1250 127-mm (5-in.) diameter PMTs mounted on each end, for a total of 12 PMTs. The scintillators were mounted vertically and shielded on the bottom, sides, and back by 5.08-cm of lead. A light-tight plastic panel on the front of the steel enclosure door permits entry of gammas to the scintillator detectors through material of low-Z. Section 2 of this report provides further fabrication details of the ALPS II sensor.

Sections 3 through 6 of this report describe the main thrust of the ALPS II experimental campaign. The campaign emphasized investigation of the use of the second ("back") PVT slab as an anti-Compton veto for reduction of low-energy gamma background in the front slab. The essential physical picture motivating this investigation is Compton scattering of a terrestrial background gamma in the front PVT slab, followed by detection of the scattered gamma in the back slab. Rejecting events in which the back slab fires in coincidence with the front should help to reduce the low-energy contribution to the front-slab background distribution arising from partial energy deposition of terrestrial gammas. Reducing this background offers the potential, in turn, to improve the sensitivity of energy-windowing algorithms that exploit the sensor response to SNM threats that populate low-energy portions of the scintillator spectrum. With this general physical picture in hand, the ALPS II campaign consisted of the following major elements:

- Mapping the single-sheet effective gamma resolution and source detection sensitivity of the sensor as a function of PMT coverage (section 3). This essentially recapitulates the laboratory-based ALPS I resolution measurement campaign within the operational context of a field-deployable sensor.
- Determining properties of the full, dual-PVT sheet response of the sensor (section 4) and investigating algorithms to extract maximum low-energy source detection sensitivity (section 6).
- Investigating an alternative to the dual-PVT sheet configuration in which the back anti-Compton veto PVT sheet is replaced with a monolithic Cerenkov slab (section 5). This variation on the ALPS II sensor, referred to as the "CASP" (Cerenkov And Scintillator Portal), exploits the physics-based energy threshold associated with Cerenkov light production, which exceeds 350

keV for incident gamma rays. The Cerenkov slab in the CASP acts as a gross-count anti-Compton slab that is inherently sensitive to energetic background gammas that have forward-scattered in the front PVT slab (and insensitive to SNM gammas that have not interacted in the front slab). Thus anti-Compton vetoing could be achieved with minimal reliance on pulse-height energy resolution in the back slab, which in turn could yield a more cost-effective dual-sheet sensor.

Section 6 details minimum detectable activity (MDA) analysis of the ALPS II and CASP experimental data, with primary emphasis placed on the sensor's low-energy response to ^{57}Co and ^{133}Ba gamma-ray sources.

A secondary theme of later stages of ALPS research, conducted in parallel with the ALPS II experimental campaign, was a laboratory investigation of the feasibility of applying Pb-loaded plastic scintillator to large-area sensors. The motivation for this investigation is that the addition of a high-Z element to plastic scintillator in modest (e.g. 2% to 10%) proportions offers substantial increases in gamma interaction probability at energies below about 200 keV, as illustrated in Figure 1.7. The addition of 5% Pb, for example, yields roughly a factor of 4 enhancement in the gamma attenuation coefficient at 100 keV, and an order of magnitude enhancement at 20 keV. In effect, the addition of the high-Z dopant increases the effective gamma attenuation thickness of the plastic by a factor of 4-10 without increasing the physical dimensions of the scintillator. Due to Compton down-scattering in cargo and other shielding materials of gammas emitted at or above about 200 keV from radioactive sources, much of the gamma flux incident on an RPM is in the neighborhood of 100 keV. Pb-loaded scintillator thus offers the possibility for significant improvements in gamma detection sensitivity in an energy region of substantial interest for threat detection in radiation portal monitors. A particular advantage is that this change could be made as a detector element replacement in currently-deployed portal monitors.

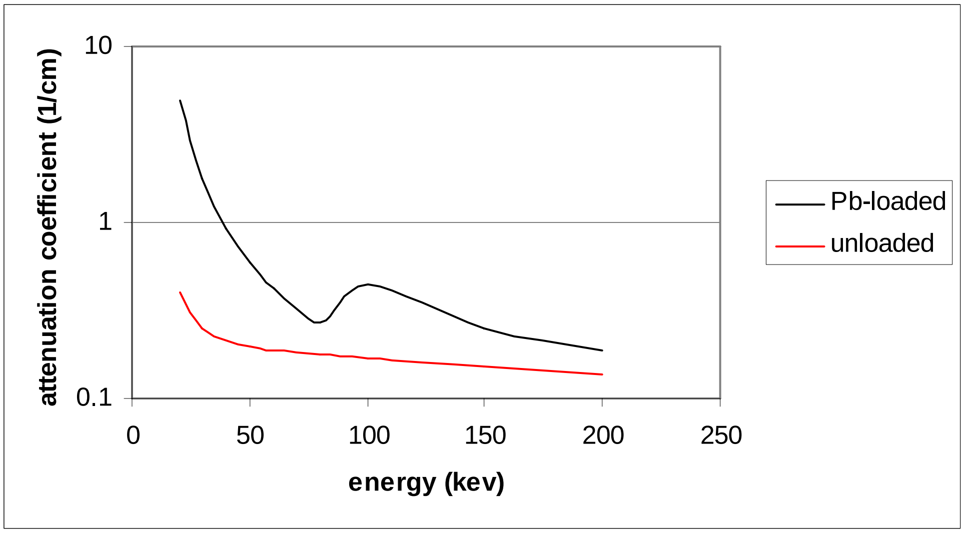

Figure 1.7. Comparison of gamma attenuation coefficients in 5% Pb-loaded and unloaded plastic scintillator.

A potential drawback to the admixture of Pb in plastic scintillator is reduction in light transmission. The light attenuation coefficient of Bicron/St. Gobain's commercially available BC-452 Pb-loaded scintillator had not been measured (or at least had not been reported) prior to the ALPS research described in section 7, and samples of varying optical opacity have been produced by Bicron ranging from clear to very dark. Bicron estimated that an optical attenuation length of approximately 1.5 meters should be achievable in Pb-loaded plastic, to be compared with the 3.8 meters attenuation quoted for their unloaded BC-408 plastic. Eljen Technology has also produced Pb-loaded scintillator and, despite some early problems with yellow coloration (a defect that severely attenuates blue scintillation light) reported successful fabrication of clear samples. Eljen also noted that the scintillation photon yield may be significantly smaller (by as much as a factor of two) in Pb-loaded plastic, in comparison to unloaded plastic. The largest samples prepared to date have been approximately 5" in diameter by 20" long. Fabricating sheets of Pb-loaded scintillator suitable for a large-area sensor has not been done to date, and lack of a commercial driver has been the primary limitation in plate-fabrication R&D at these companies such as Bicron/St. Gobain and Eljen.

The experimental campaign reported in section 7 involved a cylindrical, Pb-loaded scintillator rod (5% loading) acquired from Bicron/St. Gobain. Light attenuation and gamma sensitivity were studied in this cylindrical geometry. The primary motivation for these measurements was to rapidly acquire experience with Pb-loaded plastic in a low-risk geometry that would indicate the potential utility (or lack thereof) of the material as an alternative to PVT in large-area, monolithic slab geometry. These rod-geometry studies were conducted in a "double-ended" readout configuration, i.e. PMTs were mounted at both ends of the Pb-loaded scintillator rod. Similar studies were conducted with an unloaded plastic scintillator rod of identical dimensions to serve as a basis for comparison in order to extract as directly as possible the effects of the Pb loading.

Finally, section 8 describes analysis of a remaining aspect of the ALPS sensor that had not been captured in previous progress reports, and was not a main focus of effort in the ALPS II experimental campaign, but nevertheless merits some discussion. The bench-model ("ALPS I") incarnation of the sensor was outfitted with time-to-digital converters (TDCs) to measure the arrival time of light at each PMT relative to a specified timing fiducial (in practice, a single PMT in the multi-PMT set). The availability of relative timing information offers the potential for determining the interaction position of the incident gamma-ray in each of the sensor's scintillators. Depending upon the position resolution achievable in this interaction vertex reconstruction, some coarse imaging information on the incident gamma-ray flux could conceivably be extracted from a dual-sheet, large-area sensor with relative timing capability. The analysis and physical models outlined in section 8 represent a substantial, although not yet definitive, attempt to characterize the interaction-position information derivable from the ALPS multi-PMT relative timing data.

2.0 ALPS II Mechanical Design

2.1 ALPS II Detector Design

The ALPS II sensor (see Figure 2.1) is a second phase prototype developed with knowledge gained from the original ALPS bench model tests. This model differs from the original in many ways. While it operates on the same principles, the detector is now oriented vertically instead of horizontally, as was the original. Early testing with the original design also showed a benefit in performance when the scintillating plastic is wrapped with reflective Mylar, so the ALPS II takes advantage of this in its design.

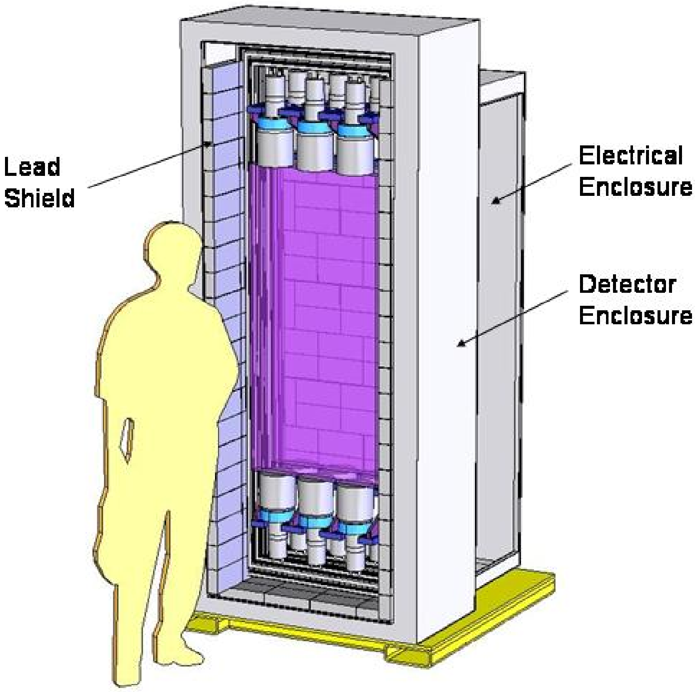

Figure 2.1. Basic ALPS II Mechanical Configuration

2.1.1 Detector Design

ALPS II is designed to be deployable outdoors, in contrast to the original sensor which was designed as a laboratory bench-testing model. The functional design criteria for ALPS II are summarized in the following list:

1. Field deployable in outdoor environment
    a. Single Pallet mount
    b. Weather tight
2. Light tight instrument enclosure
3. Internal electronics
4. Field maintainable

   a. Accessible electronics
   b. Accessible PMT maintenance/replacement
5. Shielded on 3 sides and bottom, 2” thick lead
6. Attenuator to be removable

2.1.2 Instrument Components

The primary components of the instrument are shown in Figure 2.2. The system consists of two plastic scintillating panels spaced at 7” center to center. Each panel is 50.0” high × 22.5” wide × 2” thick (127cm × 57.15cm × 7.87cm). The scintillating plastic is also wrapped with a reflective Mylar coating on four sides. The top and bottom of each panel are left uncovered to allow optical contact with the photomultiplier tubes (PMTs).

An attenuator is located midway between the plastic panels. The attenuator is constructed of 1/8” lead sheet sandwiched between two ¼” polycarbonate panels for mechanical stability. The attenuator is also 50” × 22.5” to match the area of the plastic panels. Each scintillating panel has three PMTs on each end, for a total of twelve PMTs in all. The scintillating panels are located 22” from the bottom of the enclosure and 27” from the ground when assembled on the pallet.

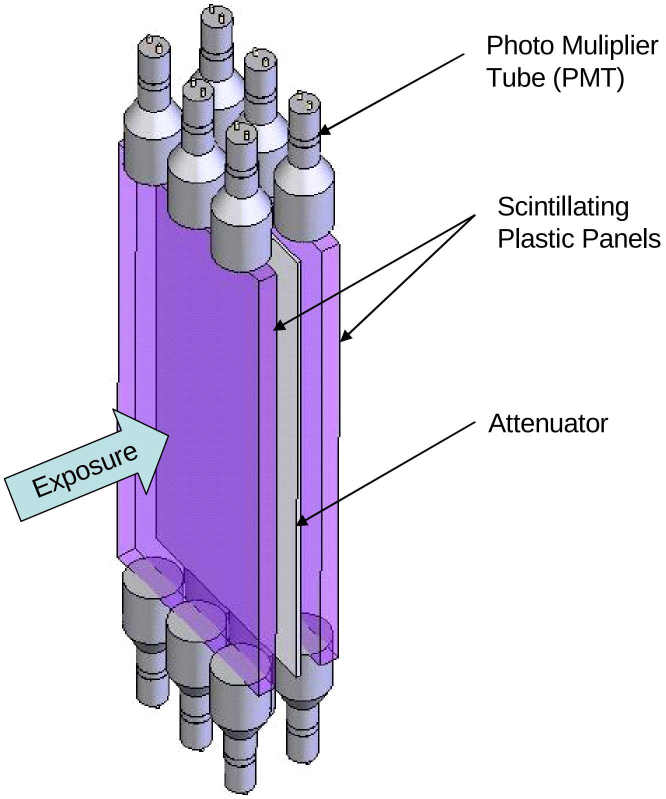

Figure 2.2. Primary ALPS II Detector Components

2.1.3 Detector Construction

The enclosure is first lined with construction grade insulation board (with 3” in the back, and with 2 ¾” on each side). This insulation extends all the way to the top of the enclosure. A 2” thick shield (lead brick) is then installed across the bottom and up back and both sides of the enclosure as shown in Figure 2.3. Figure 2.3 shows the door removed and the top section cut away to reveal the construction of the instrument enclosure. The shielding layer extends to a height of 6 feet above the bottom shield layer. The ½” plywood is placed inside the shielding to support the bricks as they are stacked. An aluminum angle is screwed into plywood at the corners to provide the necessary support to the plywood (see Figure 2.4).

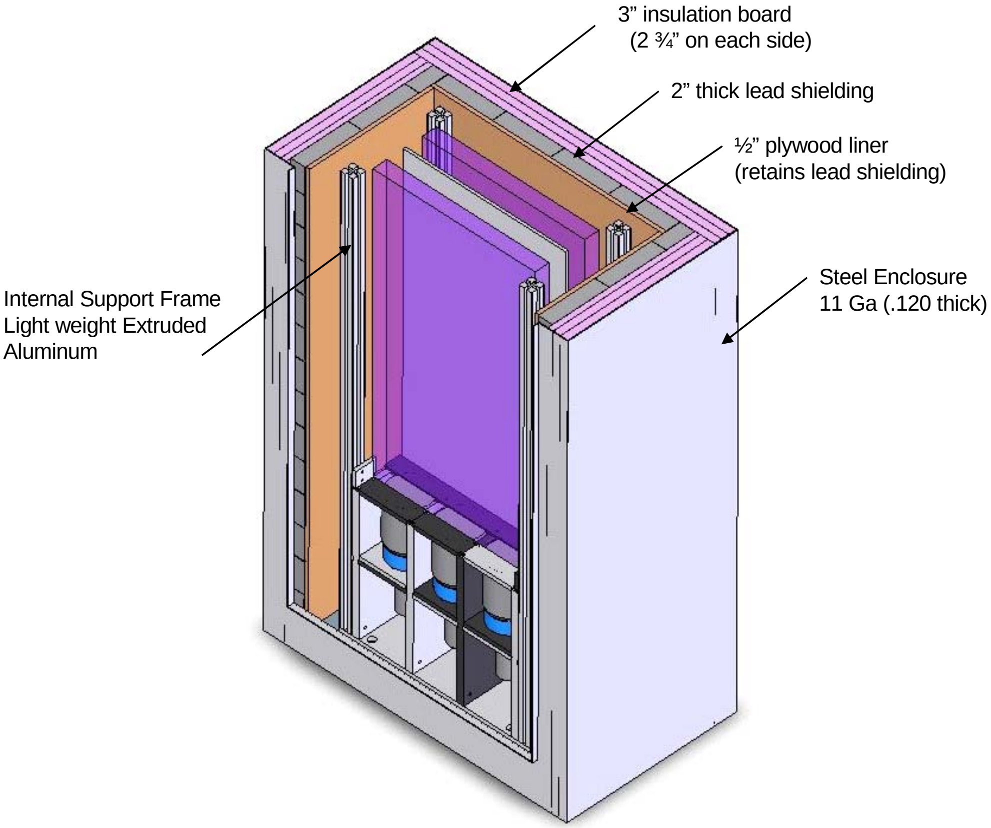

Figure 2.3. ALPS II Assembly Section

Figure 2.5 shows the internal support frame located in the enclosure during fit-up. The scintillating panels and PMTs are not installed in this figure. The complete internal support frame is removable (via fork lift) to allow full access to the instrument for maintenance/replacement of PMTs and removal/changing of the attenuation shield. The support frame is bolted down to a base plate in the enclosure and is further braced with the cross bar shown in the upper part of the enclosure.

08 19 2004 14:56

Figure 2.4. Enclosure Assembly

Figure 2.5. Internal Support Frame

The scintillating plastic panels and attenuator panel are held in place by recessed channels machined into the support frame.

2.1.4 PMT Installation

Figure 2.6 shows the three lower PMT bays. Each bay has two PMTs, one for each plastic panel. The top end is similarly outfitted, for a total of twelve PMTs. Each PMT is spring loaded to ensure good optical contact between the scintillator surface and the PMT face. This unique system allows for individual replacement or installation of each PMT. This is accomplished by locating the PMT in position with the support ring, springs and compression plate in place. Applying upward pressure on the compression plate compresses the springs, which allows the support plate to be slid into position in the side support grooves and under the compression plate as shown in the right-hand panel of Figure 2.6. This procedure is repeated for each PMT installation. The top PMTs are mounted similarly, except they are oriented so the PMT faces downward.

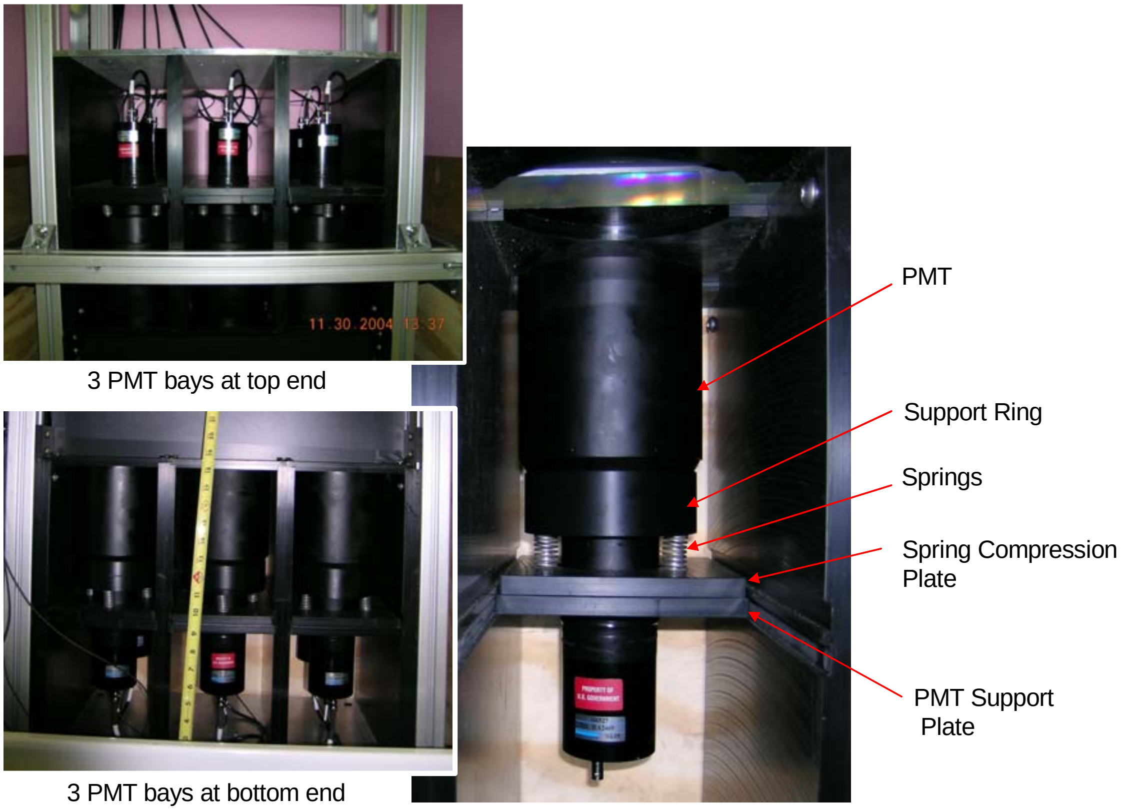

3 PMT bays at top end

3 PMT bays at bottom end

Figure 2.6. ALPS II PMT Installation

Figure 2.7 shows the instrument enclosure and electronics cabinet mounted on a steel pallet. Total weight has been estimated to be approximately 7000 pounds. The overall size of the instrument is 42” wide × 51” deep × 122” high (including lifting eyes).

2.1.5 Instrument Enclosure

The instrument enclosure itself is NEMA 4[(a)] rated for outdoor exposure. It is fitted with a black polycarbonate window (24” wide × 54” high × ¼” thick) in the door. This window is also lined on the inside with an opaque cloth, so that the enclosure is light-tight. This enclosure is 42” wide × 24”deep × 114” high and fabricated from 11 gage (.120”) carbon steel. The door opening is 103” high × 34” wide. The door itself is fitted with lift-off hinges for convenient removal.

(a) NEMA 4 - Enclosures are constructed for either indoor or outdoor use to provide a degree of protection to personnel against incidental contact with the enclosed equipment; to provide a degree of protection against falling dirt, rain, sleet, snow, windblown dust, splashing water, and hose-directed water; and that will be undamaged by the external formation of ice on the enclosure. See National Electrical Manufacturers Association (NEMA) Standards Publication No. 250 for more information.

Figure 2.7. ALPS II Enclosure

2.1.6 Electronics Enclosure

The control and high voltage electronics are mounted in a weather resistant rack cabinet directly behind the instrument cabinet. The electronics rack has front and rear doors for easy access. The rack is oriented so the doors open to the right and left sides of the assembly. Wiring between cabinets is routed through two conduits, shown in the upper left corner of Figure 2.8. A custom-built High Voltage (HV) module is mounted in the lower part of the rack as shown in Figure 2.9.

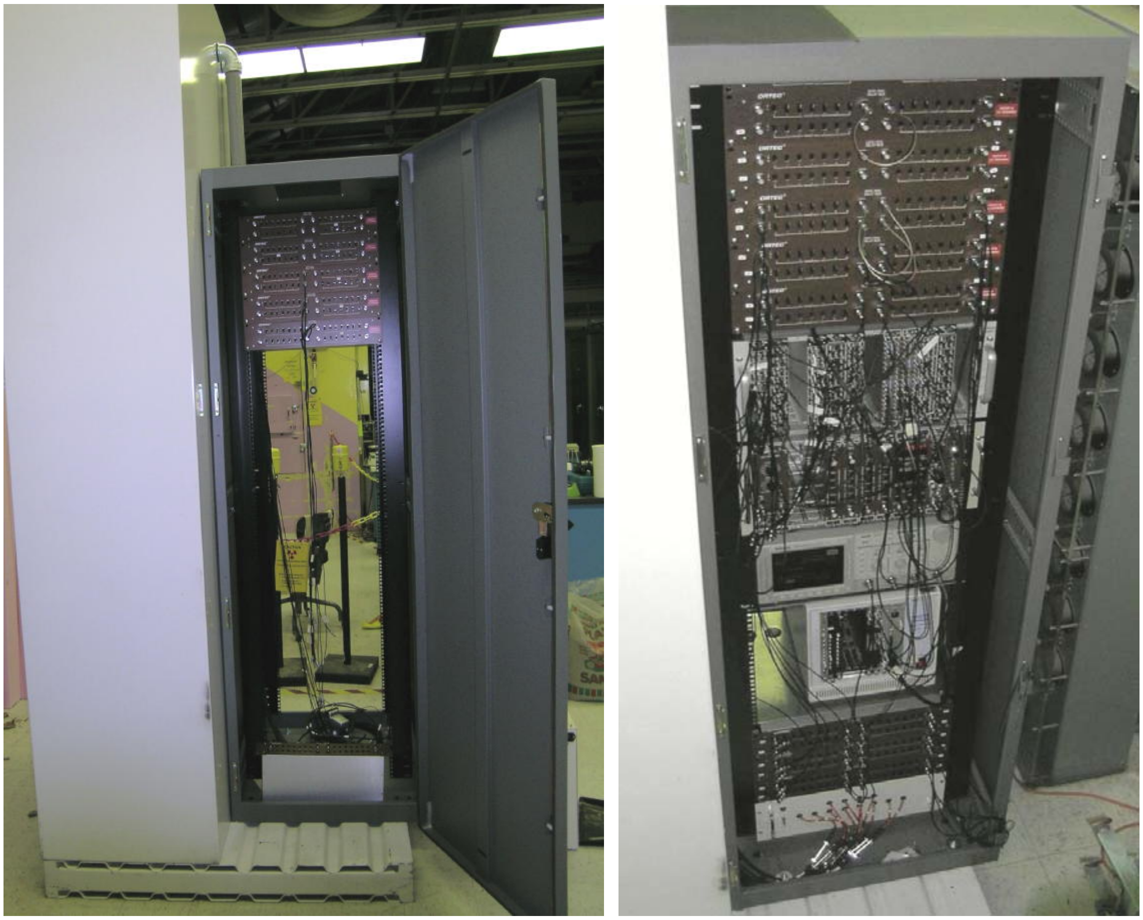

Figure 2.8. ALPS II Electronics Enclosure

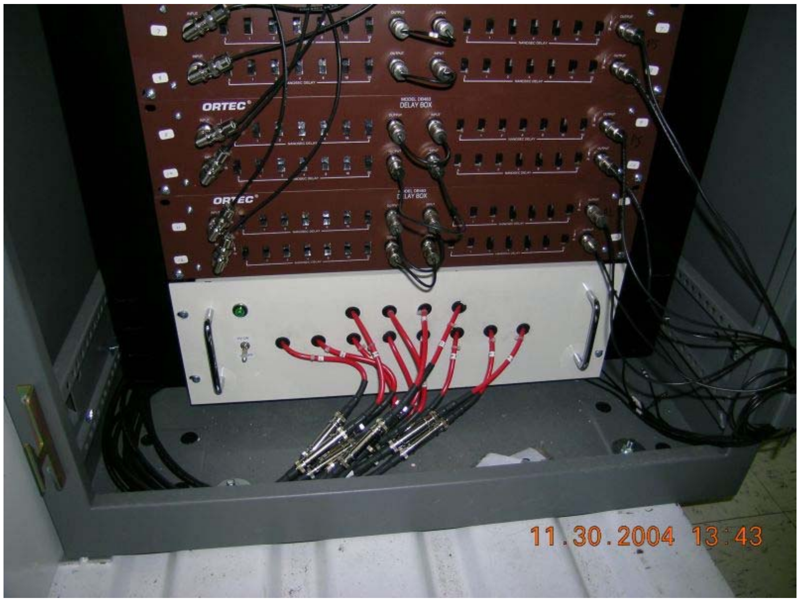

11.30.2004 13:43

Figure 2.9. Custom-built HV Module for ALPS II PMTs

3.0 ALPS II Single-Sheet Experiments

3.1 Introduction

Large-area plastic scintillators are frequently used as portal monitors to detect the passage of radioactive materials carried by humans, cars, trucks, trains, etc. Large-area scintillators are necessary to record a statistically significant number of radiation events while minimizing the time the carrier must be within the view of the portal monitor. In addition, a low background is required so that radioactive sources of concern can be detected reliably.

Sources of background include cosmic rays that tend to deposit large amounts of energy (>1 MeV) in scintillators oriented with their longest dimension in the vertical direction. Other sources of background include natural radioactivities in the environment such as ^{40}K and decay products of Th and U which can give gamma rays of about 1 MeV. In general, the radioactivities of interest for portal monitoring deposit rather small amounts of energy (<400 keV). Thus one technique for reducing background in portal monitors is to perform pulse height analysis of each event in the scintillator and to reject events with large pulse heights. In this work we study the effect of increasing the light collection efficiency of the scintillator by increasing the number of photomultiplier tubes (PMTs). Increased light collection efficiency should improve the energy resolution of the detector and thereby improve the rejection of unwanted events.

Another effect of increasing the number of PMTs is to increase the efficiency for detecting the small pulses of interest relative to the efficiency for detecting large pulses. In large scintillators, an event giving a small light output at some distance from a PMT may not produce a signal large enough to be detected because of light scattering and absorption between the event and the PMT. By surrounding the scintillator with more PMTs, the distance light must travel before reaching any PMT is greatly reduced. An event giving a large light output is likely to be observed by a distant PMT even though some of its light is attenuated before reaching the PMT.

In this section we describe the impact on energy resolution and efficiency of a large scintillator as the number of PMTs is increased from 1 to 6. The radiation sources tested included of ^{57}Co (122 keV), ^{133}Ba (356 keV), ^{137}Cs (662 keV), and ^{54}Mn (835 keV). The experiments used the ALPS II portal monitor system, outfitted as described in section 2 above. Although the ALPS II is a dual-sheet sensor, the experiments described in this section focus on the response of only a single scintillator, mapped as a function of PMT coverage. Experiments investigating dual-sheet sensor operation in particular are described in sections 4 and 5 below.

3.2 Experiment

3.2.1 Apparatus

Experiments were performed using the ALPS II portal monitor system. The ALPS II system had a slab of Bicron/Saint Gobain BC-408 scintillator of dimensions 127 × 57.15 × 5.08 cm^3. The scintillator slab had three Hamamatsu R1250 127-mm (5-in.) diameter PMTs mounted on each end for a total of 6 PMTs.(a) The scintillators were mounted vertically and shielded on the bottom, sides, and back by 5.08-cm of lead. The entire assembly was mounted in a light-tight steel box. A light-tight plastic door allowed entry of gammas to the scintillator detectors.

The initial experiments for optimizing the gain of individual PMTs were performed with all 6 PMTs mounted on the scintillator and included in the data acquisition. The experiments with fewer PMTs were performed without physically removing any of the PMTs. The high voltages to the undesired tubes were turned off, the PMT signals from those tubes were disconnected from the input to the initial fan-out, and the software code was modified to exclude any contribution from the unwanted PMTs. The three tubes on each end of the scintillator were spaced approximately at equal distances from each other and from the outside edges of the scintillator. The PMTs were labeled as 1,2, and 3 on one end, and 4, 5, and 6 on the other end such that 1 and 4, 2 and 5, and 3 and 6 were opposite each other with 2 and 5 in the middle. The 4 PMT configuration used PMTs 1, 3, 4, and 6 while the 2 PMT configuration used PMTs 2 and 5. Some data were taken in a 2 PMT configuration using PMTs 1 and 3. However PMT 3 appeared to have relatively poor light collection, probably due to poor coupling of the tube to the scintillator, so only a few of the results of this configuration are shown here.

The gamma radiation sources were mounted on the outside of the plastic door at the vertical and horizontal midpoint of the scintillators. The distance of the sources to the front face of the Front scintillator was about 10 cm. Count rates varied depending on the source and the trigger conditions for the data acquisition system, but never exceeded 100,000 counts per second (cps).

3.2.2 Data Acquisition System

The data acquisition system was composed of CAMAC and NIM data processing modules and a PC running Kmax Version 7.3 software.(b) A schematic of the data acquisition system is shown in Figure 3.1 (figures and tables referenced in section 3 are collected following section 3.4). Signals from the 6 PMTs were sent to linear fanouts (Phillips PS748). One of the signals from each fanout was delayed using Ortec DB463 modules. The delayed signals were then sent to a 16-channel CAMAC-based Charge-to-Digital (QDC) converter (Phillips PS7166) where the pulse was converted to a channel number corresponding to the integrated charge during a fixed time window. The channel numbers for all 6 PMTs were stored in a list processor (Hytec LP1342) for each event. When the buffer memory of the list processor was filled, the contents of the buffer were transferred to the computer. The list processor then continued to accept new data while the computer software processed the previous data into various histograms representing the pulse height spectra for all events.

The data acquisition system created separate histograms for each of the 6 PMTs. These histograms were useful for adjusting the high voltages on each PMT to gain match the outputs. All the PMTs (1-6) were gain matched to PMT 5. Gain matching was done for background pulse height spectra on the assumption that background events were uniformly distributed throughout the entire scintillator slab. Previous work had shown that the pulse height spectrum of a particular PMT depended on where the radiation event occurred within the scintillator. Figure 3.2 shows a comparison of background spectra in PMT 2 and PMT 5 after gain matching. Other PMTs gave equally good matches.

(a) Hamamatsu catalog number H6527 for PMT with integral tube base.

(b) Available from Sparrow Corporation, 1901 Poppy Lane, Port Orange, FL 32128.

In addition to recording the raw pulse heights for each PMT, the data acquisition system could create calculated parameters for each event. Thus the pulse heights of all six PMTs could be summed to give the total pulse height in the detector on an event-by-event basis. To compare spectra with different numbers of PMTs, the sum pulse heights were divided by the number of PMTs so that the resulting spectrum represents the average spectrum of all the included PMTs .

The width of the fixed time window for gating the QDC was 250 ns. Various requirements determined the conditions under which the QDC gate was created. Most experiments were performed with the QDC gate created only when 2 or more PMTs gave valid signals. A valid signal was generated for a PMT when the signal from that PMT exceeded the discriminator for that channel. Discriminators were set to the same value for all PMTs. Complete sets of experiments were performed at discriminator levels of 30 mV and 50 mV. For experiments where only one PMT was recorded, the requirement for 2 or more PMTs was omitted and any pulse in a PMT above the discriminator created a QDC gate. Another set of experiments was performed for only the ^{57}Co source where the QDC gate was generated whenever any PMT had a valid discriminator output.

In Figure 3.1, the QDC gate is triggered by the two-or-more discriminator output requirement. Each of the PMT signals go to discriminators that accept pulses above a specified threshold. The 6 PMTs go to an 8-channel discriminator module (Phillips PS705). This module has an output signal that is proportional to the number of channels that have been triggered simultaneously (Sum Output). The Sum Output was sent to a discriminator where the threshold was set to accept events where 2 or more PMTs had valid signals. The discriminator outputs were stretched to a width of 1.7 μs and fed back to the discriminators to inhibit acceptance of any other events until the current event had been fully processed. The Sum Output discriminator also sent a signal to other logic units to generate the QDC gate.

In all experiments, a separate 60-cycle pulser signal was included in the data stream by way of channel 15 of the QDC. The trigger for the pulser QDC gate was mixed with the trigger for valid signals by way of a coincidence unit operating in the "OR" mode. The output of this "OR" coincidence unit was stretched to 250 ns and was sent to the gate input of the QDC. This pulser signal was subject to the same dead times as the PMT signals. It was stored in a separate histogram. The integrated counts in the pulser histogram were compared to the number of events expected for the pulser for the elapsed data acquisition time. The ratio of the observed counts to the expected counts is the livetime for that particular experiment. Livetimes for background experiments were different from livetimes for runs with sources so a livetime correction was applied to all data.

3.2.3 Data Collection

All experiments recorded pulse height spectra for 300 second collection times. Sources were mounted at the horizontal and vertical midpoints of the detector on the outside of the plastic door as mentioned above. Background measurements were performed for all configurations. The discriminators on the individual PMTs were usually set at 50 mV; however, some data were obtained with discriminator levels of 30 mV and 10 mV.

3.3 Results

As the number of PMTs on a single scintillator increases, we expect the sum of the PMT signal outputs to contain a larger fraction of the total light emitted by the scintillator. Increased light collection efficiency should result in improved peak resolution (narrower peaks). In addition, events with small energy deposition or light output should be observed more efficiently because the events are more likely to be close to a PMT. In the following we will quantify these expectations for the particular size scintillator used in these experiments.

3.3.1 Resolution as a Function of the Number of PMTs

The pulse height spectra for the low-energy source ^{57}Co are shown in Figure 3.3 as a function of the number of PMTs. In Figure 3.3, only the first 60 channels out of the 256 channels full scale are shown. All spectra shown were obtained with the discriminators for individual PMTs set at 50 mV. Except for the 1 PMT data, the data acquisition accepted only those events where 2 or more PMTs had signals above the discriminator. The requirement for a trigger on 2 PMTs appears to significantly reduce the number of events at the lowest energies for the 2 PMT data relative to the single PMT data. However, with 4 or 6 PMTs, the enhancement of events at the lowest channels is quite strong.

The pulse height spectra for the ^{133}Ba source as a function of the number of PMTs are shown in Figure 3.4 and Figure 3.5. The vertical scale in Figure 3.4 is set to show the low energy portion of the spectra. The trends with PMT number are similar to those for ^{57}Co. Figure 3.5 has the vertical scale adjusted to demonstrate the changes associated with the Compton backscatter peak of the 356-keV gamma. The peak is hardly resolved with only 1 PMT. A distinct valley between the peak and lower energies becomes apparent with the 6 PMT configuration.

The pulse height spectra for the ^{137}Cs source as a function of the number of PMTs are shown in Figure 3.6 and Figure 3.7. The vertical and horizontal scales in Figure 3.6 are set to show the low energy portion of the spectra. The ^{137}Cs source has a 30 keV X-ray that appears prominently in the 1 PMT data. This peak seems highly suppressed in the 2 PMT configuration, but increases significantly for the 4 and 6 PMT configurations. Figure 3.7 shows the full range of the energy axis and has the vertical scale adjusted to demonstrate the changes associated with the Compton backscatter peak of the 662-keV gamma. There is a clear trend of improving resolution of the peak with increasing number of PMTs.

The pulse height spectra for the ^{54}Mn source as a function of the number of PMTs is shown in Figure 3.8. The full energy range is shown on the horizontal axis. There is no 30-keV X-ray in the ^{54}Mn source and therefore no strong enhancement at the lowest energies. There is a clear trend of improving resolution of the peak with increasing number of PMTs.

A similar set of pulse height spectra was obtained with the discriminators set at 30 mV. If the discriminator were cutting off a large fraction of the low-energy events, we expect the largest effect would appear in the ^{57}Co pulse height spectrum. A comparison of the ^{57}Co spectra with the 30-mV and 50-mV discriminator settings is shown in Figure 3.9 for the 6 PMT configuration. Note that there are increased counts at low channel numbers for the 30-mV discriminator setting but it is not a large effect.

The resolutions of peaks from the 3 highest-energy sources are shown in Table 3.1 for the spectra obtained with the discriminators at 50 mV and at 30 mV. The resolution is defined as the full-width-at-half-maximum (FWHM) divided by the channel number of the peak centroid. The resolutions for spectra taken with the discriminators at 30 mV are equivalent to those at 50 mV. The channel region for which the peak parameters were calculated is also shown in Table 3.1.

To illustrate the trends of resolution versus number of PMTs, Table 3.1 includes a column showing the resolution for a given number of PMTs divided by the resolution for a single PMT. For these sources the resolution clearly improves as the number of PMTs increases. The most dramatic improvement is for the ^{133}Ba source at lower energies than the other sources.

It is not clear whether the spectra for the ^{57}Co source show a peak due to the 122-keV gamma or whether the peak is an artifact of the discriminator thresholds. The resolutions for ^{57}Co are unreliable and are not shown because small changes in the peak location have a large effect on the resolution.

3.3.2 Relative Efficiency as a Function of the Number of PMTs

The measured pulse height spectra were corrected for live time and had background subtracted to obtain the net count rates. The net count rates for each of the 4 sources are given in Table 3.2 as a function of the number of PMTs. All count rates have been decay corrected to the date of Sep. 2, 2005. Count rates are shown for the sum of all events between channels 1 – 255 and for the sum of all channels over the peaks listed in Table 3.1. For each source the ratio of count rates for multiple PMTs relative to the count rate for 1 PMT is given for both the total count rates and the peak count rates. In general, count rates for the highest energy source, ^{54}Mn, change very little (<5%) as the number of PMTs increases. However, for the lowest energy source, ^{57}Co, with only 2 PMTs, the trigger requirement of 2 or more PMTs actually reduces the count rate relative to the single PMT configuration. For 4 or 6 PMTs, the ^{57}Co count rates are as much as 30% greater than the single PMT configuration. The same trends are observed with either the 50 mV discriminator settings or the 30 mV discriminator settings.

The ratio of net count rates for the two different discriminator levels are shown in Table 3.3 for the 4 sources and 4 PMT configurations. The lower discriminator level gave < 5% more counts for the 3 higher-energy sources for both the total count rates and the peak count rates whereas the ^{57}Co gave about 8% more counts for these rates. Because the effect of a lower discriminator would be most apparent at the lowest channels, Table 3.3 also gives the ratio of counts for the sum of channels 1 – 20. In this pulse height region, the ratio of count rates is essentially independent of the incident gamma energy and gives a ratio of about 8%. As the energy of the incident gamma increases, the fraction of events in the channel 1-20 pulse height region decreases. For this reason and because events in the higher pulse height region are less sensitive to the discriminator threshold, the effect of the discriminator becomes much less sensitive for sources with higher gamma energies.

3.3.3 Efficiency of ^{57}Co as a Function of the Number of PMTs Using "OR" trigger

As noted above and as displayed in Table 3.2, the QDC gate requirement of two or more PMTs in coincidence significantly reduces the data acquisition rate, particularly for the low-energy ^{57}Co source relative to the single PMT configuration. When using multiple PMTs, the two or more PMT coincidence requirement minimizes the possibility of noise or dark current distorting the spectrum at very low pulse heights. However it is of interest to determine whether this concern adversely affects the efficiency for detecting low-energy events.

A series of measurements with the ^{57}Co source was conducted using an "OR" trigger requirement. This meant that any PMT with a pulse above its discriminator level would trigger data acquisition. Discriminator levels or 30 mV and 50 mV were used. A comparison of ^{57}Co spectra for the "OR" trigger and the 2-or-more trigger is shown in Figure 3.10 for the configuration with 4 PMTs. Similar comparisons are shown in Figure 3.11 for the configuration with 2 PMTs on opposite ends and in Figure 3.12 for the configuration with 2 PMTs on the same end. In all three figures the discriminator level was 50 mV. The increase in low-energy counts for the "OR" trigger is more dramatic for the 50 mV discriminator than for the 30 mV discriminator.

Spectra were also obtained for the ^{54}Mn and ^{137}Cs sources for the 6 PMT and 30 mV discriminator configuration. The low-energy portions of these spectra for the "OR" trigger and 2-or-more trigger are compared in Figure 3.13 and Figure 3.14. Note that the spectra are rather smooth down to about channel 1 indicating that noise and dark current are not perturbing the spectra except at channel 0.

To quantify the enhanced efficiency with the "OR" trigger for low-energy events, the pulse height spectra were summed between channels 1 and 20 and compared to the corresponding counts for the 2 or more trigger configuration. These results are shown in Table 3.4 along with a few measurements of the other sources. For ^{57}Co, the efficiency for the "OR" trigger condition increases for the 2 PMT whereas for the 2-or-more trigger the efficiency decreased for the 2 PMT configuration. The efficiency for the 4 PMT configuration is even greater for the "OR" trigger than the corresponding configuration with the 2-or-more trigger. Based on these results and the spectra shown in Figure 3.10 through Figure 3.12, it appears that greater efficiency can be achieved for low-energy sources by not requiring a multiple PMT coincidence without introducing noise or dark current problems. As noted before, increasing the number of PMTs does increase the efficiency for low-energy sources by over 30%.

The high-energy sources, ^{137}Cs and ^{54}Mn, actually lost counts in the low-energy region when switching to the "OR" trigger condition. A small part of this loss can be attributed to a decrease in the total count rate over the full spectrum. For ^{137}Cs, the "OR" trigger measurement gave 3% fewer counts than the corresponding 2-or-more trigger measurement whereas the low-energy region was 10% lower. For ^{54}Mn, the "OR" trigger measurement gave 6% fewer counts whereas the low-energy region was 19% lower. The decrease in total count is probably an experimental problem related to mounting the sources or different dead time corrections. However, the larger decreases in the low-energy region are probably due to a shift of low pulse height events to higher pulse heights for the "OR" configuration. This is an unforeseen benefit as the goal of the ALPS program was to investigate ways to increase the efficiency for detecting low-energy events and avoiding interference from down-scattering of high-energy events.

3.3.4 Effect of high channel resolution at low energies

It is of interest to determine whether use of high channel resolution might improve the energy resolution particularly at low pulse heights. An experiment was performed using the 6 PMT configuration with discriminators set at 30 mV to evaluate this possibility. The normal full scale range of the QDCs was 256 channels. For the high channel resolution experiments, this full scale range was increased by a factor of 6 to 1536 channels. A comparison of the ^{137}Cs pulse height spectra taken with the normal channel resolution and the high channel resolution is shown in Figure 3.15 for the low-energy region. The peak at about channel 32 in the high channel resolution spectrum is due to the 30-keV X-ray in this source. The peak-to-valley ratio of this peak is somewhat better for the high channel resolution data. Assuming a zero energy offset at channel zero, a rough energy calibration gives about 1 keV per channel for the high channel resolution data. The three sharp spikes below the peak are not understood and may be electronic artifacts.

Confirmation of the identity of the 30-keV peak can be seen in a comparison of the low-energy region for the ^{137}Cs and ^{54}Mn sources shown in Figure 3.16. The ^{54}Mn source does not have X-rays in the 30-keV region and shows no peak in the region of the ^{137}Cs peak.

A comparison of high channel resolution data with low channel resolution data for ^{57}Co is shown in Figure 3.17. There is no particular structure observed in these spectra and thus there is no particular advantage to using high channel resolution for this source.

3.3.5 Comparison of calculated and experimental spectra

In addition to the experimental program, theoretical calculations of the ALPS scintillator response were performed to estimate the expected pulse height distributions. Energy deposition calculations employed an ALPS-specific application based upon the Geant4 radiation transport code framework, as described extensively in a previous report [Jordan et al. 2003]. The calculated energy deposition spectra were broadened by an energy-dependent Gaussian resolution function to simulate the response of the plastic scintillator. The calculated and smoothed pulse height spectra were compared to experimental data and the smoothing parameter was adjusted to give the best fit to the experimental data.

The comparison of the calculated energy deposition spectrum of ^{54}Mn with the smoothed spectrum is shown in Figure 3.18. The calculated and smoothed spectrum is compared to the experimental data in Figure 3.19. Similar spectra for ^{137}Cs are shown in Figure 3.20 and Figure 3.21, and in Figure 3.22 and Figure 3.23 for ^{133}Ba. Note that the experimental data were obtained earlier using 6 PMTs but different QDC gating requirements than those used for the spectra shown above. For these older measurements, the QDC gate was generated by a signal from any one of the PMTs on one end that was in coincidence with any one PMT signal from the other end (a 3-fold “OR” at each end followed by a two-fold coincidence). The discriminators for all PMTs were set at 20 mV. However the end-to-end coincidence cuts off more of the low-energy events than the gating system used in the more recent data discussed above.

Although the calculated energy deposition spectra show some distinct peaks due to 180 degree Compton scattering, these peaks are greatly broadened by the resolution of the plastic scintillator. Rather good agreement with the experimental spectra can be obtained with reasonable resolution functions.

3.4 Discussion

The use of more PMTs improves the pulse height resolution so that distinct peaks due to the Compton edge scattering are observed for monoenergetic gamma sources. This improved resolution means that given sufficient statistical accuracy, the pulse height spectra could be used to identify particular sources of interest for portal monitoring – especially if the sources are monoenergetic and unshielded.

The use of more PMTs did not significantly increase the total efficiency of counting high- energy gamma sources. However, the total efficiency for counting low-energy sources could be increased by at least 30% for the 6 PMT configuration compared to using only 1 PMT. If the requirement of 2 PMTs in coincidence is abandoned, the efficiency for low-energy sources might be 40% greater than the single

PMT configuration. If one looks only at the low-energy region, there may even be a decrease of 10 – 20% efficiency for the high-energy sources. This would be beneficial to low-energy source sensitivity, because it would tend to reduce background from relatively high-energy terrestrial gamma rays. The implications of these efficiency considerations for minimum detectable activity are discussed in section 7 below.

Table 3.1. Resolution of peaks as a function of the number of PMTs

Source	# PMT	Centroid (Ch. No.)	FWHM (Ch. No.)	Res. (%)	Ratio to 1 PMT	Range (Channels)
Disc. 50 mV						
^{133}Ba	6	44.39	20.97	47.2	0.656	28 - 84
^{133}Ba	4	41.65	23.18	55.7	0.773	28 - 84
^{133}Ba	2	43.43	22.44	51.7	0.718	28 - 84
^{133}Ba	1	39.23	28.25	72.0	1.000	26 - 80
^{137}Cs	6	116.42	38.13	32.8	0.838	70 - 180
^{137}Cs	4	116.55	39.12	33.6	0.859	70 - 180
^{137}Cs	2	119.90	43.51	36.3	0.928	70 - 180
^{137}Cs	1	118.25	46.22	39.1	1.000	70 - 180
^{54}Mn	6	155.01	49.14	31.7	0.858	92 - 232
^{54}Mn	4	154.15	49.33	32.0	0.866	92 - 232
^{54}Mn	2	163.46	57.04	34.9	0.945	92 - 232
^{54}Mn	1	158.97	58.73	36.9	1.000	92 – 232
Disc. 30 mV						
^{133}Ba	6	44.30	20.93	47.2	0.532	28 - 84
^{133}Ba	4	41.66	23.33	56.0	0.630	28 - 84
^{133}Ba	2	43.41	22.36	51.5	0.579	28 - 84
^{133}Ba	1	36.99	32.88	88.9	1.000	26 – 80
^{137}Cs	6	117.05	38.87	33.2	0.856	70 - 180
^{137}Cs	4	116.57	39.47	33.9	0.873	70 - 180
^{137}Cs	2	119.94	42.57	35.5	0.915	70 - 180
^{137}Cs	1	118.41	45.92	38.8	1.000	70 - 180
^{54}Mn	6	156.41	48.67	31.1	0.814	92 - 232
^{54}Mn	4	154.41	48.95	31.7	0.829	92 - 232
^{54}Mn	2	162.03	57.81	35.7	0.933	92 - 232
^{54}Mn	1	157.50	60.24	38.2	1.000	92 – 232

Table 3.2. Count rates and count rate ratios as a function of the number of PMTs

Source	# PMT	Disc. = 50 mV				Disc. = 30 mV			
		Total Count (cps)	Ratio to 1 PMT	Peak Sum (cps)	Ratio to 1 PMT	Total Count (cps)	Ratio to 1 PMT	Peak Sum (cps)	Ratio to 1 PMT
^{57}Co	6	8054	1.24	7766	1.30	8664	1.27	8395	1.33
^{57}Co	4	7744	1.20	7380	1.23	7907	1.16	7608	1.20
^{57}Co	2	5414	0.84	5062	0.85	6352	0.93	5934	0.94
^{57}Co	1	6483	1.00	5987	1.00	6824	1.00	6330	1.00
^{133}Ba	6	83282	1.14	23445	1.00	86312	1.14	24463	1.09
^{133}Ba	4	80819	1.11	24399	1.04	83426	1.10	24480	1.09
^{133}Ba	2	67965	0.93	24762	1.05	72313	0.95	24426	1.08
^{133}Ba	1	72814	1.00	23555	1.00	75950	1.00	22554	1.00
^{137}Cs	6	37886	0.91	17957	0.95	42489	1.01	20199	1.07
^{137}Cs	4	41221	1.00	19779	1.04	41800	1.00	19910	1.06
^{137}Cs	2	40423	0.98	20215	1.07	40628	0.97	19921	1.06
^{137}Cs	1	41443	1.00	18961	1.00	42009	1.00	18856	1.00
^{54}Mn	6	7151	0.96	3672	0.98	7617	1.00	3928	1.04
^{54}Mn	4	7482	1.00	3877	1.03	7551	0.99	3892	1.03
^{54}Mn	2	7349	0.98	3939	1.05	7376	0.97	3909	1.04
^{54}Mn	1	7487	1.00	3760	1.00	7645	1.00	3767	1.00

Table 3.3. Ratio of count rates at 30 mV to 50 mV discriminator levels as a function of the number of PMTs

Source	# PMT	Ratio of Total Counts Ch.(1-255)	Ratio of Counts in Peak	Ratio of Counts in Ch.(1-20)
^{57}Co	6	1.08	1.08	1.08
^{57}Co	4	1.02	1.03	1.03
^{57}Co	2	1.17	1.17	1.17
^{57}Co	1	1.05	1.06	1.06
	Ave.	1.08	1.09	1.09
^{133}Ba	6	1.04	1.04	1.03
^{133}Ba	4	1.03	1.00	1.05
^{133}Ba	2	1.06	.99	1.13
^{133}Ba	1	1.04	.96	1.07
	Ave.	1.04	1.00	1.07
^{137}Cs	6	1.12	1.13	1.14
^{137}Cs	4	1.01	1.01	1.03
^{137}Cs	2	1.01	.99	1.08
^{137}Cs	1	1.01	.99	1.07
	Ave.	1.04	1.03	1.08
^{54}Mn	6	1.07	1.07	1.07
^{54}Mn	4	1.01	1.00	1.04
^{54}Mn	2	1.00	.99	1.08
^{54}Mn	1	1.02	1.00	1.10
	Ave.	1.03	1.02	1.07

Table 3.4. Count rates (cps) for the sum of pulse height channels 1 – 20 as a function of the number of PMTs, discriminator level (50 mV and 30 mV), and type of trigger (2-or-more and "OR"). The ratios of #PMTs to 1 PMT are also given.

Source	# PMT	SUM 50 mV 2-or-more	Ratio to single PMT	SUM 50 mV "OR"	Ratio to single PMT	SUM 30 mV 2-or-more	Ratio to single PMT	SUM 30 mV "OR"	Ratio to single PMT
^{57}Co	6	7766	1.30			8395	1.33		
^{57}Co	4	7380	1.23	8327	1.39	7608	1.20	8223	1.30
^{57}Co	2*	5062	0.85	7657	1.28	5934	0.94	7866	1.24
^{57}Co	2**	3893	0.65	7298	1.22	5805	0.92	7550	1.19
^{57}Co	1	5987	1.00	5987	1.00	6330	1.00	6330	1.00
^{133}Ba	6	54990	1.25			56729	1.20	60192	1.28
^{133}Ba	4	50966	1.16			53490	1.13		
^{133}Ba	2*	37226	0.85			41974	0.89		
^{133}Ba	1	44030	1.00			47158	1.00	47158	1.00
^{137}Cs	6	9475	0.92			10760	0.97	10008	0.90
^{137}Cs	4	9908	0.96			10246	0.93		
^{137}Cs	2*	8241	0.80			8879	0.80		
^{137}Cs	1	10310	1.00			11059	1.00	11059	1.00
^{54}Mn	6	1154	0.98			1233	0.95	1059#	0.81
^{54}Mn	4	1143	0.97			1184	0.91		
^{54}Mn	2*	962	0.82			1037	0.80		
^{54}Mn	1	1178	1.00			1301	1.00	1301	1.00

2* = PMTs 2 & 5

2** = PMTs 1 & 3

Sum of channels 2-20 because a large negative count at channel 1 distorts sum.

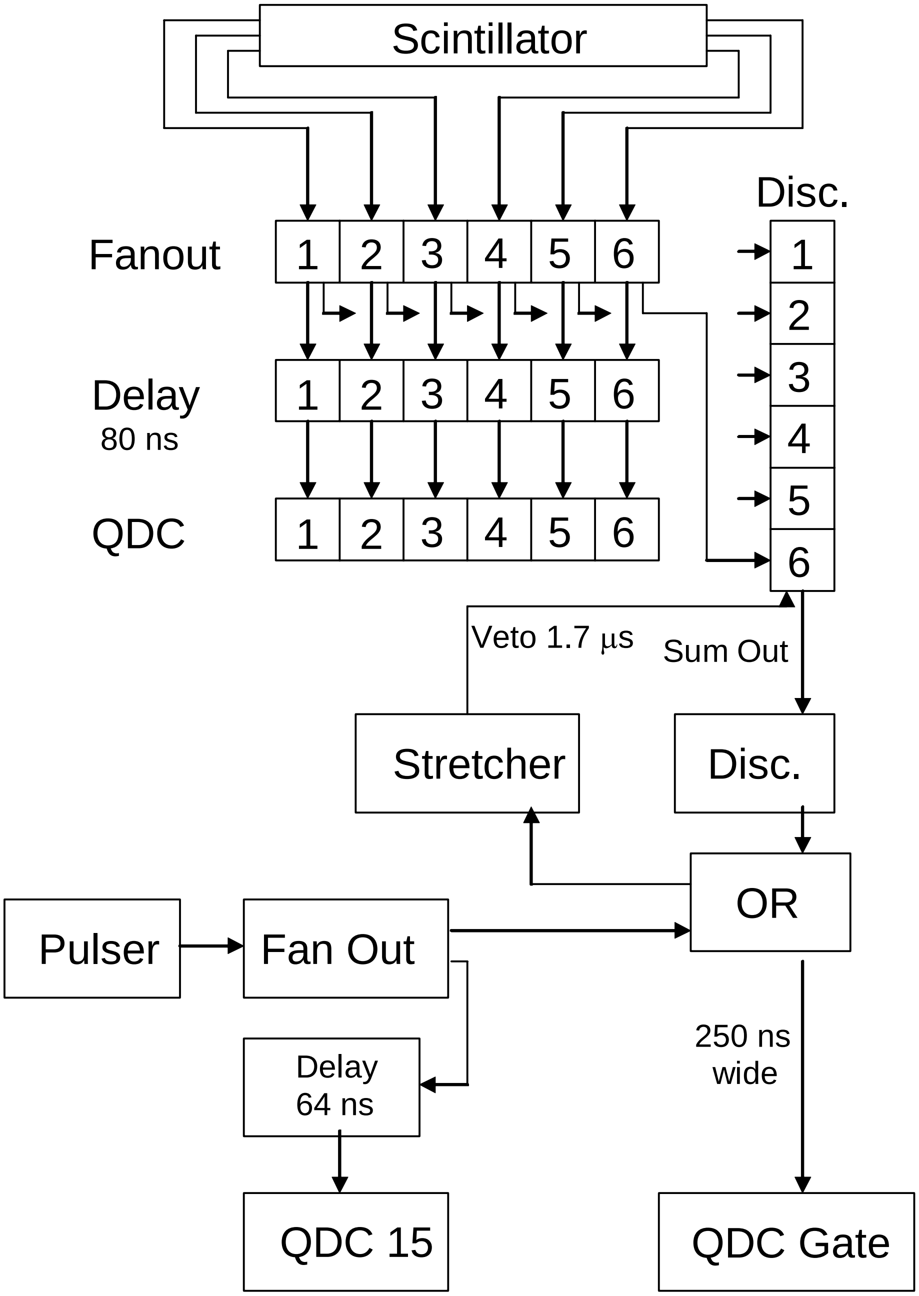

Figure 3.1. Schematic of ALPS II data acquisition system for single-sheet experiments

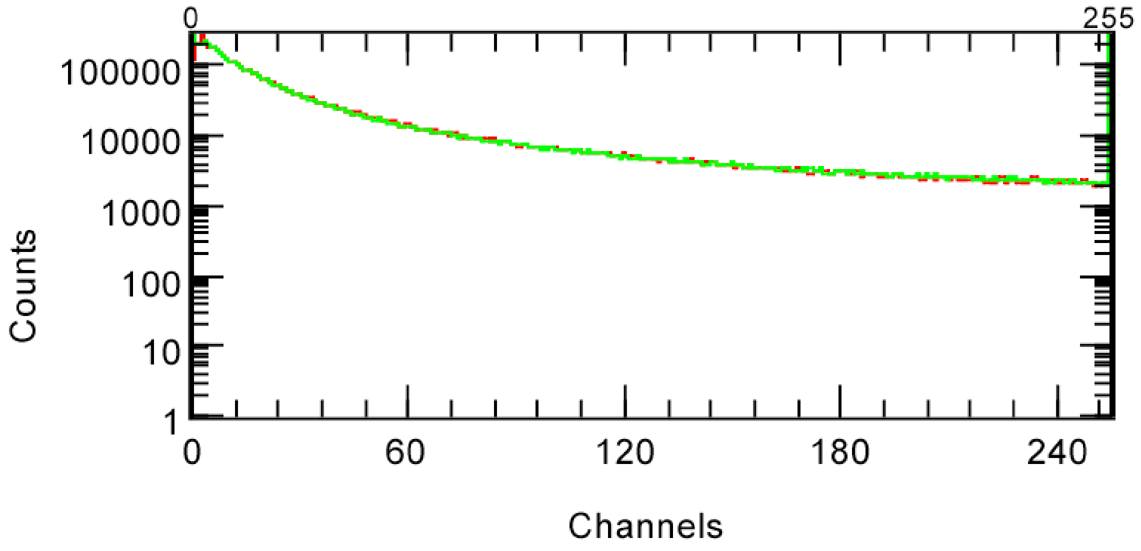

Figure 3.2. Comparison of PMT 2 (green) and PMT 5 (red) background pulse height spectra

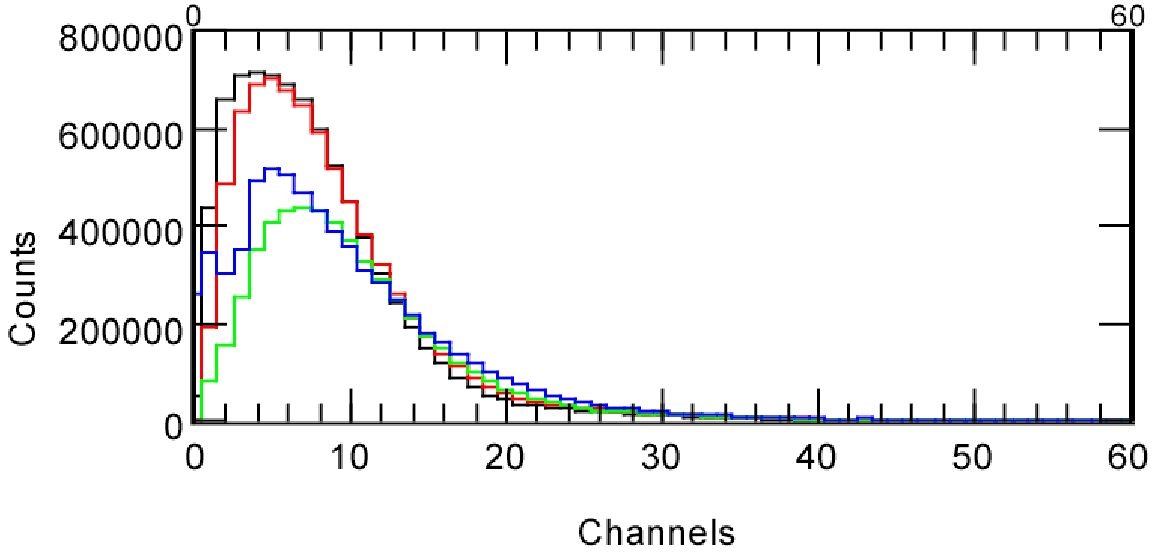

Figure 3.3. Pulse height spectra for ^{57}Co source with 1 PMT (blue), 2 PMTs (green), 4 PMTs (red), and 6 PMTs (black)

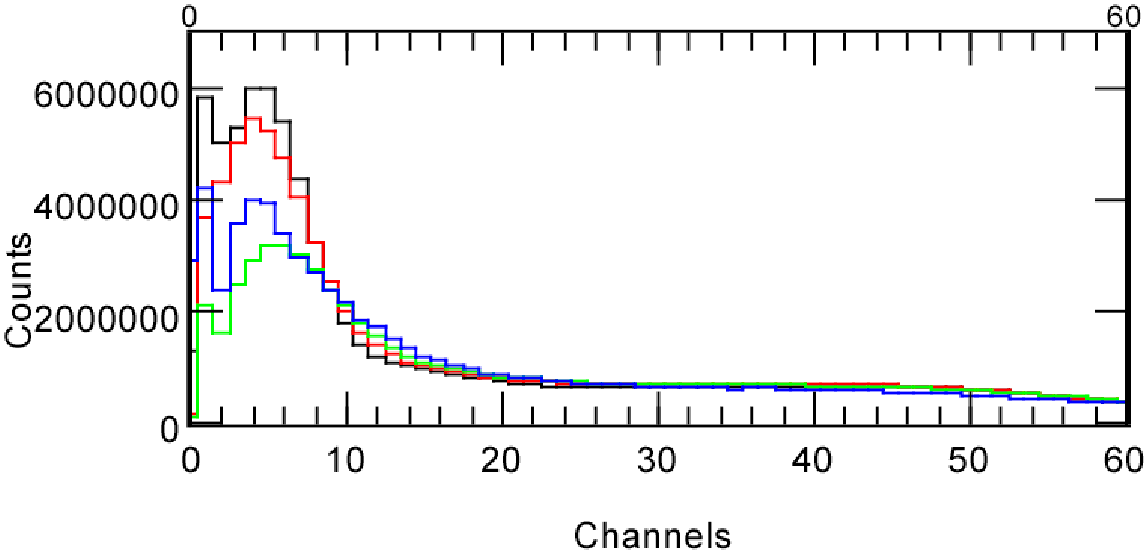

Figure 3.4. Low-Energy portion of pulse height spectra for ^{133}Ba source with 1 PMT (blue), 2 PMTs (green), 4 PMTs (red), and 6 PMTs (black)

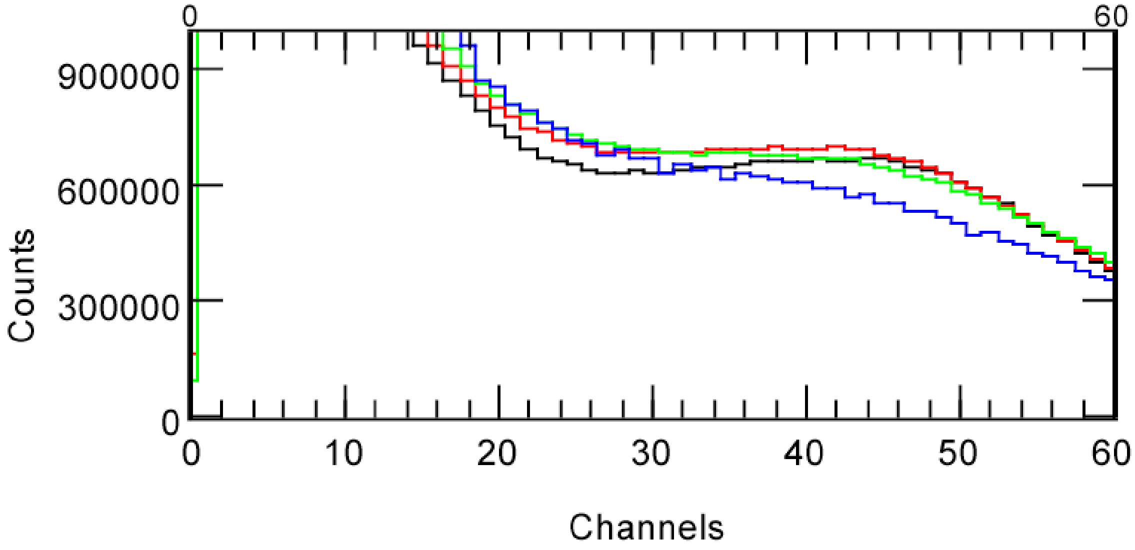

Figure 3.5. Low-Energy portion with expanded vertical scale of pulse height spectra for ^{133}Ba source with 1 PMT (blue), 2 PMTs (green), 4 PMTs (red), and 6 PMTs (black)

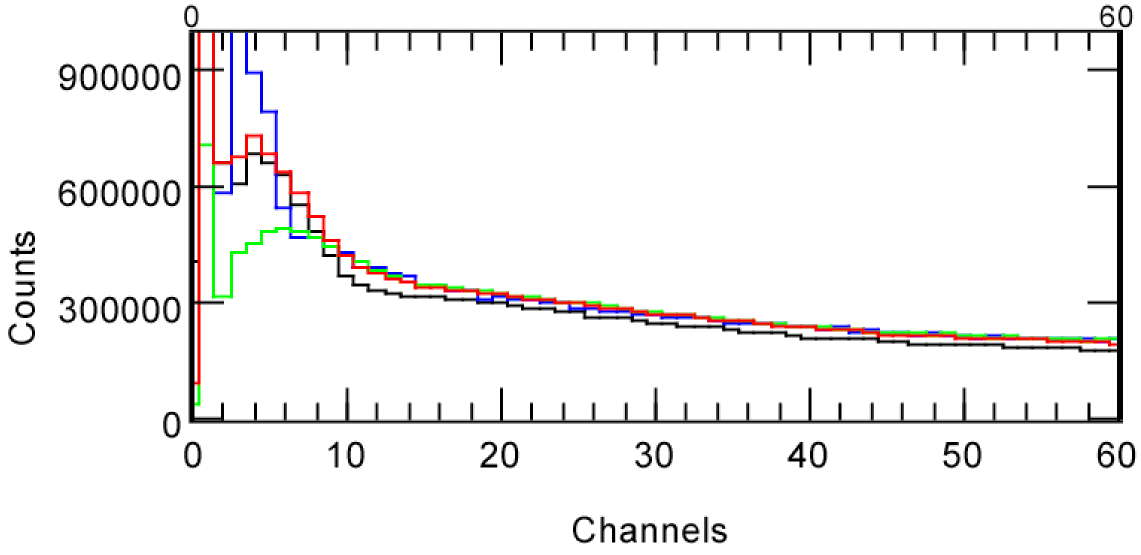

Figure 3.6. Low-Energy portion of pulse height spectra for ^{137}Cs source with 1 PMT (blue), 2 PMTs (green), 4 PMTs (red), and 6 PMTs (black)

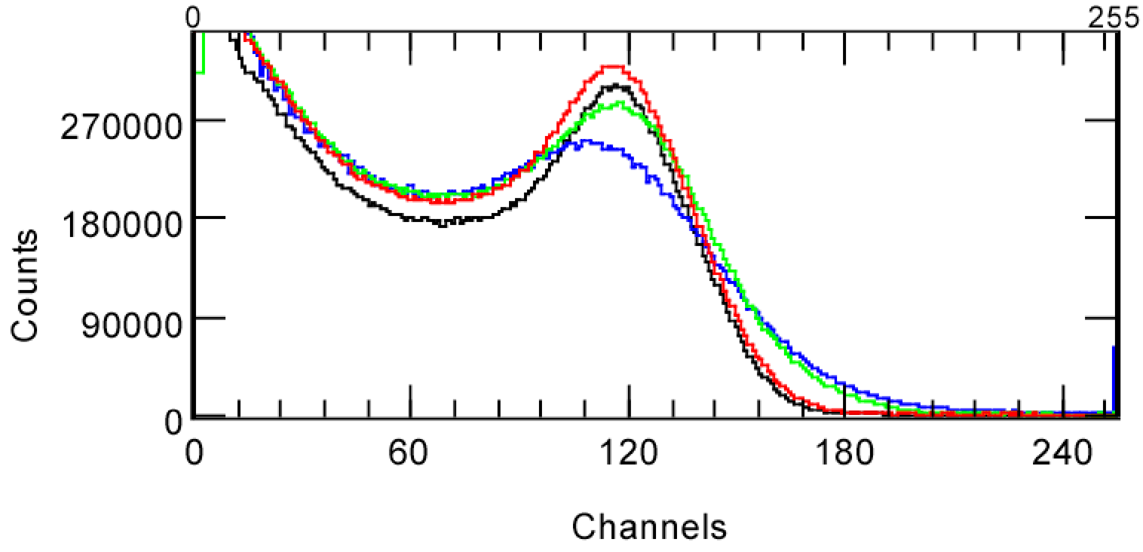

Figure 3.7. Expanded vertical scale of pulse height spectra for ^{137}Cs source with 1 PMT (blue), 2 PMTs (green), 4 PMTs (red), and 6 PMTs (black)

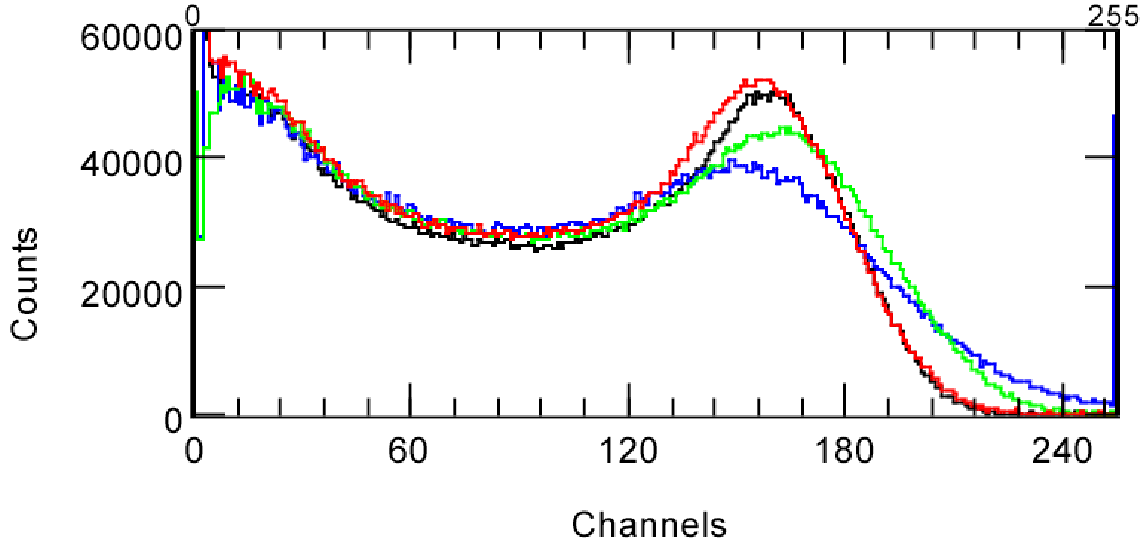

Figure 3.8. Pulse height spectra for ^{54}Mn source with 1 PMT (blue), 2 PMTs (green), 4 PMTs (red), and 6 PMTs (black)

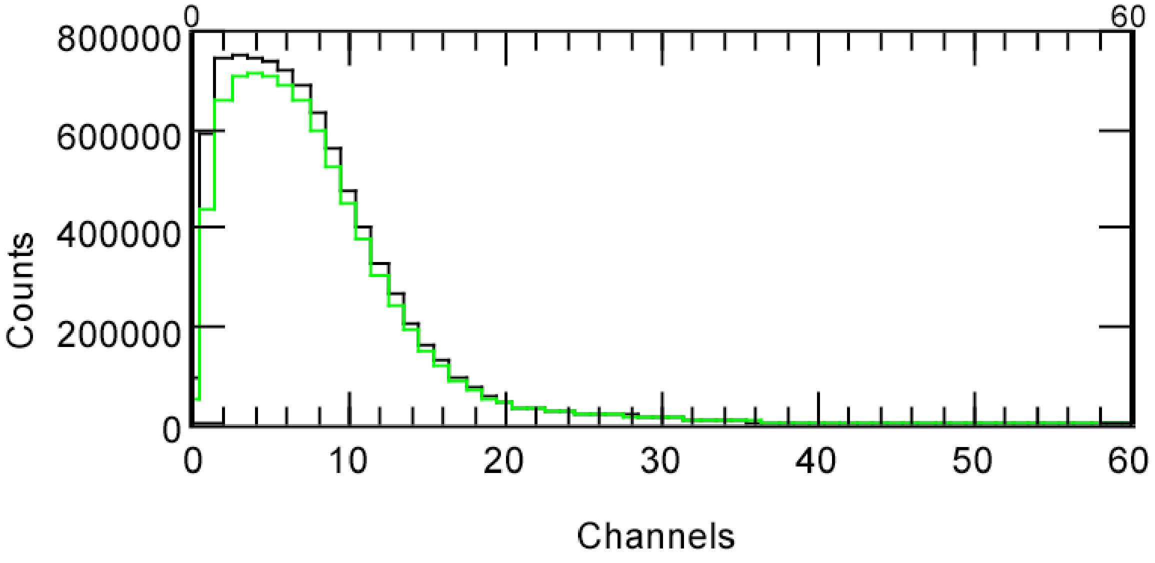

Figure 3.9. Pulse height spectra for ^{57}Co source with discriminators set at 30 mV (black) and 50 mV (black) for 6 PMT configuration

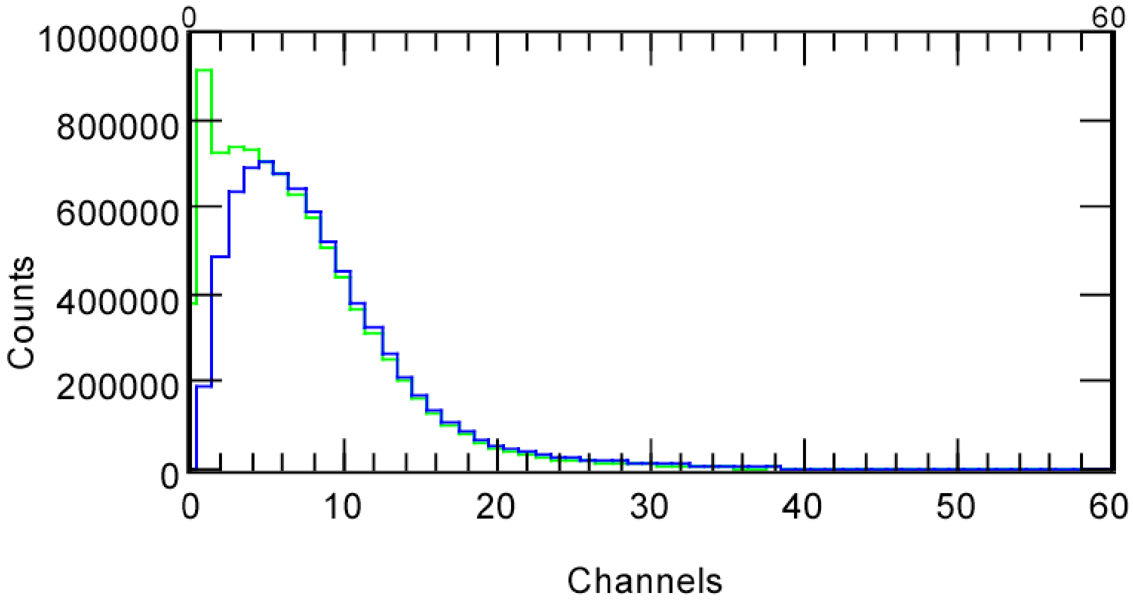

Figure 3.10. **Comparison of ^{57}Co pulse height spectra for "OR" trigger (green) and 2-or-more trigger (blue) for 4 PMT and 50 mV discriminator configuration**

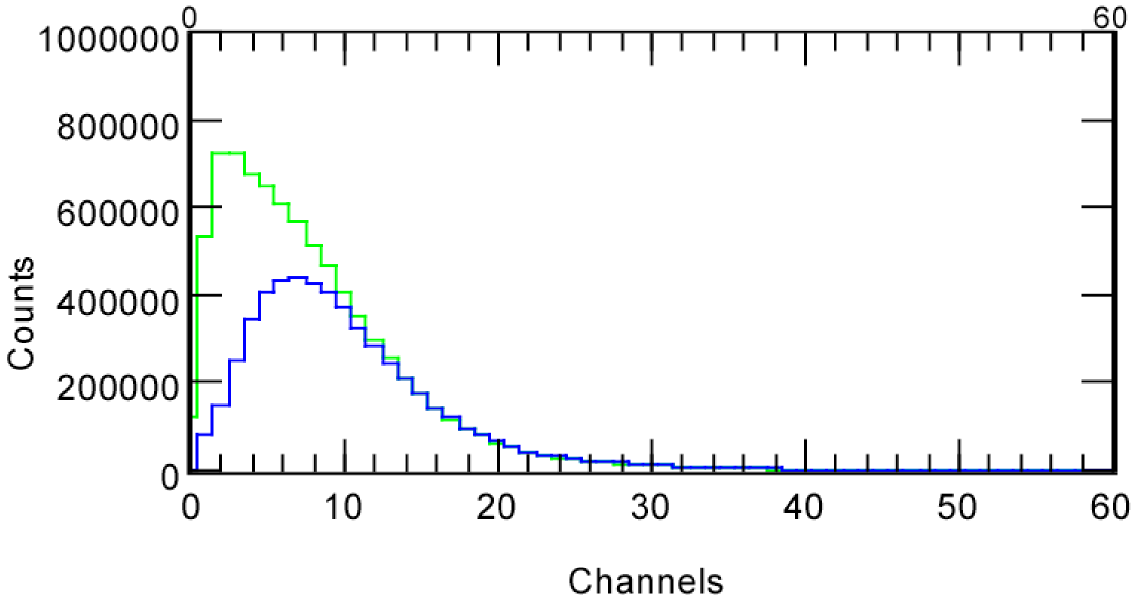

Figure 3.11. **Comparison of ^{57}Co pulse height spectra for "OR" trigger (green) and 2-or-more trigger (blue) for 2 PMTs at opposite ends and 50 mV discriminator configuration**

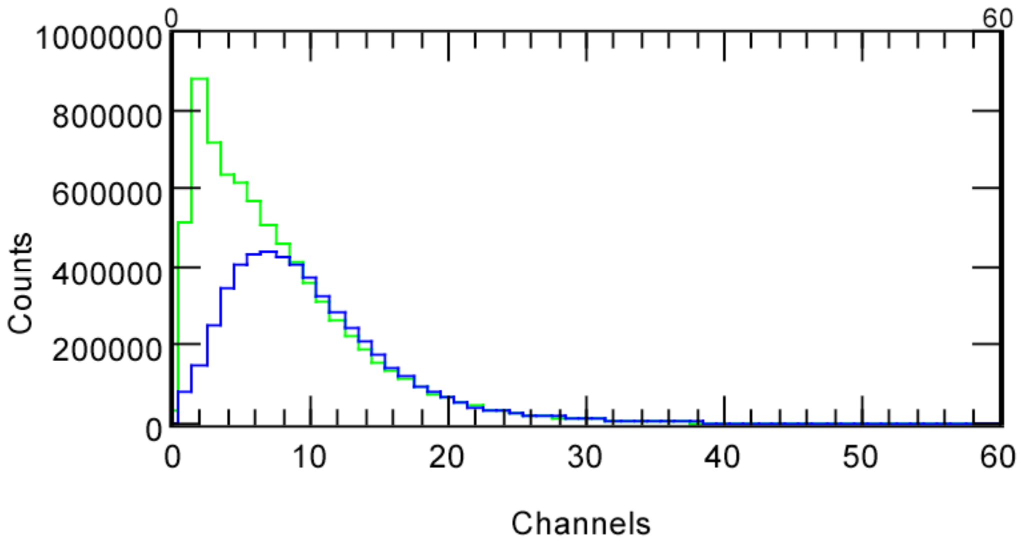

Figure 3.12. **Comparison of ^{57}Co pulse height spectra for "OR" trigger (green) and 2-or-more trigger (blue) for 2 PMTs at same end and 50 mV discriminator configuration**

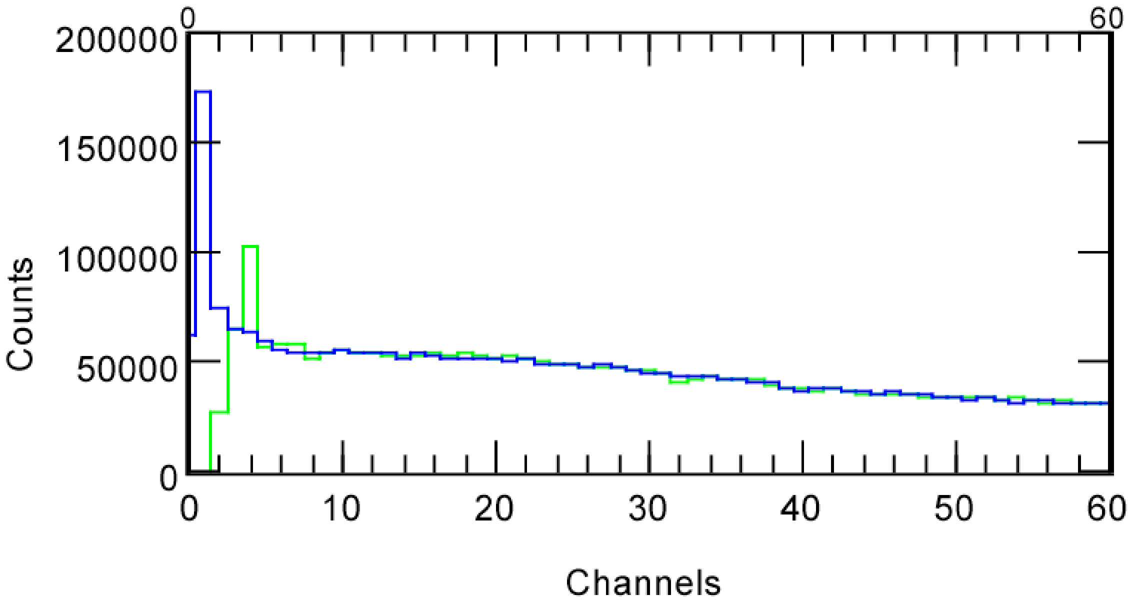

Figure 3.13. **Comparison of ^{54}Mn pulse height spectra for "OR" trigger (green) and 2-or-more trigger (blue) for 6 PMTs and 30 mV discriminator configuration**

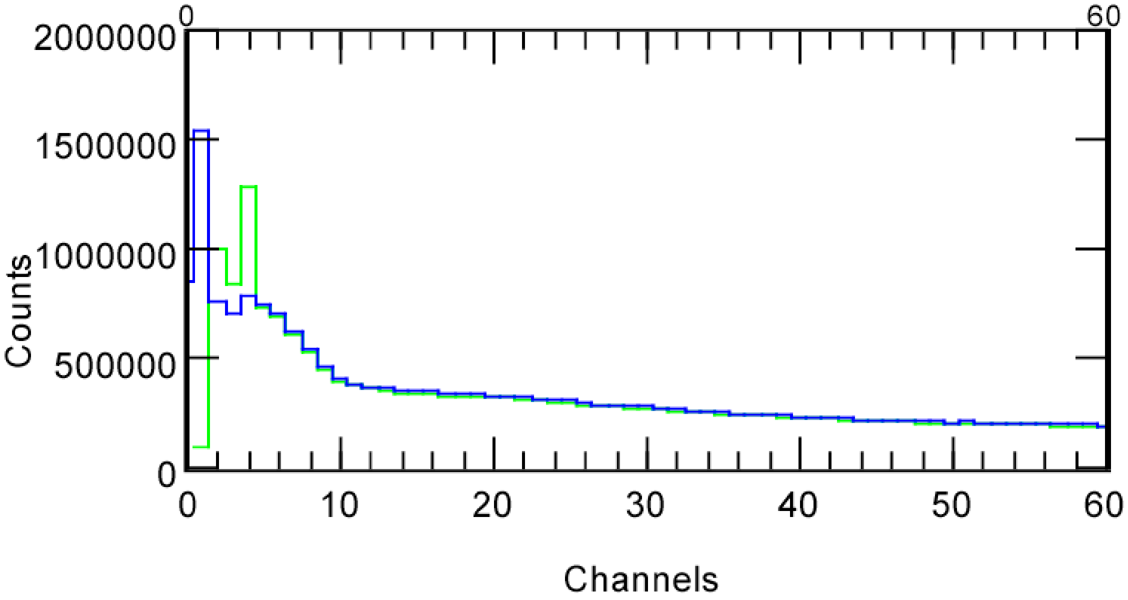

Figure 3.14. Comparison of ^{137}Cs pulse height spectra for "OR" trigger (green) and 2-or-more trigger (blue) for 6 PMTs and 30 mV discriminator configuration

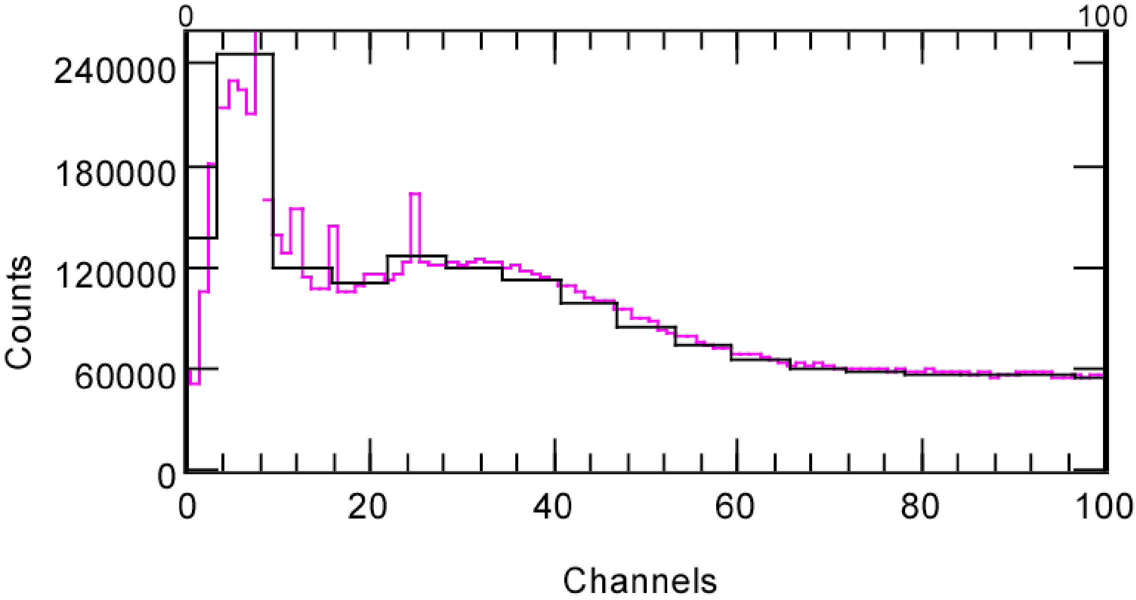

Figure 3.15. Comparison of low-energy pulse height region for ^{137}Cs source for low (black) and high (magenta) channel resolution. 6 PMTs with discriminator at 30 mV

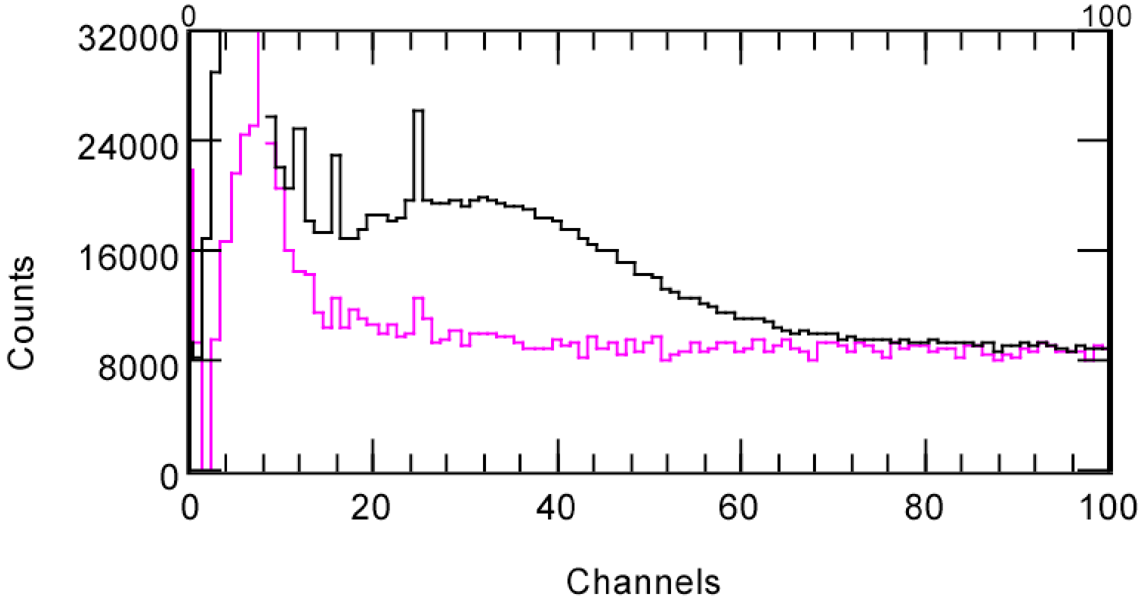

Figure 3.16. **Comparison of low energy pulse height region for ^{137}Cs (black) and ^{54}Mn (magenta) sources with higher channel resolution. 6 PMTs with discriminator at 30 mV. The peak in the ^{137}Cs spectrum at channel 32 is due to the 30-keV X-ray in this source.**

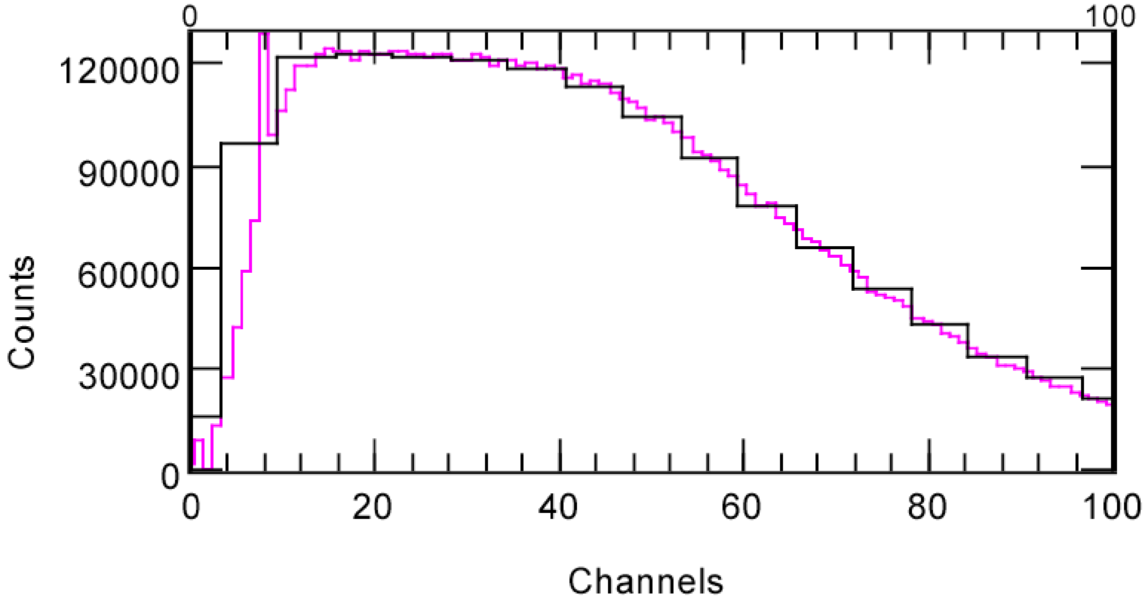

Figure 3.17. **Comparison of ^{57}Co spectra at low (black) and high (magenta) channel resolution. 6 PMTs with discriminator at 30 mV**

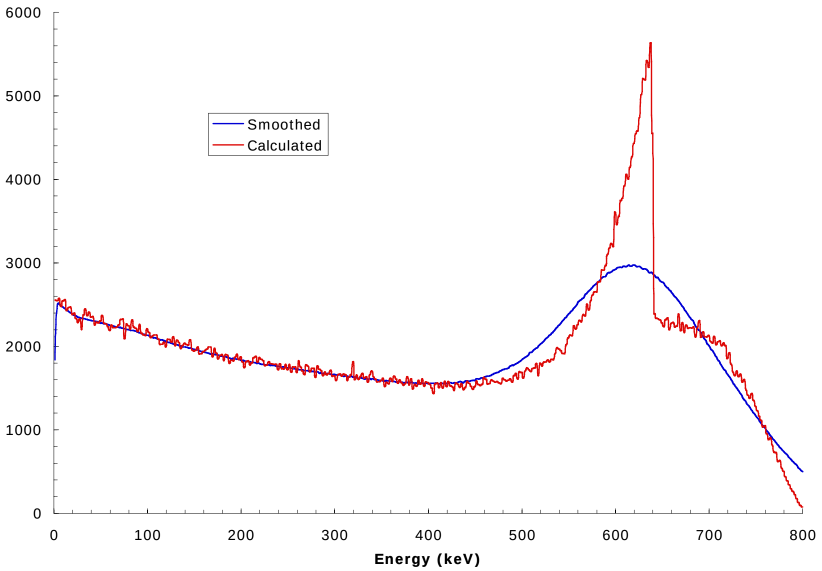

Figure 3.18. Comparison of calculated (red) and smoothed (blue) ^{54}Mn pulse height spectra. The abscissa is intensity in arbitrary units.

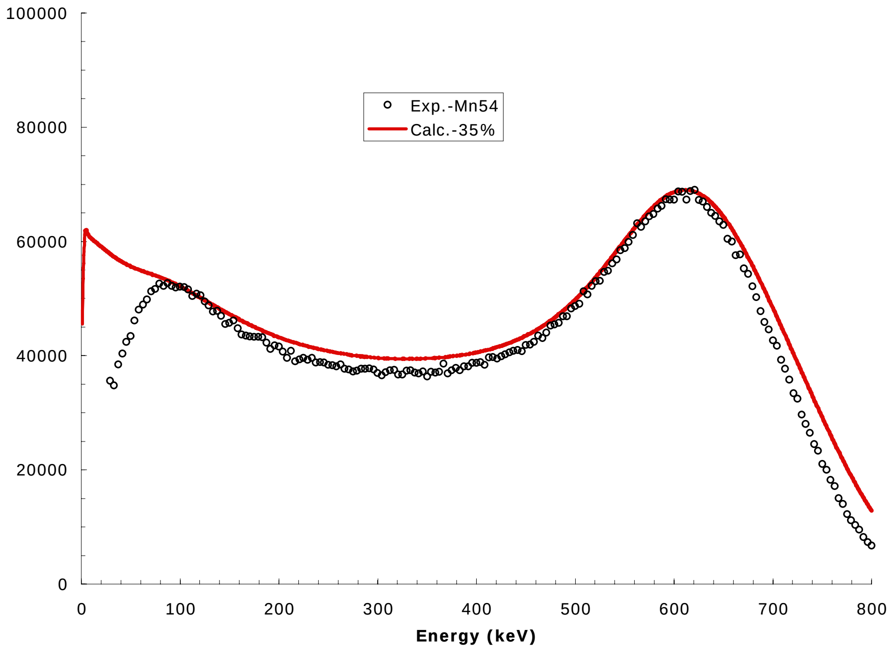

Figure 3.19. Comparison of calculated and smoothed ^{54}Mn pulse height spectra (red) with experimental data (circles). The abscissa is intensity in arbitrary units.

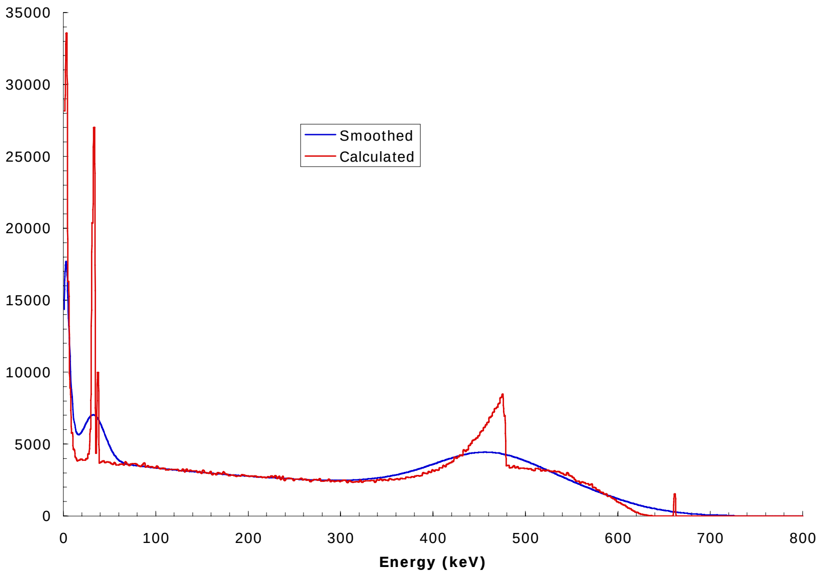

Figure 3.20. Comparison of calculated (red) and smoothed (blue) ^{137}Cs pulse height spectra. The abscissa is intensity in arbitrary units.

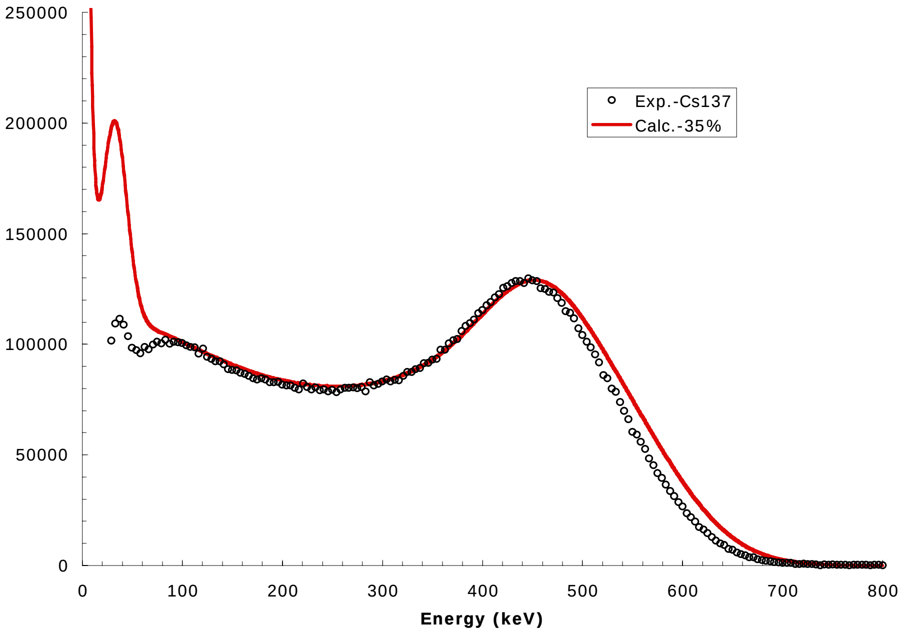

Figure 3.21. Comparison of calculated and smoothed ^{137}Cs pulse height spectra (red) with experimental data (circles). The abscissa is intensity in arbitrary units.

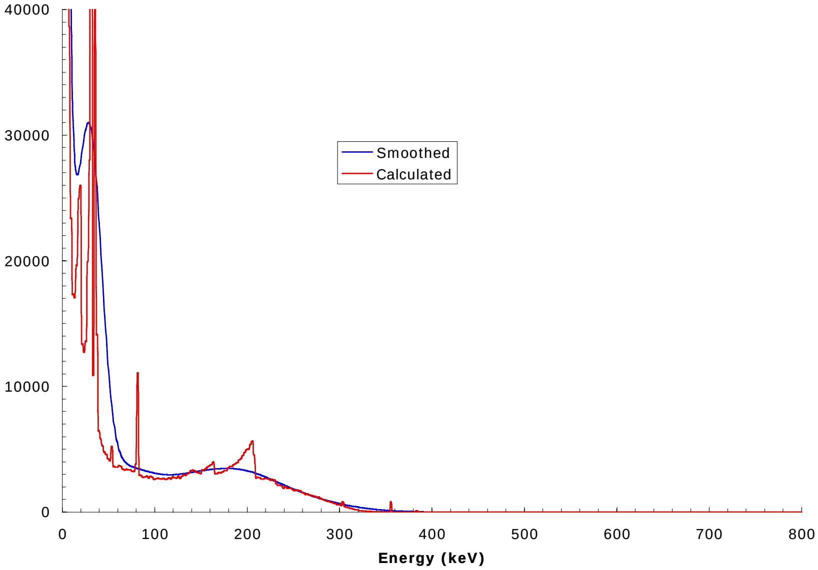

Figure 3.22. Comparison of calculated (red) and smoothed (blue) ^{133}Ba pulse height spectra. The abscissa is intensity in arbitrary units.

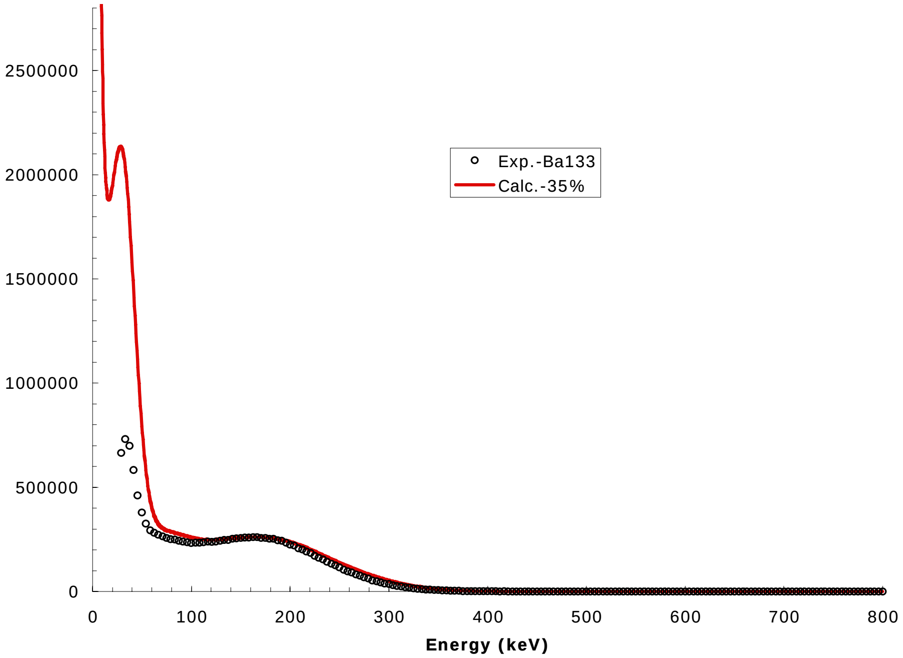

Figure 3.23. Comparison of calculated and smoothed ^{133}Ba pulse height spectra (red) with experimental data (circles). The abscissa is intensity in arbitrary units.

4.0 ALPS II Dual-sheet Plastic Scintillator Experiments

4.1 Introduction

A major interference in detection of low-energy gammas from sources of interest comes from Compton scattering in the plastic scintillator of higher-energy gammas coming from natural sources in the environment such as ^{40}K. It is possible to reduce the background from such scattering by operating the portal monitor (Front detector) in anti-coincidence with a second detector (Back detector) sensitive only to high-energy gammas. This section describes the ALPS II sensor configured with a standard plastic scintillator used as the Back (anti-coincidence) detector. Measurements were performed with and without a thin lead sheet separating the Front and the Back scintillators. Similar experiments without the lead shield but using a Cherenkov detector as the anti-coincidence detector are described in section 5 of this report.

The potential background reduction in all these experiments is based on the following assumptions. A Compton scattering event due to a low-energy gamma of interest gives a pulse in the Front detector due to the Compton scattered electron. The Compton scattered gamma gives no pulse in the anti-coincidence detector, because it either has too little energy to traverse the lead sheet, or it deposits too little energy in the back detector to trigger it. Such an event would be recorded as a valid count. Events due to a high-energy gamma Compton scattered in the Front detector give a pulse in both the Front and Back detectors, because the scattered gamma has enough energy to cause a second Compton scatter in the Back detector. Such events would be rejected. In particular, a high-energy gamma that undergoes a small-angle Compton scattering in the Front detector produces a small pulse height signal in the Front detector that interferes with detection of the small pulse height events of interest. However, the higher energy of the scattered gamma increases the probability that this event causes a pulse in the Back detector and can be rejected. This approach reduces the background for low-energy gammas by reducing the interference from high-energy gammas whether they come from natural sources in the vicinity of the portal monitor or from material passing the portal monitor.

The purpose of the work described in this section was to compare the background rejection capability of the anti-coincidence detector with and without the lead sheet, and to determine whether the anti-coincidence technique affected the efficiency for detecting the low-energy gammas of interest.

4.2 Experiment

4.2.1 Apparatus

Experiments were performed using the existing ALPS II portal monitor system. The ALPS II system had two slabs of Bicron/Saint Gobain BC-408 scintillators of dimensions 127 × 57.15 × 5.08 cm^3 separated by a gap of 13 cm. Initially, a sheet of 0.32-cm thick lead was positioned between the two scintillators. Each scintillator slab had 3 Hamamatsu R1250 127-mm (5-in.) diameter photomultiplier tubes (PMTs) mounted on each end for a total of 12 PMTs.(a) The scintillators were mounted vertically and shielded on

---

(a) Hamamatsu catalog number H6527 for PMT with integral tube base.

the bottom, sides, and back by 5.08-cm of lead. The entire assembly was mounted in a light-tight steel box. A light-tight plastic door allowed entry of gammas to the scintillator detectors.

The response of these detectors was determined for gamma radiation sources of ^{57}Co (122 keV), ^{133}Ba (356 keV), ^{137}Cs (662 keV), and ^{54}Mn (835 keV). The sources were mounted on the outside of the plastic door at the vertical and horizontal midpoint of the scintillators. The distance of the sources to the front face of the Front scintillator was about 10 cm. Count rates varied depending on the source and the trigger conditions for the data acquisition system, but never exceeded 85,000 cps.

4.2.2 Data Acquisition System and Sensor Trigger Modes

The data acquisition system was composed of CAMAC and NIM data processing modules and a PC running Kmax Version 7.3 software.(a) A schematic of the data acquisition system is shown in Figure 4.1 (figures and tables referenced in this section are collected following section 4.4). Signals from the 12 PMTs were sent to linear fanouts (Phillips PS748). One of the signals from each fanout was delayed using Ortec DB463 modules. The delayed signals were then sent to a 16-channel CAMAC-based Charge-to-Digital (QDC) converter (Phillips PS7166) where the pulse was converted to a channel number corresponding to the integrated charge during a fixed time window. The channel numbers for all 12 PMTs were stored in a list processor (Hytec LP1342) for each event. When the buffer memory of the list processor was filled, the contents of the buffer were transferred to the computer. The list processor then continued to accept new data while the computer software processed the previous data into various histograms representing the pulse height spectra for all events.

The data acquisition system created separate histograms for each of the 12 PMTs. These histograms were useful for adjusting the high voltages on each PMT to gain match the outputs. All the PMTs for the Front detector (PMTs 1-6) were gain matched to PMT 5 and all the PMTs for the Back detector (PMTs 7-12) were gain matched to PMT 11. Gain matching was done for background pulse height spectra on the assumption that background events were uniformly distributed throughout the entire scintillator slab. Previous work had shown that the pulse height spectrum of a particular PMT depended on where the radiation event occurred within the scintillator. Figure 4.2 shows a comparison of background spectra in PMT 2 and PMT 5 after gain matching. Other PMTs gave equally good matches.

In addition to recording the raw pulse heights for each PMT, the data acquisition system could create calculated parameters for each event. Thus the pulse heights of all six PMTs for the Front detector could be summed to give the total pulse height in that detector on an event-by-event basis. Likewise the pulse heights of the six PMTs for the Back detector could be summed to give the total pulse height for the Back detector. Other parameters such as the total sum of the Front and Back detectors could be calculated as desired.

The width of the fixed time window for gating the QDC was 150 ns. Various requirements determined the conditions under which the QDC gate was created. Some experiments could be performed with the QDC gate created only when valid events were detected in the Front detector, regardless of whether an event was detected in the Back detector. In other experiments, spectra could be obtained only when valid events were detected in the Back detector regardless of whether an event was detected in the Front

---

(a) Available from Sparrow Corporation, 1901 Poppy Lane, Port Orange, FL 32128.

detector. In either case, pulse height spectra for the Front and Back detectors could be obtained simultaneously.

Other experiments triggered the QDC gate only when there was a valid event in the Front detector and no valid event in the back detector. These conditions implemented a hardware anti-coincidence such that the data acquisition system processed only events in the Front detector without a simultaneous event in the Back detector. Only pulse height spectra for the Front detector could be obtained under these conditions because, by definition, there were no pulses in the Back detector.

The most general conditions allowed the QDC gate to be created whenever there were valid events in either the Front or Back detectors ("OR"). In this case, pulse height spectra could be obtained separately for the Front and Back detectors. By setting software windows on the spectra for the Front or Back detectors, the data acquisition system could create pulse height spectra for the following conditions.

1. Pulse height spectrum in Front detector for all events (coincidence and anti-coincidence).
2. Pulse height spectrum in Front detector when there was no event in the Back detector (anti-coincidence).
3. Pulse height spectrum in Front detector when there was a valid event in the Back detector (coincidence).
4. Pulse height spectrum in Back detector for all events (coincidence and anti-coincidence).
5. Pulse height spectrum in Back detector when there was no event in the Front detector (anti-coincidence).
6. Pulse height spectrum in Back detector when there was a valid event in the Front detector (coincidence).
7. Pulse height spectrum for sum of Front and Back pulse heights when there were valid events in both spectra.

The combined pulse height spectrum for the Front and Back detectors are valid only when the Front and Back detectors are the same type of scintillator and the gains have been adjusted properly.

In Figure 4.1, the QDC gate is triggered by the hardware anti-coincidence set-up. Each of the PMT signals go to discriminators that accept pulses above a specified threshold. The 6 PMTs on the Front scintillator go to an 8-channel discriminator module (Phillips PS705). This module has an output signal that is proportional to the number of channels that have been triggered simultaneously (Sum Output). The 6 PMTs on the Back scintillator were sent to an identical discriminator module. In both cases, the Sum outputs were sent to a discriminator where the threshold was set to accept events where 2 or more PMTs on each scintillator had valid signals. The discriminator outputs were stretched to a width of 1.7 μs and fed back to the discriminators to inhibit acceptance of any other events until the current event had been fully processed. The discriminator output of the Front detector was delayed by 20 ns and shortened to a 10-ns wide pulse. The discriminator pulse from the Back detector was not delayed but was converted to the complement signal and stretched to 80 ns. These two discriminator pulses were sent to an overlap coincidence unit creating the following logic.

> For an event with a valid pulse in the Front detector but no pulse in the Back detector, the complement of the Back discriminator remained at a –5 V level, the discriminator output of the Front detector switched from ground to –5 V for 10 ns, and a valid output was generated by the coincidence unit.

> If valid events were detected in both Front and Back detectors, the complement of the Back discriminator output switched from –5 V to ground for 80 ns, the discriminator output of the Front detector switched from ground to –5 V for 10 ns, but no output was generated by the coincidence unit because both coincidence inputs were not at –5 V simultaneously. The 20 ns delay on the Front detector discriminator was introduced to prevent timing jitter from causing accidental coincidence outputs.

To switch from this hardware anti-coincidence configuration to the more general "OR" trigger configuration, the output on the Sum discriminator was switched from the complement to the normal signal, the inputs to the coincidence unit were switched from the coincidence mode to the "OR" mode, and 10 ns delay was added to the Sum output of the Back detector discriminator to compensate for internal delays in the logic modules. One further change was to switch the output of the coincidence unit to trigger on the rising edge of the logic pulse rather than the falling edge.

To convert the QDC gate trigger to operate only on events from the Front detector, the general "OR" mode set-up was modified by removing the Back detector input from the coincidence module and requiring only a single input from the Front detector to trigger the QDC gate. Similarly, to obtain triggers based only on the Back detector, only the Back input to the coincidence module was enabled.

In all experiments, a separate 60-cycle pulser signal was included in the data stream by way of channel 16 of the QDC. The trigger for the pulser QDC gate was mixed with the trigger for valid signals by way of a second coincidence unit operating in the "OR" mode. The output of this "OR" coincidence unit was stretched to 150 ns and was sent to the gate input of the QDC. This pulser signal was subject to the same dead times as the PMT signals. It was stored in a separate histogram. The integrated counts in the pulser histogram was compared to the number of events expected for the pulser for the elapsed data acquisition time. The ratio of the observed counts to the expected counts is the livetime for that particular experiment. Livetimes for background experiments were different from livetimes for runs with sources so a livetime correction was applied to all data.

4.2.3 Data Collection

All experiments recorded pulse height spectra for 300 second collection times. Sources were mounted at the horizontal and vertical midpoints of the detectors on the outside of the plastic door as mentioned above. Background measurements were performed for all configurations. The discriminators on the individual PMTs were usually set at 50 mV on both Front and Back PMTs. However, some data were obtained with discriminator levels of 30 mV and 10 mV. In addition, some data were obtained with different discriminators on the Front and Back detectors. All experiments were based on valid signals being defined as two or more valid PMT signals in the Front and/or Back detectors.

Separate scalers were used to record the count rates in the Front and Back detectors and for the combined Front and Back counts. These scaler count rates were free of the livetime corrections inherent in the pulse height measurements and gave an independent measure of the actual detection rates.

As shown in the tables and figures collected below (immediately following section 4.4), data were obtained for various sources, trigger configurations, discriminator levels, and with or without the intermediate lead shield. In some cases, data were obtained in list mode as well as in the normal on-line histogramming mode. Experiments taken in list mode were usually repeated without the list mode feature mainly because livetimes were significantly smaller when in the list mode. Comparison of data taken with and without the list mode function provided a means to confirm the validity of the livetime measurement.

4.3 Results

This work was intended to answer three primary questions. The first question was whether the addition of an anti-coincidence detector made a significant reduction in the background count rates, particularly in the region of the low-energy gamma sources (^{57}Co, ^{133}Ba). The second question was whether the efficiency for detecting the low-energy gamma sources (^{57}Co, ^{133}Ba) was affected by the addition of the anti-coincidence detector. The third question was whether the anti-coincidence gating reduced the background in the low-energy region caused by high-energy gammas from a source.

To answer these questions, the pulse height spectra were integrated to obtain the total count rates over two energy regions in the spectra for the Front detector. The first energy region was from channels 0 to 60 which included all of the events from the ^{57}Co source and most of the events from the ^{133}Ba source. The second energy region was from channels 0-255 which included all events. These count rates are given in Table 4.1 for the two energy regions and for the different sources and trigger conditions when the intermediate shield was in place. Similar data are presented in Table 4.2 for experiments done without the intermediate shield. All the integrated counts have been corrected for the data acquisition live time and the decay of the sources during the time over which the experiments were conducted. The spectra were each obtained over a 300-second counting interval. All discriminators for the PMTs in the Front and Back detectors were set at 50 mV for the data shown in Table 4.1 and Table 4.2. Note that the data acquisition trigger was generated if two or more PMTs on a given detector had a pulse greater than the discriminator level.

Table 4.1 and Table 4.2 also give the ratio of counts at each trigger condition to the counts obtained as if there were only a single detector (trigger mode = Front Only). The Front Only trigger mode simulates the typical portal monitor with only a single slab of scintillator. This trigger mode was only implemented for the Cherenkov anti-coincidence experiments described in section 5 of this report. In principle, the Front Only trigger mode should give identical count rates for sources regardless of the type of detector used for the anti-coincidence experiments. In actuality, the scaler data obtained along with the spectral data for every trigger mode indicated that there were source dependent changes in efficiency between the time the present experiments were performed and the time the Cherenkov experiments were performed. In order to relate all the experiments to a single slab detector, it was necessary to correct the present data by correction factors based on the ratio of scaler counts in the present experiments to scaler counts in the Cherenkov experiments. These correction factors are given in Table 4.1 and Table 4.2 for each of the sources.

4.3.1 Background Efficiencies

We first look at the data for the background as these data are relevant to answering the first question. The “Front Only” trigger condition ignored the existence of the Back detector and acquired data only when a valid pulse was observed in the Front detector. The count rates under this trigger condition are the baseline for comparing all other trigger conditions. The “OR” trigger condition accepted data whenever there were valid pulses in either the Front scintillator or the Back scintillator. The spectra in the Front scintillator then included roughly 10% more events due to triggers in the back detector that were accompanied by very small pulses in the Front detector that were below the trigger for the Front detector. The data are shown in Table 4.1 for experiments in which the intermediate shield was present.

In order to use the Back detector as an anti-coincidence gate, a software gate was imposed on the spectra in the Front detector such that a new pulse height histogram was generated only when events in the Back detector were at very low pulse heights (channels 0-3). If the Back detector had a pulse greater than channel 3, that event was not included in the gated histogram for the Front detector. This trigger condition is called "OR with Anti" in Table 4.1. Note that this anti-coincidence gate reduced the count rate from the normal "OR" trigger by about 20% thus bringing the effective background rate down to about 90% of the value with only the single detector (Front Only). As shown in Figure 4.3, the reduced counts for the "OR with Anti" trigger mode relative to the "OR" trigger mode are all located in channels 0 and 1 in the low-energy background spectrum.

To verify whether the software anti-coincidence was functioning properly, experiments were done using a hardware gate so that data were obtained only when no valid pulse was observed in the Back detector. This slightly reduced the data acquisition rate and thus slightly raised the observed livetime which is of some benefit. However, the hardware and software anti-coincidence trigger modes gave essentially similar results.

The fractional changes in the background rates are roughly the same for the various trigger conditions regardless of whether the low-energy pulse height region or the entire pulse height region is used.

When the intermediate lead and plastic shield was removed, the low energy pulse height region had an increase of about 27% for the "OR" trigger mode as shown in Table 4.2. The background count rate in this region then dropped to about 85% of the Front Only rate when the anti-coincidence trigger modes were used. As shown in Figure 4.4, the reduced counts for the "OR with Anti" trigger relative to the "OR" trigger are primarily at channels 0 and 1, but there are reduced counts at somewhat higher channels as well.

The changes in the background count rates in the Front detector after the intermediate shield was removed are directly related to the changes in the pulse height spectra of the back detector. Figure 4.5 shows the background spectra in the low-energy region for the Back detector with and without the intermediate shield. The intermediate shield clearly reduced the number of low-energy pulses seen by the Back detector. Without the shield the number of "OR" triggers goes up due to the extra pulses in the back detector. Likewise the number of "OR with Anti" triggers goes down because the Back detector now has more valid anti-coincidence pulses.

The answer to question one depends on the type of anti-coincidence system used. The background count rates in the Cherenkov experiments (see section 5) did not change significantly for the anti-coincidence trigger modes relative to the single slab (Front Only) trigger mode. In contrast, the results for the background count rates with this scintillator anti-coincidence system showed about a 12% reduction relative to the single slab system when the intermediate shield was used. Without the intermediate shield, the reduction in background rate was about 15%.

4.3.2 Low-Energy Source Efficiencies

The data in Table 4.1 and Table 4.2 show that the background-subtracted count rates for the low-energy sources ^{57}Co and ^{133}Ba increase by 4% or less by the addition of the Back scintillator with the "OR" trigger mode. The pulse height spectra comparing the "OR" and "OR with Anti" trigger modes are shown in Figure 4.6 for the ^{57}Co source and in Figure 4.8 for the ^{133}Ba source for data obtained with the intermediate shield in place. The corresponding spectra for data taken without the intermediate shield are shown in Figure 4.7 and Figure 4.9. The software or hardware anti-coincidence gating mode did not change the count rate for the ^{57}Co source when the intermediate shield was in place. However, without the shield, the anti-coincidence mode lowered the ^{57}Co count rate to about 85% of the Front Only count rate. The ^{133}Ba source showed a decrease of about 5% in count rate relative to the Front Only mode when the software or hardware anti-coincidence requirement was imposed with the intermediate shield in place. Without the intermediate shield, the ^{133}Ba count rate decreased by 20% or 25% relative to the Front Only count rates.

With regard to question two, these results indicate that the efficiency for detecting low-energy gammas is dependent on whether or not an intermediate shield is used between the Front and Back detectors. This is in contrast to the Cherenkov experiments where little change in the ^{57}Co or ^{133}Ba count rates was observed when using the anti-coincidence mode.

4.3.3 High-Energy Source Efficiencies

The count rates for the higher-energy sources (^{137}Cs and ^{54}Mn) are significantly affected by the presence of the Back detector. Figure 4.10 and Figure 4.12 give the pulse height spectra for ^{137}Cs and ^{54}Mn, respectively, for the "OR" and "OR with Anti" trigger modes for data obtained with the intermediate shield in place. The corresponding spectra for data taken without the intermediate shield are shown in Figure 4.11 and Figure 4.13. Examination of the data with the intermediate shield for the low-energy region of the ^{137}Cs source shows that the "OR" trigger raised the count rate by about 28% whereas adding the software anti-coincidence or hardware anti-coincidence lowered the count rate to 80% of the Front Only rate. Without the intermediate shield, the low-energy region for the ^{137}Cs source had a 30% higher count rate, whereas the rate with the anti-coincidence requirement was about 70% of the Front Only count rate.

These effects are even stronger for the ^{54}Mn source. In the low-energy region and with the intermediate shield, the increase in count rate was 42% for the "OR" trigger. The "Or with Anti" mode gave75% of the original count rate and the "Hardware Anti" mode gave 70% of the original rate. Without the intermediate shield, the corresponding numbers are a 40% increase for the "OR" mode and a 40% decrease for the anti-coincidence trigger modes relative to the Front Only trigger mode.

Thus the answer to the third question is that background in the low-energy region due to high-energy gammas from a source can be significantly reduced by use of anti-coincidence techniques. However, this background reduction comes at a cost of a 15% loss in efficiency for detecting ^{57}Co unless an intermediate shield is used between the Front scintillator and the anti-coincidence scintillator. The use of an intermediate shield maintains the efficiency for detecting ^{57}Co, but the reduction in background due to high-energy sources is only about 25% instead of 40%.

4.3.4 Calibration of Energy Axis

To convert the pulse height channel number to an energy scale requires measurement of channel numbers for peaks from several sources. The peaks observed in the plastic scintillators used here are not due to the full energy of the incident gamma as is typical of NaI(Tl) or Ge detectors. For plastic scintillators, the peak is caused by the Compton edge from 180 degree scattering of the incident gamma. A further complication is the fact that resolution broadening shifts the peak to slightly lower energy than expected from the Compton scattering equation. Computer modeling using the code Geant4 has been performed to determine the distribution of energies deposited by electrons from Compton scattering events in plastic scintillators having the dimensions used in this work. The resulting energy spectrum was then broadened with a Gaussian resolution function. The width of the Gaussian resolution was varied until a reasonable agreement with the experimental peak was obtained.

In Figure 4.14 and Figure 4.15, the calculated energy deposition spectrum for ^{54}Mn is shown along with resolution broadened spectra for 3 different resolution functions. The value of the Gaussian resolution function at 200 keV was arbitrarily chosen as the identifier for a particular resolution function. In every case the resolution function was assumed to vary as 1/SQRT(E). Figure 4.14 shows the experimental spectrum when the trigger mode was the “OR” configuration. The best agreement between the experimental data and the calculated data is with the 25% resolution function. Figure 4.15 compares the experimental spectrum obtained with the software anti-coincidence trigger mode (‘”OR” with Anti’) with the calculated spectra. It appears that the anti-coincidence trigger results in slightly better resolution than the “OR” trigger mode. Note that the experimental spectra in both figures use a preliminary energy calibration based on an assumed linear energy dependence from the origin to the location of the ^{54}Mn peak.

The calculated spectra with resolution broadening allows a determination of the energy shift due to resolution broadening. The energy shift is not very sensitive to the energy of the incident gamma (at least for sources with energy above 300 keV where distinct peaks can be observed). The resolution broadened peaks shown in Figure 4.14 and Figure 4.15 are about 20 keV lower energy than the peak seen in the calculated energy deposition spectrum. An initial energy calibration curve based on the calculated Compton peak energies without resolution broadening is shown in Figure 4.16 along with a corrected calibration curve assuming that the resolution broadened peak energies are all 20 keV lower than the calculated energies.

The calibration curve resulting from the corrected data shows a channel 0 intercept of 30 keV. The ^{57}Co pulse height spectrum shown in Figure 4.6 has a cut off at channel 4 which would be 44 keV assuming the calibration is linear to low energies. The calculated Compton edge for ^{57}Co is 40.4 keV so that an energy shift due to resolution broadening would put the Compton edge significantly below the observed cut off. Alternatively, one can ask whether the ^{57}Co gamma energy is low enough that secondary gamma scatters could add to the deposited energy up to the full photopeak energy of 122 keV. In this regard, we note that the calculated energy deposition spectrum for ^{133}Ba shows a sharp peak at 80 keV corresponding to full energy deposition of the 80 keV gamma in decay of ^{133}Ba.

The calibration technique described above is difficult to apply to the low energy portion of the pulse height spectrum (<200 keV). The experimental spectrum of ^{57}Co does not show a peak due to the Compton edge of the 122-keV gamma. Although the energy deposition spectrum does show peak structure, the application of resolution broadening washes out the peak structure as shown in Figure 4.17.

In addition, the resolution broadened spectrum cannot be fit to the experimental spectrum without adjusting the energy scale. The experimental energy spectrum shown in Figure 4.17 assumes a lower energy intercept (1 keV instead of 29.7 keV) and a larger slope (5.2 keV/channel instead of 3.695 kev/chanel) than the calibration curve shown in Figure 4.16. Also note that the ^{137}Cs spectra in Figure 4.10 and Figure 4.11 show a strong enhancement at channel 5 indicating observation of the 30-keV X-ray expected in the ^{137}Cs decay scheme. Such an enhancement is not seen or expected in the ^{54}Mn spectra in Figure 4.12 and Figure 4.13.

4.3.5 Effect of Discriminator

To resolve the uncertainty in the low-energy calibration, spectra were measured at a discriminator setting of 30 mV as well as at the 50 mV setting shown in Figure 4.6 through Figure 4.13. A comparison of the ^{57}Co pulse height spectra at the two discriminator settings is shown in Figure 4.18 for the trigger mode "OR with Anti". The discriminator level at 50 mV reduces the total counts between channels 0 – 60 by 0.4% relative to the total counts at 30 mV. It thus appears that a 50 mV discriminator does not cut off a large fraction of the ^{57}Co events indicating that most of the events due to the 122 keV gamma have been observed. It is therefore likely that the energy calibration below 200 keV is not linear as suggested in Figure 4.16.

4.3.6 Effect of Livetime Differences

Given the high count rates (<85,000 cps) for 10μCi sources at about 10 cm from the scintillator and the block time of 1.7 μsec for each pulse, the measured livetimes were a significant correction to the observed spectra. The presence or absence of list mode data acquisition also affected the livetime. For the hottest sources (^{133}Ba and ^{137}Cs), the reduction in livetime was about a factor of 2. These factors allowed a comparison of spectra obtained under identical conditions except for a difference in livetime. The agreement or disagreement for two spectra measured with different livetimes enabled us to estimate the validity of the livetime correction. There was no strong correlation between the ratio of the livetime correction factors and the ratio of the livetime-corrected counts. We concluded that the livetime correction was internally consistent for data taken in these experiments.

4.3.7 Spectra for Sum of Front and Back Detectors

Because the Front and Back detectors consisted of identical scintillator material for these experiments, it is possible to obtain improved energy resolution of the peak structure by adding the pulse heights in the Front and Back detectors for coincident events. Scattering in the Front detector produces a Compton electron which deposits its energy in the Front detector and a scattered gamma that may then interact in the Back detector by a second Compton scattering event. The energy of the scattered electron is detected in the Back scintillator and the scattered gamma may or may not escape the detector system. By combining the energies in both detectors, a larger fraction of the initial gamma energy is recorded. The probability of observing coincident scattering events is enhanced by removal of the intermediate shield between the Front and Back detectors.

The data acquisition system in the "Front Only" and "OR" trigger modes allows measurement of the pulse heights in both detectors while still providing for a software anti-coincidence mode. Thus it is possible to obtain higher resolution pulse height spectra while still collecting data in the lower background anti-coincidence mode. Note that the higher resolution mode and the lower background mode are still mutually exclusive; i.e. the higher resolution data will not have the low background. Also note that the "Hardware Anti" trigger mode does not allow for measurement of spectra in the Back detector.

In order that a valid summation of the Front and Back pulse heights be done, it is necessary to first adjust the photomultiplier gains so that equal amplitude pulses are obtained for equal energy deposition in the two detectors. On the assumption that cosmic ray background will provide a uniform distribution of energy deposition events in both detectors, the photomultiplier gains were adjusted to produce comparable pulse height distributions in both detectors when no sources were present. Background spectra for the Front and Back detectors are shown in Figure 4.19 for the "OR" trigger mode, no intermediate shield, and all discriminators at 50 mV. Because the lead shield surrounds the detector assembly only on three sides and the bottom, the Front detector acts as a shield for the Back detector to reduce the number of gammas from natural background radiation that enter from the front of the detector assembly. Thus the background spectrum in the Back detector is lower than the spectrum in the Front detector. The spectrum in the Front detector also has an enhancement of low energy events as would be expected when it absorbs low energy gammas from the environment.

The background corrected spectra for the ^{57}Co source are shown in Figure 4.20 for the Front detector, the Back detector, and the Sum of the Front and Back pulse heights. Note that the addition of the Back pulse height moves the spectrum in the Front detector away from the origin and results in a distinct peak.

The background corrected spectra for the ^{133}Ba source are shown in Figure 4.21 for the Front detector, the Back detector, and the Sum of the Front and Back pulse heights. Note that the addition of the Back pulse height sharpens the peak around channel 46.

Similar data are shown in Figure 4.22 for the ^{137}Cs source. In this case the Sum spectrum clearly shows a peak at channel 6 that is in all likelihood due to the 30-keV X-ray in this source.

The three spectra for ^{54}Mn are shown in Figure 4.23. Note the improved peak-to-valley ratio for the peak at channel 162.

The ALPS II detector system could thus be used in both a portal monitoring mode or an energy analysis mode if desired.

4.4 Conclusions

This work has answered the three questions posed above.

1. The anti-coincidence gating system as implemented in this work resulted in 10% to 15% fewer counts in the low-energy pulse height region due to background events.
2. The present data show that the efficiency for detecting low-energy gamma sources is not changed by the imposition of the anti-coincidence requirement provided an intermediate shield is used between the Front and Back detectors.
3. There is a significant reduction of the count rates in the low-energy region due to sources with high-energy gammas. However the magnitude of the reduction is dependent on whether or not an intermediate shield is used between the Front and Back detectors

The reduction factor appears to increase rapidly as the energy of the gamma increases. Thus the reduction factor for ^{40}K (1461 keV), which is a common interference when looking for low-energy sources, might be much greater than the reduction factor of about 25-40% observed here for ^{54}Mn (835 keV). Depending on whether or not an intermediate shield is used, an additional reduction of about 12-15% of the environmental background can be obtained . Further evaluation is needed to determine whether these reductions are justified relative to the extra cost and complexity of the anti-coincidence system. If desired, this detector system could be used to simultaneously obtain energy information.

Table 4.1. Count rates (cps) for various sources and trigger conditions with shield.[a,b]

Source	Trigger Mode	Sum(0-60) Corr. Ave. (cps)	Sum(0-255) Corr. Ave. (cps)	Corr.Factor (scaler)[c]	X/Front Sum (0-60)	X/Front Sum (0-255)
Bgd	Front Only	4771	6049		1.000	1.000
Bgd	OR	5257	6465		1.102	1.069
Bgd	OR with Anti	4163	5240		0.873	0.866
Bgd	Hardware Anti	4292	5386		0.900	0.891
^{57}Co	Front Only	7432	7445		1.000	1.000
^{57}Co	OR	7747	7751	0.948	1.042	1.041
^{57}Co	OR with Anti	7715	7720	0.948	1.038	1.037
^{57}Co	Hardware Anti	7612	7600	0.948	1.024	1.021
^{133}Ba	Front Only	80904	84548		1.000	1.000
^{133}Ba	OR	84421	87821	0.99	1.043	1.039
^{133}Ba	OR with Anti	77519	80897	0.99	0.958	0.957
^{133}Ba	Hardware Anti	76890	80190	0.99	0.950	0.948
^{137}Cs	Front Only	20487	40274		1.000	1.000
^{137}Cs	OR	26281	44812	1.084	1.283	1.113
^{137}Cs	OR with Anti	16343	34191	1.084	0.798	0.849
^{137}Cs	Hardware Anti	16352	34277	1.084	0.798	0.851
^{54}Mn	Front Only	2785	7087		1.000	1.000
^{54}Mn	OR	3970	7752	1.159	1.425	1.094
^{54}Mn	OR with Anti	2092	5648	1.159	0.751	0.797
^{54}Mn	Hardware Anti	1964	5474	1.159	0.705	0.772

[a] All Front Only data are from Cherenkov experiments (see section 5) without intermediate shield.

[b] All other data are present experiments with intermediate shield.

[c] Correction factor accounts for changes in source efficiency between scintillator and Cherenkov experiments based on data from scaler counts.

Table 4.2. Count rates (cps) for various sources and trigger conditions without shield.[a,b]

Source	Trigger Mode	Corr. Factor (scaler)	Sum(0-60) Corr. Ave. (cps)	Sum(0-255) Corr. Ave. (cps)	X/Front Sum (0-60)	X/Front Sum (0-255)
Bgd	Front Only	1.000	4771	6049	1.000	1.000
Bgd	OR	1.000	6052	7298	1.268	1.207
Bgd	OR with Anti	1.000	3876	4873	0.812	0.806
Bgd	Hardware Anti	1.000	4226	5322	0.886	0.880
^{57}Co	Front Only	1.000	7432	7445	1.000	1.000
^{57}Co	OR	1.072	7539	7543	1.014	1.013
^{57}Co	OR with Anti	1.072	6162	6179	0.829	0.830
^{57}Co	Hardware Anti	1.072	6606	6614	0.889	0.888
^{133}Ba	Front Only	1.000	80904	84548	1.000	1.000
^{133}Ba	OR	1.125	80861	84394	0.999	0.998
^{133}Ba	OR with Anti	1.125	59874	62839	0.740	0.743
^{133}Ba	Hardware Anti	1.125	64209	67538	0.794	0.799
^{137}Cs	Front Only	1.000	20487	40274	1.000	1.000
^{137}Cs	OR	1.150	26630	44353	1.300	1.101
^{137}Cs	OR with Anti	1.150	13533	28353	0.661	0.704
^{137}Cs	Hardware Anti	1.150	14379	30726	0.702	0.763
^{54}Mn	Front Only	1.000	2785	7087	1.000	1.000
^{54}Mn	OR	1.199	3892	7511	1.397	1.060
^{54}Mn	OR with Anti	1.199	1659	4645	0.596	0.656
^{54}Mn	Hardware Anti	1.199	1711	4941	0.614	0.697

[a] All Front Only data are from Cherenkov experiments (see section 5) without intermediate shield.

[b] All other data are present experiments without intermediate shield.

[c] Correction factor accounts for changes in source efficiency between scintillator and Cherenkov experiments based on data from scaler counts.

Table 4.3. Experiments with Plastic Scintillator Anti-Coincidence System

Run No.	Source	Trigger Mode	Front Disc. (mV)	Back Disc. (mV)	List Mode	Pb & plastic shield
9099	^{54}Mn	Hardware Anti	50	50		Yes
9100	Bgd	Hardware Anti	50	50		Yes
9101	^{137}Cs	Hardware Anti	50	50		Yes
9102	^{133}Ba	Hardware Anti	50	50		Yes
9103	^{57}Co	Hardware Anti	50	50		Yes
9104	Bgd	Hardware Anti	50	50		Yes
9105	^{54}Mn	OR	50	50		Yes
9106	^{54}Mn	OR	50	50		Yes
9107	Bgd	OR	50	50		Yes
9108	^{137}Cs	OR	50	50		Yes
9109	^{133}Ba	OR	50	50		Yes
9110	^{57}Co	OR	50	50		Yes
9111	Bgd	OR	50	50	List	Yes
9112	^{57}Co	OR	50	50	List	Yes
9113	^{57}Co	OR	30	30	List	Yes
9114	Bgd	OR	30	30	List	Yes
9115	Bgd	OR	30	30		No
9116	Bgd	OR	30	30	List	No
9117	^{57}Co	OR	30	30	List	No
9118	^{57}Co	OR	30	30		No
9120	Bgd	OR	50	50	List	No
9121	^{57}Co	OR	50	50		No
9122	^{57}Co	OR	50	50	List	No
9123	Bgd	OR	50	50		No
9124	^{137}Cs	OR	50	50		No
9125	^{133}Ba	OR	50	50		No
9126	^{54}Mn	OR	50	50		No
9127	Bgd	OR	50	50		No
9129	Bgd	Hardware Anti	50	50		No
9130	^{54}Mn	Hardware Anti	50	50		No
9131	^{137}Cs	Hardware Anti	50	50		No
9132	^{133}Ba	Hardware Anti	50	50		No
9133	^{57}Co	Hardware Anti	50	50		No
9134	Bgd	Hardware Anti	50	50		No
9139	Bgd	Hardware Anti	50	50	List	No
9140	^{57}Co	Hardware Anti	50	50	List	No
9141	^{57}Co	Hardware Anti	50	50		No
9142	Bgd	Hardware Anti	50	50		No

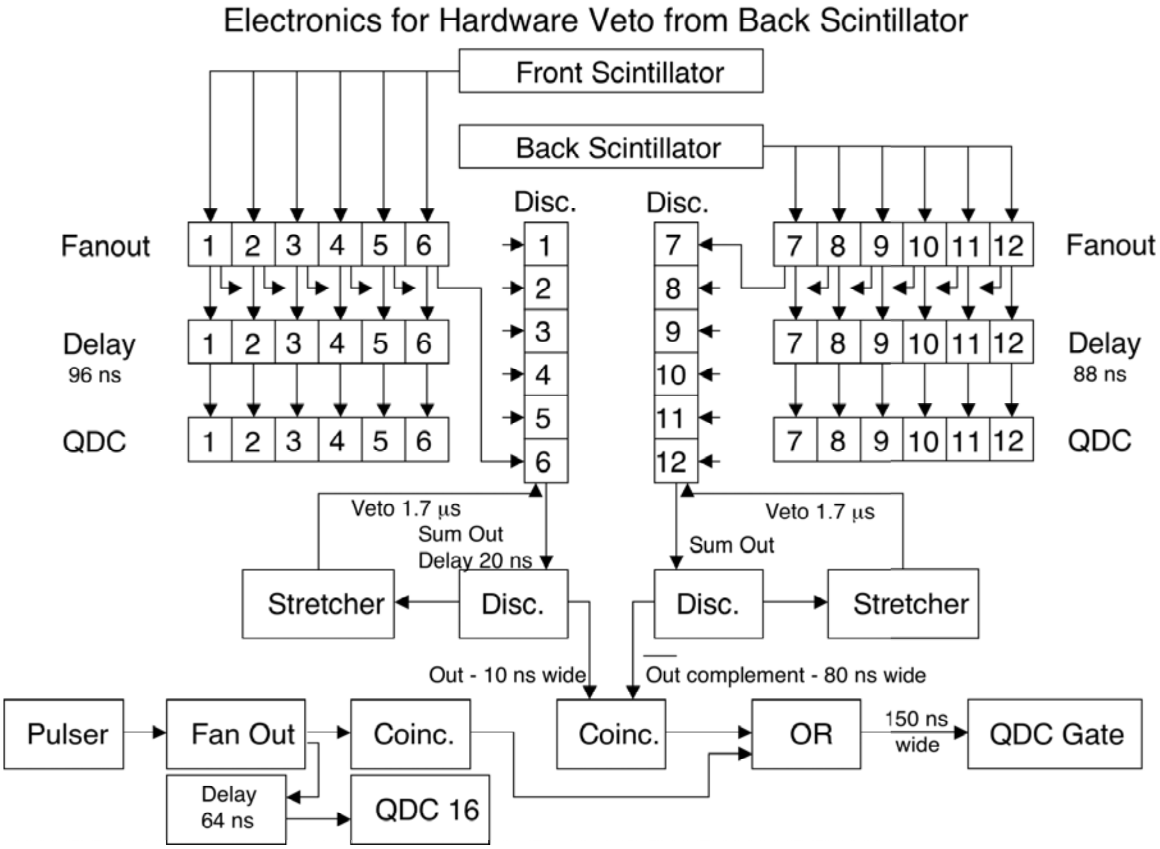

Figure 4.1. Schematic of electronic modules for data acquisition

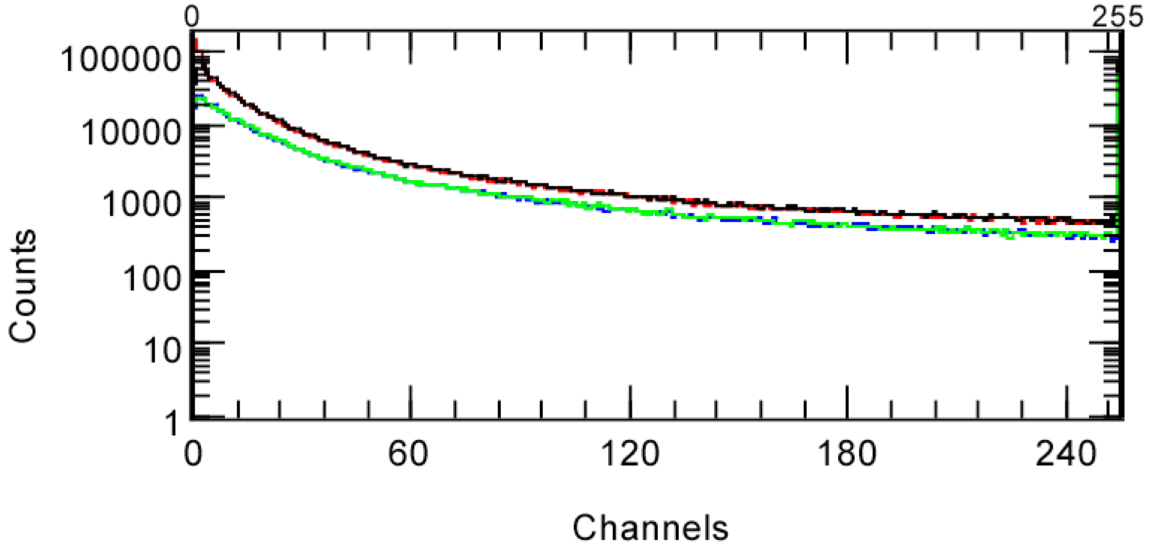

Figure 4.2. Comparison of pulse height spectra of PMT 2 (red) and PMT 5 (black) for Front detector and PMT8 (green) and PMT11 (blue) for Back detector. Background data taken with the "OR" trigger condition with all discriminator thresholds at 50 mV and with no intermediate shield.

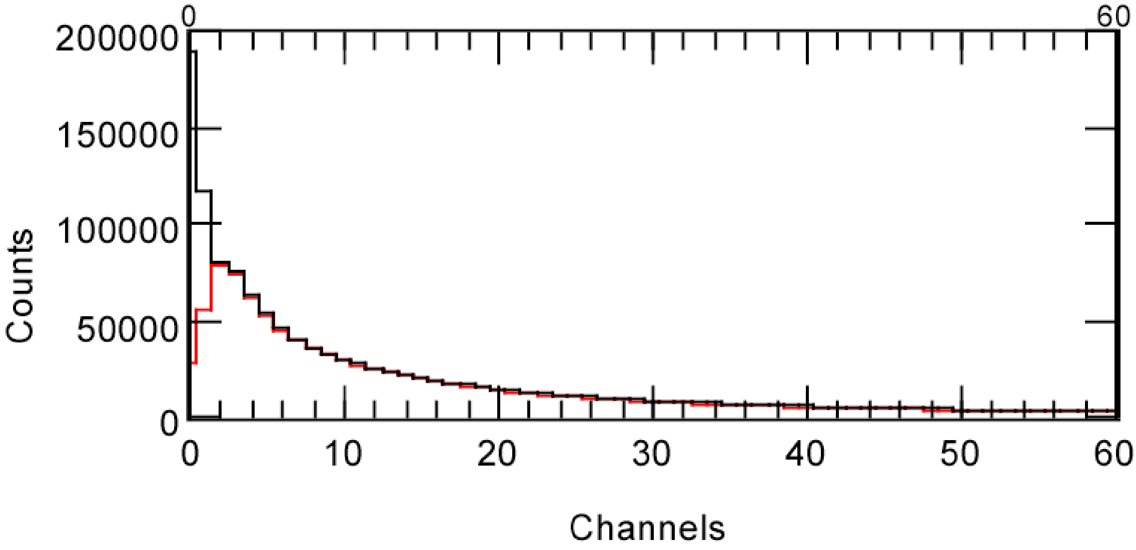

Figure 4.3. **Comparison of background pulse height spectra in Front detector with intermediate shield for low-energy region for "OR" trigger mode (black) versus "OR with Anti" trigger mode (red). All discriminator levels are 50 mV.**

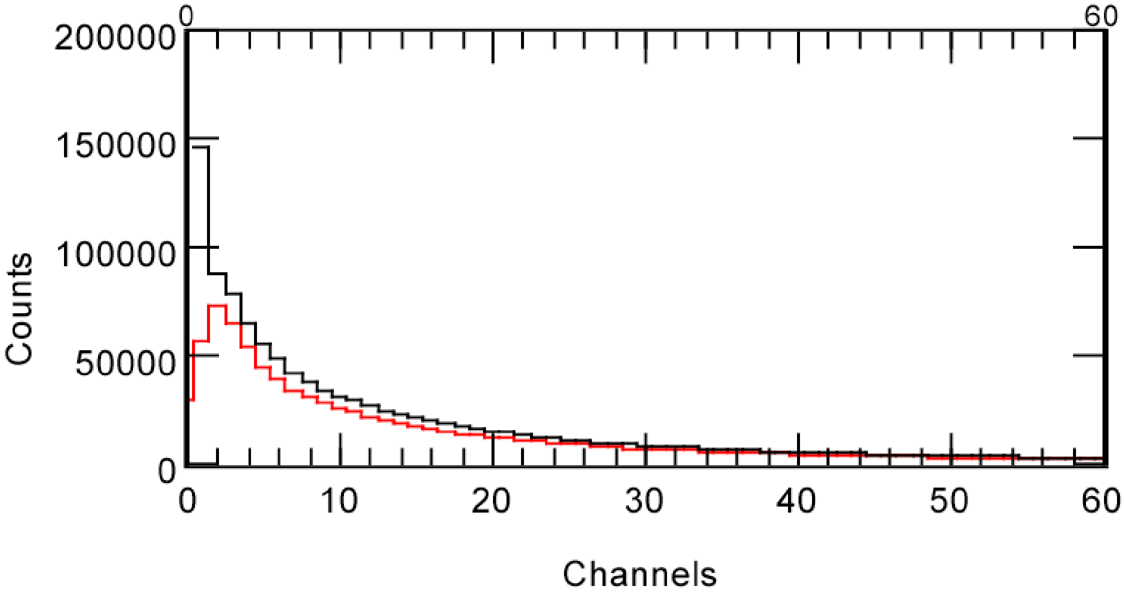

Figure 4.4. **Comparison of background pulse height spectra in Front detector without intermediate shield for low-energy region for "OR" trigger mode (black) versus "OR with Anti" trigger mode (red). All discriminator levels are 50 mV.**

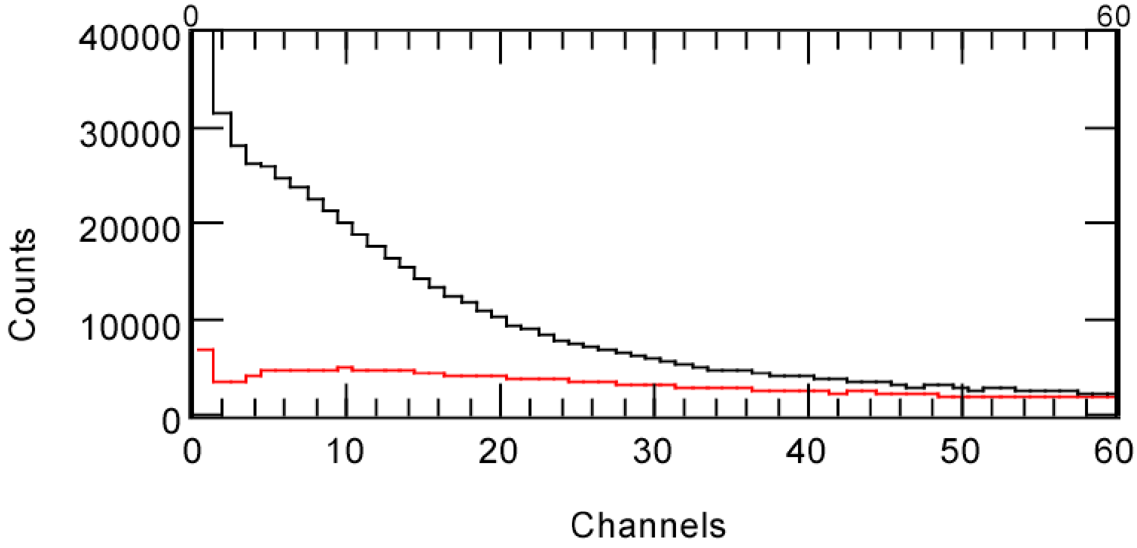

Figure 4.5. Comparison of low-energy background pulse height spectra in Back detector with (red) and without (black) intermediate shield. Data were obtained with "OR" trigger mode and all discriminators at 50 mV.

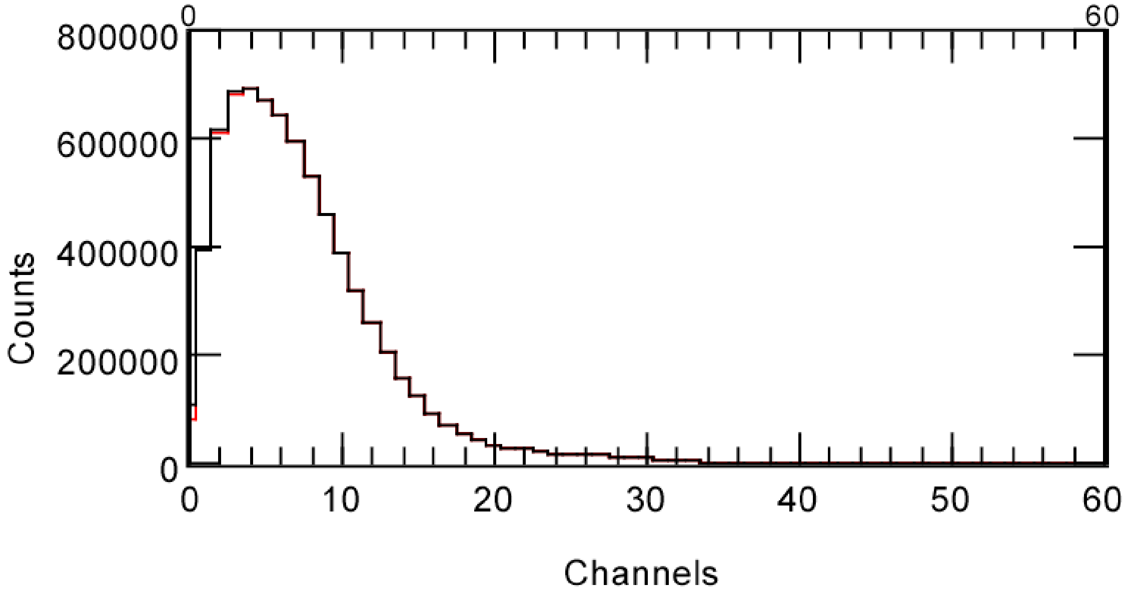

Figure 4.6. Comparison of ^{57}Co pulse height spectra in Front detector for low-energy region for "OR" trigger mode (black) versus "Or with Anti" trigger mode (red). The intermediate shield is in place. All discriminator levels are 50 mV.

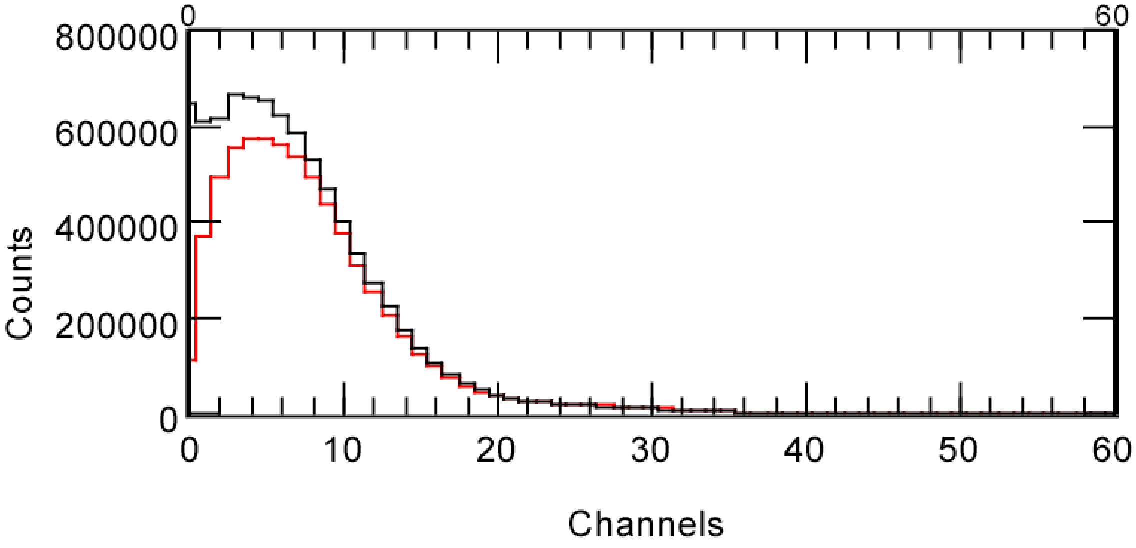

Figure 4.7. Comparison of ^{57}Co pulse height spectra in Front detector for low-energy region for "OR" trigger mode (black) versus "Or with Anti" trigger mode (red). The intermediate shield is removed. All discriminator levels are 50 mV.

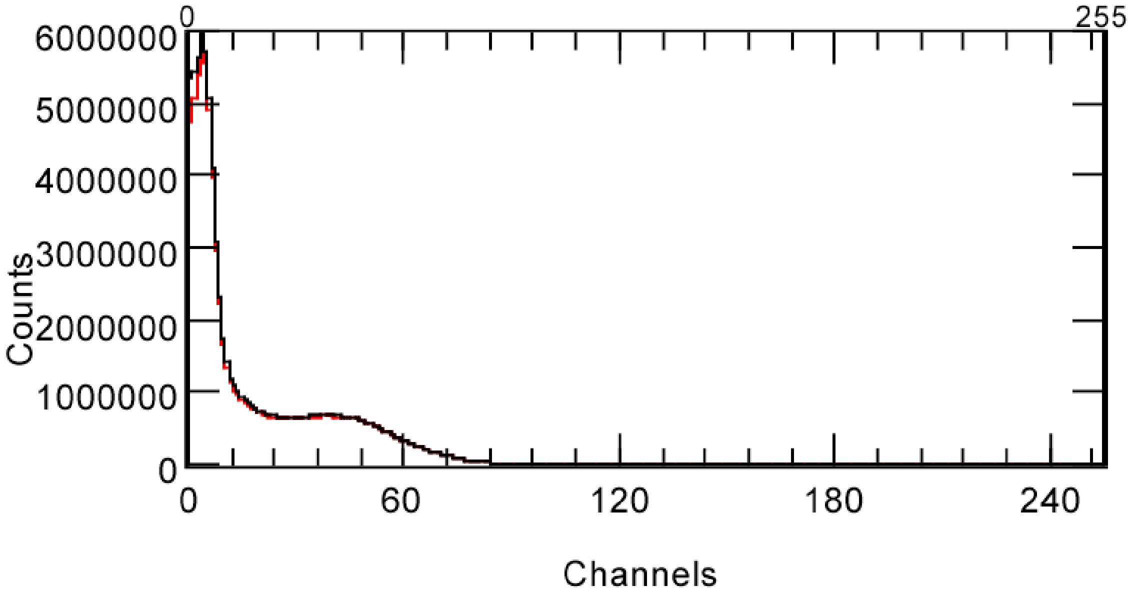

Figure 4.8. Comparison of ^{133}Ba pulse height spectra in Front detector for full-energy region for "OR" trigger mode (black) versus "OR with Anti" trigger mode (red). Intermediate shield is in place. All discriminator levels are 50 mV.

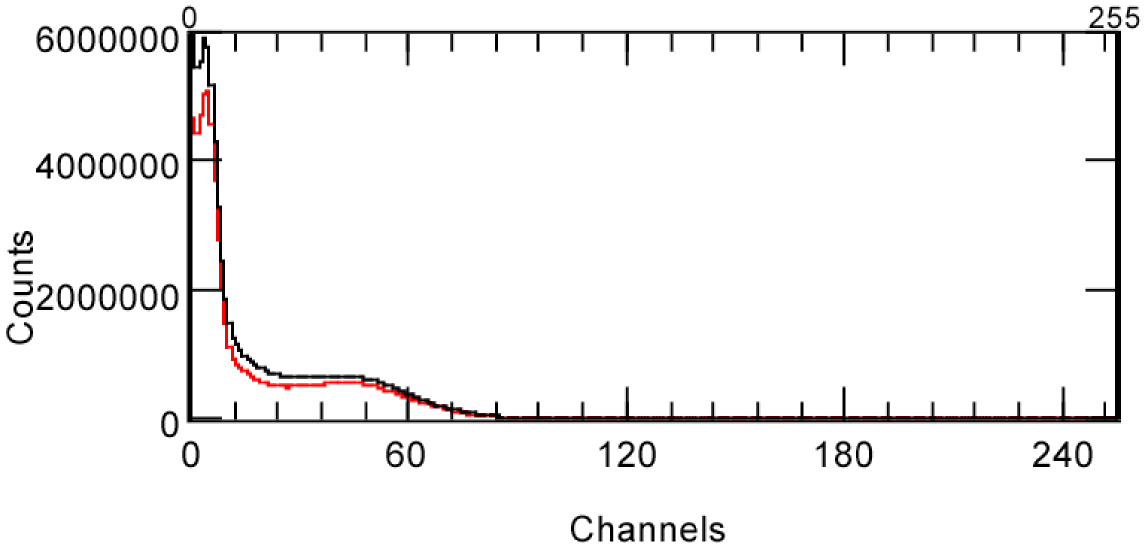

Figure 4.9. **Comparison of ^{133}Ba pulse height spectra in Front detector for full-energy region for "OR" trigger mode (black) versus "OR with Anti" trigger mode (red). Intermediate shield is removed. All discriminator levels are 50 mV.**

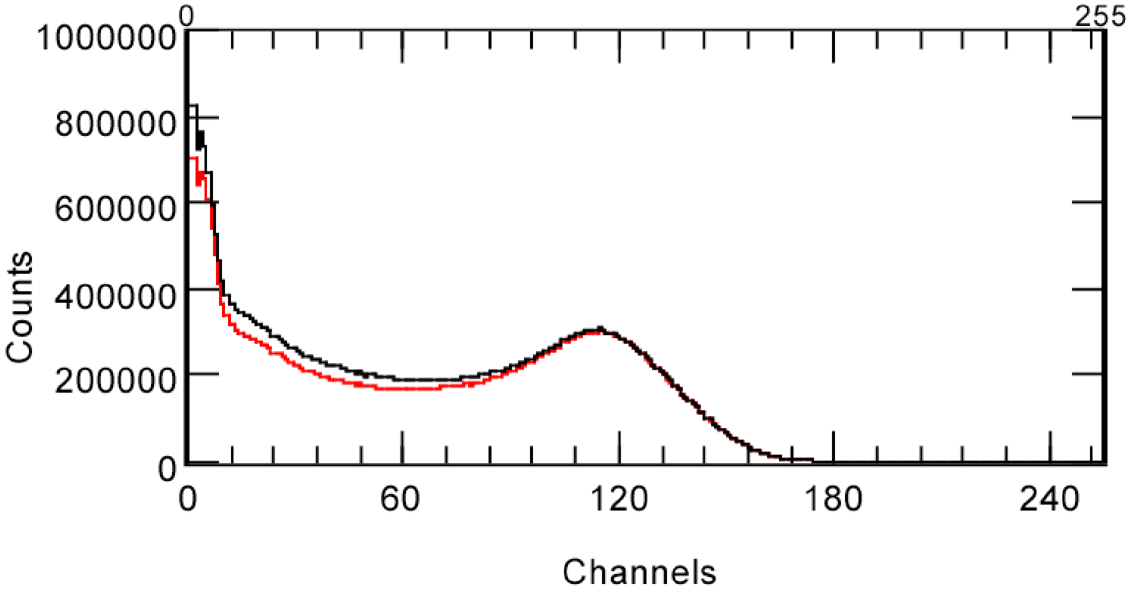

Figure 4.10. **Comparison of ^{137}Cs pulse height spectra in Front detector for full-energy region for "OR" trigger mode (black) versus "OR with Anti" trigger mode (red). Intermediate shield is in place. All discriminator levels are 50 mV.**

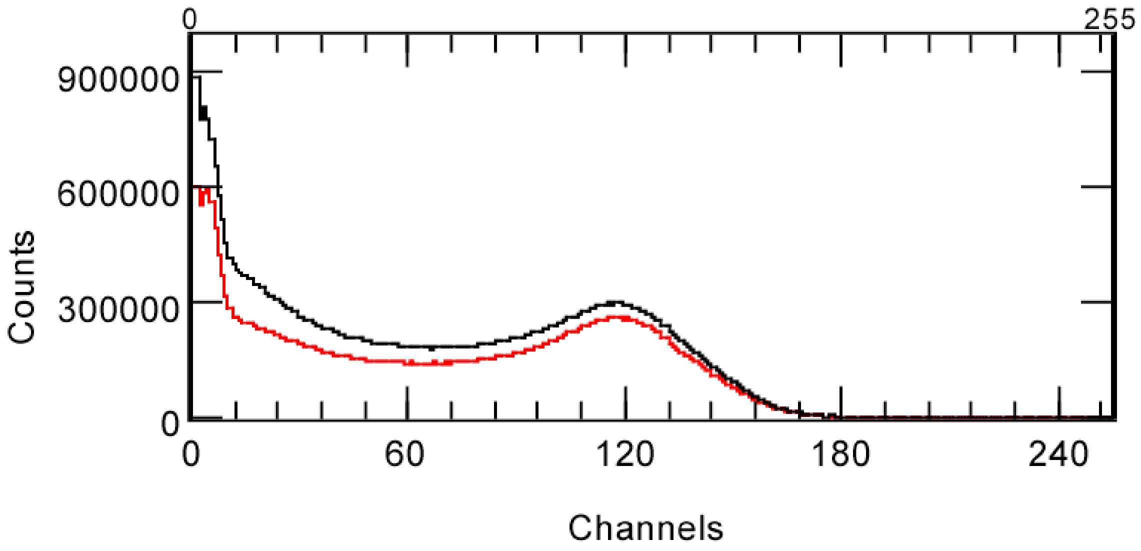

Figure 4.11. Comparison of ^{137}Cs pulse height spectra in Front detector for full-energy region for "OR" trigger mode (black) versus "OR with Anti" trigger mode (red). Intermediate shield is removed. All discriminator levels are 50 mV.

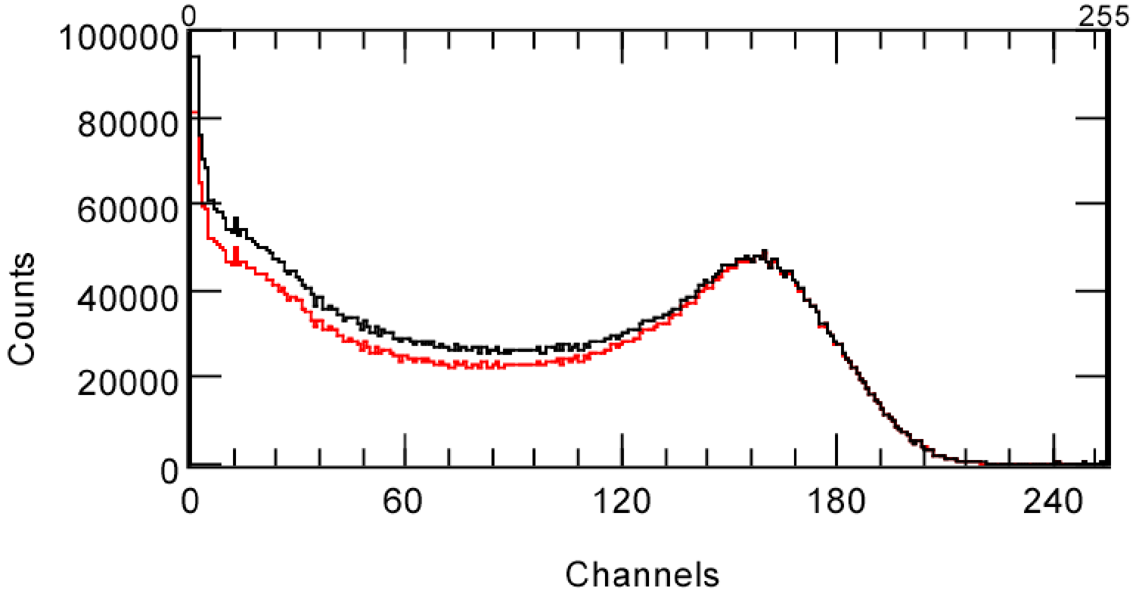

Figure 4.12. Comparison of ^{54}Mn pulse height spectra in Front detector for full-energy region for "OR" trigger mode (black) versus "OR with Anti" trigger mode (red). Intermediate shield is in place. All discriminator levels are 50 mV.

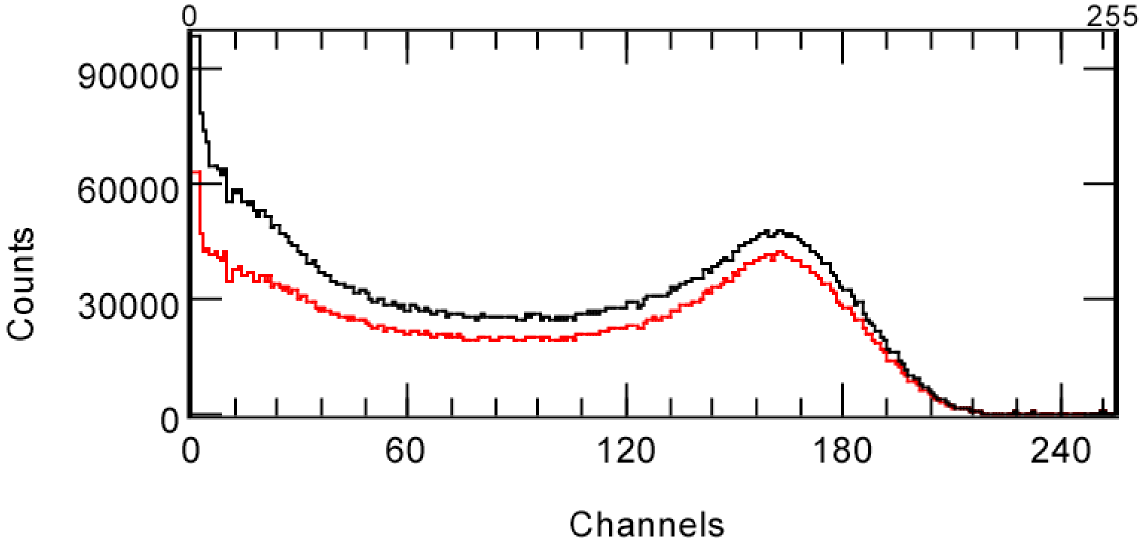

Figure 4.13. Comparison of ^{54}Mn pulse height spectra in Front detector for full-energy region for "OR" trigger mode (black) versus "OR with Anti" trigger mode (red). Intermediate shield is removed. All discriminator levels are 50 mV.

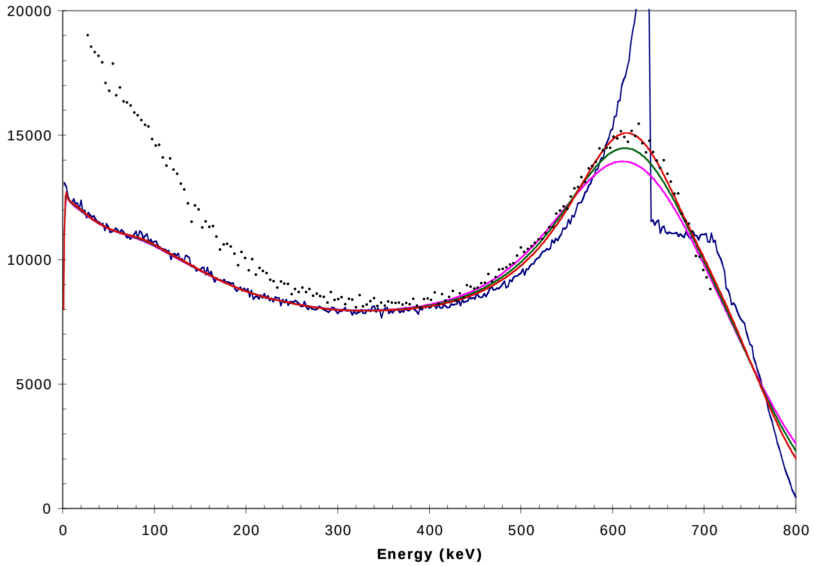

Figure 4.14. Pulse height spectrum of ^{54}Mn. Blue curve is calculated energy deposition. Red, green, and magenta curves are the calculated spectrum after resolution broadening of 25%, 30%, and 35% respectively. Black points are experimental data from "OR" trigger mode normalized to 25% calculated spectrum. All discriminator levels are 50 mV for exp. data. Abscissa is counts per channel.

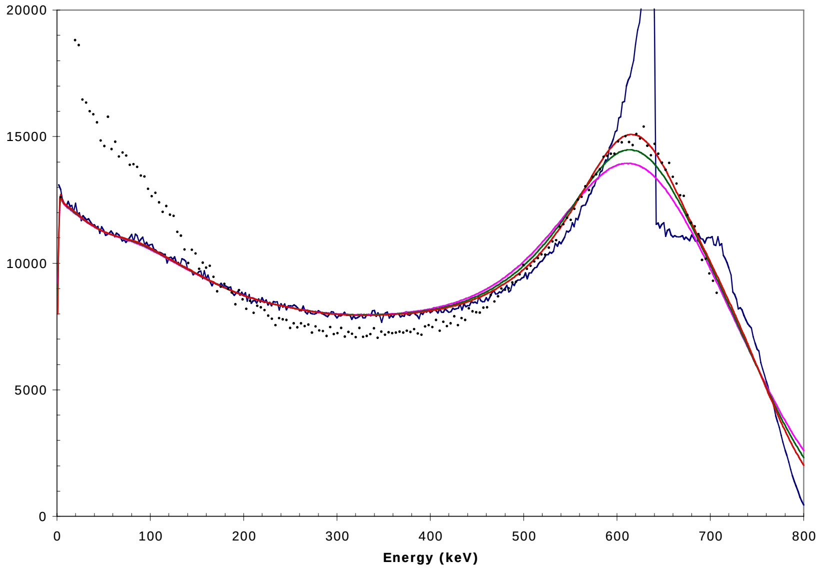

Figure 4.15. **Pulse height spectrum of ^{54}Mn. Blue curve is calculated energy deposition. Red, green, and magenta curves are the calculated spectrum after resolution broadening of 25%, 30%, and 35% respectively. Black points are experimental data from '"OR" with Anti' trigger mode normalized to 25% calculated spectrum. All discriminator levels are 50 mV for experimental data. Abscissa is counts per channel.**

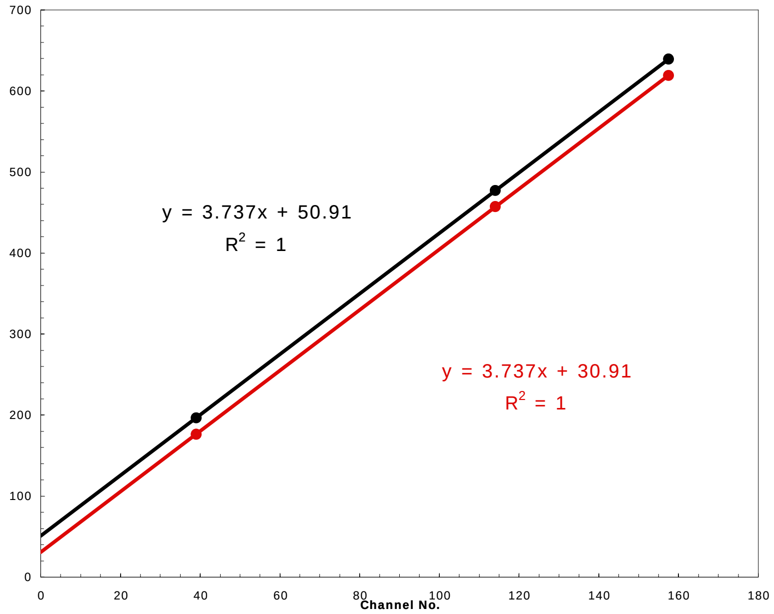

Figure 4.16. **Calibration of pulse height energy (in keV) versus channel number assuming peak centroids correspond to maximum Compton electron energy in scintillator (black curve). Red curve has corrected energies based on a 20-keV shift due to resolution broadening.**

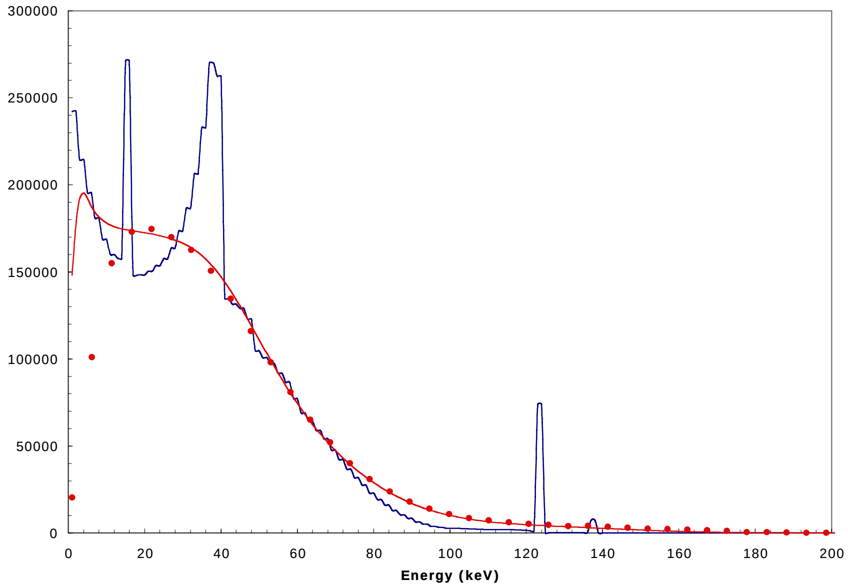

Figure 4.17. **Comparison of calculated and experimental ^{57}Co spectra. Blue curve is calculated energy deposition spectrum. Red curve is resolution-broadened calculated spectrum. Red data points are experimental spectrum normalized and with adjusted energy scale (see text). Abscissa is intensity in arbitrary units.**

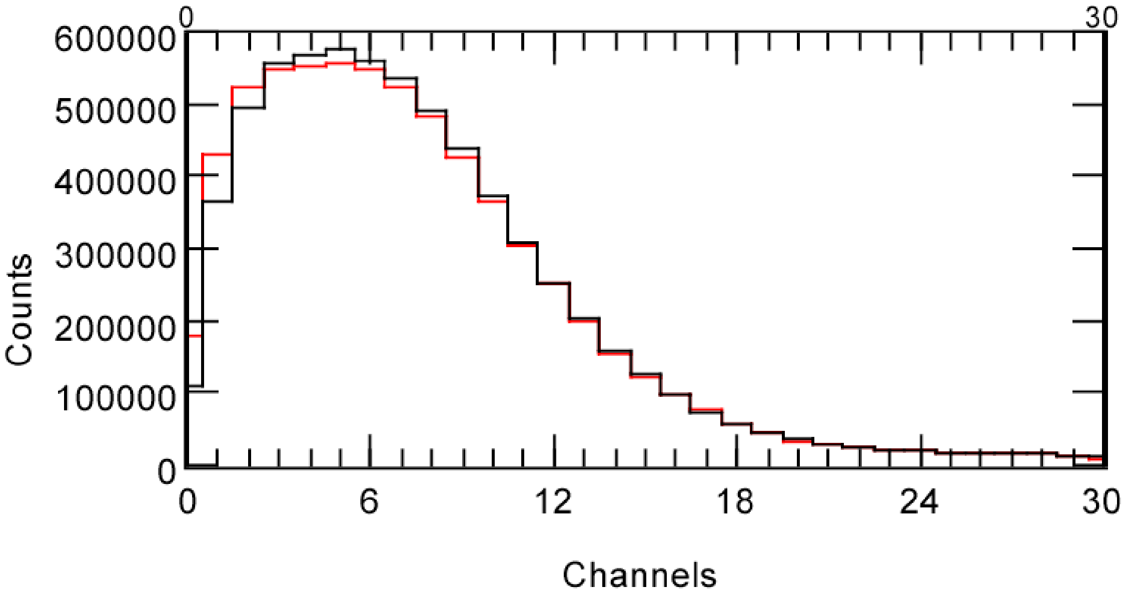

Figure 4.18. **Comparison of ^{57}Co spectra at discriminator levels of 30 mV (red) and 50 mV (black)**

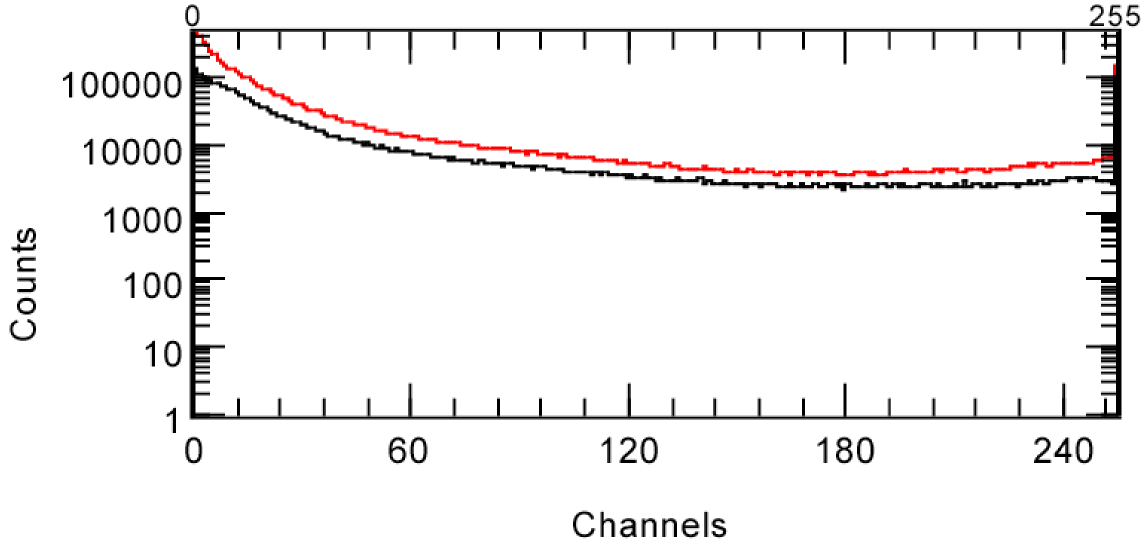

Figure 4.19. **Comparison of background spectra taken with "OR" trigger mode. Red curve is for Front detector. Black curve is for Back detector. There is no intermediate shield and the discriminators are all at 50 mV.**

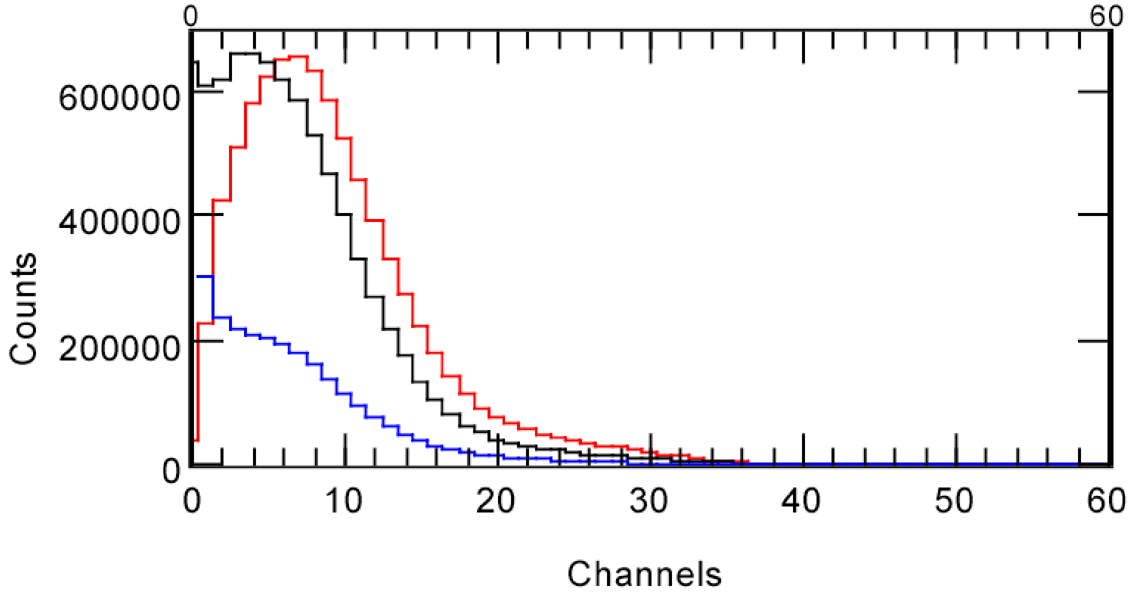

Figure 4.20. **Comparison of ^{57}Co spectra in Front detector (black), Back detector (blue), and the Sum of Front and Back detectors (red). Data are for "OR" trigger mode, no intermediate shield, and all discriminators at 50 mV.**

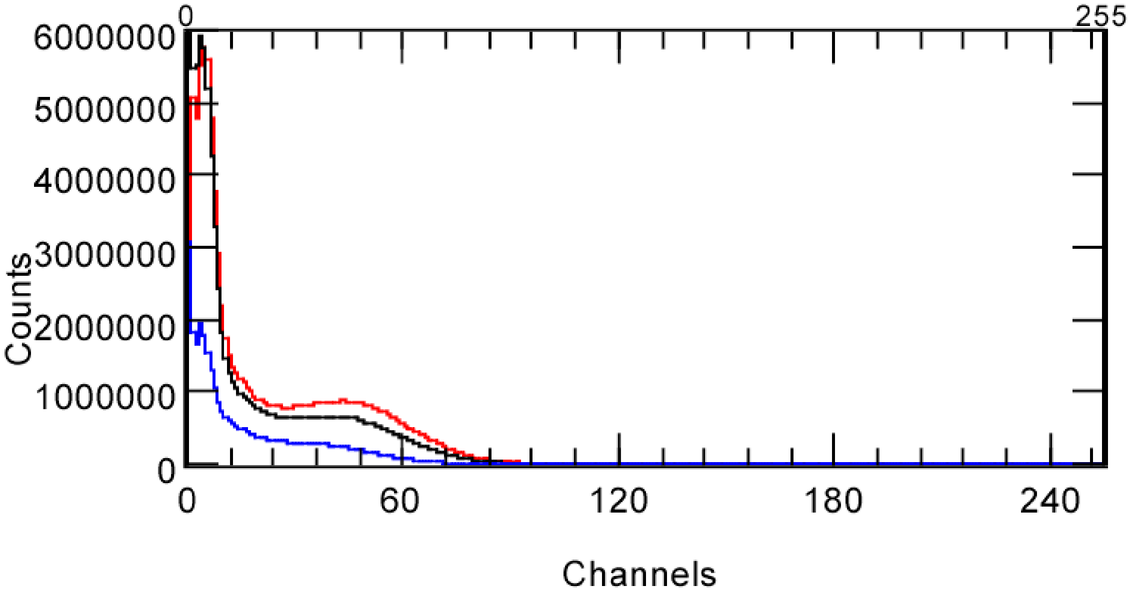

Figure 4.21. **Comparison of ^{133}Ba spectra in Front detector (black), Back detector (blue), and the Sum of Front and Back detectors (red). Data are for "OR" trigger mode, no intermediate shield, and all discriminators at 50 mV.**

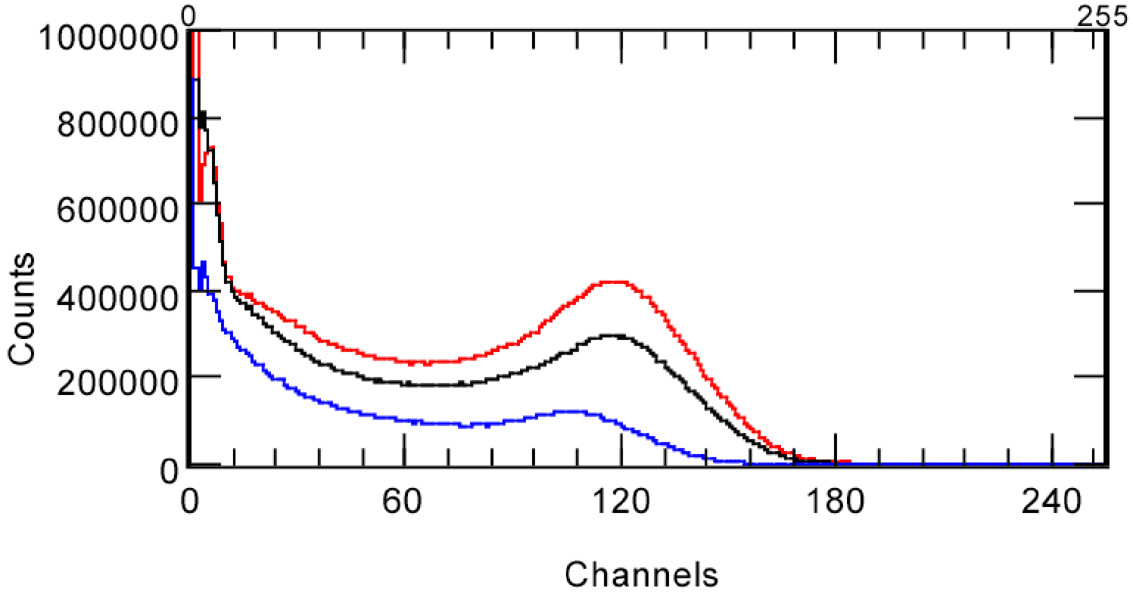

Figure 4.22. **Comparison of ^{137}Cs spectra in Front detector (black), Back detector (blue), and the Sum of Front and Back detectors (red). Data are for "OR" trigger mode, no intermediate shield, and all discriminators at 50 mV.**

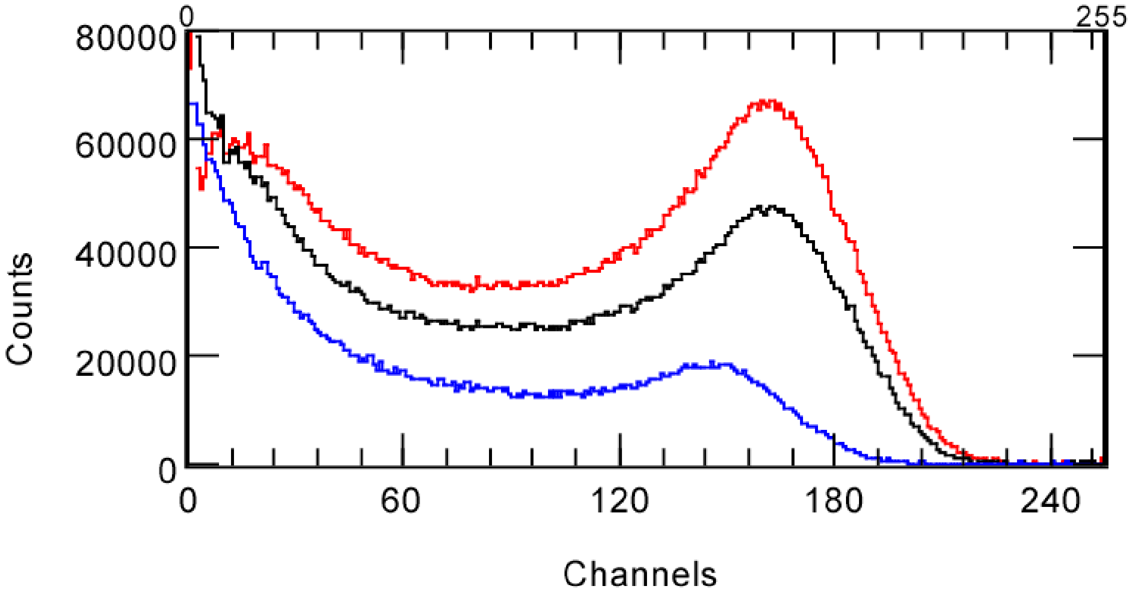

Figure 4.23. Comparison of ^{54}Mn spectra in Front detector (black), Back detector (blue), and the Sum of Front and Back detectors (red). Data are for "OR" trigger mode, no intermediate shield, and all discriminators at 50 mV.

5.0 ALPS II Cerenkov Slab ("CASP") Experiments

5.1 Introduction

As noted in section 4 above, a major interference in detection of low-energy gammas from sources of interest comes from Compton scattering in the plastic scintillator of higher-energy gammas coming from natural sources in the environment, such as ^{40}K. It is possible to reduce the background from such scattering by operating the portal monitor (Front detector) in anti-coincidence with a second detector (Back detector) sensitive only to high-energy gammas. Previous experiments, described in section 4, used a standard plastic scintillator as the anti-coincidence detector and was separated from the front scintillator by a thin lead sheet. A Compton scattering event due to a low-energy gamma of interest would give a pulse in the Front detector due to the Compton scattered electron, while the Compton scattered gamma would be absorbed in the lead sheet without giving a pulse in the anti-coincidence detector. Such an event would be recorded as a valid count. Events due to a high-energy gamma Compton scattered in the Front detector would give a pulse in both the Front scintillator and the Back scintillator because the scattered gamma would have enough energy to penetrate the lead shield. Such events would be rejected. This approach reduces the background for low-energy gammas by reducing the interference from high-energy gammas whether they come from natural sources in the vicinity of the portal monitor or from material passing the portal monitor.

The work described in this section tested an alternative approach to implementing an anti-coincidence detector. This detector was a sheet of plastic designed to respond only to the Cherenkov radiation emitted by high-energy electrons following a Compton scattering of a previously Compton scattered gamma in the Front scintillator. Low-energy gammas that Compton scatter in the Front detector do not produce a scattered gamma with enough energy to produce Cherenkov light from a second scattering in the Back detector. Conversely, high-energy gammas that scatter in the Front detector produce a higher energy scattered gamma that is sufficiently energetic to produce Cherenkov light from a second scatter in the Back detector. The purpose of this work was to compare the background rejection capability of the Cherenkov anti-coincidence detector with the previously determined capability of the lead sheet and standard scintillator used for the anti-coincidence. The combination of a Cherenkov plastic slab with a standard plastic scintillator slab was designated the Cherenkov And Scintillator Portal (CASP) configuration of the ALPS II sensor.

5.2 Experiment

5.2.1 Apparatus

Experiments were performed using a suitably-modified version of the existing ALPS II portal monitor system. The standard configuration of the ALPS II system had two slabs of Bicron/Saint Gobain BC-408 scintillators of dimensions $127 \times 57.15 \times 5.08$ cm^3 separated by a gap of 13 cm. A sheet of 0.32-cm thick lead was positioned between the two scintillators in the standard configuration. For this work the lead sheet was removed and the Back scintillator was replaced by an identically-sized plastic slab (Bicron/Saint Gobain BC-499-76 blue wavelength shifting plastic) sensitive only to Cherenkov radiation. Each detector slab had 3 Hamamatsu R1250 127-mm (5-in.) diameter photomultiplier tubes (PMTs) mounted on each end for a total of 12 PMTs.(a) The scintillators were mounted vertically and shielded on the bottom, sides, and back by 5.08-cm of lead. The entire assembly was mounted in a light-tight steel box. A light-tight plastic door allowed entry of gammas to the scintillator detectors.

The response of these detectors was determined for gamma radiation sources of ^{57}Co (122 keV), ^{133}Ba (356 keV), ^{137}Cs (662 keV), and ^{54}Mn (835 keV). The sources were mounted on the outside of the plastic door at the vertical and horizontal midpoint of the scintillators. The distance of the sources to the front face of the Front scintillator was about 10 cm. Count rates varied depending on the source and the trigger conditions for the data acquisition system, but never exceeded 85,000 cps.

5.2.2 Data Acquisition System

The data acquisition system was composed of CAMAC and NIM data processing modules and a PC running Kmax Version 7.3 software.(b) A schematic of the data acquisition system is shown in Figure 5.1 (figures and tables referenced in this section are collected immediately following section 5.4). Signals from the 12 PMTs were sent to linear fanouts (Phillips PS748). One of the signals from each fanout was delayed using Ortec DB463 modules. The delayed signals were then sent to a 16-channel CAMAC-based Charge-to-Digital (QDC) converter (Phillips PS7166) where the pulse was converted to a channel number corresponding to the integrated charge during a fixed time window. The channel numbers for all 12 PMTs were stored in a list processor (Hytec LP1342) for each event. When the buffer memory of the list processor was filled, the contents of the buffer were transferred to the computer. The list processor then continued to accept new data while the computer software processed the previous data into various histograms representing the pulse height spectra for all events.

The data acquisition system created separate histograms for each of the 12 PMTs. These histograms were useful for adjusting the high voltages on each PMT to gain match the outputs. All the PMTs for the Front detector (PMTs 1-6) were gain matched to PMT 5 and all the PMTs for the Back detector (PMTs 7-12) were gain matched to PMT 11. Gain matching was done for background pulse height spectra on the assumption that background events were uniformly distributed throughout the entire scintillator slab. Previous work had shown that the pulse height spectrum of a particular PMT depended on where the radiation event occurred within the scintillator. Figure 5.2 shows a comparison of background spectra in PMT 2 and PMT 5 after gain matching. Other PMTs gave equally good matches.

In addition to recording the raw pulse heights for each PMT, the data acquisition system could create calculated parameters for each event. Thus the pulse heights of all six PMTs for the Front detector could be summed to give the total pulse height in that detector on an event-by-event basis. Likewise the pulse heights of the six PMTs for the Back detector could be summed to give the total pulse height for the Back detector. Other parameters such as the total sum of the Front and Back detectors could be calculated as desired.

The width of the fixed time window for gating the QDC was 150 ns. Various requirements determined the conditions under which the QDC gate was created. Some experiments were performed with the QDC gate created only when valid events were detected in the Front detector regardless of whether an event was detected in the Back detector. In other experiments, spectra were obtained only when valid events

---

(a) Hamamatsu catalog number H6527 for PMT with integral tube base.

(b) Available from Sparrow Corporation, 1901 Poppy Lane, Port Orange, FL 32128.

were detected in the Back detector regardless of whether an event was detected in the Front detector. In either case, pulse height spectra for the Front and Back detectors were obtained simultaneously.

Another set of experiments triggered the QDC gate only when there was a valid event in the Front detector and no valid event in the back detector. These conditions implemented a hardware anti-coincidence such that the data acquisition system processed only events in the Front detector without a simultaneous event in the Back detector. Only pulse height spectra for the Front detector could be obtained under these conditions because, by definition, there were no pulses in the Back detector.

The most general conditions allowed the QDC gate to be created whenever there were valid events in either the Front or Back detectors ("OR"). In this case, pulse height spectra could be obtained separately for the Front and Back detectors. By setting software windows on the spectra for the Front or Back detectors, the data acquisition system could create pulse height spectra for the following conditions.

1. Pulse height spectrum in Front detector for all events (coincidence and anti-coincidence).
2. Pulse height spectrum in Front detector when there was no event in the Back detector (anti-coincidence).
3. Pulse height spectrum in Front detector when there was a valid event in the Back detector (coincidence).
4. Pulse height spectrum in Back detector for all events (coincidence and anti-coincidence).
5. Pulse height spectrum in Back detector when there was no event in the Front detector (anti-coincidence).
6. Pulse height spectrum in Back detector when there was a valid event in the Front detector (coincidence).
7. Pulse height spectrum for sum of Front and Back pulse heights when there were valid events in both spectra.

The combined pulse height spectrum for the Front and Back detectors are valid only when the Front and Back detectors are the same type of scintillator and the gains have been adjusted properly. In the present experiment, in which the Back detector consisted of a Cherenkov slab, the sum of the Front and Back detectors had no physical significance.

In Figure 5.1, the QDC gate is triggered by the hardware anti-coincidence set-up. Each of the PMT signals go to discriminators that accept pulses above a specified threshold. The 6 PMTs on the Front scintillator go to an 8-channel discriminator module (Phillips PS705). This module has an output signal that is proportional to the number of channels that have been triggered simultaneously (Sum Output). The 6 PMTs on the Back scintillator were sent to an identical discriminator module. In both cases, the Sum outputs were sent to a discriminator where the threshold was set to accept events where 2 or more PMTs on each scintillator had valid signals. The discriminator outputs were stretched to a width of 1.7 μs and fed back to the discriminators to inhibit acceptance of any other events until the current event had been fully processed. The discriminator output of the Front detector was delayed by 20 ns and shortened to a 10-ns wide pulse. The discriminator pulse from the Back detector was not delayed but was converted to the complement signal and stretched to 80 ns. These two discriminator pulses were sent to an overlap coincidence unit creating the following logic.

> For an event with a valid pulse in the Front detector but no pulse in the Back detector, the complement of the Back discriminator remained at a –5 V level, the discriminator output of the

> Front detector switched from ground to –5 V for 10 ns, and a valid output was generated by the coincidence unit.
>
> If valid events were detected in both Front and Back detectors, the complement of the Back discriminator output switched from –5 V to ground for 80 ns, the discriminator output of the Front detector switched from ground to –5 V for 10 ns, but no output was generated by the coincidence unit because both coincidence inputs were not at –5 V simultaneously. The 20 ns delay on the Front detector discriminator was introduced to prevent timing jitter from causing accidental coincidence outputs.

To switch from this hardware anti-coincidence configuration to the more general "OR" trigger configuration, the output on the Sum discriminator was switched from the complement to the normal signal, the inputs to the coincidence unit were switched from the coincidence mode to the "OR" mode, and 10 ns delay was added to the Sum output of the Back detector discriminator to compensate for internal delays in the logic modules. One further change was to switch the output of the coincidence unit to trigger on the rising edge of the logic pulse rather than the falling edge.

To convert the QDC gate trigger to operate only on events from the Front detector, the general "OR" mode set-up was modified by removing the Back detector input from the coincidence module and requiring only a single input from the Front detector to trigger the QDC gate. Similarly, to obtain triggers based only on the Back detector, only the Back input to the coincidence module was enabled.

In all experiments, a separate 60-cycle pulser signal was included in the data stream by way of channel 16 of the QDC. The trigger for the pulser QDC gate was mixed with the trigger for valid signals by way of a second coincidence unit operating in the "OR" mode. The output of this "OR" coincidence unit was stretched to 150 ns and was sent to the gate input of the QDC. This pulser signal was subject to the same dead times as the PMT signals. It was stored in a separate histogram. The integrated counts in the pulser histogram was compared to the number of events expected for the pulser for the elapsed data acquisition time. The ratio of the observed counts to the expected counts is the livetime for that particular experiment. Livetimes for background experiments were different from livetimes for runs with sources so a livetime correction was applied to all data.

5.2.3 Data Collection

All experiments recorded pulse height spectra for 300 second collection times. Sources were mounted at the horizontal and vertical midpoints of the detectors on the outside of the plastic door as mentioned above. Background measurements were performed for all configurations. The discriminators on the individual PMTs were usually set at 50 mV on both Front and Back PMTs. However, some data were obtained with discriminator levels of 30 mV and 10 mV. In addition, some data were obtained with different discriminators on the Front and Back detectors. All experiments were based on valid signals being defined as 2 or more valid PMT signals in the Front and/or Back detectors.

Separate scalers were used to record the count rates in the Front and Back detectors and for the combined Front and Back counts. These scaler count rates were free of the livetime corrections inherent in the pulse height measurements and gave an independent measure of the actual detection rates.

Data were obtained for various sources, trigger configurations, and discriminator levels as shown in the tables and figures collected below (following section 5.4). In some cases, data were obtained in list mode as well as in the normal on-line histogramming mode. Experiments taken in list mode were usually repeated without the list mode feature mainly because livetimes were significantly smaller when in the list mode. Comparison of data taken with and without the list mode function permits determination of the validity of the livetime measurement.

5.3 Results

This work was intended to answer three primary questions. The first question was whether the addition of an anti-coincidence detector made a significant reduction in the background count rates particularly in the region of the low-energy gamma sources (^{57}Co, ^{133}Ba). The second question was whether the efficiency for detecting the low-energy gamma sources (^{57}Co, ^{133}Ba) was affected by the addition of the anti-coincidence detector. The third question was whether the anti-coincidence gating reduced the background in the low-energy region caused by high-energy gammas from a source.

To answer these questions, the pulse height spectra were integrated to obtain the total count rates over two energy regions in the spectra for the Front detector. The first energy region was from channels 0 to 60 which included all of the events from the ^{57}Co source and most of the events from the ^{133}Ba source. The second energy region was from channels 0-255 which included all events. These count rates are given in Table 5.1 for the two energy regions and for the different sources and trigger conditions. All the integrated counts have been corrected for the data acquisition live time and the decay of the sources during the month and a half over which the experiments were conducted. The spectra were each obtained over a 300-second counting interval. All discriminators for the PMTs in the Front and Back detectors were set at 50 mV for the data shown in Table 5.1. Note that the data acquisition trigger was generated if two or more PMTs on a given detector had a pulse greater than the discriminator level. Table 5.1 also gives the ratio of counts at each trigger condition to the counts obtained as if there were only a single detector.

5.3.1 Background Efficiencies

We first look at the data for the background as these data are relevant to answering the first question. The “Front Only” trigger condition ignored the existence of the Back detector and acquired data only when a valid pulse was observed in the Front detector. The count rates under this trigger condition are the baseline for comparing all other trigger conditions. The “OR” trigger condition accepted data whenever there were valid pulses in either the Front scintillator or the Back scintillator. The spectra in the Front scintillator then included roughly 10% more events due to triggers in the back detector that were accompanied by very small pulses in the Front detector that were below the trigger for the Front detector. As shown in Figure 5.3, the enhanced counts for the “OR” trigger mode are all located in channels 0 and 1 in the low-energy background spectrum.

In order to use the Back detector as an anti-coincidence gate, a software gate was imposed on the spectra in the Front detector such that a new pulse height histogram was generated only when events in the Back detector were at very low pulse heights (channels 0-3). If the Back detector had a pulse greater than channel 3, that event was not included in the gated histogram for the Front detector. This trigger condition is called ‘ “OR” with Anti’ in Table 5.1. Note that this anti-coincidence gate reduced the count rate from the normal “OR” trigger by about 10% thus bringing the effective background rate back to where it was with only the single detector (Front Only). As shown in Figure 5.4, the reduced counts are primarily at channels 0 and 1, but there are slightly reduced counts at somewhat higher channels as well.

To verify whether the software anti-coincidence was functioning properly, experiments were done using a hardware gate so that data were obtained only when no valid pulse was observed in the Back detector. This slightly reduced the data acquisition rate and thus slightly raised the observed livetime which is of some benefit. However, the hardware and software anti-coincidence trigger modes gave essentially similar results.

The final trigger mode was one in which only a valid event in the Back detector allowed pulse height data to be acquired. This allowed a measure of the relative count rates due to the Front or Back detectors and also allowed measurement of the pulse height spectra in the Front detector that were in coincidence with pulses in the Back detector. For both background and source measurements, the spectrum in the Front detector was dominated by low-energy events when triggered by the Back detector. For the background measurements the count rates when triggered by the Back detector were about 12% of the count rates when triggered by the Front detector as shown in Figure 5.5. Note that most of the events in the Front detector when triggered by the Back detector are in channels 0 and 1.

5.3.2 Source Efficiencies

The data in Table 5.1 show that the background-subtracted count rates for the low-energy sources ^{57}Co and ^{133}Ba increase by 2 or 3 % by the addition of the Back scintillator with the “OR” trigger mode. The pulse height spectra comparing the “Front Only” and “OR” trigger modes are shown in Figure 5.6 for the ^{57}Co source and in Figure 5.7 for the ^{133}Ba source. The software anti-coincidence gating mode did not change the count rate for the ^{57}Co source. The ^{133}Ba source did show a slight decrease in count rate down to the original count rate when the software anti-coincidence requirement was imposed. For both sources the hardware anti-coincidence requirement brought the count rates back to within 1% of the original count rates. When the “Back Only” trigger requirement was imposed, the ^{57}Co count rate was about 0.1% of its original count rate whereas the ^{133}Ba count rate was about 1% of its original rate. These results are strong support for the assumption that the efficiency for detecting low-energy gammas is not affected by the anti-coincidence requirement.

The count rates for the higher-energy sources (^{137}Cs and ^{54}Mn) are significantly affected by the presence of the Back detector. Figure 5.8 and Figure 5.9 give the pulse height spectra for ^{137}Cs and ^{54}Mn, respectively, for the “Front Only”, “OR”, and ‘“OR” with Anti’ trigger modes. Examination of the data for the low-energy region of the ^{137}Cs source shows that the “OR” trigger raised the count rate by about 27% whereas adding the software anti-coincidence lowered the count rate to 98% and the hardware anti-coincidence lowered the count rate to 95%. The “Back Only” trigger gave a count rate of 23% indicting that the Back detector saw a significant number of events due to the ^{137}Cs source. These effects are even stronger for the ^{54}Mn source. In the low-energy region, the increase in count rate was 36% for the “OR” trigger. The ‘“Or” with Anti’ mode gave 89% of the original count rate and the “Hardware Anti” mode gave 91% of the original rate. The “Back Only” trigger mode gave 43% of the “Front Only” count rate. Thus the answer to the third question is that background in the low-energy region due to high-energy gammas from a source can be reduced by use of anti-coincidence techniques. However, this reduction may not be sufficient to justify the extra complexity of the entire detection system.

For all four sources there was very little difference between the software-generated anti-coincidence trigger mode and the hardware-generated anticoincidence mode.

5.3.3 Spectra

The effect of the anti-coincidence gating can be seen in more detail in the pulse height spectra. Comparison of spectra in "OR" trigger mode with and without the anti-coincidence gating are shown in Figure 5.10 through Figure 5.13. Note that both ^{57}Co and ^{133}Ba show almost no change when the anti-coincidence gating is turned on. Both the ^{137}Cs and ^{54}Mn show a reduction at low pulse heights due to the anti-coincidence gating but no effect on the peak at high energy due to the Compton edge.

5.3.4 Calibration of energy axis

To convert the pulse height channel number to an energy scale requires measurement of channel numbers for peaks from several sources. The peaks observed in the plastic scintillators used here are not due to the full energy of the incident gamma as is typical of NaI(Tl) or Ge detectors. For plastic scintillators, the peak is caused by the Compton edge from 180 deg. scattering of the incident gamma. A further complication is the fact that resolution broadening shifts the peak to slightly lower energy than expected from the Compton scattering equation. Computer modeling using the code GEANT has been performed to determine the distribution of energies deposited by electrons from Compton scattering events in plastic scintillators having the dimensions used in this work. The resulting energy spectrum was then broadened with a Gaussian resolution function. The width of the Gaussian resolution was varied until a reasonable agreement with the experimental peak was obtained.

In Figure 5.14 and Figure 5.15, the calculated energy deposition spectrum for ^{54}Mn is shown along with resolution broadened spectra for 3 different resolution functions. The value of the Gaussian resolution function at 200 keV was arbitrarily chosen as the identifier for a particular resolution function. In every case the resolution function was assumed to vary as 1/SQRT(E). Figure 5.14 shows the experimental spectrum when the trigger mode was the "OR" configuration. The best agreement between the experimental data and the calculated data is with the 25% resolution function. Figure 5.15 compares the experimental spectrum obtained with the software anti-coincidence trigger mode ('"OR" with Anti') with the calculated spectra. It appears that the anti-coincidence trigger results in slightly better resolution than the "OR" trigger mode.

The comparison of the experimental pulse height spectrum with the calculated spectra allows a determination of the energy shift due to resolution broadening. The energy shift is not very sensitive to the energy of the incident gamma (at least for sources with energy above 300 keV where distinct peaks can be observed). The resolution broadened peaks shown in Figure 5.14 and Figure 5.15 are about 20 keV lower energy than the peak seen in the calculated energy deposition spectrum. An initial energy calibration curve based on the calculated Compton peak without resolution broadening is shown in Figure 5.16 along with a corrected calibration curve assuming that the resolution broadened peak energies are all 20 keV lower than the calculated energies.

The calibration curve resulting from the corrected data shows a channel 0 intercept of 30 keV. The ^{57}Co pulse height spectrum shown in Figure 5.6 has a cut off at channel 4 which would be 44 keV assuming the calibration is linear at low energies. The calculated Compton edge for ^{57}Co is 40.4 keV so that an energy shift due to resolution broadening would put the Compton edge significantly below the observed cut off. Alternatively, one can ask whether the ^{57}Co gamma energy is low enough that secondary gamma scatters could add to the deposited energy up to the full photopeak energy of 122 keV. In this regard, we note that the calculated energy deposition spectrum for ^{133}Ba shows a sharp peak at 80 keV corresponding to full energy deposition of the 80 keV gamma in decay of ^{133}Ba.

The calibration technique described above is difficult to apply to the low energy portion of the pulse height spectrum (<200 keV). The experimental spectrum of ^{57}Co does not show a peak due to the Compton edge of the 122-keV gamma. Although the energy deposition spectrum does show peak structure, the application of resolution broadening washes out the peak structure as shown in Figure 5.17. In addition, the experimental spectrum can not be fit to the resolution broadened spectrum without adjusting the energy scale. The experimental energy spectrum shown in Figure 5.17 assumes a lower energy intercept (1 keV instead of 29.7 keV) and a larger slope (4.7 keV/channel instead of 3.695 keV/channel) than the calibration curve shown in Figure 5.16. Also note that the ^{137}Cs spectra in Figure 5.8 and Figure 5.12 show a strong enhancement at channel 5 indicating observation of the 30-keV X-ray expected in the ^{137}Cs decay scheme. Such an enhancement is not seen or expected in the ^{54}Mn spectra in Figure 5.9 and Figure 5.13.

5.3.5 Effect of discriminator

To resolve the uncertainty in the low-energy calibration, spectra were measured at discriminator settings of 10 mV and 30 mV as well as at the 50 mV settings shown in Figure 5.6 through Figure 5.9. A comparison of the ^{57}Co pulse height spectra at the three discriminator settings is shown in Figure 5.18. Note that as the discriminator levels are increased, the cut off shifts from channel 2 (10 mV) to channel 3 (30 mV) to channel 3.5 (50 mV) but that the counts in channel 4 and above are unchanged. The discriminator level at 50 mV reduces the total counts between channels 0 – 60 by 5% relative to the total counts at 10 mV. It thus appears that a 50 mV discriminator does not cut off a large fraction of the ^{57}Co events indicating that most of the events due to the 122 keV gamma have been observed. It is therefore likely that the energy calibration below 200 keV is not linear as suggested in Figure 5.16.

5.3.6 Effect of livetime differences

Given the high count rates (<85,000 cps) for 10 μCi sources at about 10 cm from the scintillator and the block time of 1.7 μsec for each pulse, the measured livetimes were a significant correction to the observed spectra. The presence or absence of list mode data acquisition also affected the livetime. For the most intense sources (^{133}Ba and ^{137}Cs), the reduction in livetime was about a factor of 2. These factors allowed a comparison of spectra obtained under identical conditions except for a difference in livetime. The agreement or disagreement for two spectra measured with different livetimes enabled us to estimate the validity of the livetime correction.

Table 5.2 gives the ratios of the livetime correction factors and the ratios for the corrected total counts for all 4 sources for experiments done at different livetimes. Figure 5.19 and Figure 5.20 show livetime-corrected spectra for ^{133}Ba and ^{137}Cs, respectively, taken with about a factor 2 difference in livetime. In both cases the data taken with list mode acquisition on and the lower livetime showed a corrected spectrum that was about 5% higher than data taken without the list mode on. Similar spectra for ^{57}Co taken with only a 20% lower livetime difference still showed about a 3% increase in total count for data acquired with the lower livetime as shown in Figure 5.21. Spectra for the ^{54}Mn source are shown in Figure 5.22 but note that the source was removed and replaced between the two experiments. The observed count rate difference was about 12% but this may have been due to lack of reproducibility in the source position rather than the effect of livetime differences. Because there was no strong correlation between the ratio of the livetime correction factors and the ratio of the livetime-corrected counts, we conclude that the livetime correction is internally consistent for data taken without the list mode acquisition on, but that perhaps the list mode acquisition causes about a 5% overcorrection in the livetime correction.

5.3.7 Comparison of spectra triggered by Back detector only

The pulse height spectra in the Back detector are due to light produced by Cherenkov radiation. These spectra are quite different from the scintillation light seen in the Front detector. In Figure 5.23, the pulse height spectra in the Back detector due to the Cherenkov radiation from a typical background and from the ^{54}Mn source are compared. The pulse height data were acquired only by triggers from the Back detector. Note that the Cherenkov spectra from background are spread over the entire spectrum whereas Cherenkov spectra for the ^{54}Mn source are concentrated in a peak at low pulse heights. This suggests that background in the Back detector comes from incident particles with a wide range of energies indicative of cosmic rays as well as high energy gammas. The gammas from ^{54}Mn reaching the Back detector are either unscattered gammas at 835 keV or Compton scattered gammas at less than 639 keV.

Figure 5.24 shows scintillation spectra for the background and for the ^{54}Mn source in the Front detector when triggered only by the Back detector. Both spectra are dominated by low amplitude events and have minimal structure. However, the background spectrum extends to higher pulse heights, again indicative of incident events with energies greater than the 835-keV gamma from ^{54}Mn. The spectrum from the ^{54}Mn source does not show a Compton edge. This is consistent with the incident gamma passing through the Front detector and having its first scattering event in the Back detector. In order for the Compton scattered gamma to have a second scattering event in the Front detector, it must have scattered at a large angle in the Back detector and necessarily have deposited most of its energy in the Back detector.

For the low-energy sources (^{57}Co and ^{133}Ba) relatively few gammas penetrate the Front detector and produce any Cherenkov radiation in the Back detector. As the energy of the incident gamma increases, the number of triggers from the Back detector increases rapidly and the peak in the Cherenkov spectra shifts to higher channels. This trend is illustrated in Figure 5.25 where the spectra in the Back detector for ^{137}Cs (662 keV), ^{22}Na (511 keV and 1275 keV), and ^{60}Co (1173 keV and 1332 keV) are shown. Note that the Cherenkov peak for ^{137}Cs is at channel 7, ^{22}Na has two peaks at channels 5 and 18, and ^{60}Co has one broad peak at channel 15.

The pulse height spectra in the Front detector in coincidence with triggers from the Back detector also shift to higher energy as the incident energy increases. The spectra for ^{137}Cs, ^{22}Na, and ^{60}Co are shown in Figure 5.26. Note that ^{22}Na and ^{60}Co both have coincident gamma rays as part of their decay scheme. Thus it is possible to have one gamma interact in the Back detector giving the trigger signal but the coincident signal in the Front detector is due to a Compton scatter of a different gamma from the same source. In fact, the spectrum for ^{22}Na in Figure 5.26 shows evidence of a Compton edge peak at channel 83 consistent with the location for a 511-keV incident gamma. The Compton edge for either of the two gammas from ^{60}Co would be off scale in Figure 5.26 consistent with the increase in intensity at the highest channels in the spectrum.

The rapid increase in the Back detector trigger rate as the energy of the incident gamma increases implies a correspondingly rapid increase in the anti-coincidence effectiveness. In Table 5.1, we noted that the hardware anti-coincidence mode reduced the count rate in the low-energy pulse height region by about 5% relative to the Front Only trigger mode. For the Back only trigger mode, the net ^{137}Cs trigger rate was about 4,700 cps whereas the ^{60}Co net trigger rate was about 14,500 cps. After correcting for the fact that ^{60}Co has two gammas with equal emission rate, the ^{60}Co is still about twice as efficient at generating triggers from the Back detector because of its higher energy gammas. Although the anti-coincidence efficiency for ^{60}Co was not measured in this work, we can estimate that it would be at least twice that of ^{137}Cs. It probably would be even greater because the ^{54}Mn was measured to have a 10% anti-coincidence efficiency and the ^{60}Co gamma energy is much higher than ^{54}Mn.

5.4 Conclusions

This work has answered the three questions posed above.

1. The anti-coincidence gating system as implemented in this work did not result in fewer counts in the low-energy pulse height region due to background events.
2. The present data do show that the efficiency for detecting low-energy gamma sources is not changed by the imposition of the anti-coincidence requirement.
3. There is a reduction of the count rates in the low-energy region due to sources with high-energy gammas.

The reduction factor appears to increase rapidly as the energy of the gamma increases. Thus the reduction factor for ^{40}K (1461 keV) which is a common interference when looking for low-energy sources might be double or triple the reduction factor of about 10% observed here for ^{54}Mn (835 keV). Given that no background reduction from the environment was observed in this work, further evaluation is needed to determine whether a possible 30% reduction of the interference caused by high-energy sources is justified relative to the extra cost and complexity of the anti-coincidence system.

Table 5.1. Count rates (cps) for various sources and trigger conditions

Source	Trigger	Corr. Rate Sum(0-60)	Corr. Rate Sum(0-255)	X/Front Sum(0-60)	X/Front Sum(0-255)
BGD	Front Only	4771	6049	1.000	1.000
BGD	"OR"	5254	6569	1.101	1.086
BGD	"OR" with Anti	4678	5873	0.980	0.971
BGD	Hardware Anti	4812	6031	1.009	0.997
BGD	Back Only	592	712	0.124	0.118
^{57}Co	Front Only	7432	7445	1.000	1.000
^{57}Co	"OR"	7638	7634	1.028	1.025
^{57}Co	"OR" with Anti	7638	7635	1.028	1.025
^{57}Co	Hardware Anti	7496	7519	1.009	1.010
^{57}Co	Back Only	3	4	0.000	0.001
^{133}Ba	Front Only	80904	84542	1.000	1.000
^{133}Ba	"OR"	82326	86276	1.018	1.021
^{133}Ba	"OR" with Anti	80794	84738	0.999	1.002
^{133}Ba	Hardware Anti	80674	84360	0.997	0.998
^{133}Ba	Back Only	748	752	0.009	0.009
^{137}Cs	Front Only	20487	40274	1.000	1.000
^{137}Cs	"OR"	25933	47915	1.266	1.190
^{137}Cs	"OR" with Anti	20118	41715	0.982	1.036
^{137}Cs	Hardware Anti	19386	39198	0.946	0.973
^{137}Cs	Back Only	4679	4778	0.228	0.119
^{54}Mn	Front Only	2785	7087	1.000	1.000
^{54}Mn	"OR"	3797	8348	1.363	1.178
^{54}Mn	"OR" with Anti	2473	6858	0.888	0.968
^{54}Mn	Hardware Anti	2523	6795	0.906	0.959
^{54}Mn	Back Only	1187	1244	0.426	0.176

Table 5.2. Comparison of data acquired with different livetimes

Source	Livetime	Counts	Ratio Livetimes (high/low)	Ratio Counts (low/high)
^{57}Co	0.5100	7512483	1.194	1.033
^{57}Co	0.6089	7273884		
^{133}Ba	0.0757	89029030	2.498	1.058
^{133}Ba	0.1891	84162144		
^{137}Cs	0.1465	41243828	2.166	1.053
^{137}Cs	0.3173	39165407		
^{54}Mn	0.5321	7448994	1.144	1.128
^{54}Mn	0.6089	6601915		

Table 5.3. Experiments with Cherenkov Anti-Coincidence System

Run No.	Source	Trigger Mode	Front Disc. (mV)	Back Disc. (mV)	List Mode
9148	^{57}Co	Back only	50	50	
9149	^{109}Cd	Back only	50	50	
9150	^{133}Ba	Back only	50	50	
9151	^{137}Cs	Back only	50	50	
9152	^{54}Mn	Back only	50	50	
9153	^{22}Na	Back only	50	50	
9154	^{60}Co	Back only	50	50	
9156	^{133}Ba	Back only	50	50	
9158	^{133}Ba	Back only	30	30	
9159	^{133}Ba	Back only	10	10	
9162	^{57}Co	OR	10	10	
9163	^{57}Co	OR	30	10	
9166	^{57}Co	OR	30	30	
9167	^{57}Co	OR	50	30	
9170	^{57}Co	OR	50	50	
9171	^{57}Co	OR	30	50	
9174	^{57}Co	OR	50	50	
9178	^{54}Mn	OR	50	50	
9180	^{137}Cs	OR	50	50	
9182	^{133}Ba	OR	50	50	
9184	^{57}Co	OR	50	50	
9187	^{54}Mn	OR	50	50	Yes
9188	^{137}Cs	OR	50	50	Yes
9189	^{133}Ba	OR	50	50	Yes
9190	^{57}Co	OR	50	50	Yes
9193	^{57}Co	OR	50	50	
9194	^{57}Co	OR	50	30	
9197	^{57}Co	OR	50	10	
9198	^{57}Co	OR	50	10	Yes
9201	^{57}Co	OR	50	30	Yes
9202	^{57}Co	OR	50	50	Yes
9206	^{57}Co	OR	50	50	Yes
9207	^{57}Co	OR	50	50	
9210	^{57}Co	OR	30	50	Yes
9211	^{57}Co	OR	30	50	
9214	^{57}Co	OR	10	50	Yes
9215	^{57}Co	OR	10	50	

Run No.	Source	Trigger Mode	Front Disc. (mV)	Back Disc. (mV)	List Mode
1004	^{54}Mn	Hardware Veto	50	50	Yes
1005	^{137}Cs	Hardware Veto	50	50	Yes
1006	^{137}Cs	Hardware Veto	50	50	
1007	^{133}Ba	Hardware Veto	50	50	
1008	^{133}Ba	Hardware Veto	50	50	Yes
1009	^{57}Co	Hardware Veto	50	50	Yes
1010	^{57}Co	Hardware Veto	50	50	
1011	^{54}Mn	Hardware Veto	50	50	
1013	^{57}Co	Hardware Veto	50	30	
1014	^{57}Co	Hardware Veto	50	10	
1017	^{57}Co	Hardware Veto	30	10	
1018	^{57}Co	Hardware Veto	30	30	
1021	^{57}Co	Hardware Veto	30	50	
1103	^{54}Mn	Front Only	50	50	
1105	^{137}Cs	Front Only	50	50	
1106	^{133}Ba	Front Only	50	50	
1107	^{57}Co	Front Only	50	50	

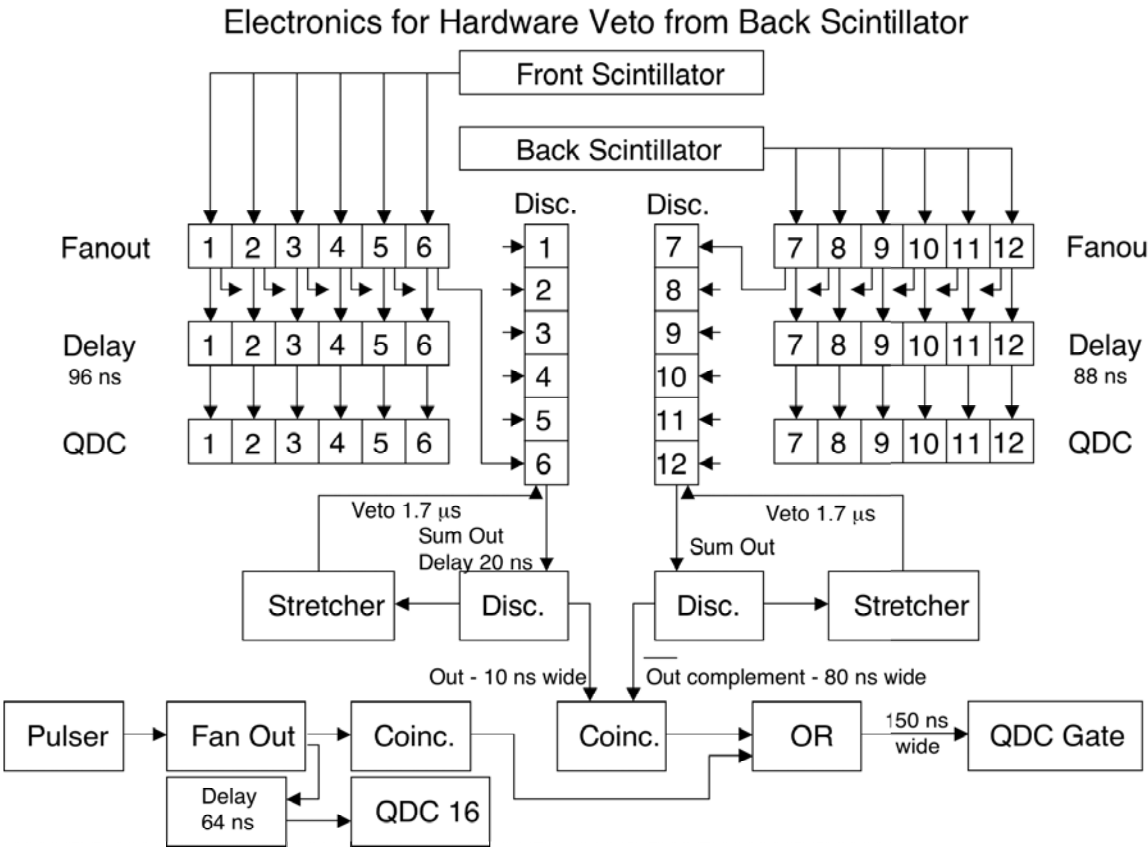

Figure 5.1. Schematic of electronic modules for data acquisition

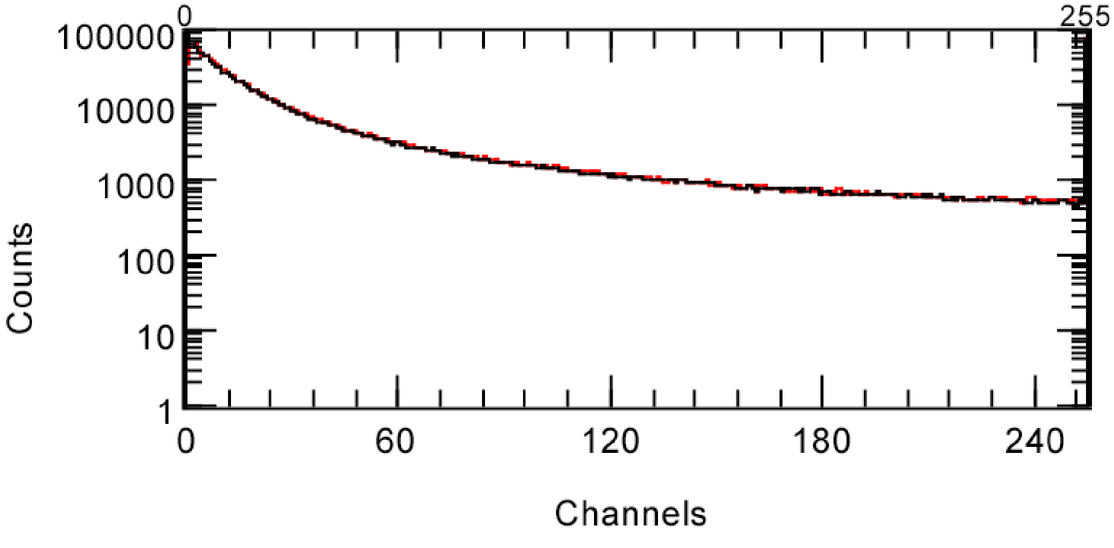

Figure 5.2. Comparison of PMT 2 (red curve) and PMT 5 (black curve) pulse height spectra for background data taken with the "OR" trigger condition with all discriminator thresholds at 50 mV.

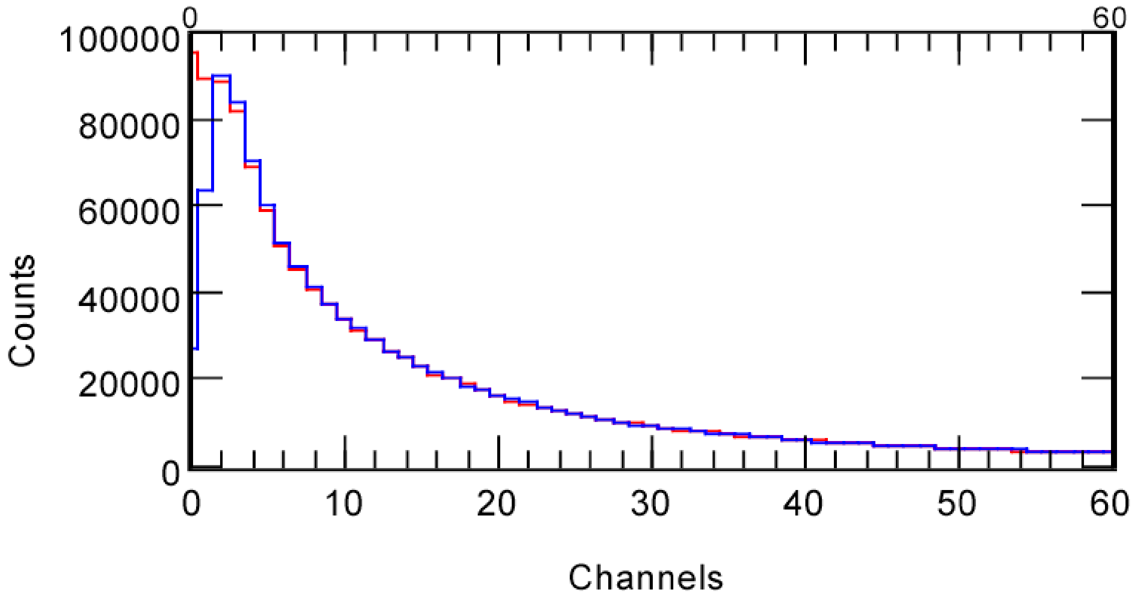

Figure 5.3. Comparison of background pulse height spectra in Front detector for low-energy region for "Front Only" trigger mode (blue curve) versus "OR" trigger mode (red curve)

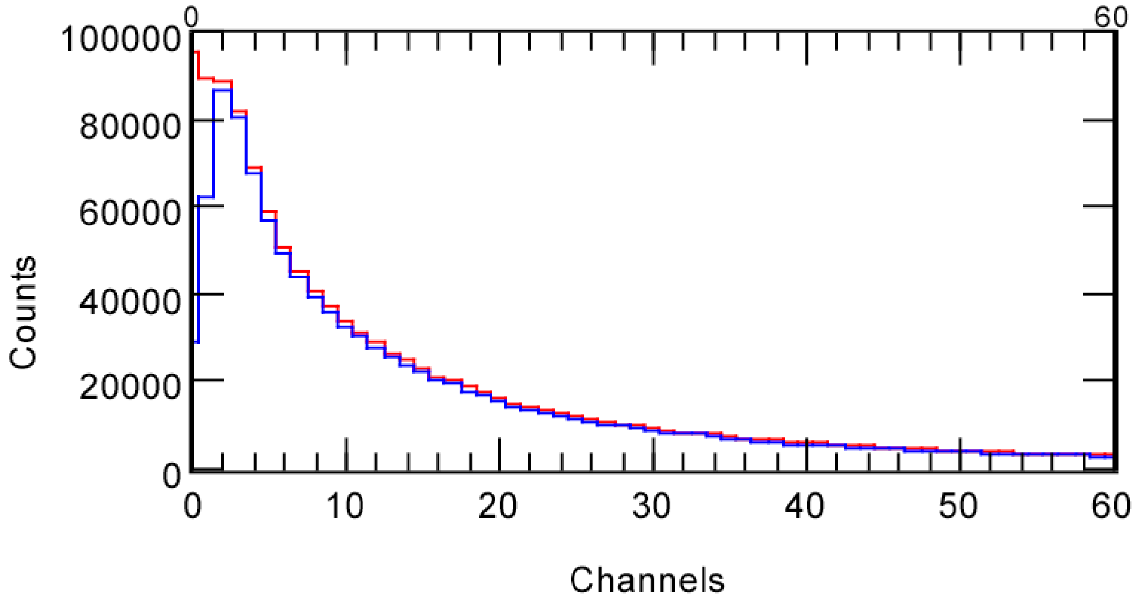

Figure 5.4. Comparison of background pulse height spectra in Front detector for low-energy region for ' "OR" with Anti' trigger mode (blue curve) versus "OR" trigger mode (red curve). All discriminator levels are 50 mV

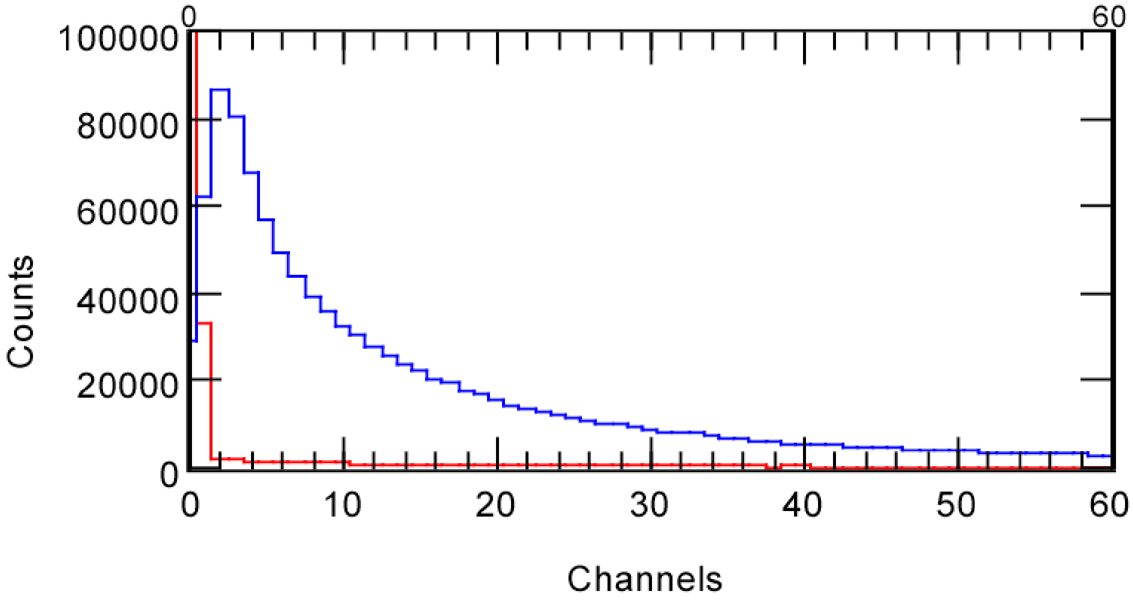

Figure 5.5. **Comparison of background pulse height spectra in Front detector for low-energy region for "Front Only" trigger mode (blue curve) versus "Back Only" trigger mode (red curve). All discriminator levels are 50 mV.**

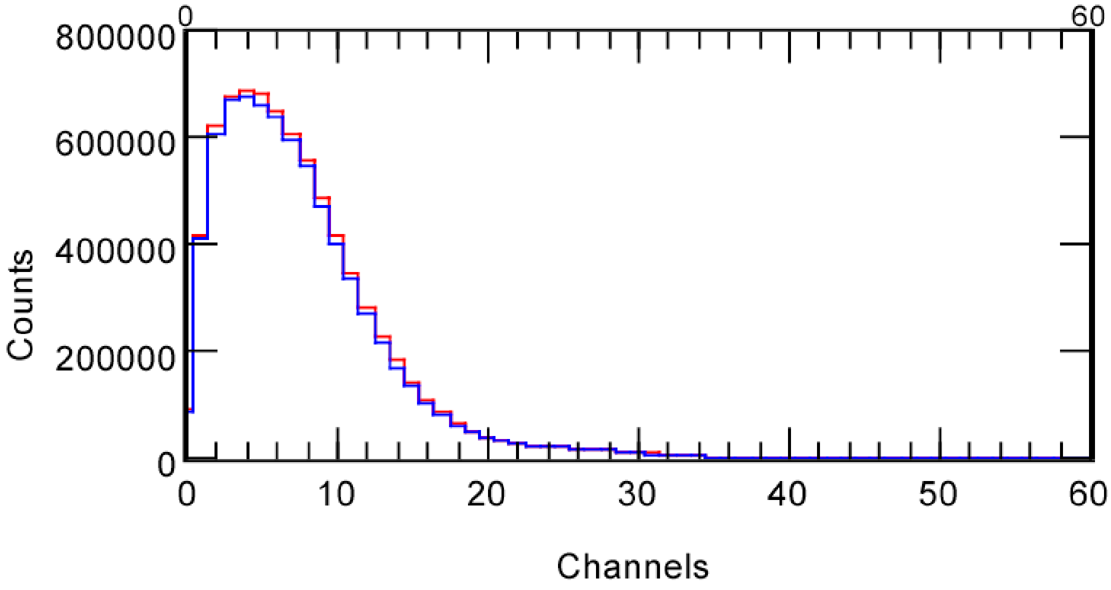

Figure 5.6. **Comparison of ^{57}Co pulse height spectra in Front detector for low-energy region for "Front Only" trigger mode (blue curve) versus "OR" trigger mode (red curve). All discriminator levels are 50 mV.**

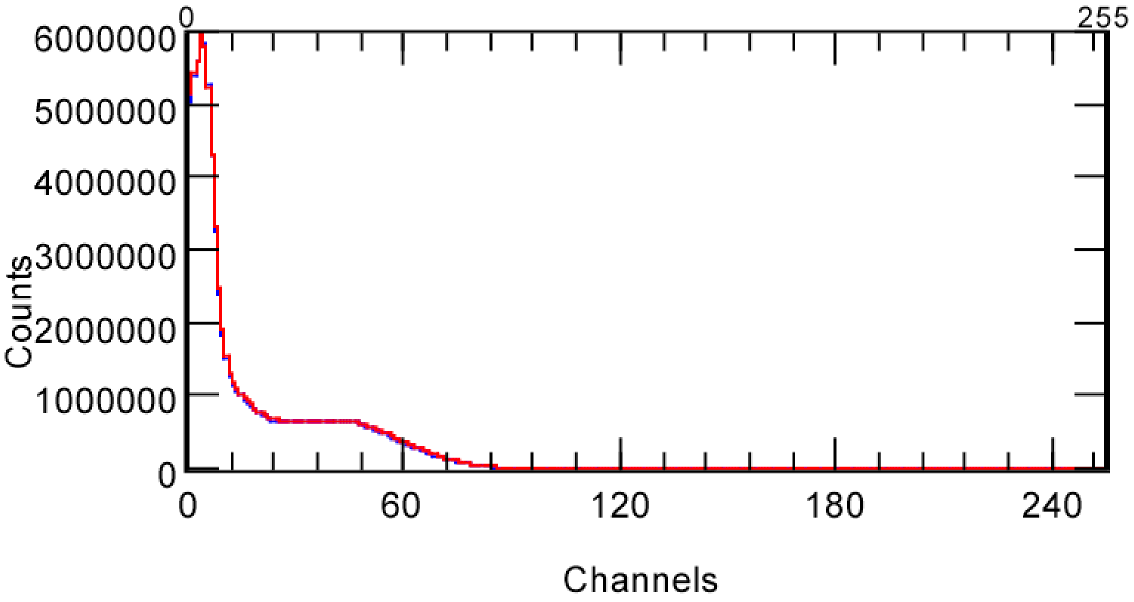

Figure 5.7. **Comparison of ^{133}Ba pulse height spectra in Front detector for full-energy region for "Front Only" trigger mode (blue curve) versus "OR" trigger mode (red curve). All discriminator levels are 50 mV.**

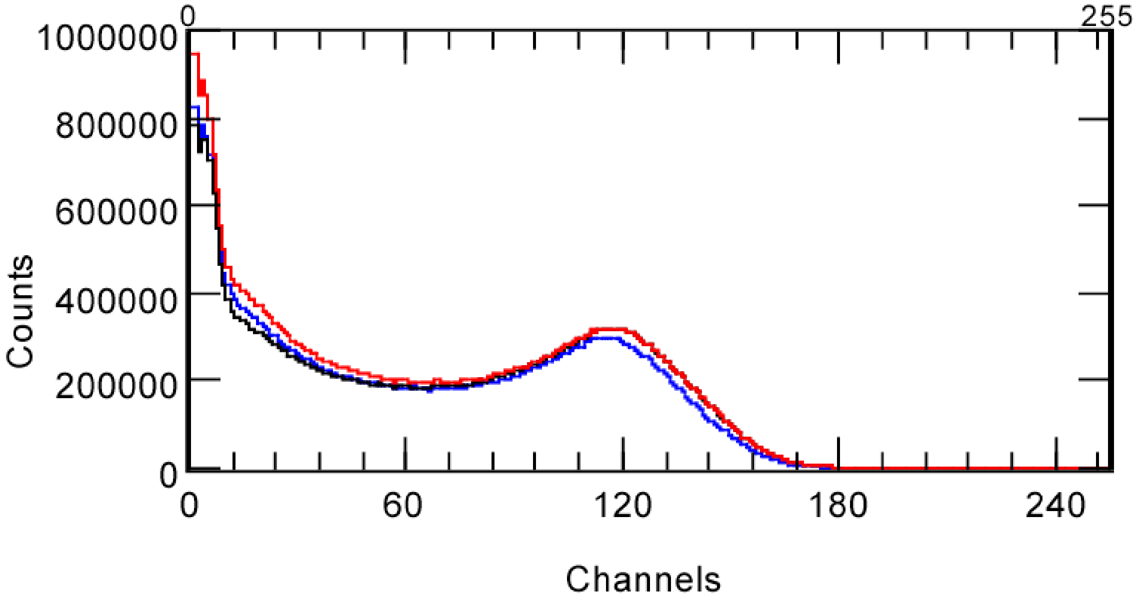

Figure 5.8. **Comparison of ^{137}Cs pulse height spectra in Front detector for full-energy region for "Front Only" trigger mode (blue curve), "OR" trigger mode (red curve), and '"OR" plus Anti' trigger mode (black). All discriminator levels are 50 mV.**

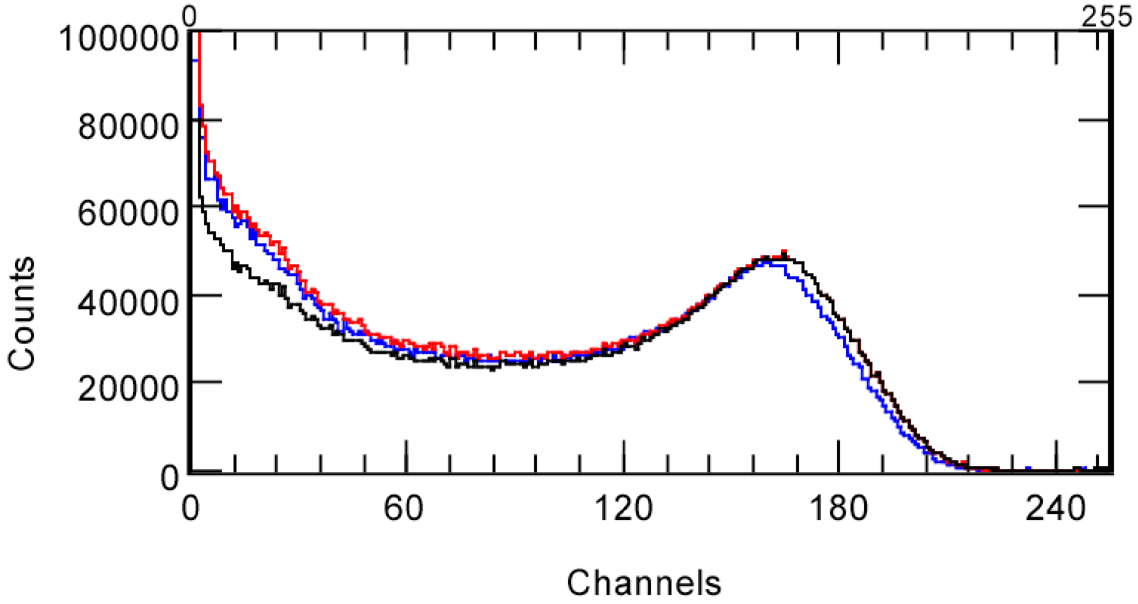

Figure 5.9. Comparison of ^{54}Mn pulse height spectra in Front detector for full-energy region for “Front Only” trigger mode (blue curve), “OR” trigger mode (red curve), and ‘“OR” plus Anti’ trigger mode (black). All discriminator levels are 50 mV.

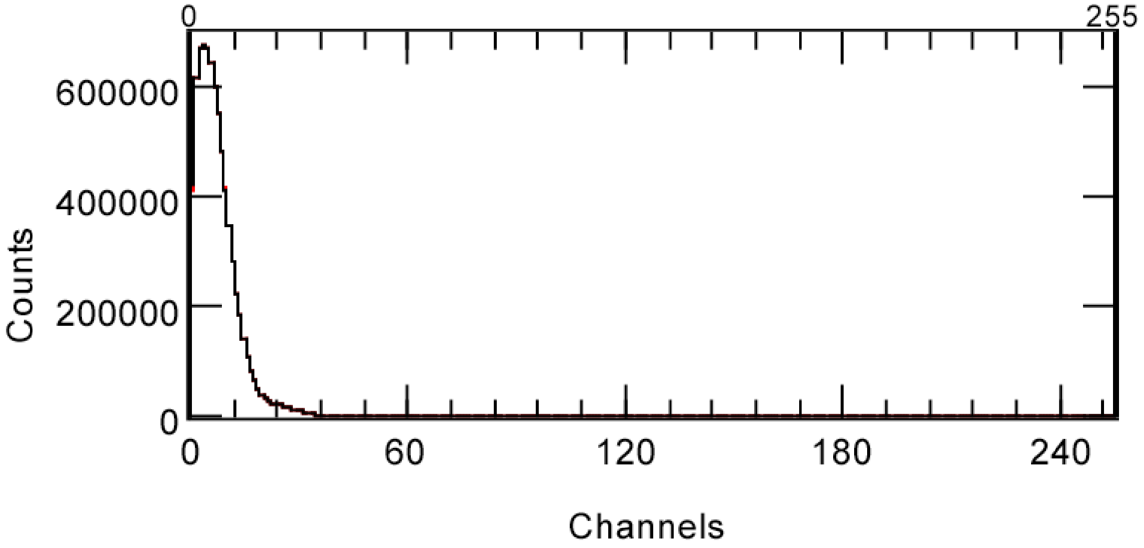

Figure 5.10. Comparison of ^{57}Co pulse height spectra in Front scintillator when triggered by Front or Back signals in “OR” mode (red curve) or by anti-coincidence with Back scintillator in ‘“OR” plus Anti’ mode (black curve). All data taken with discriminator thresholds at 50 mV.

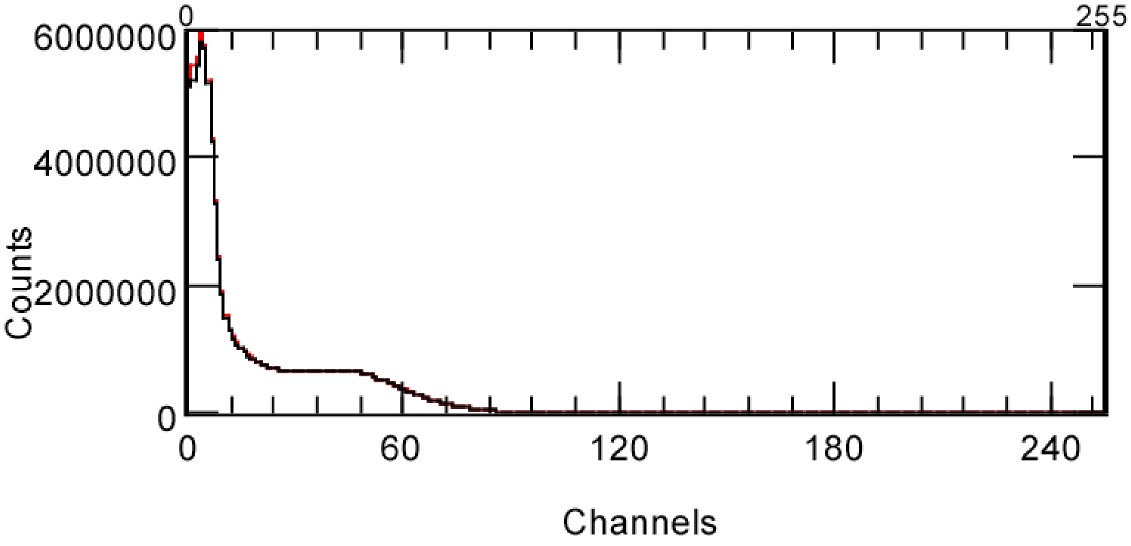

Figure 5.11. Comparison of ^{133}Ba pulse height spectra in Front scintillator when triggered by Front or Back signals in "OR" mode (red curve) or by anti-coincidence with Back scintillator in '"OR" plus Anti' mode (black curve). All data taken with discriminator thresholds at 50 mV.

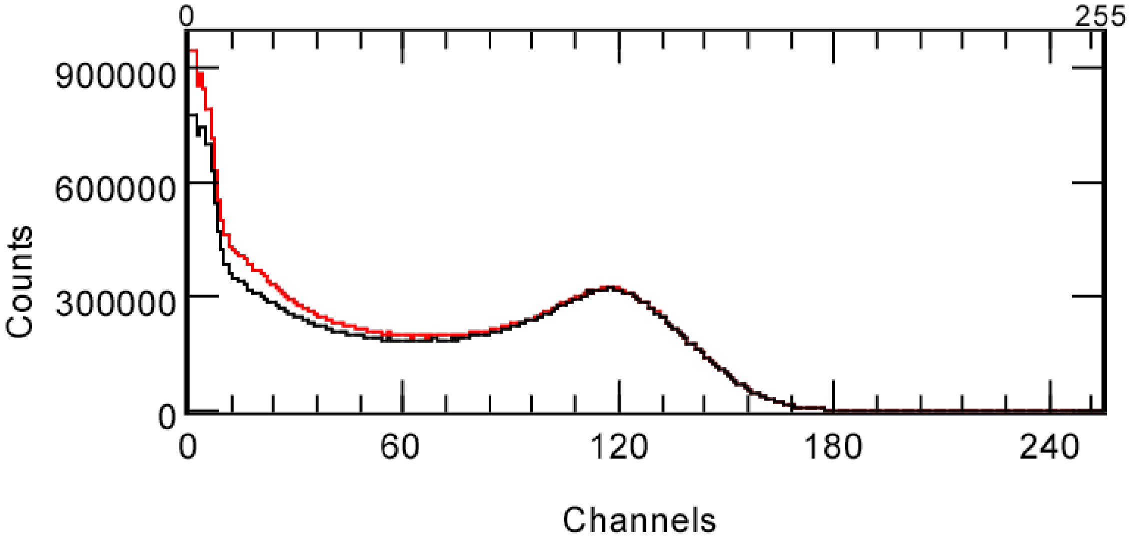

Figure 5.12. Comparison of ^{137}Cs pulse height spectra in Front scintillator when triggered by Front or Back signals in "OR" mode (red curve) or by anti-coincidence with Back scintillator in '"OR" plus Anti' mode (black curve). All data taken with discriminator thresholds at 50 mV.

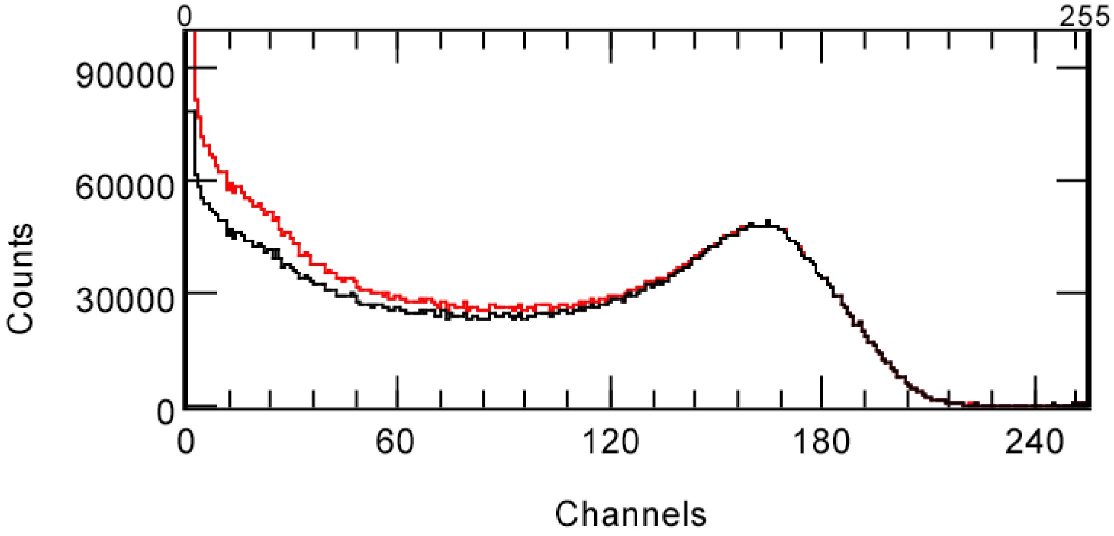

Figure 5.13. **Comparison of ^{54}Mn pulse height spectra in Front scintillator when triggered by Front or Back signals in "OR" mode (red curve) or by anti-coincidence with Back scintillator in '"OR" plus Anti' mode (black curve). All data taken with discriminator thresholds at 50 mV.**

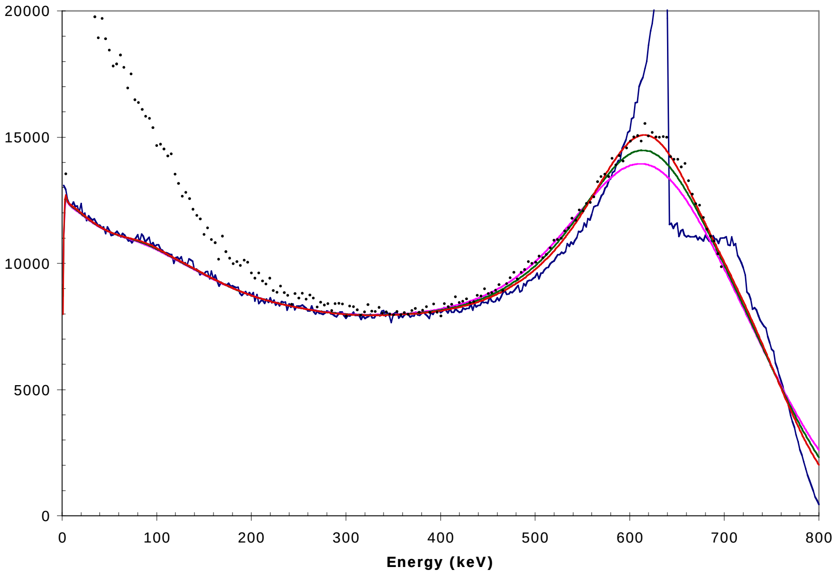

Figure 5.14. **Pulse height spectrum of ^{54}Mn. Blue curve is calculated energy deposition. Red, green, and magenta curves are calculated spectrum after resolution broadening of 25%, 30%, and 35% respectively. Black points are experimental data from "OR" trigger mode normalized to 25% calculated spectrum. All discriminator levels are 50 mV for exp. data. Abscissa is intensity in arbitrary units.**

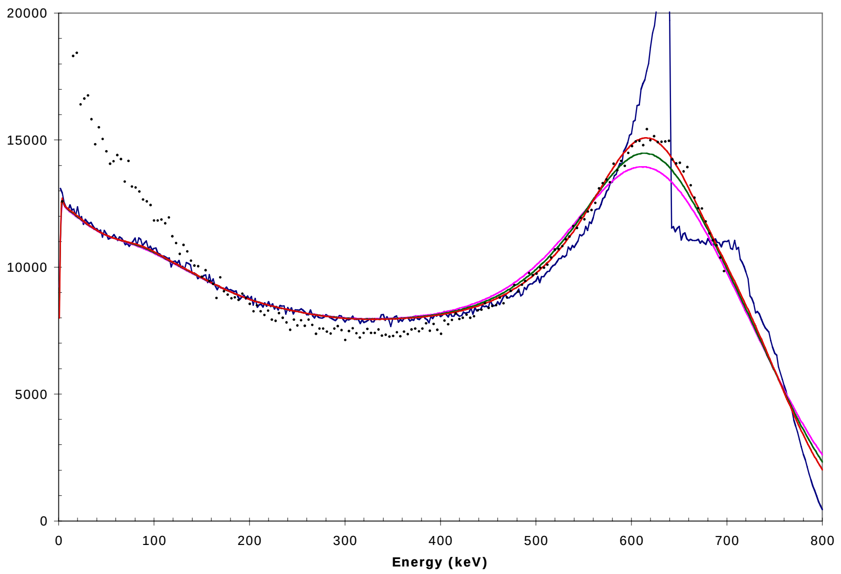

Figure 5.15. **Pulse height spectrum of ^{54}Mn. Blue curve is calculated energy deposition. Red, green, and magenta curves are calculated spectrum after resolution broadening of 25%, 30%, and 35% respectively. Black points are experimental data from '"OR" with Anti' trigger mode normalized to 25% calculated spectrum. All discriminator levels are 50 mV for experimental data. Abscissa is intensity in arbitrary units.**

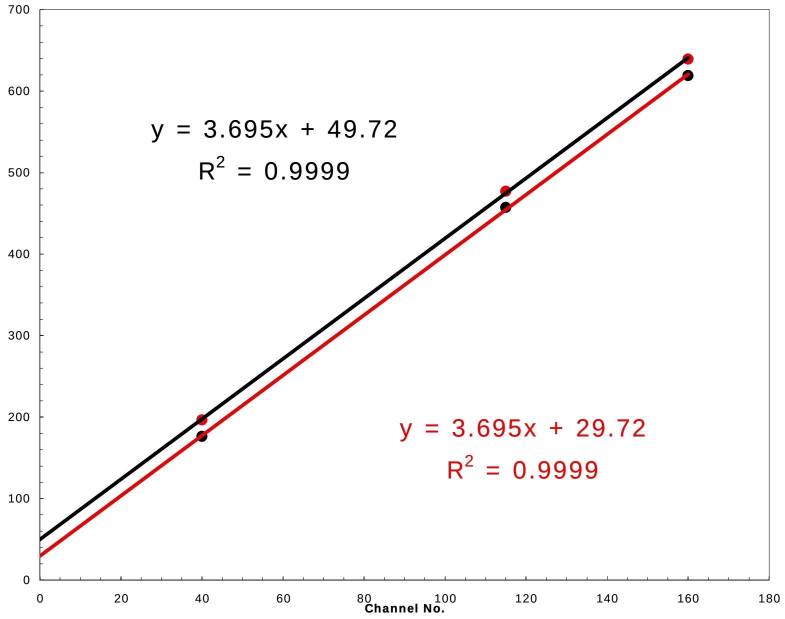

Figure 5.16. **Calibration of pulse height energy (keV) versus channel number assuming peak centroids correspond to maximum Compton electron energy in scintillator (black curve). Red curve has corrected energies based on a 20-keV shift due to resolution broadening.**

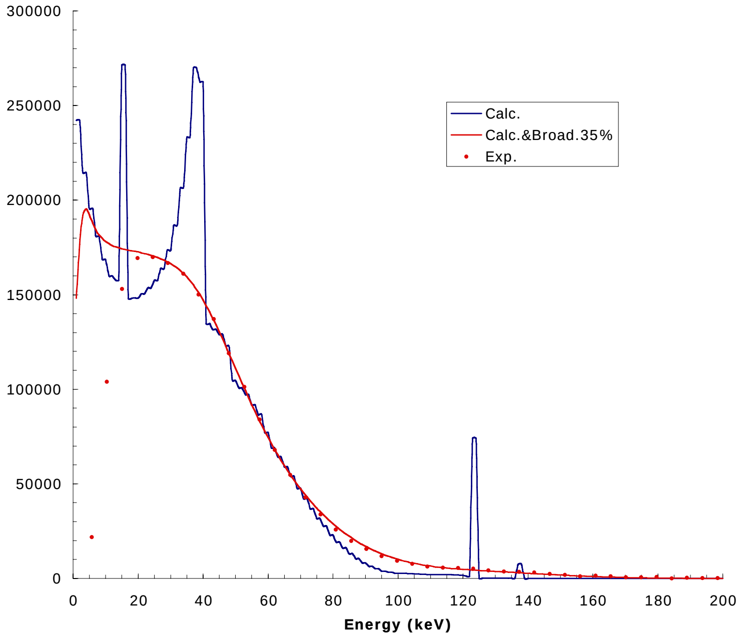

Figure 5.17. **Comparison of calculated and experimental ^{57}Co spectra. Blue curve is calculated energy deposition spectrum. Red curve is resolution-broadened calculated spectrum. Red data points are experimental spectrum normalized and with adjusted energy scale (see text). Abscissa is intensity in arbitrary units.**

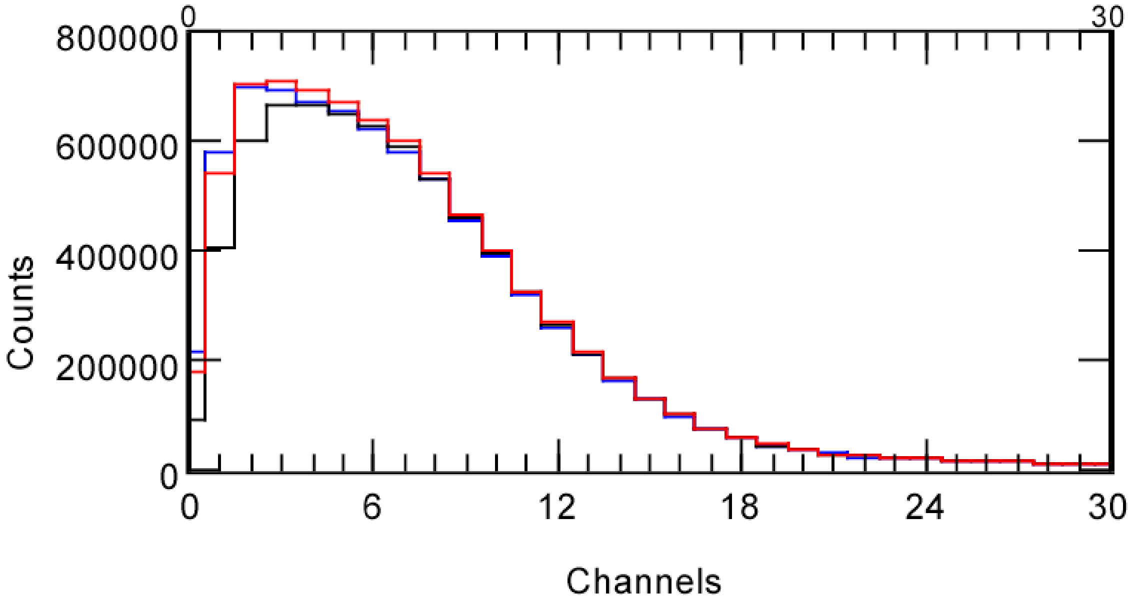

Figure 5.18. **Comparison of ^{57}Co spectra at discriminator levels of 10 mV (blue), 30 mV (red), and 50 mV (black).**

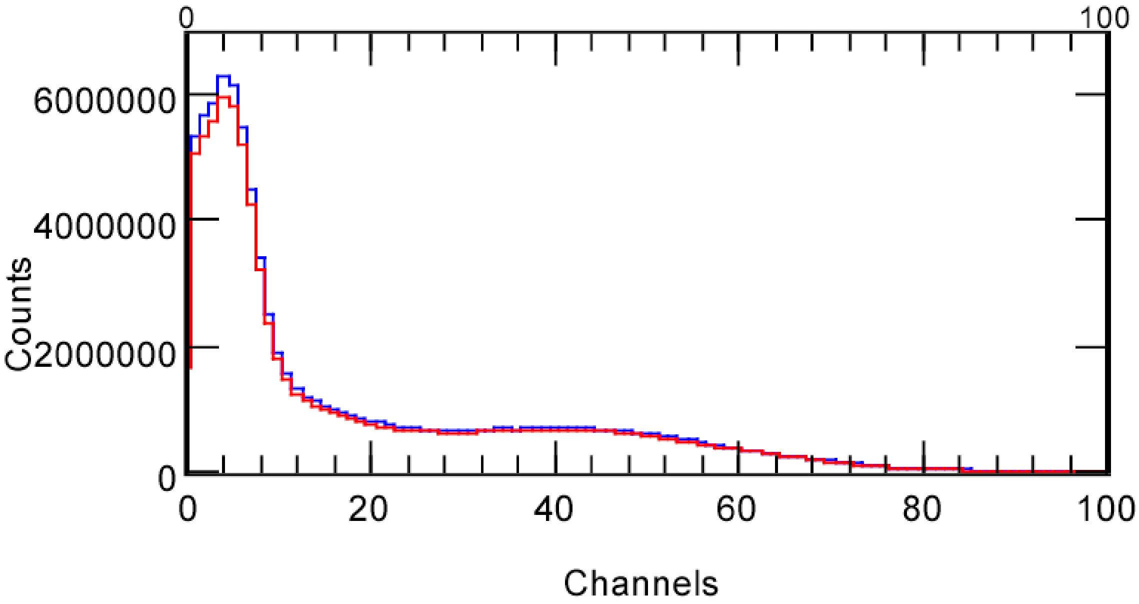

Figure 5.19. Comparison of ^{133}Ba spectra taken with Hardware Veto trigger mode. Blue curve is data taken with list mode acquisition on and a livetime of 0.0757. Red curve is data taken without list mode and a livetime of 0.1891.

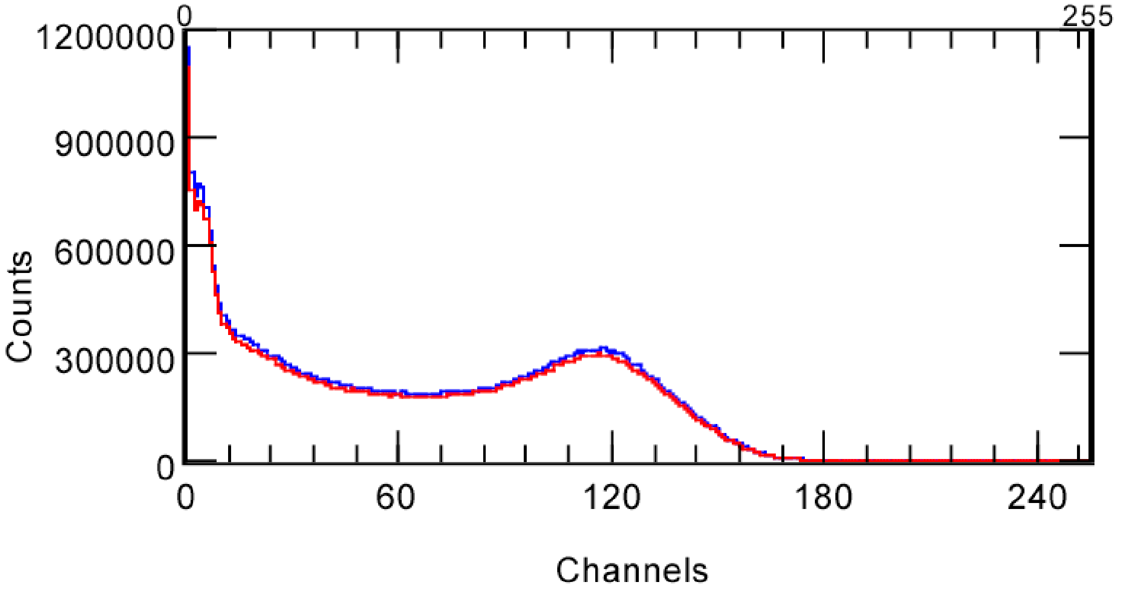

Figure 5.20. Comparison of ^{137}Cs spectra taken with Hardware Veto trigger mode. Blue curve is data taken with list mode acquisition on and a livetime of 0.1465. Red curve is data taken without list mode and a livetime of 0.3173.

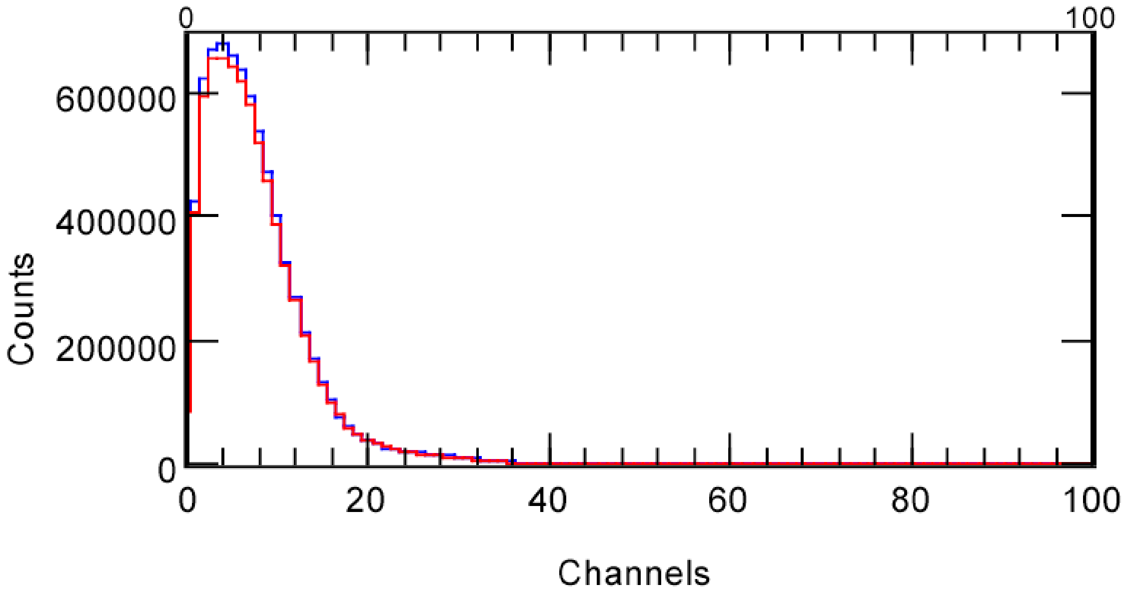

Figure 5.21. Comparison of ^{57}Co spectra taken with Hardware Veto trigger mode. Blue curve is data taken with list mode acquisition on and a livetime of 0.5100. Red curve is data taken without list mode and a livetime of 0..6089.

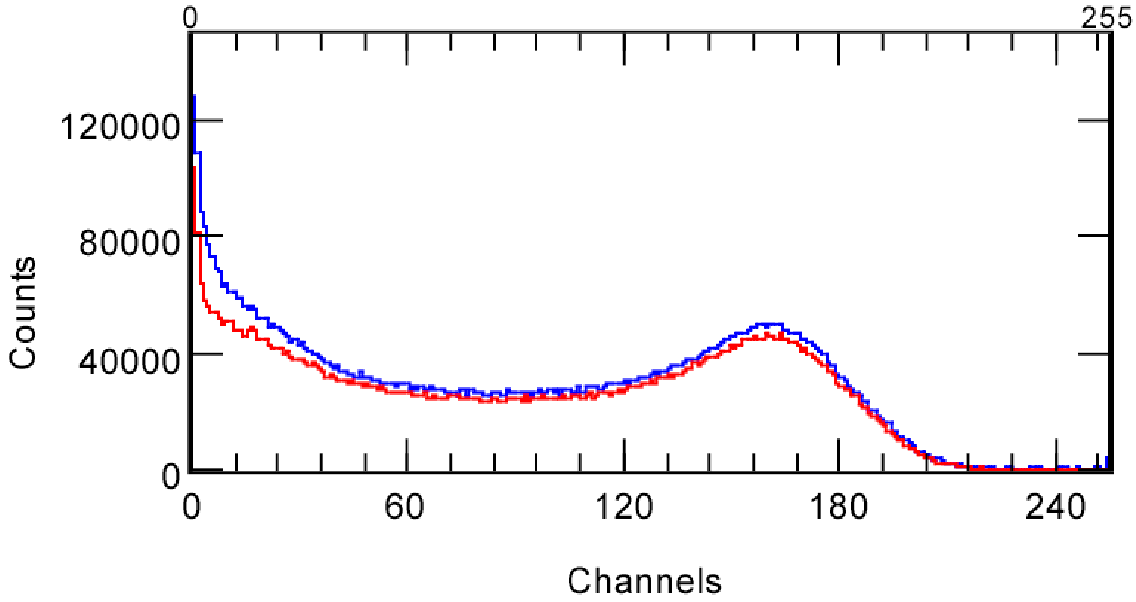

Figure 5.22. Comparison of ^{54}Mn spectra taken with Hardware Veto trigger mode. Blue curve is data taken with list mode acquisition on and a livetime of 0.5321. Red curve is data taken without list mode and a livetime of 0.6232.

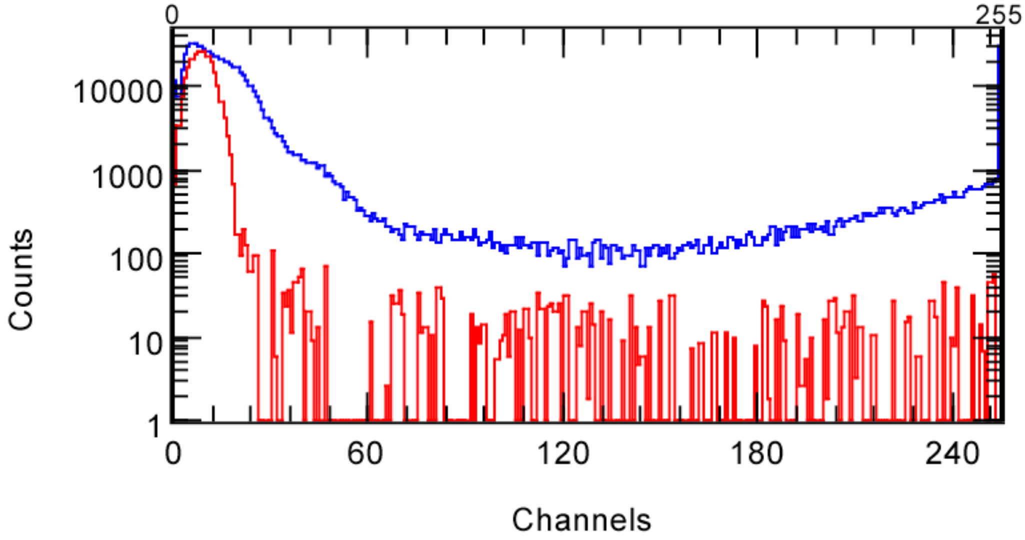

Figure 5.23. Comparison of Cherenkov pulse height spectra in Back detector for Background (blue) and ^{54}Mn (red) when data acquisition triggered only by Back detector. The vertical normalization is purely arbitrary.

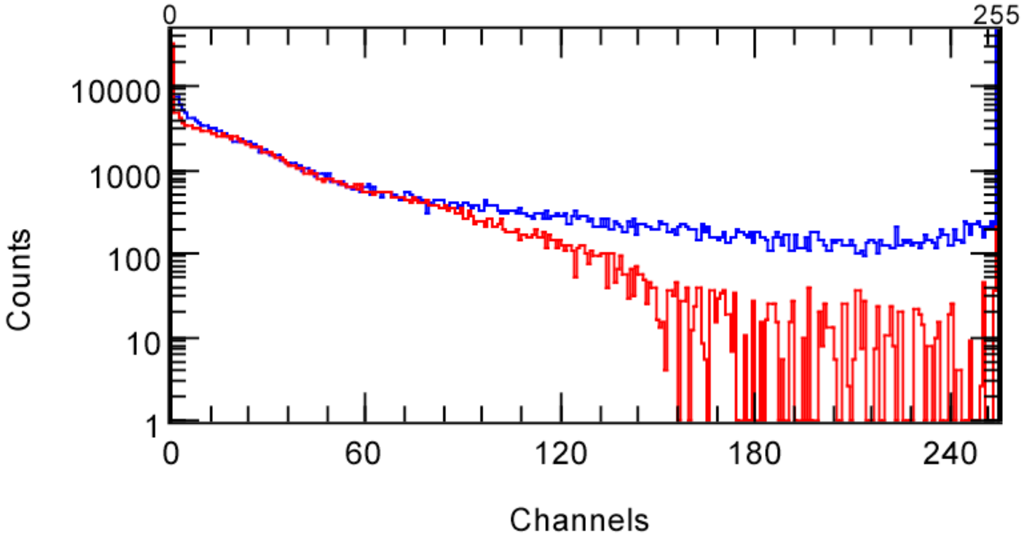

Figure 5.24. Comparison of pulse height spectra in Front detector for Background (blue) and ^{54}Mn (red) when data acquisition was triggered only by Back detector. The vertical normalization is purely arbitrary.

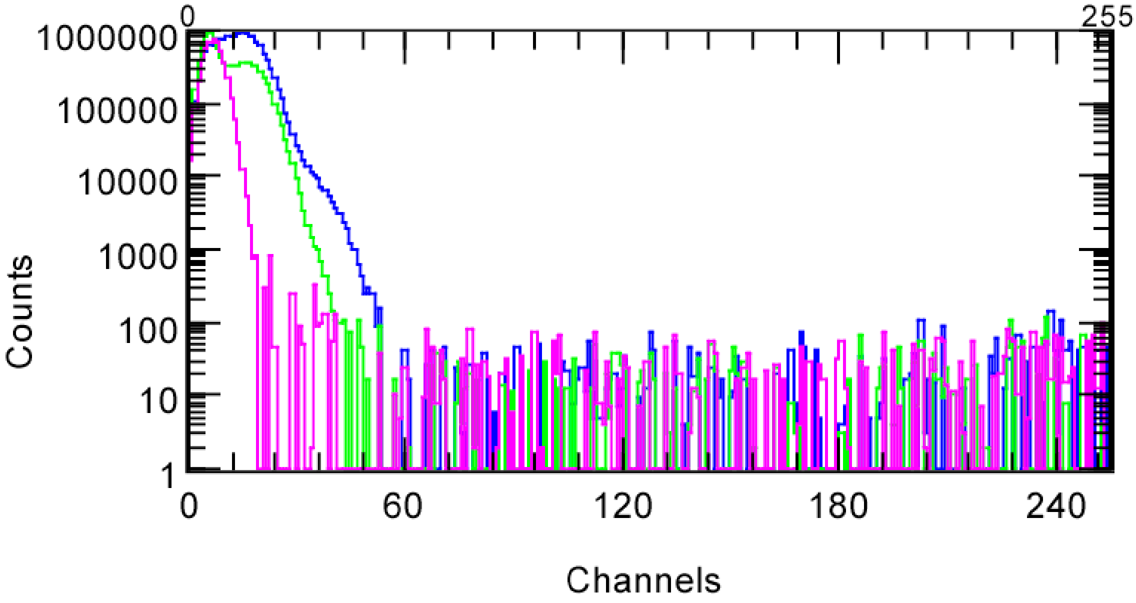

Figure 5.25. **Comparison of Cherenkov pulse height spectra in Back detector for ^{137}Cs (magenta), ^{22}Na (green), and ^{60}Co (blue) when data acquisition was triggered only by Back detector. The vertical normalization is purely arbitrary.**

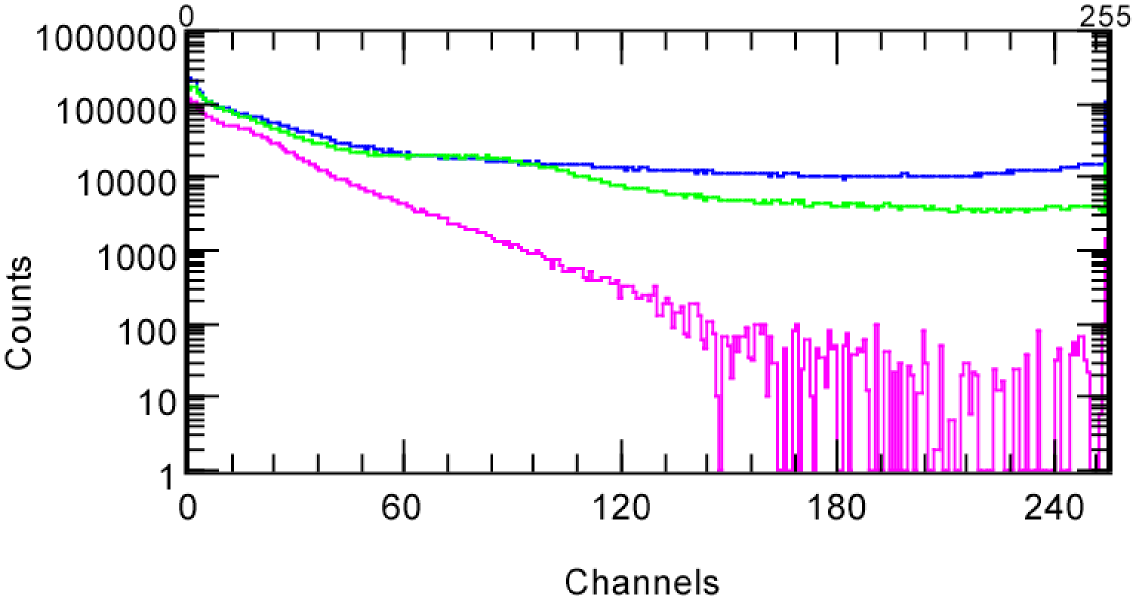

Figure 5.26. **Comparison of pulse height spectra in Front detector for ^{137}Cs (magenta), ^{22}Na (green), and ^{60}Co (blue) when data acquisition was triggered only by Back detector. The vertical normalization is purely arbitrary.**

6.0 Minimum Detectable Activity Analysis

6.1 Introduction

An important radiation detection sensitivity metric is the minimum detectable source activity that a sensor can register in a particular operational scenario, and with a specified level of statistical confidence. Essentially all of the gamma measurements performed with various incarnations of the ALPS sensor consist of point-source calibration exposures performed at relatively small standoff distances, and over relatively long measurement times, that yield spectra of unrealistically high statistical precision compared to the brief drive-by traversals typical of a radiation portal monitor (RPM). The goal of the analysis described in this section is to estimate minimum detectable activity (MDA) of the various ALPS sensor configurations, within a realistic RPM operational context, by drawing upon relevant quantities (such as intrinsic detection efficiency and background rate) extracted from the static-source calibration measurements.

The calibration measurements performed with the Pb-shielded ALPS II sensor and its "CASP" alternative configuration consisted of positioning a gamma source at the center of the front door of the cabinet housing the sensor. The source activities were typical of gamma "check" or "button" sources, i.e. approximately 1 microCi. Measurement times were 300 seconds. Background measurements of 300 second duration were interspersed with the gamma source measurements. The following assumptions were made to compute the MDAs under typical operating conditions for an RPM:

1. The background spectrum accumulated under RPM conditions is assumed to correspond to a 30 second dwell time in which no vehicle traverses the portal.
2. The standoff distance from the gamma source to the front scintillator of the RPM is taken to be 1.52 meters (5 ft), corresponding to one-half the width of a 3.04 meter (10 ft) lane.
3. The drive-by speed is 5 miles/hr, and the solid angle subtended by the sensor is averaged over a portion of the drive-by path. Dwell time assumed for the RPM exposure is specified in an OUO version of this report [Jordan et al. 2007].
4. MDAs are calculated to yield 99% detection probability and 0.1% false alarm probability.

Because spectral information is available from the ALPS II sensor, both spectral and gross-count algorithms were used to determine the MDA. The spectral algorithms for both single-sheet and dual-sheet sensor configurations exploit an "energy windowing" approach to predicting the expected background counts in the low-energy portion of the spectrum. Energy windowing algorithms in general accumulate spectrum counts in two or more bins, or windows, and attempt to characterize ratios of these binned counts for terrestrial background radiation and benign (i.e., naturally-occurring) radioactive sources. Observed count ratios falling outside a specified range of statistical variation are interpreted as indicative of the presence of the threat source of interest. The energy-windowing algorithms applied to the ALPS sensor used two windows only, at "low" and "high" energies, respectively. The count ratio Low/High is first measured under terrestrial background conditions. In an exposure of the sensor to a source of interest (with energy deposition predominantly falling within the low-energy window), the count measurement in the high-energy window, in conjunction with the known Low/High background ratio, yields a prediction of the expected background counts in the low-energy window. An excess of counts above this prediction provides the signature of the presence of the source of interest. In the single-sheet configuration, only the Front scintillator's spectrum contributes to energy windowing and the source-detection algorithm. In the dual-sheet configuration, depending upon the hardware trigger conditions, the Back scintillator spectrum may also contribute to the energy windowing. In particular, the definition of the "high-energy" window can be generalized to include the sum of both Front and Back high-energy counts. The anticipated benefit of this generalized windowing scheme is a more statistically precise measurement of the background Low/High ratio, because two sheets of scintillator contribute to the high-energy window counts. (Note that in hardware "Compton anti-coincidence" data collection modes, in which firing of the Back detector veto's the Front scintillator, this summed-window approach is not applicable. This is true in particular of the CASP configuration of the sensor, in which the Back detector consists of a Cerenkov counter.)

General computational considerations for all MDA algorithms (gross-count and spectral) included the following. To account for assumption (1) above, i.e. 30-second dwell time for "inter-vehicle" background accumulation, the 300 second background spectra recorded in the static measurement sets must be scaled down by a factor of 10. Poisson statistical variations are calculated on the basis of the scaled background counts alone (i.e. scaled background counts, B, are assumed to have standard deviation $\sqrt{B}$), neglecting the small statistical uncertainty on the 300-second background spectrum. To account for the difference in standoff distance between the static source measurements and the RPM assumption, (2) above, the intrinsic detection efficiency, i.e. the detection efficiency for gammas incident on the front scintillator of the ALPS sensor, must be computed from the observed (net) source signal detection rate and the solid angle subtended by the front scintillator. The measured intrinsic detection efficiency is then assumed to be independent of standoff distance and is combined with the calculated solid angle at the assumed RPM half-lane standoff.

An important consideration in quoting the sensitivity of the ALPS sensor is that the rack-mounted, modular electronics and Kmax-based, computer-controlled data acquisition system incorporated in the detector readout is appropriate for laboratory research, but does not permit the optimal data throughput achievable with, for example, dedicated onboard electronics implementing "front-end" pulse processing via, e.g., field programmable gate arrays. The livetime of the ALPS sensor, i.e. the fraction of time in which the sensor's pulse processing electronics and data acquisition system can accept new data from the sensor, was typically 75% to 80% for background measurements (data acquisition rate ~5 to 6 kHz), dropping to as low as 30% to 40% for the highest-rate gamma source measurements (~50 kHz event rate). As noted in other sections of this report, the ALPS livetime is monitored and a correction applied to both source and background measurements in order to determine the sensor's detector-intrinsic, or "hardware", gamma detection rate, i.e. the rate at which the sensor could collect data if outfitted with a zero-deadtime data acquisition system. To account for the best-case scenario of essentially zero-deadtime data collection capability at the terrestrial background counting rate, and to help isolate detector performance effects that are independent of the data collection capability, all MDAs below are reported at two livetime values:

- The background livetime in effect during the laboratory measurement; and
- The 100% livetime limit, representing the best-case scenario with dedicated, optimized electronics.

The deadtime introduced by the source signal at count rates corresponding to calculation of the MDA is assumed to be negligible. This is physically reasonable in the weak-source detection regime relevant to determining the MDA. With this assumption in hand, it is unambiguous to speak of the sensor performance "at" a specified livetime for background data collection.

6.2 Results

The MDA results are summarized below for several configurations of the ALPS sensor:

1. Single-sheet, in which event-trigger definition and pulse-height information was based on the front scintillator only;
2. Dual-sheet, in which both the front and back scintillators participated in the trigger logic and spectral information was extracted from both;
3. CASP, in which the back scintillator sheet of the ALPS was replaced with a Cerenkov slab, which acted as a hardware anti-Compton veto in the trigger definition.

6.2.1 Single-sheet configuration

Table 6.1 and Table 6.2 below display the intrinsic detection efficiencies and (gross-count) background rates for the ^{57}Co and ^{133}Ba source measurements, respectively, as functions of the number of PMTs included in the trigger (and in formation of the energy deposition spectra) and the discrimination threshold. The single-sheet trigger conditions, labeled “multiplicity trigger” in the captions of the tables and figures to follow, correspond to the requirement that the output of at least two PMTs must exceed the pulse-height discriminator threshold. Table 6.3 displays the spectral (i.e., two energy-window) MDA’s for ^{57}Co and ^{133}Ba. Figure 6.1, Figure 6.2, and Figure 6.3 plot, respectively, the terrestrial background rates, ^{57}Co intrinsic efficiency, and the ^{57}Co MDA as functions of the PMT configuration, while Figure 6.4 and Figure 6.5 display the intrinsic efficiency and MDA, respectively, for ^{133}Ba. Note that a similar picture emerges for both source types: Detection sensitivity improves substantially when the number of PMTs is increased from one to two. However, as the number of PMTs is increased beyond two, an increase in detected background rate accompanies the improvement in the intrinsic efficiency. These two competing effects partially cancel one another and yield relatively minor improvement in the MDA as the number of PMTs increases beyond two. Reducing the PMT discrimination threshold produces a similar effect, in that both the background and detection efficiency increase. Thus the MDA is relatively stable against changes in threshold as large as 40%.

Table 6.1 ALPS II single-sheet detection efficiencies and background rates for ^{57}Co measurements, multiplicity trigger.

# PMTs	Threshold (mV)	Intrinsic Efficiency	Background Rate (cps)	Background Livetime (%)
6	50	58.0	5420	84.5
6	30	59.1	5510	84.4
4	50	53.3	5270	85.9
4	30	54.7	5490	85.2
2 (opposite)	50	40.2	4380	87.2
2 (opposite)	30	45.8	4460	86.7
2 (same, bottom)	50	31.4	3810	89.0
2 (same, bottom)	30	34.2	3920	88.7
2 (same, top)	50	46.2	4430	87.3
1	50	46.6	5600	83.0
1	30	48.5	5980	81.6

Table 6.2 ALPS II single-sheet detection efficiencies and background rates for ^{133}Ba measurements, multiplicity trigger.

# PMTs	Threshold (mV)	Intrinsic Efficiency	Background Rate (cps)	Background Livetime (%)
6	50	33.7	5220	86.2
6	30	34.7	5420	84.4
4	50	33.3	5300	85.6
4	30	33.8	5480	85.5
2 (opposite)	50	28.3	4400	87.0
2 (opposite)	30	30.5	4440	87.4
2 (same, bottom)	50	24.7	3830	88.8
2 (same, bottom)	30	25.4	3930	88.9
1	50	30.5	5630	82.6
1	30	31.5	6010	81.4

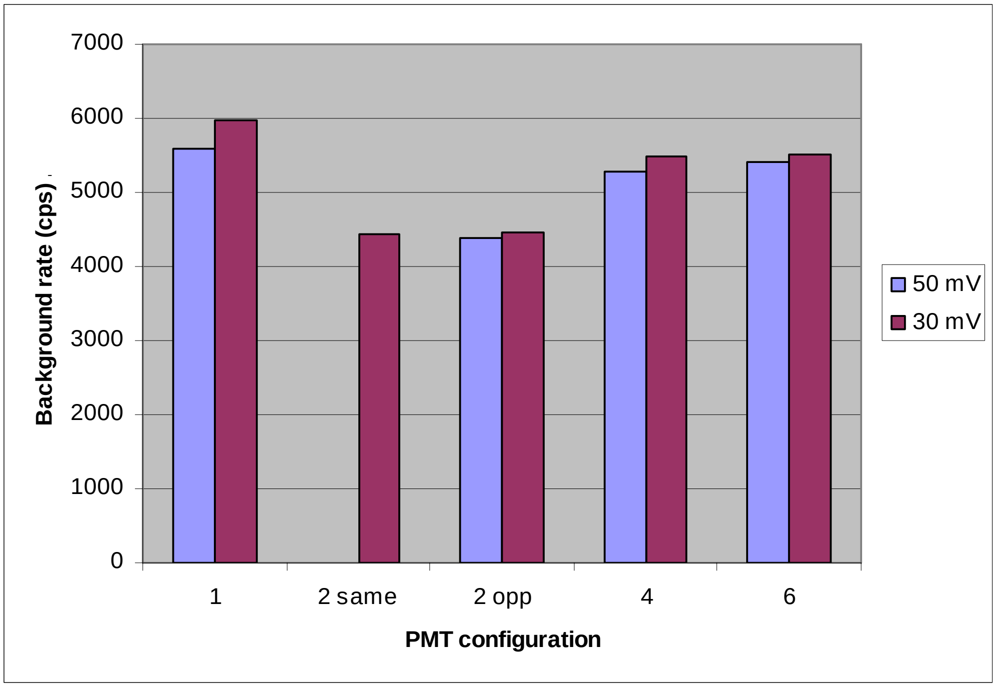

Figure 6.1 ALPS II Single-sheet background rates vs. PMT configuration, multiplicity trigger.

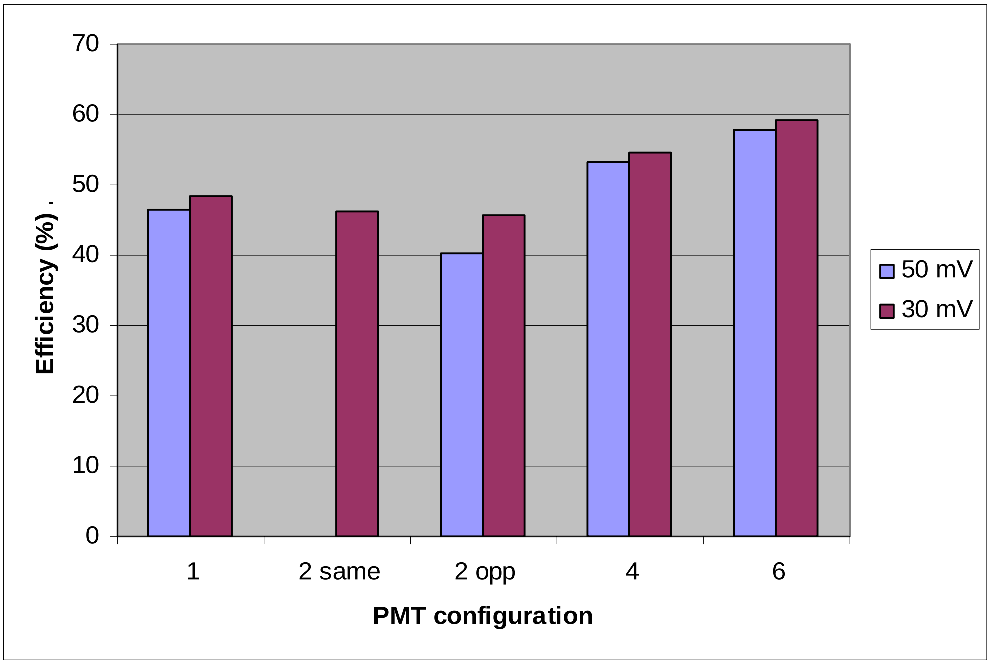

Figure 6.2 ALPS II Single-sheet ^{57}Co intrinsic detection efficiency vs. PMT configuration, multiplicity trigger.

Table 6.3 ALPS II Single-sheet ^{57}Co and ^{133}Ba MDAs, multiplicity trigger, spectral (2 energy-window) background-prediction algorithm, 99% DP, 0.1% FAP. The effect of increasing the data acquisition livetime from its value as measured for terrestrial background with the existing ALPS apparatus (i.e., livetimes as displayed in Table 6.1 above) to 100% is illustrated.

		^{57}Co		^{133}Ba	
# PMTs	Threshold (mV)	MDA at Background Livetime (microCi)	MDA at 100% Livetime Limit (microCi)	MDA at Background Livetime (microCi)	MDA at 100% Livetime Limit (microCi)
6	50	1.35	1.24	1.47	1.37
6	30	1.35	1.24	1.49	1.37
4	50	1.31	1.22	1.49	1.32
4	30	1.34	1.24	1.45	1.34
2 (opposite)	50	1.50	1.40	1.62	1.51
2 (opposite)	30	1.39	1.29	1.52	1.42
2 (same, bottom)	50	1.68	1.58	1.54	1.45
2 (same, bottom)	30	1.59	1.50	1.54	1.45
2 (same, top)	50	1.35	1.26	--	--
1	50	2.36	2.15	2.50	2.27
1	30	2.48	2.24	2.66	2.40

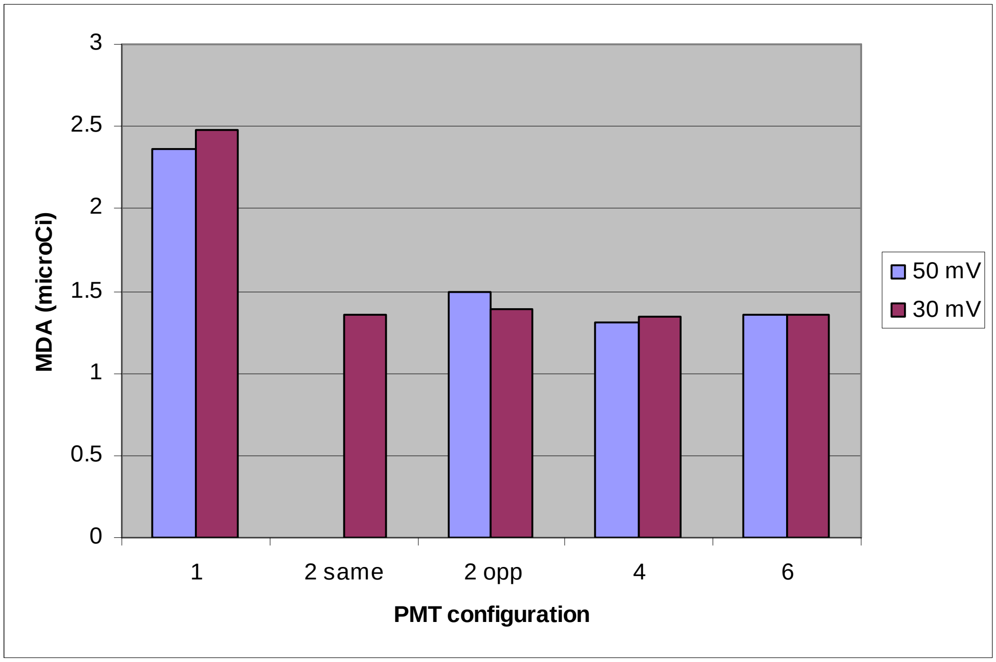

Figure 6.3 ALPS II Single-sheet ^{57}Co MDA vs. PMT configuration, multiplicity trigger. MDAs correspond to background livetimes as measured. Spectral (two energy-window), background-prediction algorithm used for the MDA calculation, 99% DP, 0.1% FAP.

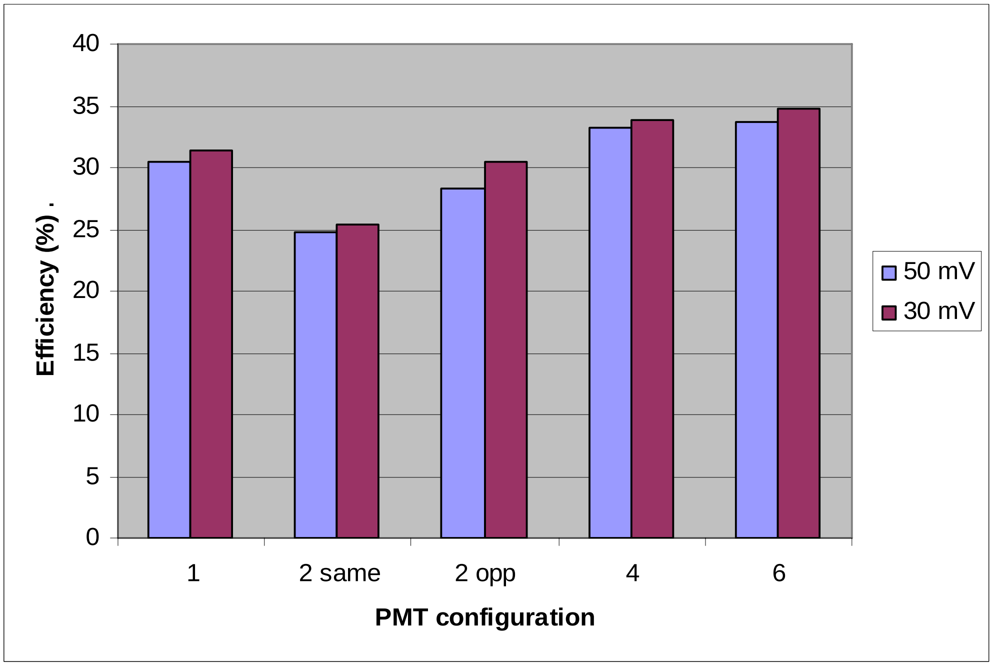

Figure 6.4 ALPS II Single-sheet ^{133}Ba intrinsic detection efficiency vs. PMT configuration, multiplicity trigger.

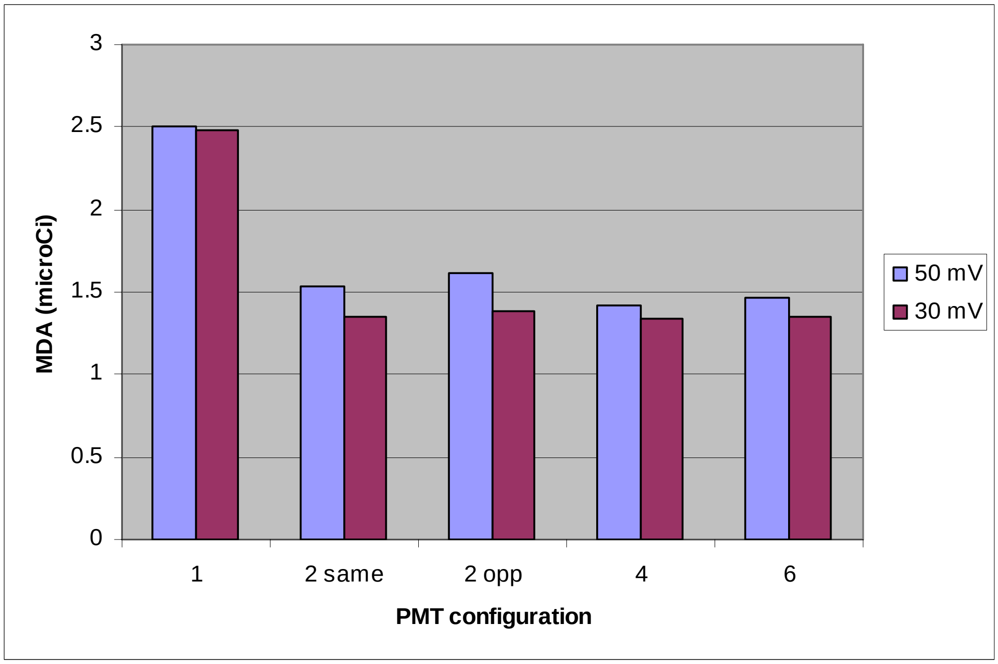

Figure 6.5 ALPS II Single-sheet ^{133}Ba MDA vs. PMT configuration, multiplicity trigger. MDAs correspond to background livetimes as measured. Spectral (two energy-window), background-prediction algorithm used for the MDA calculation, 99% DP, 0.1% FAP.

Table 6.4 below compares results for different single-sheet MDA algorithms. The spectral, or two energy-window, algorithm has been discussed above. The gross-count algorithm applies a traditional Currie equation analysis to the summed counts of the entire Front-sheet pulse-height spectrum. The "narrow-window" algorithm is similar to the gross-count algorithm, but uses only a relatively narrow spectral window containing the source-induced counts. In both the gross-count and narrow-window algorithms, the absolute intensity of the background is assumed to remain unchanged when the sensor is exposed to the source of interest, and thus these algorithms would be applicable only when suppression of terrestrial background by the inspected vehicle can be safely neglected. In contrast, the two-window spectral algorithm does not assume that the overall background intensity remains unchanged during the vehicle traversal, but only that the *shape* of this distribution is unchanged (so that the ratio of low- to high-energy count windows should provide a reliable prediction of the expected count rate in the low-energy portion of the spectrum, in the absence of a true source). Note that the narrow-window algorithm uses essentially the same low-energy window as the 2-window algorithm to capture the source-induced counts, but without attempting to predict the low-energy response on the basis of a high-energy window. This prediction is rendered unnecessary by the assumption of unchanged background intensity during the traversal. The narrow-window algorithm improves on the gross-count algorithm's sensitivity by reducing the size of the source-induced region of interest (ROI) and, thus, the background in this ROI.

Table 6.4 ALPS II Single-sheet ^{57}Co and ^{133}Ba MDAs, multiplicity trigger, 30 mV threshold, for various MDA algorithms, 99% DP, 0.1% FAP. The various algorithms are described in the text.

	^{57}Co MDA (microCi)			^{133}Ba MDA (microCi)		
# PMTs	Spectral (2-window) Algorithm	Narrow-window Algorithm	Gross-count	Spectral (2-window) Algorithm	Narrow-window Algorithm	Gross-count
6	1.35	0.82	1.05	1.49	0.57	0.65
4	1.34	0.86	1.13	1.45	0.58	0.68
2 (opposite)	1.39	0.92	1.21	1.52	0.60	0.66
2 (same)	1.35	0.90	1.19	1.54	0.67	0.74
1	2.48	1.17	1.36	2.66	0.72	0.77

6.2.2 Dual-sheet configurations

The results of the dual-sheet MDA analysis are summarized in Table 6.5 through Table 6.8, which display the ^{57}Co (Tables Table 6.5 Table 6.6) and ^{133}Ba (Table 6.7 Table 6.8) MDAs assuming (1) background livetimes as measured with the existing data acquisition system, and (2) the physical limit of 100% livetime. The entries labeled "ALPS" correspond to the standard dual-PVT scintillator slab configuration of the sensor, and the entries labeled "CASP" correspond to the configuration in which the rear scintillator slab was replaced with a Cherenkov plastic slab. Note that consideration of the dual-sheet results at 100% livetime are particularly important for consistent comparison with the single-sheet results presented in the previous section, because the larger data volume collected in the dual-sheet mode generally yielded smaller livetimes (by as much as one part in eight) relative to single-sheet mode.

As described elsewhere in this report (see sections 4 and 5 above), the dual-sheet measurements were performed under two distinct sets of hardware trigger conditions. In the mode labeled "F OR B", an event was recorded whenever either the front (F) or back (B) detectors fired. Under these trigger conditions, the data acquisition system collected pulse-height information for both F and B detectors. In both online and offline (i.e., list-mode) software analysis of the data stream, the F detector's pulse-height distribution was histogrammed, gated on the condition that the B detector did not fire. Essentially the same spectral (i.e., two energy-window) MDA algorithm previously applied to data collected in single-sheet mode (as outlined in section 6.2.1 above) was applied to this anti-coincidence gated, front-detector spectrum. In addition, the "F OR B" trigger also collected events in which the B detector fired, regardless of whether the F detector fired. (The diagram in Figure 6.6 summarizes the information content of the "F OR B" hardware trigger mode, and the use made of the resulting software-gated spectra.) A dual-sheet version of the spectral MDA algorithm exploits the pulse-height information collected from the B detector, predicting the expected counts in the low-energy portion of the F detector's spectrum on the basis of the measured background ratio $F_L/(F_H + B_H)$, where F and B denote front and back detector counts, respectively, and L and H refer to the low-energy and high-energy windows, respectively. The essence of this approach is that both the F and B detectors sample the high-energy content of the incident gamma flux, and the ratio of this (generalized) high-energy spectrum to the low-energy spectrum in the F detector furnishes the key observable in evaluating statistical significance of the low-energy counts observed in the

F detector. This approach is labeled the "dual-sheet spectral algorithm" in the MDA Tables Table 6.5 through Table 6.8.

In the hardware trigger mode labeled "F AND (~B)," a valid event is recorded only when B does not fire. Thus the anti-coincidence veto is enforced in hardware, and only the front detector's (hardware gated) pulse-height spectrum is available for analysis. In this trigger mode for the two-PVT slab "ALPS" mode, and in the PVT + Cherenkov slab "CASP" mode, the MDA analysis was restricted to application of the same single-sheet, two energy-window algorithm used in the single-sheet analysis of section 6.2.1.

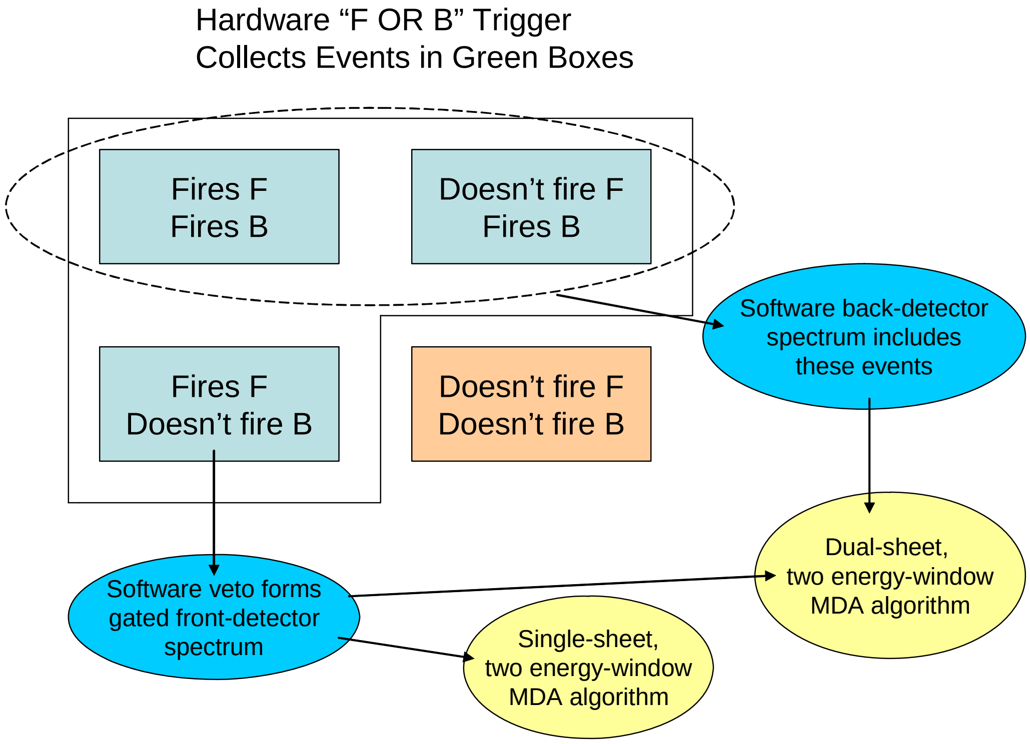

Figure 6.6 Schematic illustration of the relationship of the ALPS dual-sheet event classes collected using the "F OR B" hardware trigger, the pulse-height spectra formed in software, and the use of these spectra in the MDA analysis.

Table 6.5 ALPS II and CASP dual-sheet ^{57}Co MDAs, 50 mV threshold, for various sensor configurations, trigger conditions, and MDA algorithms, 99% DP, 0.1% FAP. The MDAs are quoted assuming as-measured background livetimes.

Configuration	Hardware Trigger Logic	Intrinsic Efficiency (%)	Background Rate (cps)	^{57}Co MDA (microCi)		
				Spectral (2-window) Algorithm	Dual-sheet Spectral Algorithm	Gross-count
ALPS, Pb in	F OR B	54.5	4840	1.41	1.26	1.12
ALPS, Pb in	F AND (~B)	54.2	4800	1.39	--	1.10
ALPS, Pb out	F OR B	48.6	4390	1.59	1.37	1.22
ALPS, Pb out	F AND (~B)	48.4	4440	1.54	--	1.18
CASP	F OR B	56.8	5330	1.45	--	1.13
CASP	F AND (~B)	55.0	5430	1.49	--	1.17

Table 6.6 ALPS II and CASP dual-sheet ^{57}Co MDAs, 50 mV threshold, for various sensor configurations, trigger conditions, and MDA algorithms, 99% DP, 0.1% FAP. The MDAs are quoted assuming 100% background livetime.

Configuration	Hardware Trigger Logic	Intrinsic Efficiency (%)	Background Rate (cps)	^{57}Co MDA (microCi)		
				Spectral (2-window) Algorithm	Dual-sheet Spectral Algorithm	Gross-count
ALPS, Pb in	F OR B	54.5	4840	1.22	1.10	0.98
ALPS, Pb in	F AND (~B)	54.2	4800	1.24	--	0.98
ALPS, Pb out	F OR B	48.6	4390	1.37	1.18	1.05
ALPS, Pb out	F AND (~B)	48.4	4440	1.37	--	1.06
CASP	F OR B	56.8	5330	1.27	--	0.99
CASP	F AND (~B)	55.0	5430	1.31	--	1.03

Table 6.7 ALPS II and CASP dual-sheet ^{133}Ba MDAs, 50 mV threshold, for various sensor configurations, trigger conditions, and MDA algorithms, 99% DP, 0.1% FAP. The MDAs are quoted assuming as-measured background livetimes.

Configuration	Hardware Trigger Logic	Intrinsic Efficiency (%)	Background Rate (cps)	^{133}Ba MDA (microCi)		
				Spectral (2-window) Algorithm	Dual-sheet Spectral Algorithm	Gross-count
ALPS, Pb in	F OR B	32.7	4740	1.57	1.29	0.68
ALPS, Pb in	F AND (~B)	32.3	4800	1.57	--	0.68
ALPS, Pb out	F OR B	27.9	4380	1.78	1.41	0.78
ALPS, Pb out	F AND (~B)	28.5	4430	1.69	--	0.73
CASP	F OR B	35.3	5340	1.56	--	0.67
CASP	F AND (~B)	33.9	5420	1.64	--	0.70

Table 6.8 ALPS II and CASP dual-sheet ^{133}Ba MDAs, 50 mV threshold, for various sensor configurations, trigger conditions, and MDA algorithms, 99% DP, 0.1% FAP. The MDAs are quoted assuming 100% background livetime.

Configuration	Hardware Trigger Logic	Intrinsic Efficiency (%)	Background Rate (cps)	MDA (microCi)		
				Spectral (2-window) Algorithm	Dual-sheet Spectral Algorithm	Gross-count
ALPS, Pb in	F OR B	32.7	4740	1.37	1.13	0.60
ALPS, Pb in	F AND (~B)	32.3	4800	1.40	--	0.61
ALPS, Pb out	F OR B	27.9	4380	1.53	1.21	0.67
ALPS, Pb out	F AND (~B)	28.5	4430	1.52	--	0.66
CASP	F OR B	35.3	5340	1.37	--	0.59
CASP	F AND (~B)	33.9	5420	1.44	--	0.62

In general, the following conclusions may be drawn from the tabulated dual-sheet MDAs:

- The MDAs computed using the standard spectral (two energy-window) algorithm as applied to the software-gated anticoincidence, and hardware-veto anticoincidence, front-detector pulse height spectra agree to better than 5%. This indicates that the impact of the back detector as an anti-Compton veto is “well understood” to the extent that its function in a hardware veto trigger can be replicated in software using the more inclusive “front or back” trigger.
- In neither the ALPS nor the CASP sensor configurations is the low-energy sensitivity substantially improved (relative to the single-PVT sheet mode) by the application of the anti-Compton veto. Comparing “100% livetime” entries in Table 6.3 and Table 6.6, for example, none of the dual-sheet MDAs is a marked improvement on the single-sheet ^{57}Co value of 1.24 μCi.
- The Cherenkov slab is a slightly less effective means of implementing anti-Compton vetoing than the simple (passive) expedient of introducing a Pb absorber between the two PVT sheets of the

standard ALPS II sensor. The least effective approach is the dual-PVT configuration without the Pb absorber. In this case, the substantial drop in intrinsic detection efficiency manifested in the anti-Compton gated front-detector spectrum (relative to the Pb-absorber configuration) strongly suggests that the back detector is "over-vetoing" gamma rays of interest. That is, low-energy incident gammas that deposit a small amount of energy in the front detector and then fire the back detector are more likely to be vetoed without the Pb absorber, resulting in an undesirable drop in the intrinsic detection efficiency for the low-energy source events.

- The use of the back detector's high-energy spectral information to enhance the statistical precision of the expected "low-to-high" energy-window count ratio typically yields about a 10% (^{57}Co) to 18% (^{133}Ba) improvement in detection sensitivity relative to the single-sheet MDA algorithm (as applied to the anti-Compton gated front detector spectrum).

6.3 Discussion: Light collection efficiency and MDA

It is clear from the results presented in section 6.2.1 above that the MDA does not improve linearly with increased PMT coverage. The following simple numerical model can be used to help clarify the limitations of improved light-collection as a means of enhancing low-energy detection sensitivity in a monolithic slab detector. To a very good approximation, the light collection efficiency in a monolithic slab of PVT is proportional to the total photocathode area viewing the scintillator edge, which is in turn proportional to the number of PMTs. The average number of photoelectrons, N_{PE}, produced in a single PMT due to the deposition of energy, ΔE, by a gamma ray interacting in the plastic may be expressed as

$$N_{PE} = \Delta E \varepsilon_{scint} \varepsilon_{coll} \varepsilon_{QE} \quad , \quad (1)$$

where ε_{scint}, ε_{coll}, ε_{QE} are, respectively, the efficiency for generation of scintillation light (in e.g. photons/MeV), the light collection efficiency, and the quantum efficiency of the PMT, respectively. Assuming a fixed threshold on the PMT output (expressed in photoelectrons, or PEs), increasing the total number of scintillation photons collected per unit of energy deposited in the scintillator yields an effective decrease in the system's deposited energy threshold as follows:

$$\frac{\Delta E_2^{thresh}}{\Delta E_1^{thresh}} = \frac{\varepsilon_{coll,1}}{\varepsilon_{coll,2}} \quad , \quad (2)$$

where the indices 1 and 2 refer, respectively, to two different PMT configurations yielding light collection efficiencies $\varepsilon_{coll,1}$ and $\varepsilon_{coll,2}$. In order to achieve this reduction in threshold, a hardware summation of the PMT signal outputs must be performed prior to discriminating the signal. Depending upon the distribution of deposited energy in the scintillator from the gamma source of interest, this effective threshold reduction may produce a substantial increase in the low-energy signal rate. However, this increase in signal rate comes at a price, because an increase in the number of PMTs yields both an increase in the total dark count rate (again, if the PMT signals are ganged prior to discrimination) and an increase in the detection efficiency for ambient gammas. Both of these effects tend to increase the total background rate observed in the system and partially cancel the improvement in detection sensitivity that would otherwise accompany the increased signal rate. Because the MDA of the system for a fixed observation time, t, scales roughly as follows,

$$\mathbf{MDA} \propto \frac{\sqrt{\mathbf{Bt}}}{\varepsilon_{\mathbf{detect}}\mathbf{t}}, \quad (3)$$

where B is the total background rate and $\varepsilon_{\mathbf{detect}}$ is the overall detection efficiency for the source gammas of interest, the effect of an increase in PMT coverage on the detection sensitivity depends upon the detailed behavior of B and $\varepsilon_{\mathbf{detect}}$ with increasing light collection efficiency. Given a fixed energy deposited in the scintillator by a source gamma of interest, three detection regimes can be identified, depending upon the relationship in the original portal system of the mean number of PEs (which, in turn, are proportional to the deposited gamma energy via Eq. 1 to the pulse-discrimination threshold:

1) $\mathbf{N_{PE}} >> \mathbf{N_{PE}^{thresh}}$: In this case, the gamma detection efficiency of the original system is already saturated (i.e., dominated by the interaction of the incident gamma-ray with the scintillator, rather than the efficiency of scintillation light collection), and an increase in light collection efficiency yields little increase in the total signal rate at fixed energy deposition. An increase in PMT coverage will tend to increase the background rate and can actually decrease the portal sensitivity.
2) $\mathbf{N_{PE}} < \mathbf{N_{PE}^{thresh}}$: The sensitivity of the original system to the deposited energy is essentially zero in this case (i.e. infinite MDA), so that an increase in the light collection efficiency can "push" the mean number of PEs over the threshold. The improvement in signal detection thus dominates the increase in background, and an increase in PMT coverage will tend to eliminate "blindness" to the gamma energy deposition.
3) $\mathbf{N_{PE}} \approx \mathbf{N_{PE}^{thresh}}$: The original system is partially responsive to the deposited energy, and an improvement in light collection efficiency will increase both B and $\varepsilon_{\mathbf{detect}}$ in (Eq. 3). Assuming that the total background rate (dark current plus ambient gamma background rate) is proportional to the number of PMTs, then it is clear from Eq. 3 that $\varepsilon_{\mathbf{detect}}$ must increase at least as fast as the square root of the number of PMTs in order to yield a net improvement in the MDA. In the extreme case that the signal detection efficiency also varies linearly with the number of PMTs (unlikely if the original discriminator threshold is close to 1 PE), then the MDA would improve roughly as the reciprocal square-root of the number of PMTs This extreme provides a useful upper bound on the possible improvement.

Throughout this discussion, it has been assumed that a hardware sum of the PMT outputs (e.g., passive "ganging" of outputs) is performed prior to discrimination. Alternatively, the set of PMT signals can be discriminated individually, and the resulting logic pulses subjected to an appropriate multiple-PMT coincidence requirement. The advantage of this scheme is that the dark current contribution to the multiple-PMT background can be essentially eliminated, because the dark currents in different PMTs are uncorrelated in time. However, any multi-PMT coincidence requirement typically reduces the signal detection efficiency relative to that obtainable in the hardware-sum scheme (assuming fixed discriminator thresholds in the two schemes). Whether an improvement in MDA is possible with a coincidence scheme then depends on the contribution of the dark current to the background singles rate in each PMT. In the limit of zero dark current, and assuming regime (3) for the original PE collection above, imposing a coincidence requirement simply reduces the ambient gamma background detection efficiency and the signal detection efficiency by roughly the same factor, resulting in decreased sensitivity (i.e., an increased MDA). On the other hand, if dark currents constitute a significant portion of the background signals rate, it is difficult to exclude *a priori* the possibility of improved sensitivity with an appropriate coincidence trigger.

7.0 Pb-Loaded Scintillator Experiments

7.1 Abstract

Attenuation lengths of scintillation light in normal plastic scintillator (Bicron/St. Gobain BC-408) and 5% lead-loaded scintillator (BC-452) were measured using gamma radiation sources. Relative efficiencies of various gamma sources were also measured. We conclude that the shorter attenuation length and lower light output of the lead-loaded scintillator makes it unsuitable for large volume scintillators for use in radiation portal monitors.

7.2 Introduction

It has been proposed that lead-loaded plastic scintillators might have much higher efficiency for low-energy gamma rays of concern in radiation portal monitors. The higher efficiency arises from the possibility of higher interaction probabilities for photoelectron production because of the presence of lead in the scintillator. Unfortunately, lead-loaded scintillators tend to absorb or scatter scintillation light, leading to short attenuation lengths and smaller pulse height amplitudes. The work described in this section was initiated to determine experimentally whether lead-loaded scintillators would be advantageous for use in large-area scintillators required for portal monitors.

Large area lead-loaded scintillators are not available in flat sheets that are normally used in radiation portal monitors. Cylindrical rods of lead-loaded scintillator are available commercially only up to diameters of 5.08 cm. We attempted to purchase cylindrical rods 50.8-cm long by 5.08-cm diameter with lead loadings of 1%, 5%, and 10%. However, the vendor was only able to supply a rod with 5% lead loading (BC-452). Attempts to produce the 1% and 10% loadings resulted in scintillators that were yellow colored indicating poor light transmission. For comparison purposes we purchased a normal plastic scintillator rod (BC-408) with the same dimensions.

7.3 Experimental

The scintillators were mounted in a light-tight black box and coupled to 5.08-cm diameter photomultiplier tubes (PMTs) on each end (Hamamatsu - model R329-02 PMT, model E5859-01 tube base). The high voltages on the PMTs were adjusted to give pulse height spectra with equal gains from each tube. Signals from the PMTs were sent to a NIM module fan-out (Phillips PS748). One signal from the fan-out was delayed using an Ortec DB463 delay box and sent to an input of CAMAC-based Phillips 7166 Charge to Digital Converter (QDC). Another fan-out signal was sent to a Phillips PS730 discriminator. The discriminator outputs for each PMT were then sent to an Ortec CO4020 logic unit operating in coincidence mode. The coincidence output was stretched and used as the gate for the PS7166 QDC. The coincidence output was also used to block the inputs of the discriminator for 1.7 μs until the signals had been fully processed by the data acquisition system. The outputs of the QDC are channel numbers representing the integrated charge associated with each event. The data acquisition system included a Hytec LP1342 list processor that stored the channel numbers from both PMTs in a buffer memory. When the memory was full, the data were transferred to the computer in a block memory transfer. This buffer memory allows data acquisition rates of about 10,000 events per sec with minimal dead time.

While the CAMAC hardware was acquiring new data, the data acquisition software processed the previous data into histograms showing the pulse height distributions for pulses in the left PMT, the right PMT, and a two-dimensional display of left PMT pulse heights versus right PMT pulse heights. In addition, the software calculated the sum of the two pulse heights and the geometric mean of the two pulse heights for storage in histograms giving the average pulse height and the mean pulse height. Previous work with large scintillators has shown that the mean pulse height distribution gives slightly better resolution than the sum pulse height. Because of the coincidence requirement for gating the QDC, pulse height data were obtained only for coincidence events.

7.3.1 Attenuation Length

The procedure for measuring the attenuation length involved use of a gamma source mounted on a 5.08-cm thick lead brick having a 1.9-cm diameter hole for collimation. The scintillator was mounted inside the light-tight box close to an outer wall. The source and collimator were mounted outside the box but could be aligned with fiducial marks indicating the location along the axis of the scintillator cylinder. The source was about 16 cm from the surface of the scintillator. Most measurements of attenuation length were made by taking measurements at 5.08-cm intervals along the axis of the cylinder over the range from –20.3 cm to +20.3 cm relative to the midpoint of the cylinder. Data were obtained for bare scintillators and for the scintillators wrapped in 3 layers of Teflon tape.

Three methods were used for analysis of the attenuation length. The preferred method is to plot the location of a distinctive peak in the pulse height spectrum of a single PMT as a function of the location of the source along the axis. Plastic scintillators do not give a distinctive photopeak corresponding to the full energy of the gamma ray. However, monoenergetic gamma rays give a broad peak corresponding to the Compton edge (the maximum energy given to a recoiling electron by a gamma ray scattering at 180 degrees off an electron). In the present work, the peak due to the Compton edge from a ^{54}Mn source could be followed as a function of location only with the BC-408 scintillator. Examples of ^{54}Mn spectra in the Left PMT are given in Figure 7.1. Similar results were obtained with a ^{137}Cs source. Lower energy sources or sources with multiple gammas did not give observable peaks. No peaks were seen in the BC-452 scintillator. Examples of the resulting attenuation curves are given in Figure 7.2 for the no-wrapped BC-408 scintillator with the ^{54}Mn source.

A second method of analysis was to calculate the mean value of the pulse height distribution of a single PMT as a function of location along the axis of the scintillator. This method was compared to the results of the first method for the ^{54}Mn and ^{137}Cs sources in BC-408. The results were generally the same indicating that the mean value of the distribution could be used for those cases where no peak was seen in the pulse height spectra.

The third method was used only with the ^{109}Cd source that has a dominant low-energy gamma ray (88 keV). Because the pulse height spectrum clusters close to the region just above the discriminator, it was hoped that the shift of the pulse height spectrum to lower amplitudes as the source was moved farther from a given PMT would give a representation of the light attenuation. Instead of integrating the number of pulses above the threshold in the pulse height spectrum, we simply recorded the number of counts above the discriminator in scalers that were independent of the coincidence requirement. This technique confirmed that the attenuation length was large for BC-408 and small for BC-452 but the detailed results seemed to depend on the high voltage applied to the PMTs and seemed too erratic to be depended upon.

For each method of analysis the results were plotted as a function of the location of the source. An exponential function was fitted to the data points. The attenuation length was the reciprocal of the coefficient in the exponent for the fitted curve. Most of the fits had R^2 values of >0.9 although a few fits had R^2 values as low as 0.5.

7.3.2 Relative Efficiency

Relative efficiencies of the BC-408 and BC-452 scintillators were obtained by measuring the count rates of various sources located at the midpoint along the axis of the scintillators. No collimation was used. The sources were at a distance of about 16 cm from the surface of the cylinders so a broad region of the scintillator was illuminated but it was not uniformly distributed. The sources used were ^{109}Cd, ^{241}Am, ^{57}Co, ^{133}Ba, ^{137}Cs, ^{54}Mn, and ^{60}Co with weighted average energies ranging from 27- to 1253-keV. Efficiencies were calculated for the Left PMT and Right PMT in singles mode and for the PMTs in coincidence. All sources were 10 μCi except for the ^{137}Cs source which was 1 μCi and the ^{241}Am source which was 100 μCi. Sources were decay corrected to the date of the measurements. For sources with multiple gamma rays and/or prominent X-rays, a weighted average energy was used when plotting efficiency versus energy. The total gamma emission rate for all gammas was used for the source strength so the reported efficiencies represent the efficiency for detecting one gamma at the weighted average energy. No correction has been made for the solid angle of the source-to-detector geometry, but this was constant for all sources.

7.4 Results and Discussion

7.4.1 Attenuation Length

The results of the attenuation length measurements are given in Table 7.1. In general we expect the attenuation length should be independent of which PMT data was used for the measurement. The fact that this assumption is not always observed in the present data is an indication of the accuracy of the measurements. Because measurements were made with different analysis techniques, high voltages, wrapping conditions and scintillator types, we will examine each of these effects in the discussion below.

Table 7.1. Attenuation lengths for various conditions of scintillator type, wrapping, PMT high voltages, and measurement technique

Exp. I.D.	Source	Scintillator	Wrapping	Runs	Left HV	Right HV	Technique	Attenuation Length Left PMT (cm)	Attenuation Length Right PMT (cm)	Mean Pulse Height Channel Left PMT at -8 in.	Mean Pulse Height Channel Right PMT at +8 in.	Notes
A	^{54}Mn	BC408	No Wrap	505-528	-1640	-1600	Peak Centroid	278	270			
B			No Wrap	505-528	-1640	-1600	Mean Channel	217	270	95.8	78.9	
C			No Wrap	753-761	-1566	-1545	Peak Centroid	125	147			
D			No Wrap	753-761	-1566	-1545	Mean Channel	141	143	89.6	98.4	
E			Wrap	729-737	-1566	-1545	Peak Centroid	70	78			[a]
F			Wrap	729-737	-1566	-1545	Mean Channel	97	154	156.7	161.7	[b]
G		BC452	No Wrap	545-564	-1640	-1650	Mean Channel	29	30	50.3	51.8	
H			No Wrap	718-726	-1645	-1549	Mean Channel	26	27	74.2	55.7	
I			Wrap	708-716	-1645	-1548	Mean Channel	22	24	86.5	62.5	
J	^{137}Cs	BC408	No Wrap	776-784	-1566	-1545	Peak Centroid	256	217			
K			No Wrap	776-784	-1566	-1545	Mean Channel	159	154	59.6	69.5	
L			Wrap	739-747	-1566	-1545	Peak Centroid	69	94			
M			Wrap	739-747	-1566	-1545	Mean Channel	72	100	128.5	135.5	
N	^{109}Cd	BC408	No Wrap	764-773	-1566	-1544	Scaler Counts	625	400			
O			Wrap	748-750	-1566	-1545	Scaler Counts	455	455			
P												
Q		BC452	No Wrap	5/20/05	-1650	-1650	Scaler Counts	32	36			
R			No Wrap	606-626	-1695	-1653	Scaler Counts	588	-714			[c]
S			Wrap	694-702	-1645	-1548	Scaler Counts	66	11			[d]
T			Wrap	704-706	-1645	-1548	Scaler Counts	27	28			

[a] Most peaks are off-scale – only locations far from PMT were included in fit.

[b] Include saturated counts at channel 255.

[c] Right attenuation length has wrong sign.

[d] Background is uncertain.

Comparison of results using the peak centroid method and mean channel method are possible for the ^{54}Mn and ^{137}Cs sources in the BC-408 scintillator only. In Table 7.1 such comparisons for experiments A and B, C and D, and L and M show good agreement. The comparison is not valid for experiment E and F because most of the peaks were off scale. Experiments J and K do not show agreement for unknown reasons. We conclude that the mean channel results for BC452 can be compared with the mean channel or peak channel results for BC408.

We expected no dependence of the attenuation length on high voltage of the PMTs. However, both the peak channel method and mean channel method for the ^{54}Mn source in BC-408 (experiment A and B) give attenuation lengths that are about a factor of 2 greater than the attenuation lengths observed at lower voltages (experiment C and D). One possible explanation may be related to the quality of the coupling between the PMTs and the scintillator. Between experiments A and B and C and D, the PMTs were removed from the BC-408 scintillator, mounted on the BC-452, and then remounted on the BC-408. Table 7.1 also gives the mean channel for the left PMT when the source was located close to the left PMT and the mean channel for the right PMT when the source was at the same distance from the right PMT. Usually an increase of 100 V in the PMT voltage makes a big increase in the gain. As shown in Table 7.1, the mean channels for experiments B and D are essentially the same at the different voltages. It is possible the coupling of the PMT to the scintillator in experiments A and B was not as good as in experiments C and D causing the lower than expected mean pulse height and longer than expected attenuation length.

Wrapping the scintillators with three layers of Teflon tape definitely increased the light output of both the BC-408 and BC-452 scintillators. Comparisons of the no wrap and wrapped scintillators must be done for those experiments where the high voltages were comparable. This requirement was met for the ^{54}Mn source in BC-408 (experiment D versus experiment F), ^{54}Mn in BC-452 (experiment H versus experiment I), and ^{137}Cs in BC-408 (experiment K versus experiment M). Large increases in the mean channel of the pulse height distributions for the ^{54}Mn and ^{137}Cs sources in BC-408 and smaller increases for ^{54}Mn in BC-452 were observed as shown in Table 7.1. However, the observed attenuation lengths decreased when the scintillators were wrapped. These results might be explained by the way the measurements were performed. The assumption of a single exponential to fit the data as a function of location is probably not accurate. In most of the plots versus location, the data points close to a given PMT tended to decrease more rapidly than expected by a single exponential. Attenuation lengths are usually measured for scintillator lengths that are considerably longer than the 50-cm lengths available in this work. Thus short distances close to the PMT may not be representative of the bulk material. Wrapping the scintillators may have accentuated the light collection at close distances to the PMT, thus giving unusually large pulse height distributions and shortening the apparent attenuation length.

In spite of the problems in measuring attenuation lengths discussed above, the comparison of attenuation lengths in BC-408 and BC-452 is quite unambiguous. Experiments C and D for ^{54}Mn in unwrapped BC-408 can be compared with experiments G and H for ^{54}Mn in unwrapped BC-452. In BC-408 attenuation lengths of about 140 cm were observed whereas in BC-452 the attenuation lengths were about 30 cm under similar conditions. When both scintillators were wrapped, the BC-408 gave attenuation lengths of about 100 cm whereas the BC-452 gave attenuation lengths of about 20 cm (experiments E and F versus experiment I).

As mentioned above, the ^{109}Cd source gave a pulse height distribution very close to the discriminator threshold, so that the peak channel and mean channel methods could not be applied. The scaler count method gave long attenuation lengths for both the unwrapped and wrapped BC-408 scintillator and short attenuation lengths for both the unwrapped and wrapped BC-452 scintillator (experiments N-T).

7.4.2 Relative Efficiencies – All Sources

The relative efficiencies for sources with various energy gammas are summarized in Table 7.2. Data are shown for the BC-408 scintillator, the BC-452 scintillator, and the BC-408 scintillator wrapped with one layer of Teflon tape. Figure 7.3 through Figure 7.5 compare the relative efficiencies as a function of gamma energy for the Left PMT, the right PMT, and the Coincidence mode, respectively. Note that the ^{137}Cs source was 10 times weaker than the other sources and thus was particularly sensitive to the background. The background for singles count rates in either PMT decreased gradually after the scintillator was placed in the black box. In particular, the efficiencies shown for the ^{137}Cs efficiency for the PMT singles measurements for the unwrapped BC-408 and BC-452 scintillators may be too high because of this changing background. The BC-408 wrapped data do not have this problem because a background was taken just before the ^{137}Cs measurement.

In general, although the pulse heights are larger for the wrapped scintillators as indicated in Table 7.1, the relative efficiencies are only slightly greater for the wrapped BC408 scintillator compared to the no wrap BC-408 scintillator. If we ignore the suspect ^{137}Cs data, the relative efficiencies tend to increase as a function of gamma energy for the PMT singles count rates in BC-408. However, the coincidence count rates are rather constant as a function of gamma energy.

A major motivation for these measurements was the expectation that low energy gammas might have much greater efficiency for the lead-loaded scintillator (BC-452) than for the standard scintillator (BC-408). Figure 7.3 through Figure 7.5 show that the BC-452 efficiencies are comparable to the BC-408 efficiencies for gamma energies below 150 keV but are much lower for higher energy gammas. Note that these results are specific for the particular configuration tested in this work. The very short attenuation length for BC-452 means that although the lead may significantly increase the interaction probability of low energy gammas, the low-energy efficiency averaged over a 50-cm long scintillator is no better than the scintillator with no lead. The even longer scintillators used in portal monitors would show much lower efficiency averaged over the entire scintillator for low energy gammas for BC-452 relative to BC-408. If the goal is to design a portal monitor where the high-energy gamma efficiency is reduced relative to the low-energy efficiency, then the length of the scintillator should be less than 50 cm in order to maximize the benefit from increased interaction probability in the lead-loaded scintillator. This effect is enhanced in the singles measurements compared to the coincidence measurements as shown by the ratio of ^{54}Mn efficiency to ^{241}Am efficiency. This ratio is 2.6 for the Left PMT in BC-408 compared to a ratio of 1.3 for the BC-452. Likewise, the ratio is 3.0 for the Right PMT in BC-408 compared to 1.2 in BC-452. The corresponding ratios for the Coincidence efficiencies are 1.7 in BC-408 and 1.6 in BC-452. Thus the ratio of efficiency for high-energy gammas to low-energy gammas hardly changes for the coincidence measurements, but the ratio changes by more than a factor of 2 in the singles measurements.

Table 7.2. Relative efficiency for a single gamma corresponding to the weighted average energy of the gamma spectrum

Source	Scintillator	Wrapping	Runs	Left HV	Right HV	Relative Efficiency Left PMT (%)	Relative Efficiency Right PMT (%)	Relative Efficiency Coincidence (%)	Weighted Average Energy (keV)
^{54}Mn	BC408	No Wrap	644	-1594	-1544	4.46	5.00	2.00	835
^{60}Co	BC408	No Wrap	652	-1594	-1544	4.37	4.31	1.80	1253
^{137}Cs	BC408	No Wrap	645	-1594	-1544	6.09	8.37	2.00	613
^{133}Ba	BC408	No Wrap	646	-1594	-1544	2.53	2.58	1.82	130
^{57}Co	BC408	No Wrap	648	-1594	-1544	2.91	2.74	2.54	122
^{241}Am	BC408	No Wrap	651	-1594	-1544	1.70	1.69	1.19	54
^{109}Cd	BC408	No Wrap	649	-1594	-1544	0.90	0.78	0.90	27
^{60}Co	BC452	No Wrap	637	-1700	-1604	1.93	2.17	1.57	1253
^{54}Mn	BC452	No Wrap	630	-1700	-1604	2.08	2.37	1.77	835
^{137}Cs	BC452	No Wrap	631	-1700	-1604	2.28	3.20	1.86	613
^{133}Ba	BC452	No Wrap	632	-1700	-1604	2.04	2.42	1.49	130
^{57}Co	BC452	No Wrap	634	-1700	-1604	2.51	3.08	1.82	122
^{241}Am	BC452	No Wrap	636	-1700	-1604	1.62	1.96	1.13	54
^{109}Cd	BC452	No Wrap	635	-1700	-1604	0.67	0.98	0.28	27
^{60}Co	BC408	Wrap (T)	678	-1574	-1543	5.13	5.33	1.89	1253
^{54}Mn	BC408	Wrap (T)	671	-1574	-1543	4.61	4.66	2.03	835
^{137}Cs	BC408	Wrap (T)	672	-1574	-1543	3.72	3.57	2.05	613
^{133}Ba	BC408	Wrap (T)	673	-1574	-1543	2.74	2.77	1.91	130
^{57}Co	BC408	Wrap (T)	675	-1574	-1543	3.23	3.22	2.75	122
^{241}Am	BC408	Wrap (T)	677	-1574	-1543	1.90	1.92	1.39	54
^{109}Cd	BC408	Wrap (T)	676	-1574	-1543	1.05	1.04	0.97	27

(T) Scintillator wrapped with 1 layer of Teflon tape.

7.4.3 Relative Efficiencies–^{54}Mn, ^{137}Cs, and ^{109}Cd–Collimated at Center

The relative efficiencies of the selected sources ^{54}Mn, ^{137}Cs, and ^{109}Cd were measured at the midpoint location using the lead collimator. Thus the majority of interaction events in the scintillator occurred about 25 cm from either PMT. The results are summarized in Table 7.3. For the BC-408, wrapping the scintillator improved the single PMT efficiencies for the ^{54}Mn and ^{137}Cs sources by roughly 30% to 40% without improving the coincidence efficiency. For the BC-452, wrapping the scintillator did not improve the singles or the coincidence efficiencies for ^{54}Mn. However, wrapping the BC-452 did seem to improve the efficiency for the low energy ^{109}Cd source in contrast to the BC-408 which showed almost no increase with wrapping.

For the high-energy ^{54}Mn source, the efficiency was not very sensitive to the high voltage indicating that the bulk of the pulse height spectrum was well above the discriminator threshold at all the voltages used. The efficiency for the ^{109}Cd source might be expected to be very sensitive to the high voltage but the present data are inconclusive.

A striking feature of the results is the roughly 8 times larger efficiency for ^{137}Cs compared to ^{54}Mn for the BC-408 scintillator for both the singles and the coincidence measurements. The energies of the dominant gammas are 0.662-MeV and 0.835-MeV for ^{137}Cs and ^{54}Mn, respectively. The two sources were measured without any changes to the PMT coupling or background effects between sources. Thus the large change in efficiency for sources so close in energy seems anomalous.

The relative efficiencies for the collimated ^{109}Cd source in BC-408 are lower than those for the un-collimated source by about a factor of 4. This is consistent with the expectation that events located at the midpoint of the scintillator are more likely to be attenuated or lost.

7.4.4 Efficiency as a Function of Discriminator

Another question of interest to this work is the dependence of the efficiency on the discriminator level, particularly with respect to the low-energy sources represented by ^{57}Co and ^{109}Cd. This was examined in two ways. The first way involved measuring the pulse height spectra for the two sources and for both scintillators using the coincidence gate based on the standard discriminator settings of 10 mV for each PMT. The integrated number of counts after background subtraction was calculated between a threshold channel number and the maximum channel number. The integrated number of counts was converted to a relative efficiency after correcting for the source strength, the counting time, and the data acquisition live time. The results for spectra from the Left PMT are plotted in Figure 7.6. Although not shown here, the results for spectra from the Right PMT are equivalent. The results can be summarized by saying that the efficiency is greater for the higher-energy ^{57}Co source than the lower-energy ^{109}Cd source and is also greater for the BC-408 scintillator than the BC-452 scintillator. In every case the efficiency falls off as the threshold channel is raised.

Table 7.3. Relative efficiencies for collimated sources at midpoint of scintillators

Source	Scintillator	Wrapping	Runs	Left HV	Right HV	Efficiency Left PMT (%)	Efficiency Right PMT (%)	Efficiency Coinc. (%)	Notes
^{54}Mn	BC408	No Wrap	518	-1640	-1600	1.07	1.14	0.55	
		No Wrap	757	-1566	-1545	0.98	1.04	0.50	
		Wrap	733	-1566	-1545	1.35	1.53	0.55	[a]
	BC452	No Wrap	553	-1640	-1650	0.57	0.57	0.49	
		No Wrap	722	-1645	-1549	0.57	0.55	0.47	
		Wrap	712	-1645	-1548	0.55	0.56	0.48	[a]
^{137}Cs	BC408	No Wrap	776	-1566	-1545	7.61	8.28	4.59	
		Wrap	743	-1566	-1545	10.56	11.97	4.92	[a]
^{109}Cd	BC408	No Wrap	768	-1566	-1544	0.25	0.25	0.21	
		Wrap	748	-1566	-1545	0.25	0.26	0.21	
	BC452	No Wrap	5/20/05	-1650	-1650	0.16	0.15		
		No Wrap	616	-1695	-1653	0.06	0.06	0.06	
		Wrap	706	-1645	-1548	0.20	0.19	0.09	[a]

[a] Wrapped in 3 layers of Teflon

The second method was intended to correlate the hardware discriminator level with the specific thresholds in the pulse height spectra. Pulse height spectra were obtained with the additional hardware discriminator levels of 50 mV on both PMTs and 100 mV on both PMTs. The spectra were integrated over the entire range of channels and the efficiency was calculated in the same manner as above. By comparing the resulting efficiencies to the corresponding values for the plots in Figure 7.6, we can determine that the 50-mV discriminator settings correspond to a threshold at channel 10 in Figure 7.6 and the 100-mV discriminator settings correspond to a threshold channel of about 18 in Figure 7.6. It is clear that the discriminators should be set at the lowest possible value (10 mV) to maximize the efficiency.

7.4.5 Efficiency as a Function of Location in Scintillator

The relative efficiency was calculated for the Left PMT, the Right PMT, and the Coincidence as a function of the location of the interaction in the scintillator. An example of the results is shown in Figure 7.7 showing the ^{54}Mn source in BC-408 and in Figure 7.8 showing the ^{54}Mn source in BC-452. The efficiency for a single PMT decreases as the location of the interaction is moved farther from a particular PMT. However, the closest data point to a particular PMT is lower than the expected trend. A simple geometric calculation shows that the spreading of the collimated gamma beam is slightly greater than the 5-cm distance of the center of the gamma beam to the PMT, indicating that some of the gamma beam might not have interacted in the scintillator for this location. This affects the resulting efficiency at both ends of the scintillator as most clearly seen in the data for the wrapped BC-408 scintillator.

The efficiency for the coincidence count rate of ^{54}Mn is relatively flat as a function of location and is rather similar for both the BC-408 and BC-452 scintillators. The coincidence efficiency for ^{109}Cd is also flat for both scintillators but is 2.5 times lower in BC-452 than in BC-408.

7.5 Conclusions

The attenuation lengths for BC-452 measured here are much shorter in lead-loaded BC-452 than in standard BC-408 scintillator. The hoped-for increased efficiency for low-energy gammas was not sufficient to compensate for this reduced light transmission in these 50-cm long samples. It is true that the ratio of efficiencies for low-energy gammas to high-energy gammas can be increased by the use of lead-loaded scintillator. However this benefit is degraded by the loss in overall efficiency for the larger-size scintillators desired for portal monitor applications.

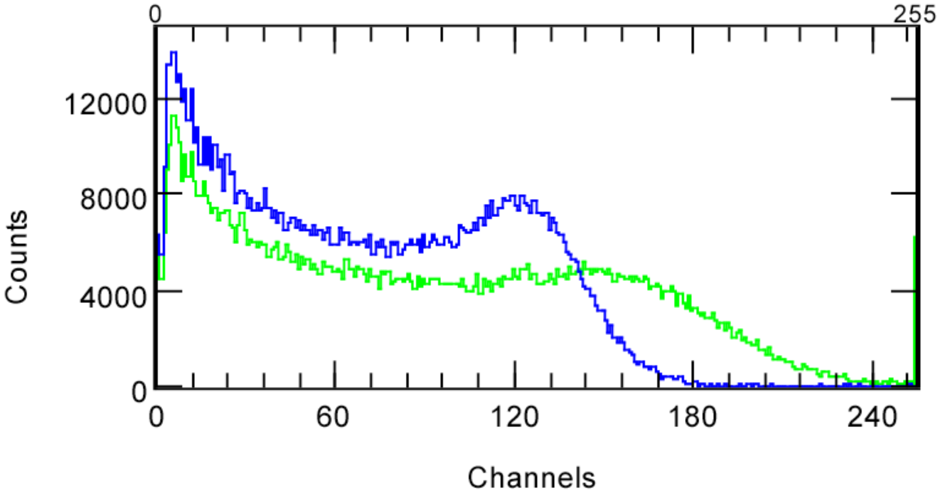

Figure 7.1. Pulse height spectra for ^{54}Mn in Left PMT with BC-408 scintillator. Green curve is for source location at 10.2 cm from Left PMT. Blue curve is for source location at 40.6 cm from left PMT.

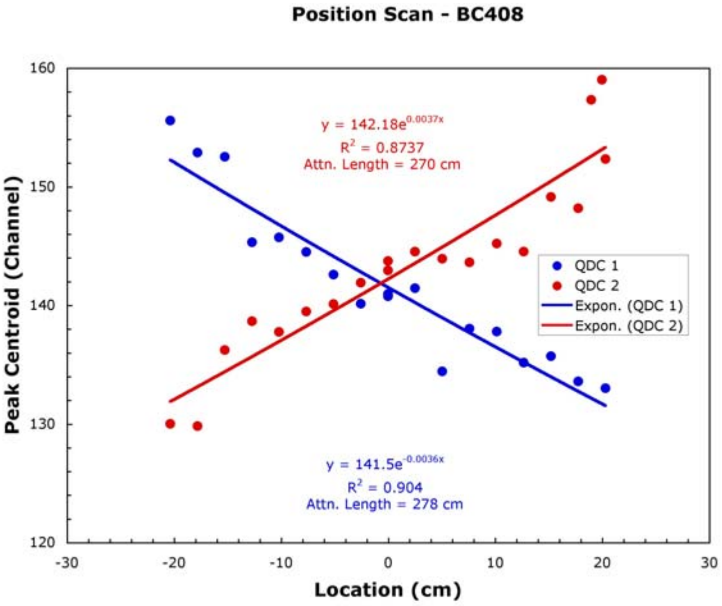

Figure 7.2. Peak channel of the Compton edge peak as a function of source location for ^{54}Mn with BC-408 scintillator. Blue curve is for the Left PMT. Red curve is for the Right PMT. Data points have been fitted with an exponential function.

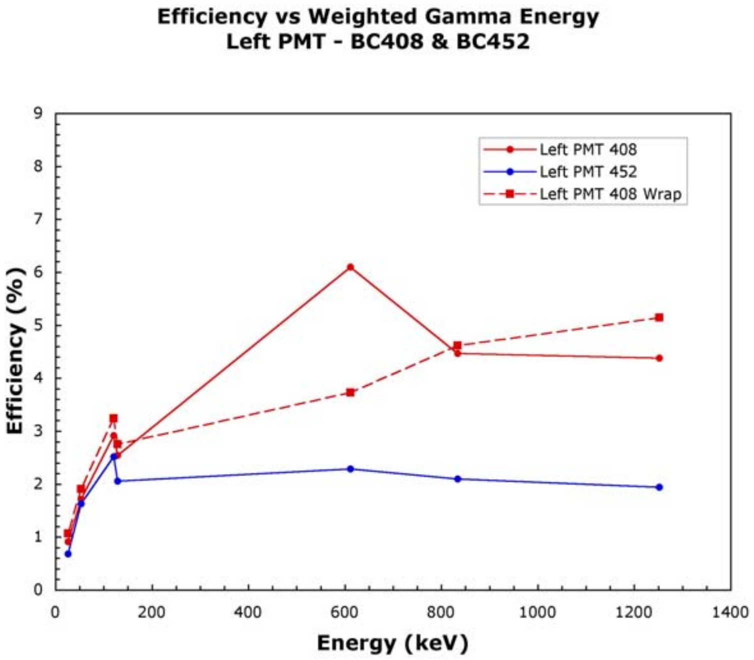

Figure 7.3. **Relative efficiency as measured by Left PMT of BC-408 and BC-452 scintillators as a function of gamma energy. See text for definition of efficiency and energy.**

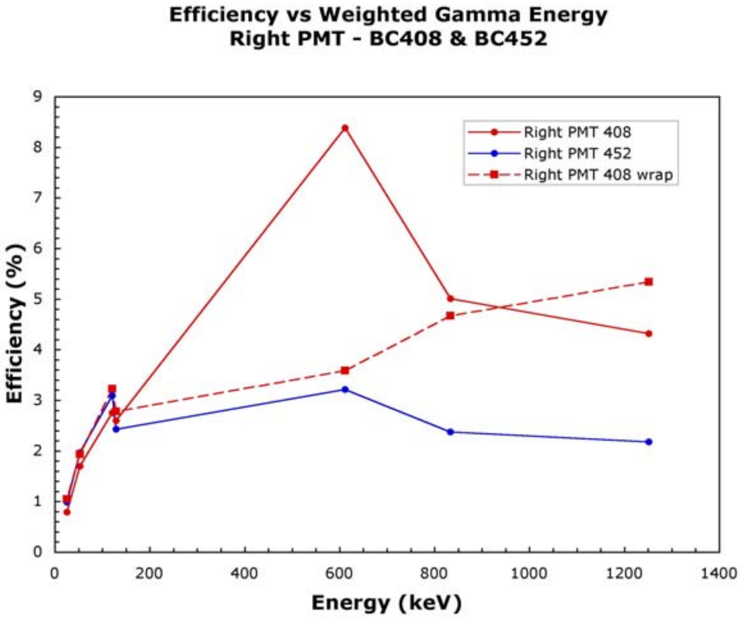

Figure 7.4. **Relative efficiency as measured by Right PMT of BC-408 and BC-452 scintillators as a function of gamma energy. See text for definition of efficiency and energy.**

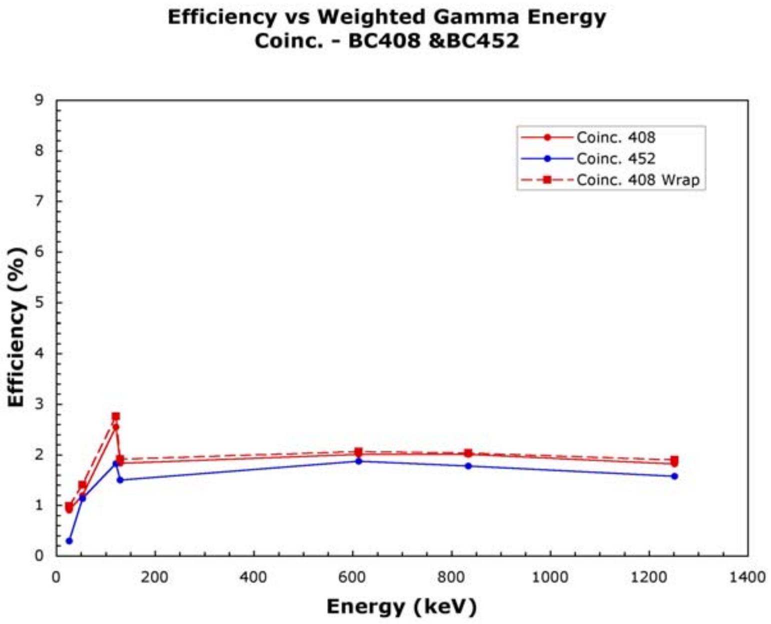

Figure 7.5. Relative efficiency as measured by the coincidence of the Left PMT and Right PMT of BC-408 and BC-452 scintillators as a function of gamma energy. See text for definition of efficiency and energy.

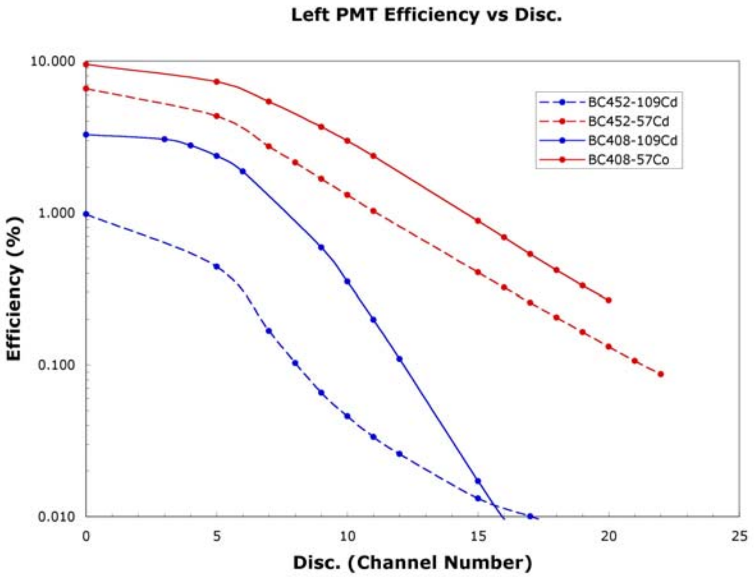

Figure 7.6. Relative efficiencies for ^{109}Cd and ^{57}Co as a function of the lower channel number for a window set on the pulse height spectra.

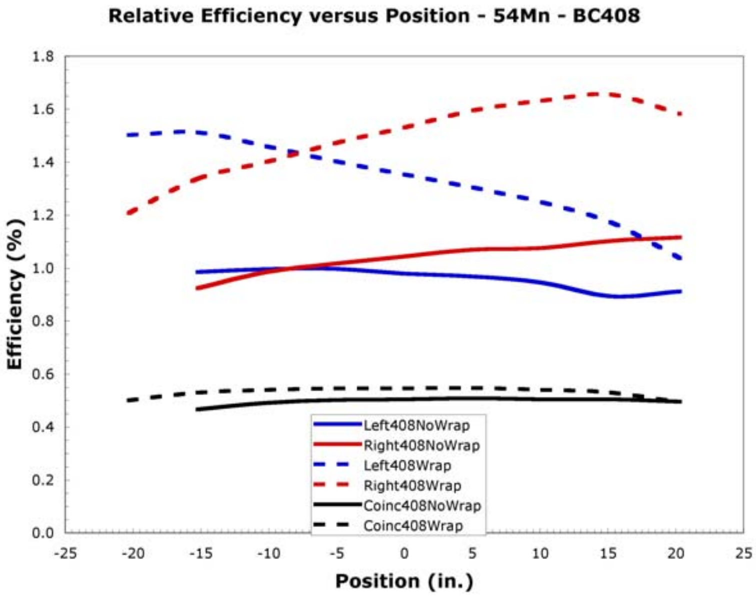

Figure 7.7. **Relative efficiency as a function of the location of the interaction as it is moved farther from a particular PMT. The scintillator is BC-408.**

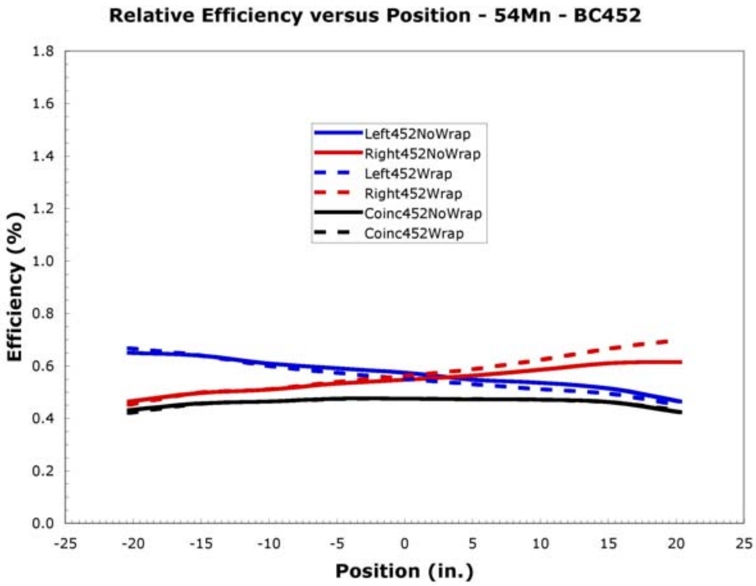

Figure 7.8. **Relative efficiency as a function of the location of the interaction as it is moved farther from a particular PMT. The scintillator is BC-452.**

8.0 ALPS TDC Analysis

8.1 Introduction

The goal of the time-to-digital converter (TDC) analysis for the ALPS project was to investigate the possibility of improving the spectral information from the plastic scintillator detectors by correcting for position dependence of the incident gamma. An alternative goal was to determine a method of combining the amplitudes of the signals from the various PMTs which exhibited minimal position dependence. This section details some of the findings of this study. Note that all results have been background subtracted and normalized to counts per bin per second unless noted otherwise.

8.2 Position Reconstruction

For general applications, the position at which a particle enters the scintillator is not known a priori. To be able to correct for possible position dependence in the observed pulse height, one must be able to reconstruct the incident position from the available detector information. The differences of TDC signals from the PMTs are a logical place to look for such information. For example, in a simple line-of-sight picture of a long, narrow detector with two PMTs on the far ends, the TDC difference contains information on the distance of the incident particle from the PMTs. In addition, TDC differences are independent of the how the common TDC signal (either common start or common stop) is formed, making them a more robust signal to examine.

Event mode data were recorded with a ^{90}Sr source placed at various positions along the top of the ALPS scintillator with four PMTs attached. Five sets of measurements were conducted with each set consisting of placing the source at several positions along a line. As seen in Figure 8.1, we define these lines as: Trace 1(2) is the line along the long direction of the scintillator between PMTs 1 and 4 (2 and 5). Traces A, M, and L are along the short direction of the scintillator 2" from PMTs 1-3, in the middle of the scintillator and 2" from PMTs 4-6, respectively. List-mode analysis of the data was performed using the CERN Physics Analysis Workstation (PAW) software. The TDC differences were histogrammed, and the positions of the peaks in histograms were determined by fitting a symmetric Gaussian peak to a region of approximately $\pm1.3\sigma$ around the peak center. The results of this TDC difference analysis for the five traces are shown in Figure 8.2.

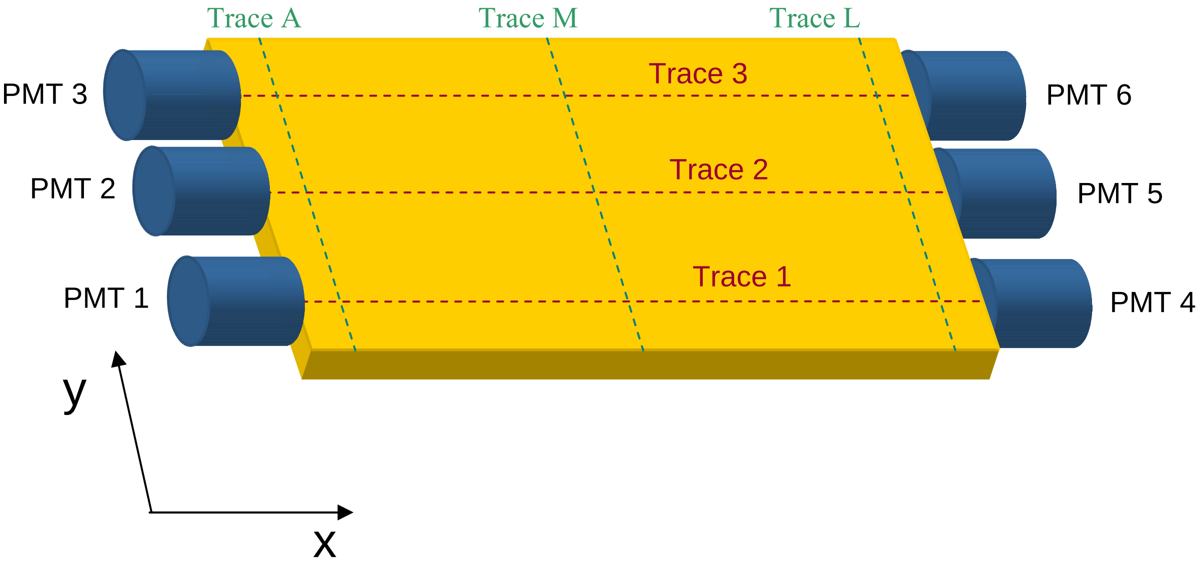

Figure 8.1. Diagram of single sheet of the ALPS plastic scintillator sensor with 6 PMTs attached directly to the plastic. Orientation of coordinates and some source location "traces" are defined. For the 4 PMT setup, only PMTs 1, 3, 4 and 5 are used.

Several observations can be made about these figures:

- From some traces, a given value of the TDC difference can correspond to more than one location. This lack of one-to-one character of the TDC difference on the position significantly complicates any algorithm for extracting the interaction location based on TDC information. This problem occurs only at the ends of the scintillators.
- Near the outer 10" of the scintillator, the TDC information appears to provide enough information to reconstruct both the *x* (long direction) and *y* (short direction) of the interaction point.
- The reconstruction of *y* in the central 30" of the scintillator is not possible. The FWHM of the TDC distributions is about 70-80 channels. The peaks of the distributions would need to be about one FWHM apart to reliably reconstruct a position from the TDC differences on an event-by-event basis. This deficiency, however, may not be significant if there is also little *y*-dependent correction required to the signal amplitude.
- Traces A, M and L provide more information as to *y* dependence. Near the PMTs, the TDC differences vary strongly (traces A and L), but near the middle of the scintillator along *x* (trace M), the differences are much smaller.

A simple line-of-sight model was developed to test the origin of the TDC difference behavior. The model assumes that the time differences in the TDCs are simply the difference in the line-of-sight distance from the interaction point to the two PMTs. As seen in Figure 8.3, the model works reasonably well qualitatively in that it describes the shapes of most of the lines. However, the model fails to describe the amplitudes of the variations well, at least for the equivalent of trace L, and fails to describe the doublevalued nature of some of the lines for trace 1. These results suggest that when the interaction point is near an edge of the scintillator the dominant contribution to light collected at the PMT involves one or more bounces off the scintillator walls.

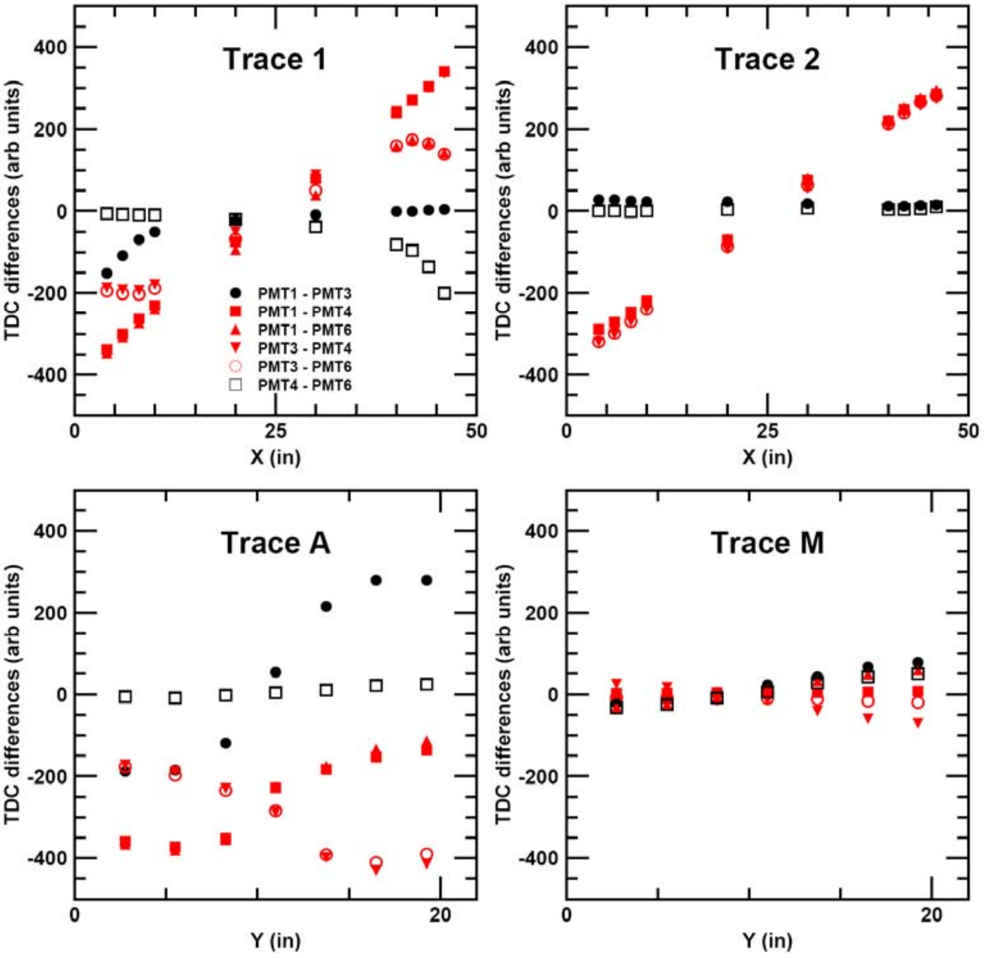

Figure 8.2. TDC difference analysis summary for the traces using a ^{90}Sr source at various positions on the scintillator. All figures share the same legend. See text and Figure 8.1 for the definition of the traces.

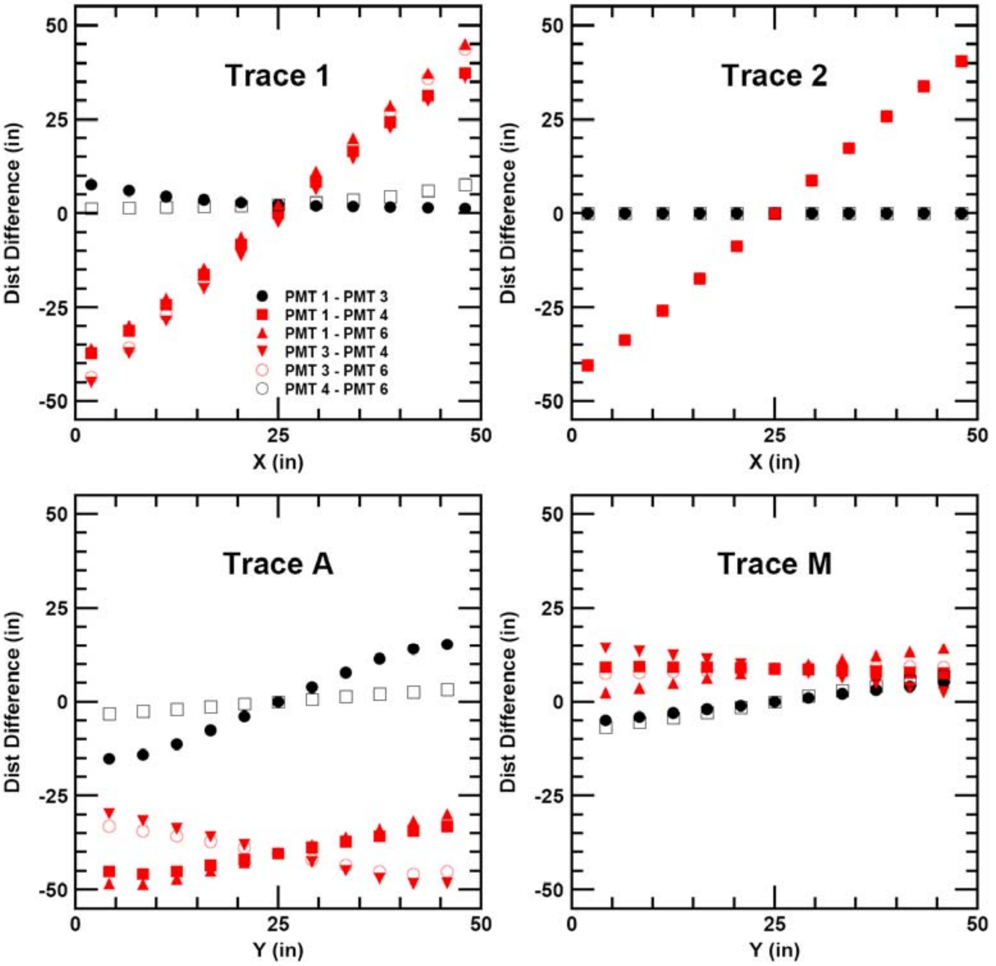

Figure 8.3. Simple model of TDC differences for various pairs of PMTs for 4 different traces. The difference in distances from the interaction point to the pair of PMTs is plotted along the ordinate.

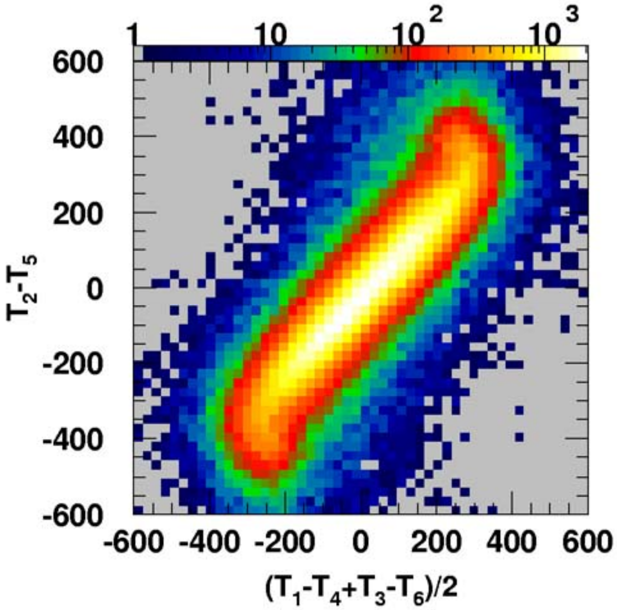

Figure 8.4. Demonstration of relationship of T_2-T_5 and (T_1-T_4+T_3-T_6)/2 using the six PMT setup and a distant, uncollimated gamma source.

In Figure 8.2a and b, there is clear evidence of a simple linear relationship between the *x* position and the TDC difference of the two PMTs closest to the interaction point but on opposite sides of the scintillator, e.g. PMTs 1 and 4 if the interaction point is along trace 1. This result agrees with a simple physics picture of the TDC difference. For the two and six PMT setups, the TDC difference of PMT 2 and 5, T_2-T_5 where T_i is the TDC value from PMT *i*, is assumed to be proportional to the *x* position. For the four PMT setup, the average of the differences of 1 and 4 and of 3 and 6, i.e. (T_1-T_4+T_3-T_6)/2 is used. These combinations of TDC differences are collectively referred to as ΔT, where it is understood that ΔT depends on the PMT configuration.

Figure 8.4 is a two-dimensional plot of T_2-T_5 versus (T_1-T_4+T_3-T_6)/2 for the 6 PMT setup, which demonstrates that these two quantities are close to equivalent, except near the edges of the scintillator (large TDC differences).

It is important to clearly understand the differences between the *x* position and ΔT. Any hypothesized correction will be based on the *x* position; however the only means to correct for the position dependence of the signal amplitude are the TDC differences. A clear understanding of how ΔT deviates from strict proportionality to *x* as *y* varies is important.

This investigation started with a plot of the geometric mean(a) versus T_2-T_5 for an uncollimated ^{207}Bi source 53" from the scintillator for the six PMT setup, as seen in Figure 8.5. In the top plot in which no ADC overflows are allowed, the phase space is in the shape of a triangle. The calculation of the geometric mean uses all ADC values, so that a large geometric mean requires all ADC values to be large.

(a) The use of the geometric mean is discussed in more detailed later. We define the geometric mean as the square root of the products of the sums of the signals on each side of the scintillator.

This is only possible near the center of the scintillator, which leads to the triangular shape. This observation also implies that when no ADC overflows are permitted, the range in T_2-T_5 is reduced and this reduction is more significant for larger geometric means. For the case shown, the ^{207}Bi peak around channel 1300 is only reduced from ~600 channels wide to ~500.

In the right plot of Figure 8.5, in which no requirement is placed on the individual ADC values, extra structure develops. The only requirements placed on this data are no TDC overflows and no pulser events. There appears to be a concave arch around a geometric mean of 3000 supported by two pillars around T_2-T_5 of ±250. The arch is caused by ADC overflow events. The origin of the pillars is more complicated.

It was hypothesized that the pillars are generated by the multi-valued correlation of the TDC differences with the actual position as shown in Figure 8.2. As a result of this multi-valued nature, the *y* dependence of the uncorrected signal amplitude becomes significant near the ends of the scintillators near the PMTs. For events in the 1/3 of the scintillator between PMT 2 and 5, the TDC difference T_2-T_5 is a reasonable approximation to the *x* position of the interaction point in the scintillator. However, once the interaction point goes outside the central range in *y* (outside of the 1/3 of scintillator previously mentioned), the absolute value of T_2-T_5 levels off, or even decreases, toward the extremes in *x*. The pillars observed in the right plot of Figure 8.5 are generated by events near the extremes in *x* and outside the central range in *y*, in other words, these events are in the corners of the scintillators. These pillars are not observed in the left plot of Figure 8.5 because the available phase space is reduced by the no ADC overflow requirements.

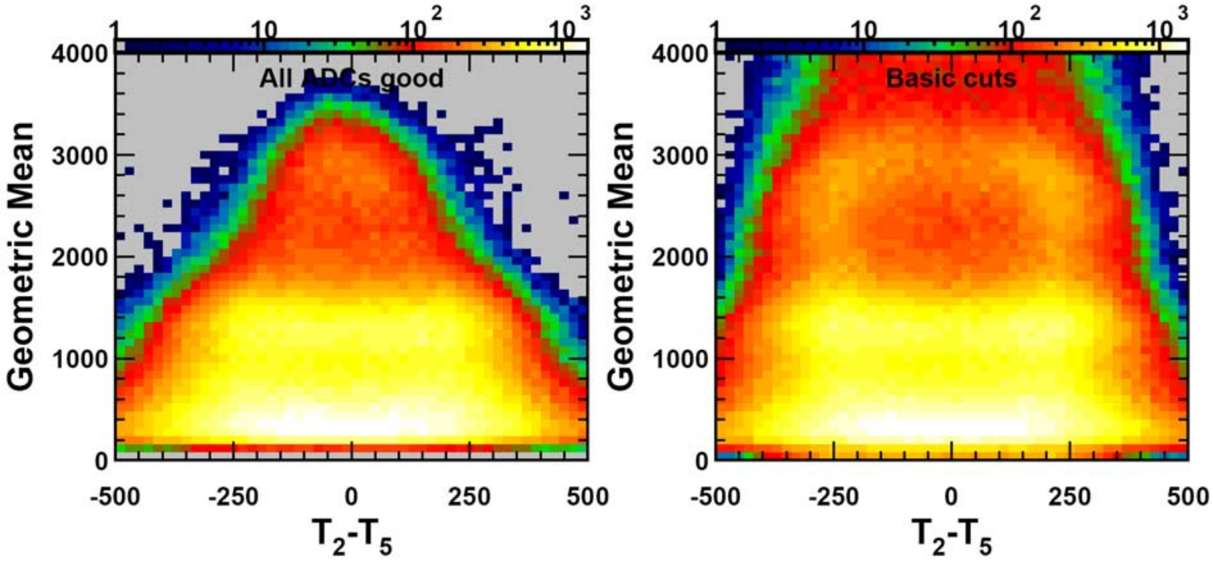

Figure 8.5. Plot of geometric mean of ADCs versus T_2-T_5 for distant, uncollimated ^{207}Bi data. Data is not background subtracted. The left plot requires that all ADCs do not have overflows, whereas the right plot does not make this requirement. Note that the *z* axis (color) is in log scale.

Given these observations, there are two possible courses of action: 1) determine the *y* dependence of the T_2-T_5 to get a better estimate of the reconstructed *x* position, or 2) remove the events in these pillars from the analysis so that they do not complicate the interpretation. The latter approach was chosen because it was believed to be easier and as valuable if there are adequate statistics.

The next step was to identify ways to eliminate events on the sides of the scintillator and especially events in the corners of the scintillator. The TDC differences between PMTs on the same side of the scintillator are an obvious candidate. Plots of these TDC differences versus T_2-T_5 are shown in Figure 8.6. These quantities, T_1-T_3 and T_4-T_6, demonstrate peculiarities at the extremes of the scintillators. Cuts of $|T_1$-$T_3|<100$ and $|T_4$-$T_6|<100$ were established to eliminate events incident near the edges of the scintillator. These cuts are referred to as the "corner" cuts because they are designed to eliminate events in the corners of the scintillators.

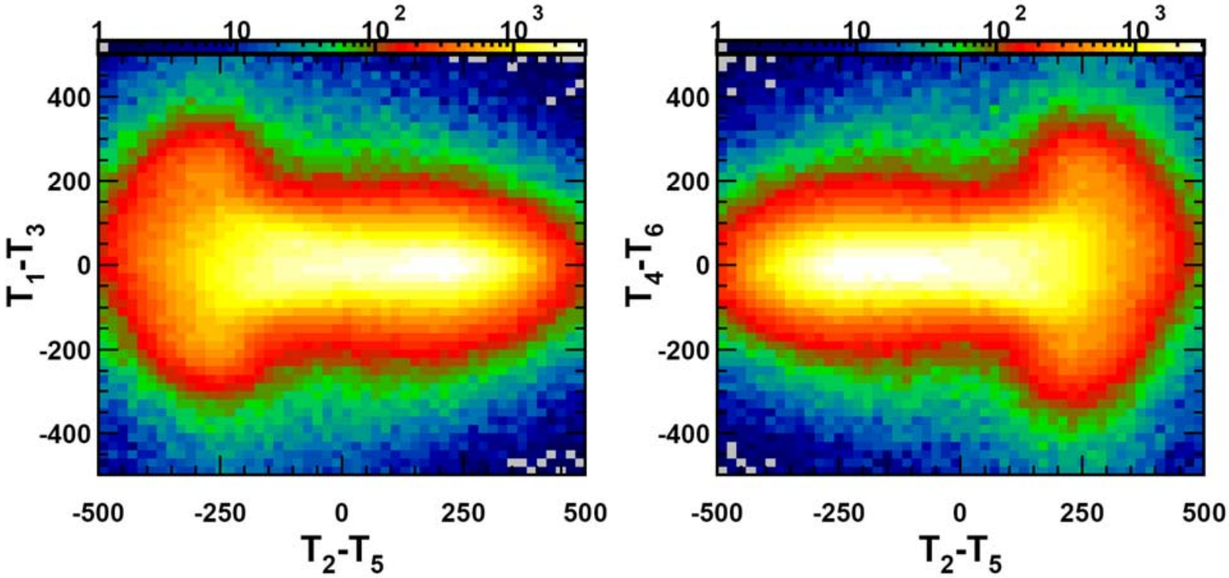

Figure 8.6. Plots of T_1-T_3 versus T_2-T_5 (left) and T_4-T_6 versus T_2-T_5. (right) Note that the *z* axis is in log scale, which tends to visually exaggerate the importance of the events at the extremes of T_2-T_5.

Figure 8.7 and Figure 8.8 demonstrate some characteristics of these cuts.. Figure 8.7 shows the 1-D histograms of T_2-T_5 and of the geometric mean for various cuts. These plots confirm that the corner cuts remove events near the extremes of T_2-T_5, that there is less spectral information for events that survive one or both corner cuts, and that the T_2-T_5 distribution is fairly flat for events that survive both corner cuts. The latter observation suggests that the label of "corner cuts" is a misnomer. The various plots of Figure 8.8 clearly establish that the events surviving the corners cut also generated the pillars seen in Figure 8.5.

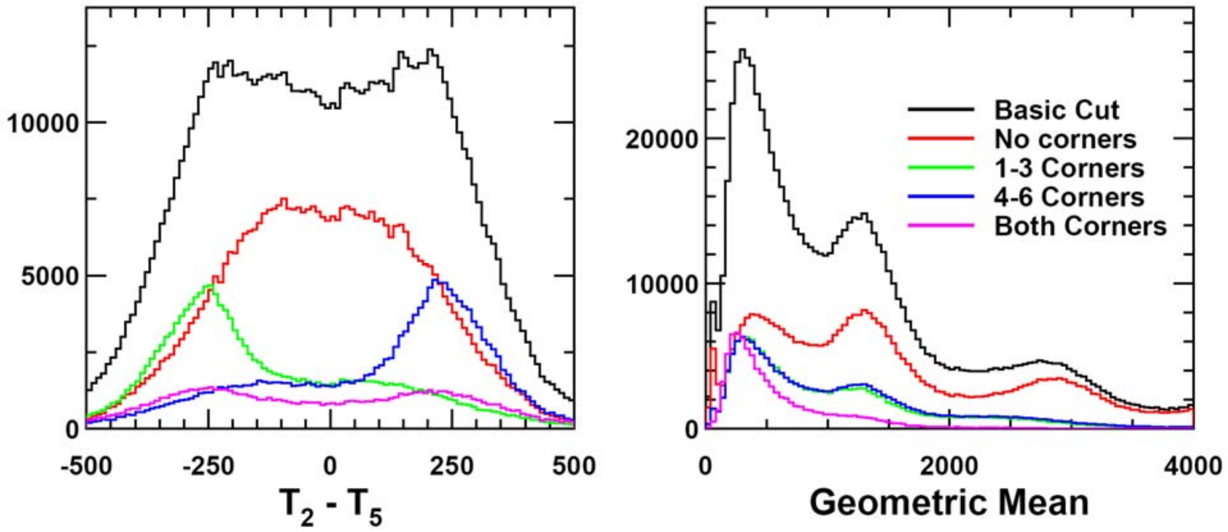

Figure 8.7. Histograms of T_2-T_5 and geometric mean for various cuts, as labeled in the right plot for a distant ^{207}Bi source. These plots are not corrected for background. Abscissa for both plots is counts per histogram channel.

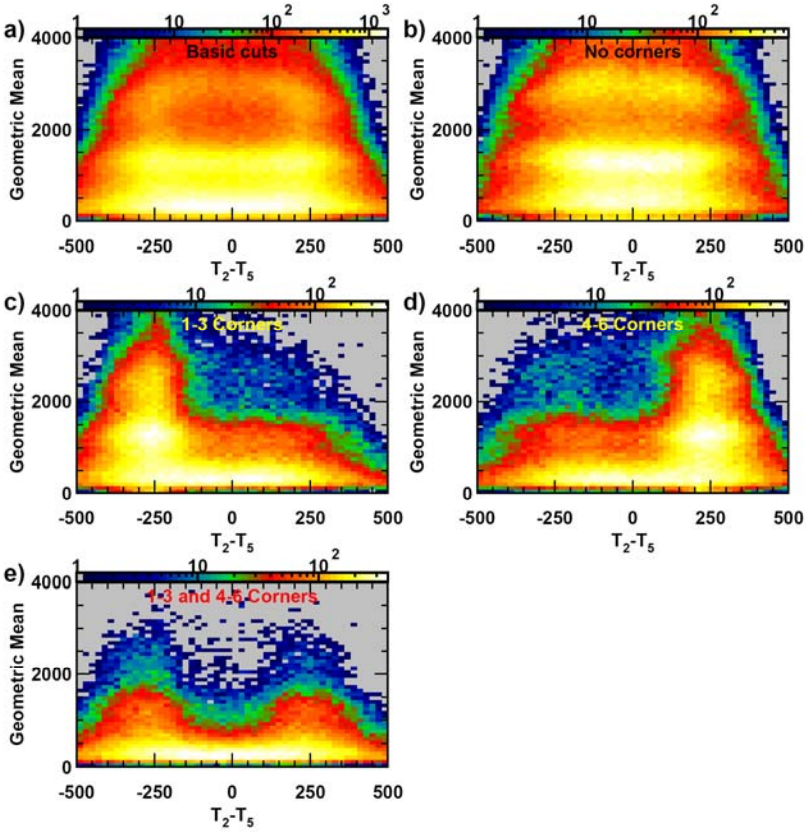

Figure 8.8. Plots of the geometric mean from the ^{207}Bi run versus T_2-T_5 for various cuts: a) basic cuts, b) basic cuts and no corners cuts, c) basic cut and 1-3 corner cut, d) basic cut and 4-6 corner cut, e) basic cut and both corner cuts.

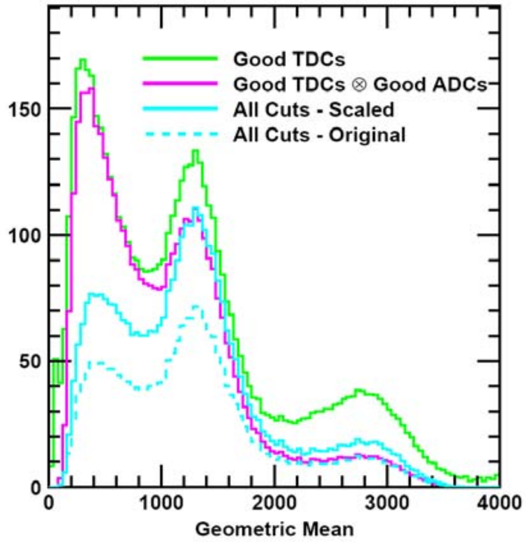

Figure 8.9. Plot demonstrating the impact of the "No Corners" cut on the geometric mean of the ^{207}Bi run. Events which survive the basic good TDC cut are histogrammed in green while those that survive both the good TDCs and ADCs cuts are in magenta. For the dashed cyan histogram, the no-corners cut is also applied. The solid cyan curve is the dashed cyan curve scaled so that peak amplitude near channel 1300 is identical to the good TDCs and ADCs histogram. Abscissa is counts per histogram channel.

The impact of the "No corners" cut can be clearly seen in Figure 8.9. The "No corners" cut eliminates about one-half of the events, but it increases the peak to valley ratio of the Compton peak at channel 1300.

8.3 Event Selection

In addition to the "no corners" cut, a few other cuts were applied to the data. These cuts are defined in Table 8.1. Pulser events were eliminated by requiring a pulser TDC time-out. It was decided that only events in which all PMTs had signals would be analyzed. This requirement simplifies the analysis and hopefully does not bias the investigation by significantly impacting the selection of events. Given this requirement, all PMT TDCs were required not to time out. To simplify the analysis, no ADC overflows were permitted. The impact of the no ADC overflow cut is show in Figure 8.10. The most important points are the green circles and squares for the mean of the distributions of the arithmetic and geometric mean. For all traces, the no ADC overflows cut shows less variation than only the no TDC timeout cut. For instance, for trace 1 the geometric mean for the no TDC timeout cut varies by 30%, whereas with the addition of the no ADC overflow cut the variation is only 12%. In addition, the distribution changes from concave to convex.

Table 8.1. Definition of cuts used in the analysis

Label	Description	Logic for 6 PMT Setup
Good TDCs	No TDCs with timeouts and all TDC differences of opposite pairs are within a reasonable range	$\prod_{i=1}^{6}(T_i < 4090) \otimes \lvert T_1\text{-}T_4\rvert<500 \otimes \lvert T_2\text{-}T_5\rvert<500 \otimes \lvert T_3\text{-}T_6\rvert<500$
Good ADCs	All ADCs have neither overflows or are below a minimum threshold	$\prod_{i=1}^{6}(63 < A_i < 4090)$
No Corners	TDC differences of PMTs on the same sides the scintillator are not large	$\lvert T_1\text{-}T_3\rvert<100 \otimes \lvert T_4\text{-}T_6\rvert<100$

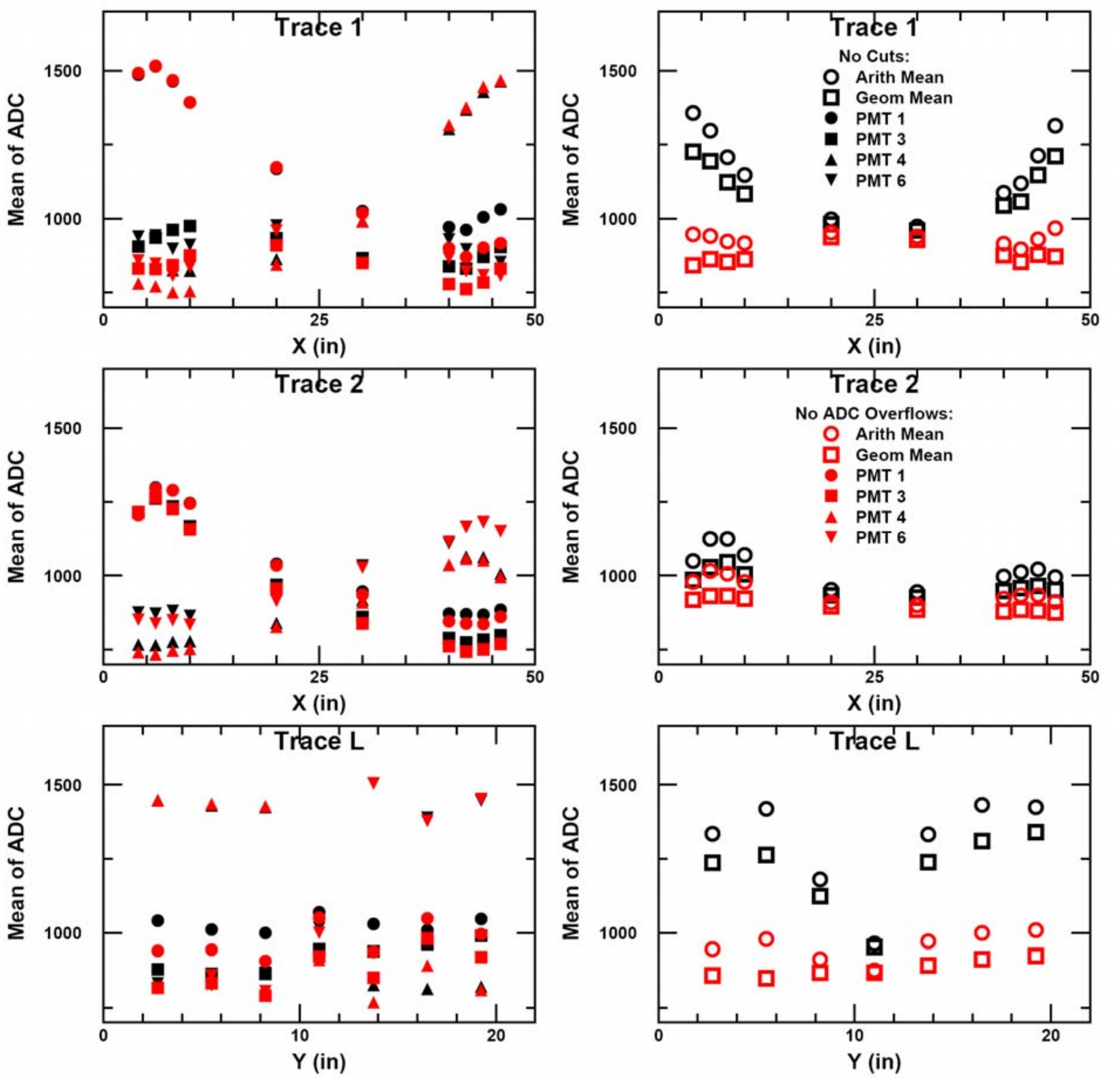

Figure 8.10. Plots of the means of the distribution of individual ADCs and sums of ADCs versus source position. The left column contains plots of the individual PMT ADC values. The right column contains plots of the combined ADC values, i.e. arithmetic and geometric means. The red markers indicate means of ADC histograms on which no cuts where placed, whereas the black markers indicate those on which a no ADC overflow cut was made. The top row is for trace 1, the middle row if for trace 2, and the bottom row is for trace L. This data was taken with a ^{90}Sr source with the 4 PMT setup.

The no ADC overflow cut will reduce the number of analyzed events near the edges of the scintillators. For a ^{90}Sr source 2” from a PMT, 40% of the events are lost when one applies the no ADC overflow cut. For the same source near the middle of the scintillator, essentially no events are lost when this cut is applied. Application to a different incident spectrum will remove a different fraction of events. It is anticipated that the position correction to the signal amplitude will depend roughly quadratically on the *x* position, so that the events at extreme *x* are most sensitive to the position correction; the no ADC overflow cut removes events mostly from these extreme *x* regions. For this reason, maximizing the range in the reconstructed *x* position is important. However, without sophisticated and as yet undeveloped algorithms, there is no simple means to determine spectroscopic information when one or more of the ADCs overflow, so the events removed by the no ADC overflow case are not useful for spectral analysis. These events, however, may be useful in an energy window analysis if one is able to establish a lower limit of the possible energy.

A summary of the impact on event rates of various cuts is provided in Figure 8.11 and Table 8.2. These results are from measurements with a ^{207}Bi source 53” above the scintillator using the 6 PMT setup. All cuts significantly reduce the lowest energy contributions, and the Good ADCs significantly reduced the highest energy contributions as well. Table 8.2 contains a list of the fraction of events for cut data compared to uncut data for several different energy ranges.

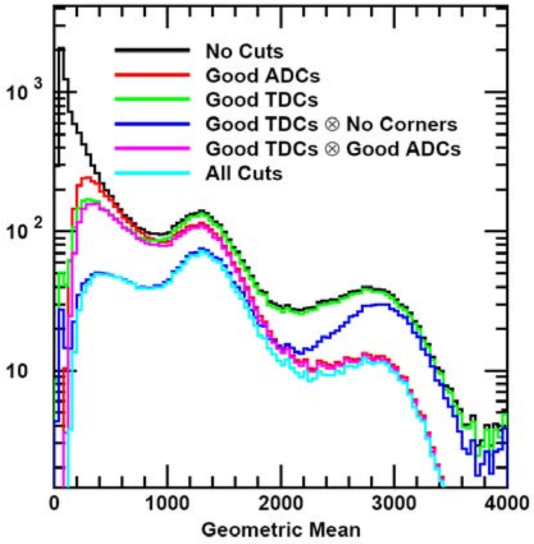

Figure 8.11. **Histograms of a distant ^{207}Bi source demonstrating the impact of various cuts. Note that the abscissa is in log scale. Abscissa is counts per histogram channel.**

Table 8.2. **List of the percentage of events that survive various cuts in a given region of interest in the geometric mean of the ADCs.**

	Percentage of Total Events in Given Region			
	0-500	**1000-1500**	**2500-3300**	**Full Range**
Good ADCs	25.8	82.8	31.8	43.8
Good TDCs	20.4	94.3	95.5	48.1
Good TDCs and no Corners	6.1	52.2	75.0	23.9
Good TDCs and ADCs	16.9	78.8	30.5	36.2
All Cuts	5.0	49.9	28.5	18.9

8.4 Reconstruction of Signal Amplitude

A fundamental question of the TDC analysis is how to combine the ADC information to reconstruct the signal amplitude. Two possibilities were investigated, the arithmetic mean and the geometric mean. The justification for the arithmetic mean is its simplicity and universality. The justification for the geometric mean is that it will tend to remove position dependence in the amplitude due to attenuation of the signal as it passes through the scintillator. Consider a long, narrow scintillator of length L, with an attenuation length of α, and one PMT on each end. If a gamma ray interacts with the scintillator at location x centimeters away from PMT 1, then the observed amplitude of the signals in the two PMTs will be:

$$A_1 = A_0\, e^{-\alpha x/L} \quad \text{and} \quad A_2 = A_0\, e^{-\alpha(L-x)/L},$$

where A_0 is the theoretical amplitude of the signal at the interaction point if there is no attenuation in the scintillator. Thus, in this simple picture the geometric mean of A_1 and A_2 is independent of x.

When there are multiple PMTs on one side of a scintillator, the calculation of the geometric mean becomes ambiguous. One could, for instance, take the N^{th} root of the product of N PMTs. Alternatively, one could separately average the PMTs for both sides and then take the square root of the product of those averages. The later approach was chosen for the determination of the geometric mean.

The variations of the arithmetic and geometric means for different incident location of a gamma source(a) are shown in Figure 8.12. These plots show the position of the Compton peak versus the location of the source. The location of the Compton peak was determined from a fit to the measured spectrum. The fitting function consisted of the sum of a linear background (continuum region) and a Gaussian peak (peak region). The wiggles in the Trace L data reflect the impact of moving in front of, and then between, adjacent PMTs. The trace 2 distribution varies by 14% at the extremes of x compared to the center.

(a) The β data is problematic, as the mean of the amplitude distributions reflects signal size, subtle differences in the distribution for different interaction locations, and potentially threshold effects. Because of the difficultly of reliably interpreting the β data results, the location of a Compton peak of a gamma source was used to monitor the gain of the signal as a function of interaction location.

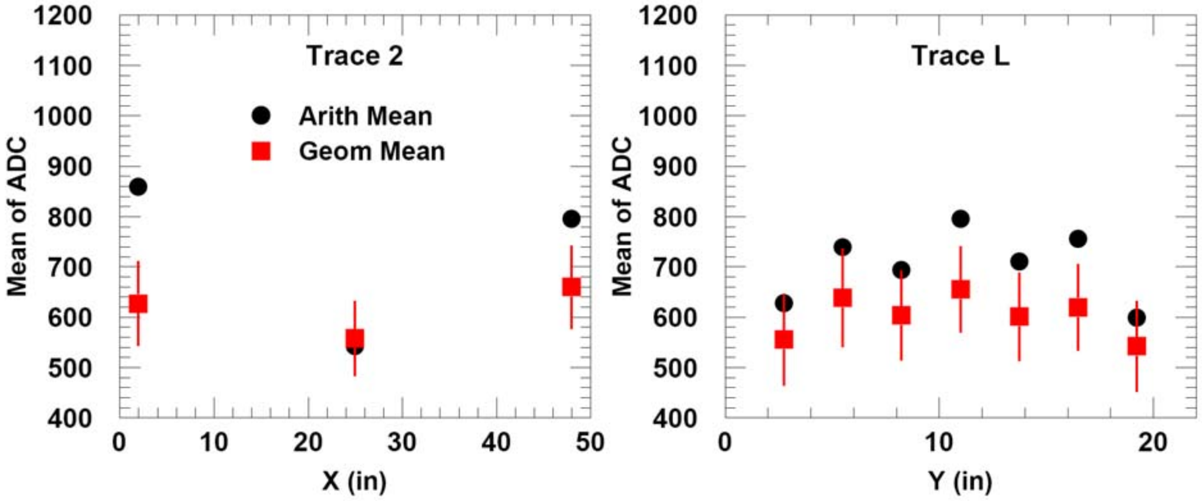

Figure 8.12. Plots of Compton peak positions versus various locations for the six PMT setup. The left plot is for trace 2 and the right for trace L. No ADC Overflows were permitted for this collection of data. The vertical red lines denote the width of the Compton peak, which is roughly consistent for all types of calculated means.

A demonstration of the potential dependence of the signal amplitude on ΔT is provided in Figure 8.13. The 2 PMT detector setup was exposed to a distant ^{22}Na uncollimated source. The plot on the left is a 2-dimensional histogram of the arithmetic mean versus T_2-T_5. This plot was divided into 10 subplots along the T_2-T_5 axis, and each of these subplots was projected onto the arithmetic mean axis for a series of one dimensional histograms referred to as *slices*. For each slice, the peak near 1600 was determined from a Gaussian fit. The mean of the Gaussian is shown on the left plot as the black and red dots. The uncertainty in the fitted mean of the peak is also plotted, but only for the outer two slices are the uncertainties larger than the symbol plotted. A symmetric quadratic fit to the points yields the red curve shown in the left plot. The right plot shows the 5 slices for which T_2-T_5>0. These histograms clearly show the Compton peak shifting and broadening as T_2-T_5 becomes larger. This drifting of the peak is noticeable but not large. The widening of the peaks as T_2-T_5 becomes larger may be due to an increased sensitivity to the *y* position of the interaction point near the edges of the scintillator (no TDC cuts to remove “corner” events were used).

Another comparison of the arithmetic and geometric means is shown in Figure 8.14. This plot compares the arithmetic and geometric means for distant uncollimated ^{207}Bi source on the six PMT setup. In the 2D plots, the arithmetic mean appears to have a slightly stronger dependence on T_2-T_5 than the geometric mean. In the 1D plot, the Compton peak of the arithmetic mean is at a slightly higher location and is slightly wider than for the geometric mean. The standard deviations of the Gaussian fits to the Compton peaks around channel 1300 are shown in the plot legend.

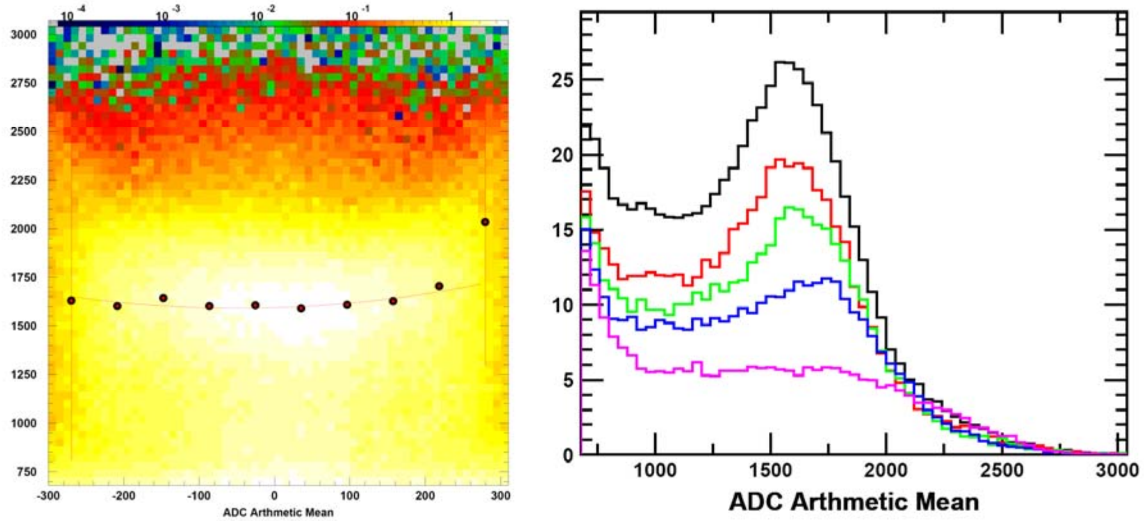

Figure 8.13. Plots from ^{22}Na data with the 2 PMT setup. The plot on the left shows the ADC arithmetic mean (ordinate) versus T_2-T_5 (abscissa). The points represent fits to the slices, and the red curve is a quadratic fit to the points. The plot on the right shows histograms of the ADC arithmetic mean for slices 6-10. The abscissa of this plot is counts per histogram channel. The amplitude of the Compton peak at 1600 decreases as the slice number increases. See text for futher description.

It should be noted the PMT gains were not perfectly matched. A few different ways to determine the correction to finely gain-match the PMTs were investigated. The variations in the gain corrections were usually less than 10%, and the corrected gains had almost no impact on the observed results. For this reason, the gain corrections were not applied to the data for any of the analysis.

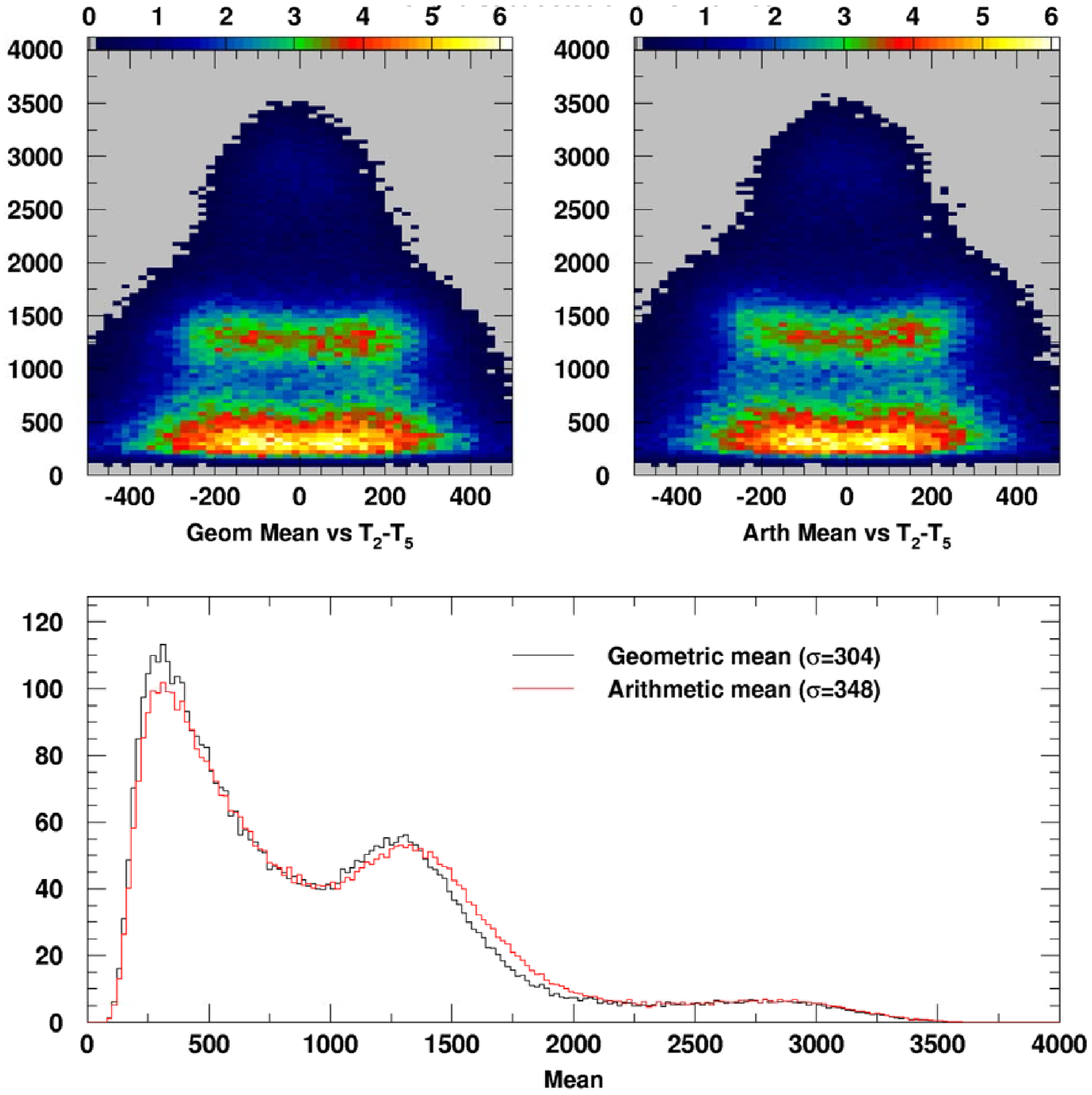

Figure 8.14. Comparison of geometric and arithmetic means for the 6 PMT setup with a distant uncollimated ^{207}Bi source. The top two plots show the geometric mean (abscissa, left) and arithmetic mean (abscissa, right) versus T_2-T_5 (ordinate, both plots) The bottom plot shows histograms of the two means overlaid. The abscissa of the bottom plot is counts per histogram channel.

8.5 Amplitude Correction

The next step is to determine the amplitude correction. Several different types of data have been collected that may be helpful to determine the correction. Measurements were conducted with beta sources, usually ^{90}Sr, at various locations on the top of the scintillator. Measurements were also conducted with gamma sources, sometimes collimated and sometimes uncollimated, either at various locations on top of the scintillator or suspended above the center of the scintillator to approximate a distant point source and to provide nearly uniform irradiation of the scintillator.

Figure 8.15 is a comparison of different ways to extract the *ΔT* dependence of the signal amplitude from the beta source data. Three basic approaches to determine the signal amplitude were investigated: determine the mean of the histogrammed signal, determine the channel in which the observed spectrum is a specified height, or determine the channel above which the spectrum integrates to a specified number of counts. These approaches are referred to as the "mean," the "equal height" and the "equal area" approaches, respectively. One set of points from the gamma slice technique, which will be discussed later, is also shown for comparison. In the figure, the means of the histograms of the geometric mean with and without software gain matching of the PMTs are plotted; there is essentially no difference between the two. While the techniques agree for the middle third of the time difference region, they disagree significantly for the outer thirds. The equal height and equal area approaches are consistent with each other; however these approaches are sensitive to variations in both the signal amplitude and collection efficiency due to incidence location. Variations in the detector efficiency near the extremes in *x* may explain the dramatic down turn for the outer portions. The mild disagreement between the means of the betas and the means of the gamma slices near the edges is because the gamma slices are averaged over all *y* whereas the beta means are for a single *y* location. This difference is most important at the extreme *ΔT* of the scintillator.

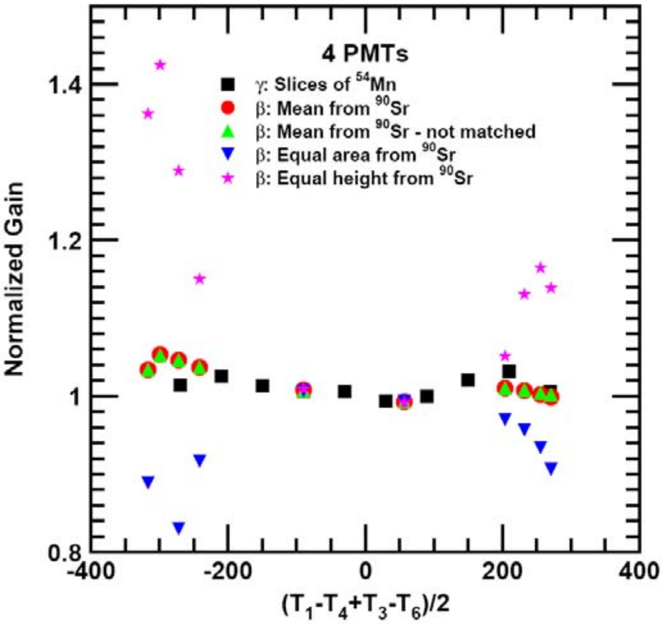

Figure 8.15. Comparison of techniques to determine the signal amplitude from the geometric mean of the PMTs for the 4 PMT setup. Most of the techniques are for a beta source. The red and green markers show the means of the histograms of the geometric means with and without software gain matching, respectively. The blue and the magneta points are for the equal area and equal height approach.

A comparison of the signal amplitude calculated with the geometric mean as a function of *ΔT* for various gamma sources is shown in Figure 8.16. For all gamma analyses, the location of the Compton peak is used. These locations are then normalized by the Compton peak location for the central *ΔT* value (either central TDC difference or source location near the central *x*). The same slicing method as discussed for the two PMT case for Figure 8.13 is used for most examples. ^{54}Mn is shown in red for both the 4 PMT setup and the 6 PMT setup. ^{207}Bi (not background subtracted) and ^{137}Cs for the 6 PMT setup is also shown. In addition to the sliced gamma data, collimated gamma source (^{137}Cs) and discrete-location beta source results are also shown in Figure 8.15. This data was collected over a period of about 5 months. The discrete-location gamma source data set is dramatically different from all other data. Although it should not explain this difference, the PMT gains were set differently for this data than for the later six PMT gamma source data. Quantitatively, the other data sets do not agree well, although the range of the results implies that there is only about a 5% variation of the signal amplitude determined from the geometric mean on ΔT.

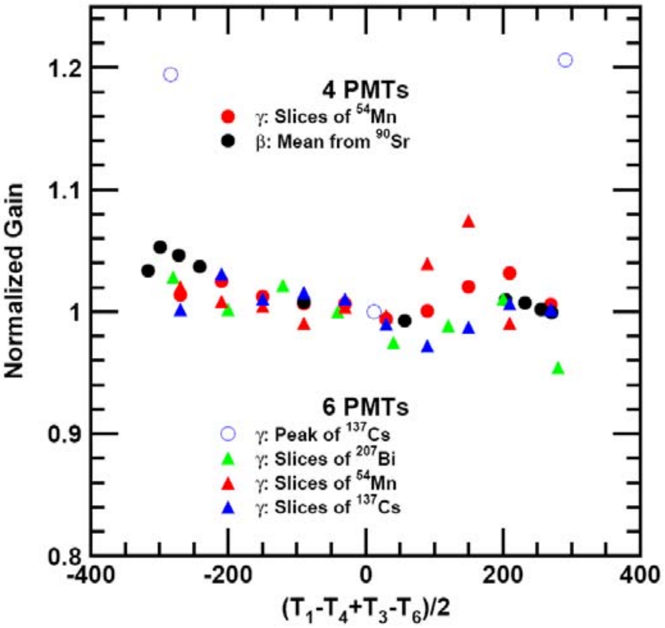

Figure 8.16. Comparison of amplitude dependence on TDC differences for different gamma sources and different PMT setups.

As a simple first attempt, the variation of the signal amplitude with interaction position was corrected using a symmetric quadratic function of T_2-T_5. The amplitude of the correction was taken from the discrete-location ^{137}Cs data for the six PMT setup; specifically, the multiplicative correction was 20% for $|T_2\text{-}T_5| = 400$. A range of correction amplitudes were investigated with the philosophy that the optimum correction should yield the minimum peak width and maximum peak-to-valley ratio. A sample of the results is shown in Figure 8.17. The scale factor of 0.0 corresponds to no correction, whereas a scale factor of 1.0 corresponds to the full correction described above.

The width and peak-to-valley ratio versus the correction factor for a ^{137}Cs and a ^{207}Bi source are shown in Figure 8.18. Results both with and without the no corners cuts are shown. The width is defined as the width of the peak at 80% of the maximum divided by the peak location multiplied by 100. In general, the no corners cut makes the peak narrower and improves the peak-to-valley ratio. Neither of these measures varies strongly with the correction factor, although there appears to be a slight preference in most of the sets of data for a correction of 0.2. However, it could be argued as vigorously that these results show no optimum correction factor. The conclusion is that over this range of correction factors, the applied correction has no significant impact on the energy resolution.

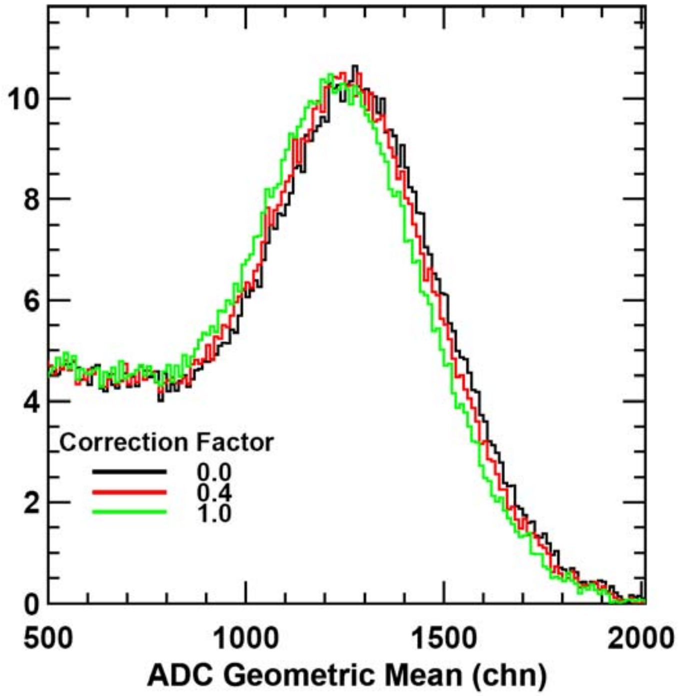

Figure 8.17. **Histograms of ADC geometric mean histogram of the Compton peak from ^{137}Cs source after applying the position correction with various factors for correction amplitude. Abscissa is counts per histogram channel.**

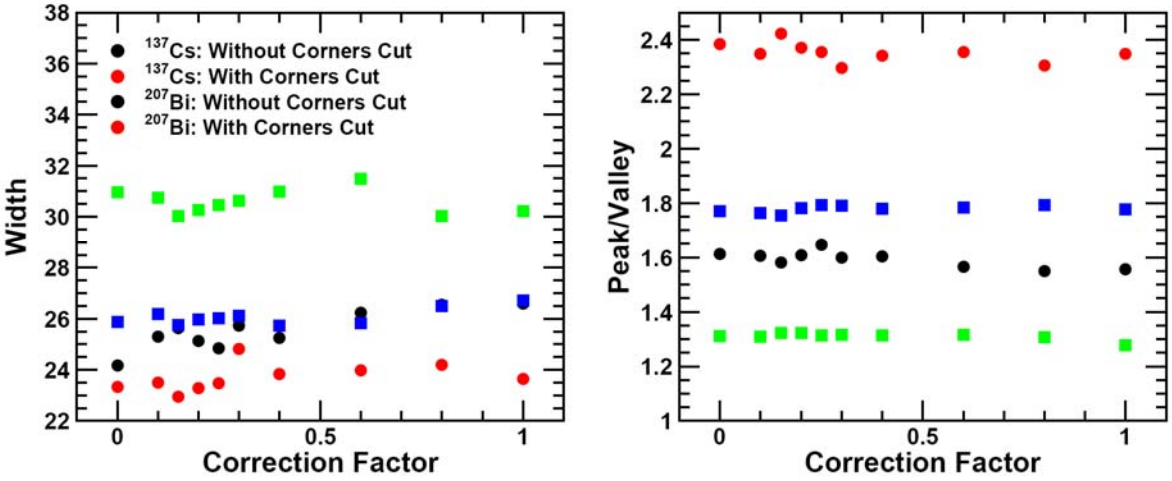

Figure 8.18. **Plots of the widths (left) and peak/valley (right) for various correction factors for the amplitude of the position correction. Results from two sources, ^{137}Cs and ^{207}Bi, are shown as well as results with and without applying the “No Corners” cut.**

A Monte Carlo investigation was conducted in an effort to understand the ineffectiveness of the position correction. It was assumed that the measured signal amplitude had a Gaussian distribution peaked at channel 400 and had a sigma of 100. The centroid of this distribution was allowed to vary quadratically with ΔT with the same amplitude and over the same range in ΔT as the simple correction applied to the data with the correction factor equal to one. This distribution was generated randomly. The impact on the energy distribution will depend on the ΔT distribution. Two distributions were investigated: a flat distribution which would provide the maximum sensitivity to the position correction and an actual distribution taken with a distant ^{137}Cs source. Histograms of the resulting signal amplitude distributions are shown in Figure 8.19. For the realistic ΔT distribution, the width increases by only 2.2%, but the peak centroid shifts 3.8%. For the flat distribution, which should be considered as a worst case scenario, the width increases by only 6.8% and the centroid shifts by 9.4%. Thus, given the worst case flat distribution ΔT distribution and a correction that is probably too large considering Figure 8.16, the impact of the position dependence of the incident location on the signal amplitude is only 6.8%, thus supporting the observation that spectral information is not significantly enhanced by correcting for incident location.

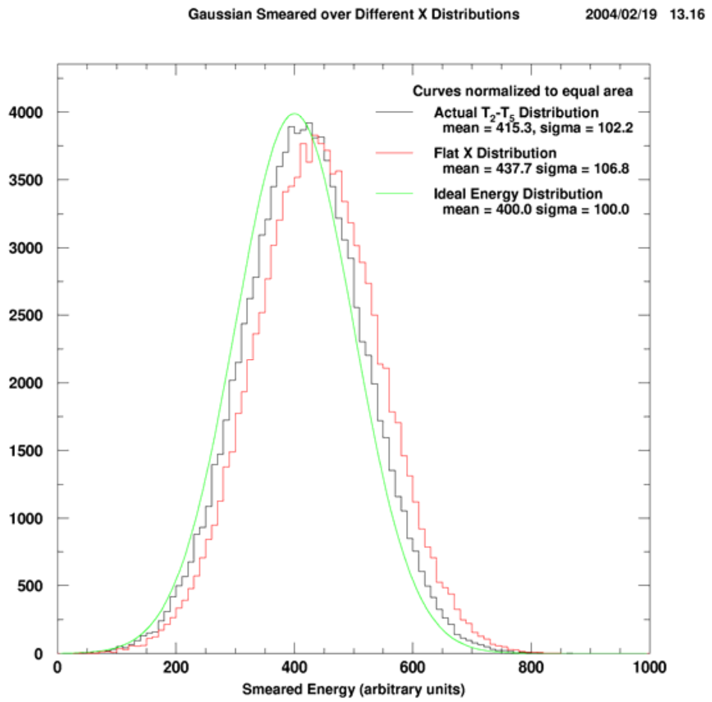

Figure 8.19. Histograms of numerical model of effect of position dependence of the signal amplitude. Abscissa is counts per histogram channel.

9.0 Conclusions

The primary objective of the ALPS project was to investigate technical paths forward to extracting as much low-energy gamma-ray detection sensitivity and source-characterization information from plastic scintillator as possible. The three predominant themes of these investigations included the following:

- Maximize light collection efficiency from a single large-area sheet of plastic scintillator, and optimize hardware event trigger definition to retain detection efficiency while exploiting the power of coincidence to suppress single-PMT “dark current” background;
- Utilize anti-Compton vetoing and supplementary spectral information from a co-located secondary, or “back” detector, to both (1) minimize Compton background in the low-energy portion of the “front” scintillator’s pulse-height spectrum, and (2) sharpen the statistical accuracy of the front detector’s low-energy response prediction as implemented in suitable energy-windowing algorithms; and
- Investigate alternative materials to enhance the intrinsic gamma-ray detection efficiency of plastic-based sensors.

Insofar as low-energy detection sensitivity is concerned, the ALPS project demonstrated only modest improvements in PVT minimum detectable activity (MDA) as functions of (1) the number of PMTs participating in an (optimal) hardware trigger, and (2) the availability of anti-Compton veto and/or supplementary spectral information from a co-located monolithic detector. In particular, although single-sheet readout schemes consisting of two or more PMTs were shown to have markedly greater sensitivity than a single-PMT readout scheme, relatively little further improvement in detection sensitivity resulted from increasing the number of PMTs beyond two. This evaluation depends to some extent upon the MDA algorithm used and, in turn, upon the portal monitor application of interest. For large-vehicle traversals of RPMs in which the vehicle itself significantly attenuates the terrestrial background incident on the sensor, the use of an energy-windowing algorithm is intended to mitigate the effect of “baseline suppression” that can severely limit the sensitivity of simple gross-count algorithms. The improvement in light collection efficiency and energy-deposition resolution afforded by the ALPS sensor’s increased PMT coverage was not found to yield corresponding sensitivity benefits to this type of two-window algorithm. However, as shown in section 6.2.1, an alternative spectral algorithm that assumes an *unattenuated* terrestrial background distribution during the RPM traversal can benefit significantly from the reduction in ROI width afforded by improved resolution. The effects of baseline suppression can be safely ignored in this limit, which is expected to describe most passenger-automobile and human foot-traffic scenarios to a reasonable approximation. Enhanced-resolution PVT readout schemes, such as those developed in this project, may well offer an attractive means of improving source detection sensitivity in sensors intended for these applications.

The impact of anti-Compton vetoing on source detection sensitivity in the presence of typical terrestrial backgrounds was found to be decidedly modest, whether implemented using standard PVT or a Cherenkov plastic slab as the co-located “back” detector. Exploiting spectral information from the back detector, in contrast, afforded some noticeable enhancement in detection sensitivity, on the order of 10% to 20% for ^{57}Co and ^{133}Ba sources, respectively. The experimental work performed in this project alone, however, cannot rule out the possibility that similar (or better) sensitivity enhancements could be achieved simply by using a single scintillator slab with substantially greater thickness than the 2” (5.08

cm) slabs used in the ALPS sensor. In general, the detection sensitivity analysis presented in section 6 offers little compelling evidence for dual-sheet architecture (or anti-Compton vetoing) as an effective next-generation technology for monolithic-slab gamma-ray portal monitors. However, it should be noted that this analysis does not fully exploit the measurement result, cited in the conclusion of section 4, that the background-suppression effect improves with increasing gamma-ray energy. A dual-sheet sensor may provide an effective technique for suppression of low-energy background generated by high-energy gammas emitted by naturally occurring radioactive material (NORM) sources. Because the MDA analysis of section 6 takes into account only the (typical) terrestrial background distributions measured by the ALPS II in the experimental campaign, the value of this background mitigation technique for high-energy NORM sources was not fully explored. It is also worth pointing out in passing that dual-sheet geometry may represent a promising approach to achieving cost-effective, large-area fast neutron spectroscopy by an appropriate combination of time-of-flight (TOF) and recoil-proton pulse height methods. Follow-on activities to the current project have, in fact, successfully demonstrated use of the ALPS II apparatus for fast neutron detection by the TOF method; this research is described elsewhere [Jordan et al., 2005].

By far the most promising result of the project involves the implications of enhanced energy deposition resolution for improved source characterization capability, rather than enhanced low-energy detection sensitivity *per se*. PVT suffers from two significant disadvantages as a spectroscopic detector material: low average Z (and thus, correspondingly poor photopeak fraction for reasonable sensor thickness), and poor energy resolution. As described in section 8 of this report, investigations of Pb-loaded PVT offer little promise for this particular material as a practical means of remedying the photopeak efficiency shortfall in large-area, monolithic-geometry sensors. However, as Figure 1.2 and Figure 1.3 indicate, there is no question that a sufficient increase in light collection efficiency can yield a dramatic improvement in energy-deposition resolution (on the order of 60% improvement, for a six-PMT readout in comparison to a single PMT) for a large-area plastic scintillator sensor. That this resolution enhancement can be achieved without sacrificing intrinsic detection efficiency, via application of an appropriate “multiplicity” trigger in which any two PMTs firing in coincidence suffices to register a valid event, is another significant achievement of the project. We do not suggest that this improvement in energy resolution remedies entirely the lack of significant photopeak detection efficiency in PVT (in any but the thickest monolithic slabs), but it does encourage investigation of alternative spectroscopic techniques that seek to extract maximal source identification information from the shape of the Compton continuum. Sensor applications that require identification of, or discrimination among, a limited set of gamma-ray emissions from a few candidate sources of interest, as measured under relatively well-understood background conditions, might well benefit from a spectroscopic characterization technique that exploits a relatively high-resolution measurement of the shape of the Compton edge. Although a thorough investigation of Compton-continuum spectroscopy techniques fell somewhat outside the ALPS project’s scope, the project has helped to quantify the extent to which reasonably practical enhancements in the light-collection efficiency of large-area PVT sensors can be expected to improve their measurement of the Compton continuum.

10.0 References

[Jordan et al. 2003] Jordan DV, BD Geelhood, PL Reeder, DL Stephens, RC Craig, and JI McIntyre. 2003. *Progress Report on the Advanced Large-Area Plastic Scintillators (ALPS) Project*. PNNL-14283, Pacific Northwest National Laboratory, Richland, WA.

[Jordan et al. 2005] Jordan DV, PL Reeder, M Cooper, KR McCormick, AJ Peurrung, GA Warren. 2005. *Methods and Instruments for Fast Neutron Detection.* PNNL-15214, Pacific Northwest National Laboratory, Richland, WA.

[Jordan et al. 2007] Jordan DV, PL Reeder, KR McCormick, DL Stephens, LC Todd, GA Warren, BD Geelhood, JM Alzheimer, SL Crowell, WA Sliger. *Advanced Large-Area Plastic Scintillator (ALPS) Project (ALPS): Final Report.* PNNL-14283 Final. 2007.

[Reeder et al. 2003] Reeder PL, DL Stephens, DV Jordan, RC Craig, and B Geelhood. 2003. *Progress Report for the Advanced Large-Area Plastic Scintillator (ALPS) Project: FY 2003 Final*. PNNL-14490, Pacific Northwest National Laboratory, Richland, WA.